UNIVERSIDADE
BEIRA INTERIOR

CFD Modelling of 3D Effects in Cycloidal Rotors

A Performance Analysis Assessment with Design Guidelines

Mehdi Habibnia Rami

Tese para obtenção do Grau de Doutor em

Engenharia Mecânica

(3º ciclo de estudos)

Orientador: Prof. Dr. José Carlos Páscoa Marques

Covilhã, setembro 2021

Jury of the Doctoral Exam

The doctoral exam took place on September 6, 2021, at 14:30, with a jury consisting of the following members:

Doctor Paulo Jorge dos Santos Pimentel de Oliveira, Full Professor at Universidade da Beira Interior;

Doctor José Carlos Fernandes Teixeira, Full Professor of school of Engineering, Universidade do Minho;

Doctor Luís Manuel de Carvalho Gato, Full Professor at Instituto Superior Técnico da Universidade de Lisboa;

Doctor José Carlos Páscoa Marques, Associate Professor at Universidade da Beira Interior;

Doctor António Manuel Gameiro Lopes, Assisstant Professor at the faculty of Science and Technology of Universidade de Coimbra;

Doctor Miguel Ângelo Rodrigues Silvestre, Assisstant Professor at Universidade da Beira Interior.

Dedication

”To my lovely family and all the ones who were a positive torch in my life”

Acknowledgment

First of all I would like to thank my supervisor, Prof Jose Páscoa for believing in me and for giving me the great opportunity to do this PhD. Thank you Prof Páscoa, as much for the entire thing that you have provided for me to work. I really enjoyed the moments that we had conversations about work and future and everything, specially the moments that you put me back in the correct way of thinking. It was a great pleasure and honor to have your support. It will be a pleasure for me to have opportunities to do research under your supervision.

I want to thank all my colleges (Dr. Mahdi Abdollahzadeh, Dr. Fred Rodrigues, Filipe Dias, Reza Pendar, Odelma Teixeira, Hugo Canilho, Dr. Periyadurai and Dr. Amine Benmousa) in the ClusterDEM lab that made me happy and made the working condition full of energy and happiness. Indeed, besides being colleagues you were my truly friends that helped me to adapt myself to the new life in Covilhã.

This project is mainly supported by the project Centro-01-0145- FEDER-000017—EMaDeS—Energy, Materials and Sustainable Developement, cofinanced by the Portugal 2020 Program (PT2020), within the Regional Operational Program of the Center (CENTRO2020) and the European Union through the European Regional Development Fund (ERDF). I would like to thank the support from European Union project of Cycloidal Rotor for Optimized and Propulsion (CROP) within the 7th Framework Programme under Grant No. 323047. This work was carried out in C-MAST–Center for Mechanical and Aerospace Sciences and Technologies, Research Unit No. 151.

Thank You All

Resumo

O rotor cicloidal (ciclorotor) é um sistema propulsivo revolucionário que, até à data, não foi alvo de um estudo suficientemente sistemático, em particular no que diz respeito aos seus diferentes aspetos de projeto e aplicações. Como tal, a presente investigação apresenta um estudo sobre a viabilidade do conceito de propulsão a ciclorotor para um veículo aéreo não tripulado (UAV) capaz de pairar, sendo este estudo feito a partir de modelação usando dinâmica de fluidos computacional (CFD) e uma rede neural artificial (ANN). As simulações numéricas ou CFD incluem medições do desempenho e do campo de escoamento de um ciclorotor com 0,8 metros de envergadura e igual diâmetro. As simulações consideram diversas condições de operação e várias fases de voo. A capacidade de pairar, as fases de descolagem e de voo horizontal, o funcionamento a baixa altitude, e ainda os efeitos tridimensionais (3D), neste caso produzidos pelas placas finais nas laterais do ciclorotor estudados para esta escala. Para além disso, é proposto um sistema inovador de propulsão que recorre à combinação de dois ciclorotores e de um sistema de asa dupla com atuadores a plasma, o qual foi objeto de submissão de patente. São apresentadas numerosas simulações para os diferentes tipos de estratégias de voo, e de condições de funcionamento, as quais foram realizadas e gravadas numa base de dados de resultados de CFD. Subsequentemente, toda a informação obtida a partir do cálculo numérico é processadas em algoritmos ANN, tendo em vista uma análise e otimização adicional, em particular sobre todas as condições e modos de funcionamento avaliados. A análise ANN permite propor, com elevada eficácia computacional, as condições ótimas de operação para os vários tipos de funcionamento já mencionados, tendo por base os parâmetros de carga, os coeficientes das forças, e de figura de mérito, com vista a analisar o desempenho. As condições de operação do presente estudo incluem ainda uma gama de ângulos de oscilação da inclinação das pás, e de velocidades de rotação, as quais são definidas em função do modo de voo, o qual define os diferentes regimes, onde se incluem o pairar, o voo de baixa altitude, ou ainda descolagem e voo horizontal. Através de medições sistemáticas e de análise das variáveis de desempenho aerodinâmico foi possível compreender o efeito da velocidade de rotação, amplitude de inclinação das pás, a posição do eixo de inclinação das pás, a velocidade de cruzeiro/voo horizontal, a velocidade de decolagem, isto tudo a diferentes níveis de altitude. As medições de tração demonstraram ser distintas para diferentes regiões do trajeto circunferencial do ciclorotor. O perfil de NACA 0012 foi utilizado para todas as simulações realizadas durante o presente trabalho. Na base da análise ANN, foi considerada uma metodologia de controlo ativo, o que significa que tempos de oscilação de pás, definidos de forma inteligente, são propostos para cada uma das condições de funcionamento, o que resulta num maior desempenho aerodinâmico e num aumento de eficiência propulsiva. Isto é conseguido mantendo a geometria de ciclorotor mas, ao invés de modificar a inclinação das pás em tempos fixos do ciclo de rotação, propõe-se um funcionamento alternativo com variação dos tempos de oscilação dos respetivos ângulos de inclinação de acordo com o posicionamento azimutal da pá. Esta estratégia permitiu obter um incremento significativo no rendimento global do ciclorotor para cada modo

de voo e respetivas condições de funcionamento. No que diz respeito à atração do jato de escoamento descendente, o qual é libertado pela parte inferior do ciclorotor, é apresentada uma patente que pretende direcionar o jato descendente para um canal, o qual é constituído por um sistema de asa dupla que é colocado entre os ciclorotores frontal e traseiro, sendo estes dois os constituintes do inovador sistema de propulsão. Portanto, ao invés de simplesmente libertar o jato descendente como num ciclorotor tradicional, este é aqui processado e conduzido pelas asas para o rotor traseiro, o qual funciona a maior velocidade angulares e tem uma menor escala comparativamente ao ciclorotor frontal.

Palavras-chave

Rotores Cicloidais, CFD, OpenFOAM, Rede neural artificial, Otimização, VTOL, UAV, Voo horizontal, Fase de decolagem, Cruzeiro, Pairar.

Abstract

The cycloidal-rotor (cyclorotor) is a revolutionary propulsion system that has not been systematically studied in the past in terms of its different aspects and applications. Therefore, the current research presents the viability of the cyclorotor concept for powering a hovering-capable unmanned scale aerial vehicle (UAV) through both computational fluid dynamics (CFD) and also artificial neural network (ANN) analysis. Numerical or CFD simulations included both performance and flow field measurements on a cyclorotor of span and diameter equal to 0.8 meter. The simulations consist of diverse operating conditions and under various flight phases. Hovering capabilities, forward-flight and lift-up phases, operating under at close-ground flight levels, and three-dimensional (3D) effects of the end-plates in the sides of cyclorotor in this scale. Furthermore, a novel propulsion system by using a coupled combination of two cyclorotors and pair-wing system by using plasma actuators is also presented in the current study as a recent patent. Numerous simulations for various types of flight strategies and operating conditions are performed and recorded as a database from the CFD phase. Subsequently, all the data from the numerical computations are processed in ANN algorithms for further analysis and optimizations for all of the assessed operating conditions in all modes. The ANN analysis could effectively propose an optimal condition for all the above-mentioned operations on the basis of the loading parameters, force coefficients, and figure of merit for efficiency analysis. The operating conditions in the current study refers to the ranged of pitching oscillation angles, and rotation speed, and the flight mode defines the different flying regimes such as hovering, close-ground, or lift-up and forward-flight concepts. Systematic and aerodynamic performance measurements and analysis have been conducted to understand the effect of the rotational speed, blade pitching amplitude, pitching axis location, forward/cruise speed, take-off speed, different ground height-levels. Force measurements showed to be distinctive in different regions on the circular trace of the traversing blades. The NACA 0012 profile is considered constantly for all the simulations in the current work. On the basis of ANN analysis, an active control methodology, meaning that smart pitching schedules are proposed for each of the operating conditions, that results in higher aerodynamic performance and efficiency augmentation. This happens by keeping the cycloidal definition in these rotor types, but instead of running the blades in a constant schedule over cycles, we proposed an alternative varying pitch schedule in accordance to the blade position which is called azimuth angle. This revealed significant enhancement in the overall cyclorotor efficiency at each flight mode and operating condition. Concerning the attraction of downwash jet flow from the bottom region of the cyclorotors, the present patent illustrates to guide the downwash jet through a nozzle duct which is consisted of double wings in the middle of two cyclorotors in the front and rear part of the propulsion mechanism. Thus, instead of washing away the downwash jet, we process it and make a possible running flow to face the rear rotor which operates at higher angular velocities and smaller scale compared with that of front cyclorotor.

Keywords

Cycloidal Rotors, CFD, OpenFOAM, Artificial Neural Network, Optimization, VTOL, UAV, Forward Flight, Take-off phase, Cruise, Hover.

Contents

List of Figures

List of Tables

Nomenclatures

N	number of blades in cyclorotor
R	cyclorotor radius
c	blade chord
A	rectangular projected area
b	span
Ω	rotation speed
θ	pitching angle
δ	in-cage flow inclination angle
α	in-cage downward flow angle
β	downwash flow angle
Ψ	azimuthal angle
C_p	power coefficient
C_T	thrust coefficient
Fx	horizontal force
Fy	vertical force
H	height
T_N	net thrust of the cyclorotor
P.L	power loading
D.L	disk loading
F.M	figure of merit
ANN	artificial neural network
AC	active control
ρ	density
U	flow field velocity
N_h	number of hidden neurons
$\theta(\Psi)$	pitch angle of the blade at the corresponding azimuth
$\theta_{(top)}$	the maximum pitch angle at the top positions of cyclorotor
$\theta_{(bottom)}$	the maximum pitch angle at the bottom positions of cyclorotor
P	pitching oscillation angle
P_N	net power consumed by cyclorotor while operating
M	momentum
F_X	horizontal force produced
F_Y	vertical force produced
Φ	net thrust vector angle
R_C	relation coefficient
A_P	predicted value
a	measured value
μ_{A_P}	mean predicted value
μ_a	mean measured value
X, Y, Z	axis coordinates

VTOL	vertical take-off and landing
STOL	short take-off and landing
EUS	external up-stroke
EDS	external down-stroke
IUS	internal up-stroke
IDS	internal down-stroke
R_{fr}	front rotor radius
R_{rr}	rear rotor radius
O_{fr}	front rotor center
O_{rr}	rear rotor center
C_{Bfr}	blade chord of front rotor
C_{Brr}	blade chord of rear rotor
α_{TW}	top-wing angle with horizontal axis
α_{BW}	bottom-wing angle with horizontal axis
E_1	entrance length of pair-wing (distance between the leading edges of top and bottom wings)
E_2	exit length of pair-wing (distance between the trailing edges of top and bottom wings)
W_1	the horizontal length between the center points of the front and rear cyclorotors
W_2	the horizontal length between the center points of the front cyclorotor and the bottom wing leading edge
W_3	the horizontal length between the leading edges of top and bottom wings
W_4	the horizontal length between the trailing edges of top and bottom wings
W_5	the horizontal length between the center points of the front cyclorotor and the bottom wing trailing edge
H_1	the vertical length between the center points of the front cyclorotor and the top wing leading edge
H_2	the vertical length between the center points of the front cyclorotor and the bottom wing leading edge
H_3	the vertical length between the top and bottom wing trailing edges
H_4	the vertical length between the center points of the rear cyclorotor and the top wing trailing edge
L_{TW}	chord length of the top wing
L_{BW}	chord length of the bottom wing
$D_{AMI(}B_{1)}$	AMI circle diameter of the blades in front rotor
$D_{AMI(}f_{1)}$	AMI circle diameter of the rotating frame in front rotor
$D_{AMI(}B_{2)}$	AMI circle diameter of the blades in rear rotor
$D_{AMI(}f_{2)}$	AMI circle diameter of the rotating frame in rear rotor

Chapter 1

Introduction

In recent years, interest has been growing in vertical take-off and landing (VTOL) vehicles, which can prove to be an extremely important asset to various applications in the future, especially where the crafts are land terrain restricted. Rescue missions, pay-load carriages in dense forests, fire fighters, surveillance, high maneuvering missions and so on are a short list of applications in this regard. In term of their operational benefits and performances, cycloidal rotors can be proposed as possible alternatives for the conventional screw propeller used in helicopters.

1.1 Literature Survey

The tendency to equip aircraft with cycloidal rotors as means of Vertical Take-Off and Landing (VTOL) propulsors has increased in recent years [2]. Considerably lower noise production and more stable hover and vertical displacements in comparison with those of conventional screw propellers, as used in helicopters, are the main reasons to witness this tendency.
Aircraft being capable of VTOL and hover are increasingly emerging in various critical and routine applications. Rescue missions in roads and environmental disasters, observance and monitoring-based carriers, surveillance cameras, payload carriage in situations like transmitting forest tree are, just to mention a few examples. Within VTOL category, numerous designs have been proposed along the years. Helicopters are the most typical crafts in this kind, but concerning the thrusting mechanism, several alternatives are yet in hand. Nevertheless, each of them has their own strength and weakness points, thus, one should select a design to utilize it toward the desired output and try to overcome the drawbacks and sophistication in this regard.
The current work deals with the cycloidal rotor which was initially introduced as a novel conceptual design of propellers by a German origin researcher Fredric Kurt Kirsten. His collaboration with Boeing company then led to Kirsten-Boeing propellers reported in 1926 [3]. This was considered as the onset of a new practical generation of blades operating in a cage-like assemble which was totally different from those of conventional propellers, in terms of exerting all sections of blades in span-wise direction a fairly equal action into the fluid. There exist some research reports concerning cyclorotors within the first two starting decades until 1940s. It was by then the subject of many research that was afterwards lost for a long period of about 50 years. In an effort from BOSCH Aerospace incorporation in 1998, the operational efficiency of a UAV size cyclorotor was examined and built using modern methods and knowledge. With their full-scale design, the most astonishing feature of their report was the considerably low noise-pollution characteristic of the current

operating mechanism [4]. The advent of more efficient coding and computing resources made the numerical investigations on this state of the art complicated mechanism more feasible since the era of late 20th century. In Japan, Onda et al. [5] whose work was mainly on Lighter Than Air (LTA) vehicles, like airships, have also started to utilize the cycloidal rotors in their configurations instead of conventional propeller-type thrusters. It actually was a modified prototype of ACROSTAT airship design which was previously reported [6]. Fast functioning and better control-ability due to employing these rotors were the attained enhancements observed in their design from what they have declared with conventional propellers [7, 8, 9].

Parametric optimization of cyclorotor is pursued by Hwang et al. [10, 11]. They intended to track the optimizing steps from the very basic parameters like number of blades, sizes, radius, spar positioning within blades, number of plies by which the blades are coated, weight, etc, all considered simultaneously in their survey. Experimental tests, CFD approach and Genetic algorithm were some methods they worked with. In another work, which is being conducted both experimentally and numerically, the authors introduced a somewhat new design of the operating cyclocopter [12]. They have equipped the craft with four functioning rotors acting in two pairs, with each of these running on opposite directions to counteract the resultant undesired torque. Their design intended to provide up to 166 N thrust. Their experiment showed up about 15 percent higher power consumption than the design expectations. In spite of unstable vertical flight control, they have indicated that a praising achievement was attained in hovering regime.

In an article in 2005, Yun et al.[13] performed a predominantly analytic study in order to reveal a clear insight of how to determine the thrust vectoring in cycloidal rotors. They applied ”eccentricity” in both terms of magnitude and phase angle in their parametric designs. Applying eccentricity to the operational process enables the controlling mechanism to actively shift the resultant thrust vector to the desired direction. One of the main studies can be attributed to [1] and a complementary in [14], which was accompanied by experimental, numerical and analytical investigation on a typical UAV type cyclocopter. Prior to carrying out the tests, they have gone through analytics to identify the rotor specifications which would best fit in terms of performance for a UAV by using a modified version of Stream-tube model for a more accurate response in cyclorotors, this was initially developed for Darrieus wind turbines [15]. Thus, they have manifested the following five major results drawn from their study pertinent to the dominant flow acting through the rotor (Fig.1.1):

1. The inflow velocity at 0° and 180° of azimuthal angles is about zero.

2. The inflow moves vertically downward when passing the top half circle, and deflects towards the rotation direction as it passes the bottom half circle path.

3. If considering counter-clockwise direction and giving positive and negative signs to the inflow and outflow, respectively, the arc between 0° to 270° in azimuth is posi-

tive and from the latter up to 360° consists predominantly of negative sign.

4. The occurrence of tilted downwash while exiting the rotor stems from the inherent flow behavior from within the rotor itself.

5. Another very important finding was that the curvilinear pattern of the exerted flow, to the cyclorotor, results a cambered-like behavior in the blades whereas in fact, they are all symmetrical. This issue is assumed as the key source of higher lifting force attained from bottom half of rotor compared to the top one.

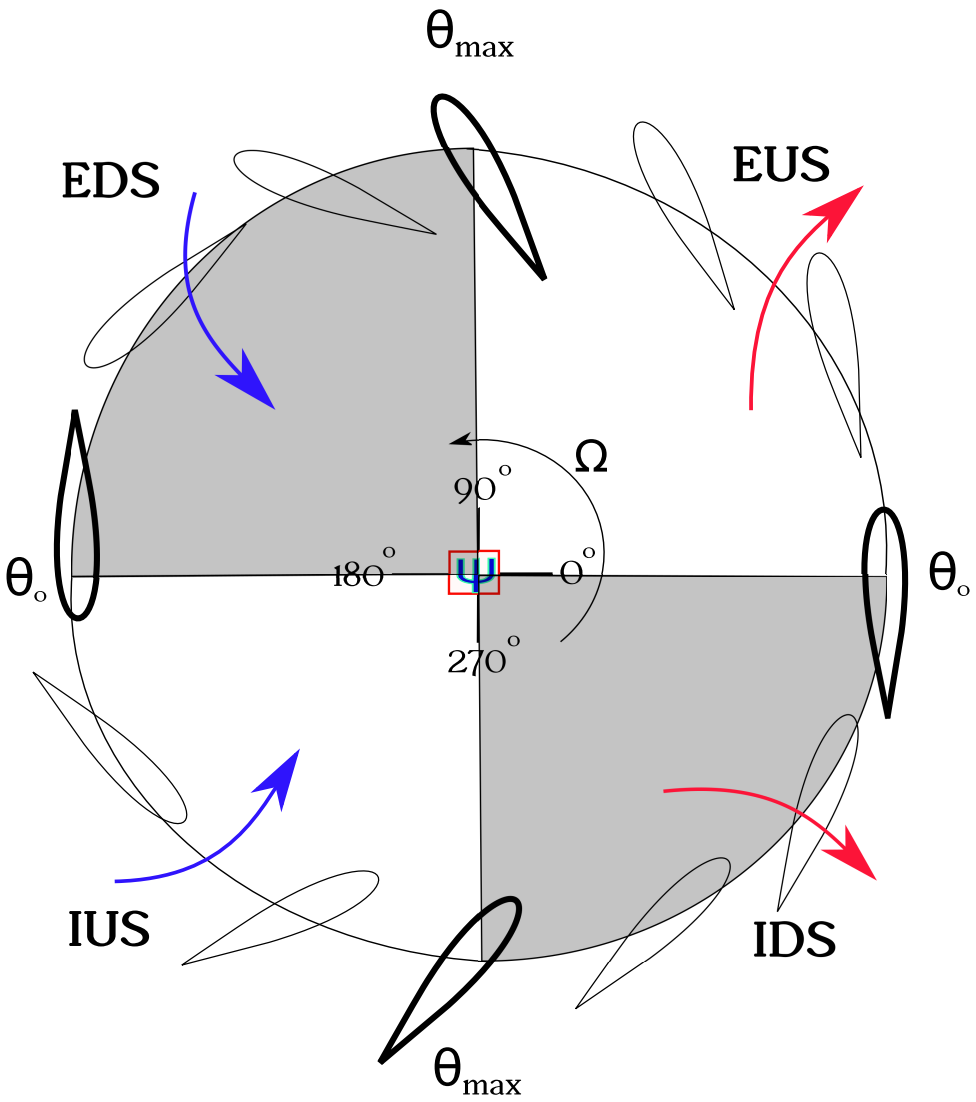

Figure 1.1: Schematic of blade settlement and operating procedure in a typical cyclorotor.

Ilieva et al. [2, 16] have surveyed an overview on the diverse propulsion mechanism being proposed over the years, especially on airships till recent modern innovations. They came to clarify the benefits and drawbacks of these propelling systems in terms of functionality, operating efficiency, power feeding and so on. They also introduced the MAAT

project being held in European Union, a major project on high altitudes airships. Several studies indeed have been applied on different rotor-thrusters in aircraft [17, 18] which the interactions of blades or propellers are making significant impact on the overall efficiency of the crafts, like what also happens in cycloidal rotors.

A historical review of the publications and reports specifically on cyclorotors or cyclogyro designs has been filed in 2009 by Curtis et al. [19]. Further, Benedict et al. [20, 21] in university of Maryland conducted extensive research on MAV scale cycloidal rotor crafts both experimentally and numerically. In one of their studies they have presented a relatively light MAV design flying with double-counter rotating 3-bladed cycloidal rotors in sides, with a total 290 g craft net weight. They performed detailed tests while considering various parameters such as different blade profiles, blade thicknesses and different sizes in further investigations.

Gagnon et al. [22, 23, 24, 25] have also conducted detailed investigations from an aerodynamic and aeroelastic point of view. In their former referred article, they conducted that a 50 percent input power reduction will be achieved if the cycloidal rotor is replaced with conventional tail rotor of a helicopter. They effectively used different approaches as CFD, analytical models and theory to deeply study numerous featuring parameters in cyclorotors. Blade number, rotation speed, rotor sizing, blade flexibility and pitching schedule were brought into consideration as variables to study. In terms of flexibility of blade profiles, they stated that it can not lead to better aerodynamic improvements, to reduce the rigidity of profiles since blades deform, their effective AOAs change accordingly and, thus, efficiency drop is evident in their analyses as well. Stability analysis of a modeled rotor was also the topic of a joined numerical and analytical work from Navazi and Hojjati [26]. Under CROP title, a European Union project [27] was developed on cyclorotors, Leger et al. [28, 29] attempted to analytically evaluate and study different working principles of a cyclorotor in hover state. Study and calculations of mechanical means for pitching motions, eccentricity variations, optimum mechanical dimensions, angular velocities and efficiency comparisons of their optimum design has been performed for BOSCH, IAT21 and Seoul National University design. In a further numerical modeling [30], Leger and his colleagues targeted 3D effects presence, specifically in the region between the endplates and the propeller tip, where flow leakage is more imminent. CROP project report was then issued by [31]. Within the same project, Xisto et al. [32] brought to study the feasibility assessment of employing Dielectric Barrier Discharge (DBD) plasma actuators in cyclorotors. They aimed to consider the stall conditions where pitching amplitudes exceed a critical value and separations occurs and thus flow losses become inevitable. They reported that applying DBD was not an effective method to delay stall occurrence but showed great performance in resulting into a higher level of lift coefficient in the downstroke portion phase. DBD plasma actuators are still susceptible to be the subject of further detailed study, although a much better understanding of the existing complexity in cyclorotor flow behavior is vitally important.

The issue of ground effect has been the target of some researchers as are presented in [33, 34, 35, 36, 37]. The attempt was to study the effects of ground hight level (static and

dynamic) on the flight means. These articles are conducted using several approaches of experimental, analytical and numerical simulations to study the ground effects on different geometries from canard, wings and different airfoils. These studies are definitely important since the subject of the current study also concerns the ground effect in several operating conditions and heights to predict the optimum functionality of a typical UAV cyclorotor. In [33], they studied the operating status of a combination of wings and and tail, concerning the ground effect and their relative positions. They proposed a mathematical model by which the aerodynamic optimization of wing-in-ground (WIG) craft could be possibly predictable.

It worth to mention, the environmental effects are becoming essential in some essence, where the ceiling effects are also becoming the target of investigations like the study of Kocer et al. [38] in a VTOL UAV quadrotor.

In a comprehensive study carried out both experimentally and numerically from Yu et al. [39], forward flight efficiency has been the main research subject. They featured the effects of advance ratio and blade numbers as the influential parameters. The authors indicate that reaching the same efficiency as the screw propellers is feasible in cyclorotors for flights. 3 and 4-bladed cyclorotors showed the best obtained efficiency in terms of blade numbers. As they have declared, the more blade numbers, the less vibrations and better mechanical efficiency. They achieved higher efficiencies with moderate to high advance ratios. Moreover, the blade vortex interactions (BVI) become less in higher advance ratios.

The performance of seven turbulence models were studied by Singh and Pascoa [40] on a single blade oscillations of a cycloidal rotor. The authors checked the accuracy of the results obtained and performed a comparison among all with the experimental results. They have stated that SST-SAS and SAS were the two models being capable of better capturing and predicting the flow. Their attempt was to study a single oscillating blade under pre-stall, stall and post-stall conditions. In a numerical analysis conucted by Rami and Pascoa [41] , considered various oprating condition with pitching angles and rotating speed. In addition, their concern was to simulate and predict the optimum state of operating condition while in close distance with ground-surface level. They concluded different efficiencie could obtain while the cycorotor operates in different altitudes as a propulsion system of a VTOL aircraft.

In the current study, the main focus has been laid on the operating traits of a cyclorotor-thruster aircraft in its vertical take-off and landing phases. Technically, these phases are always considered as critical modes in flying aircraft regardless of their type, whether are happening horizontally like in normal airplanes or vertically in helicopters.

As was indicated in a technical report from National Aeronautics and Space Administration (NASA) [42], cyclorotors are propulsors in which the downwash flow convects in a pile-like flow, shedding out from the bottom side of rotor. This concentrated massive volume of flow can undoubtedly play significant role on the overall functionality of a cyclorotor aircraft, especially in its close-ground level flying operations.

1.2 Objectives of The Current Research and Thesis

In the current research framework, it is tried to have a wider look to more distinctive aspects of operations and flight phases that have not been studied in details before. The hovering efficiency, the effects of applying endplates to the sides of the cyclorotor, forward-flight and lift-up phase considerations on operation, the near-ground effects of operations at different height levels and altitudes, and a novel propulsion mechanism based on two cyclorotors and pair-wing system which was submitted as an international patent are only some of the different aspects that have been worked throughout this thesis.
The base of the present work is initially started with computations and simulations using CFD in the OpenFOAM toolbox. Later on, the concept of using deep learning and neural network analysis was added to work to assess the different operations in view to optimize operation and introduce performance enhancements. Thus, by using artificial neural network (ANN), all the database which was derived and collected from the CFD simulations is analyzed in learning algorithms and ran into an optimizations procedure in order that the cyclorotor may reach better operations and higher efficiencies. Therefore, all the different aspects of this research work have been supported by both CFD and ANN analysis as is illustrated in the subsequent chapters.

Chapter 2

Hovering Performance and Optimization

[1]

2.1 Overview

The cycloidal rotor was proposed as a novel propulsion concept for the vertical take-off and landing (VTOL) aircraft [2]. This system, as is presented in Fig.2.1, comprises a set of blades positioned in an orbital arrangement in which two centers are featuring in its operational dynamics [43]; the rotating center which is placed in the mid-point of the circular trace, and the center of pitching oscillations called pivot point which is defined along the blade chord-line where the angle of attack (AOA) can be adjusted. The third dimension is also symmetrically extended in "Z" axis known as the span-wise direction. The very unique features of this settlement, as a rotary device, are briefly stated as following [1, 14]; i) since the rotating speed and the dynamic characteristics are similar in span-wise axis, the aerodynamic behavior of these systems can fairly be considered the same in this direction, whereas the operating status of the conventional propellers alters locally from tip to hub. ii) the simultaneous rotating and oscillating dynamic in the cyclorotor enhances the maneuverability of the VTOL aircraft in operational conditions [44]. This also effectively contributes to control blade stall. iii) considerably lower noise production in this system due to its lower rotational speed, and lower frequencies of tip vortices shedding [45, 46, 47], are other remarkable advantage of the cyclorotor, as compared with conventional propellers in helicopters. Since the initial collaboration between Kirsten–Boeing [3] in 1926, several attempts have been made to further enhance the efficiency of the cyclorotor. Aerial and naval craft geometries, dynamics control, mechanical structures, airship propulsion systems [48], hovering state and forward flight considerations comprise all the major research fields which were investigated. aeroelasticity, blade number and shape profiles, the use of double endwalls to restrict the cyclorotor cage, and sizing issues, are also the other areas of recent research that worth to mention.
Recently, a multi-disciplinary study is reported by Tang et al. [49] in which they established an optimization approach using a surrogated model and genetic algorithm. They achieved approximately +20% increase in the figure of merit (F.M), being this variable a reference of aerodynamic enhancement in cyclorotors, at hovering state. There is a continuous progress in this field, and the work done by Yun et al. [1] and Lee et al. [50] also investigated the functional analysis of a 110 kg multi-rotor UAV cyclocopter at the

[1] Based on the work submitted to Journal of Aerospace Science and Technology, Active Control Assessments towards Optimizing the Performance of a Cycloidal rotor at Hover; A Coupled CFD and ANN Methodology, n° pages (50) , 2020

Seoul National University. Besides the experiments in tethered flight tests, they also carried computational fluid dynamics simulations (CFD) studies in order to verify their designs. They refer that a reasonable hovering and maneuvering capability was attained in payload-carrying (2 kg) mode with their vehicle. In another UAV scale aircraft, Hwang et al. [12] attempted to employ pair-cyclorotors on each side of the aircraft which is called the four-rotor cyclocopter. This system was optimized using counteracting rotors due to torque concerns and showed $\approx 15\%$ enhancement in thrust production by providing about $166N$ thrust.

For small size cyclorotors as the ones used in micro air vehicles (MAV), Benedict et al. [51] provided a comprehensive survey on experimental test, numerical simulations and analytic modeling. They provide informative and detailed studies on rotor size, blade number, blade profile, and, finally they carried out successful real tests of a micro scale (290 kg) aerial vehicle.

A low-order blade-element model, named flux-line theory, was developed by Adams and Chen [52] in order to predict the performance of cycloturbines. Their new proposed theoretical model was capable of reducing the dependency on the blade element model. It was able to effectively diagnose the optimum operating states for a specific cycloturbine. They clearly mentioned that, although their research was for a turbine which uses variable pitching oscillation, such as a cycloidal rotor, their developed flux-line model can be used in optimization of hovering and forward-flight propelling cyclorotors. A new low dissipation method for flows with vortex generating states is presented from Sun et al. [53]. Their method is capable of accurately predicting the highly sensitive flows with the minimum numerical dissipation.

A European Union project entitled "CROP" was developed with the intention to work on aerodynamic efficiency, optimizations and designing the most promising configurations of cyclorotors as propulsion systems. Leger et al. [28, 30, 29] made detailed analytical studies to detect the optimal mechanical dimensions under specific operating conditions. Their model was able to compute the dynamic and kinematic behavior of a UAV-scale cyclorotor operating in hover. Using a pure analytical framework, they also validated their model against CFD and experiments. The authors investigated the 3D effects and flow leakage in an endwall restricted cyclorotor. The application of dielectric barrier discharge (DBD) plasma actuators was also proposed under the same project. The researchers [32, 54] studied the flow behavior and stall considerations in different oscillating angles. They investigated different parameters to assess the accuracy of the methods in computing cyclorotor performance. Furthermore, the numerical predictions coupled with neural network analysis and optimization of the interaction of the downwash flowfield with ground, in a UAV-scale cycloidal rotor, were investigated in [41, 47].

Ground effect has also been surveyed in several studies [33, 34, 35, 36, 37]. These researchers considered the ground level effects on the propulsion systems like propellers. The referred studies are essentially important for the lift-up or the landing modes of the aircraft flight phases.

In naval propulsion applications, several studies have been addressing the modeling and

optimization of cycloidal propellers, especially about their pitching schedule. Voith-Schneider propellers, which are quite well-known, involved an arrangement with cyclorotor blades and are used in marine and submersible applications [55, 56]. Their studies were mostly focused on improving the thrust performance of this propulsion system to attain higher efficiencies and are the only real application of cyclorotor in routine operation as of today. Attempts have been put on optimizing the operation conditions, considering different designs and applications [57].

In rotary devices like turbines and cycloidal rotors, the flowfield, especially on the blade surface, is highly sensitive to the instant oscillating-rotating motions. The flow structure complexity involve different aspects, like separation, wakes, and stall phenomena which should be considered when analyzing performance issues and flow loss [58, 59, 60]. Moreover, dynamic stall concerns for rotor fans and compressor operations at unsteady flow conditions is studied by [61] and [62]. However, novel techniques like the area based applying plasma actuators on surfaces, for flow control, separation avoidance and boundary-layer flow enhancement, are proposed and went through detailed practical investigations [63, 64, 65, 66, 67].

In spite of numerous studies conducted on cyclorotors since almost a century ago, the lack of sufficient analysis, database, and new designs and concepts in this field is clearly sensible. Actually, the researchers were trying to propose a novel propulsion mechanism by using cyclorotors as a substitution to the conventional propellers in helicopters. On the other hand, the cyclorotors are operating at comparatively higher functional complexity compared with those propellers. This complexity is originated from the positioning of the blades and the coupled measurements of pitching and rotation of the blades. Moreover, the flow is actually processed while passing through the cyclorotor cage. Thus, due to the sophisticated operational design and complex flow feature of these propulsion systems, there exist numerous issues yet to be considered and studied. Structural design, system weight, control dynamics, power supply, operating conditions, applicable aircraft scales, blades type, and flowfield concerns, are some areas to name which still need to be considered with the aim of analyzing them to achieve better efficiencies.

Simultaneous multi-motion displacement of the blades in a cycloidal rotor highlights the sophistication and, hence, the importance of comprehensive and detailed flow studying on these devices. To this end, in the current work, it is tried to better study and diagnose the flowfield behavior at different operating conditions. Numerical computations are first used to predict the performance of a UAV-size cyclorotor in several operating conditions, in 2D and 3D simulations. The focus was laid on tracking the blades in one complete route to observe the local behavior of flow and its interaction with blade movements. The concern was to evaluate the moving style of the blades and how it affects the performance of the cyclorotor. The next step was to proceed to achieve an optimum design using ANN. This was accomplished by feeding and training the ANN with the results previously attained from the CFD phase. Subsequently, the optimum operating states were obtained from the ANN analysis for the cyclorotor operating at hover. ANN was able to propose a better pitching oscillation curve for each rotating speed and thus enhancing the operating

efficiency to considerably higher values. This approach can be proposed for active control of pitch angle, according to the rotational speed and the local azimuth (Ψ°), to reach higher operational efficiencies.

2.2 Cycloidal Rotors Operation

2.2.1 System Configuration

A cyclorotor in general, is comprised of a specific diagonal settlement of blades that trace a defined pitching schedule over the circular movement. This system can be proposed to operate in diverse scales and missions. They can either be used in aircraft for producing thrust, or in stationary wind turbines for energy productions.
As is depicted in Fig.2.1, the local position on the circular trajectory is found by azimuthal angle Ψ. It should be noted that the pitching extremes in the present UAV-scale cycloidal rotor occur at the top and bottom locations, which correspond to $\Psi = 90^\circ$ and $\Psi = 270^\circ$, respectively. All the illustrations herein are based on counter-clockwise rotating direction. Aside from the center of each airfoil, a Pivot Point is also prescribed to impose the pitch angle of each blade (see Fig.2.1).

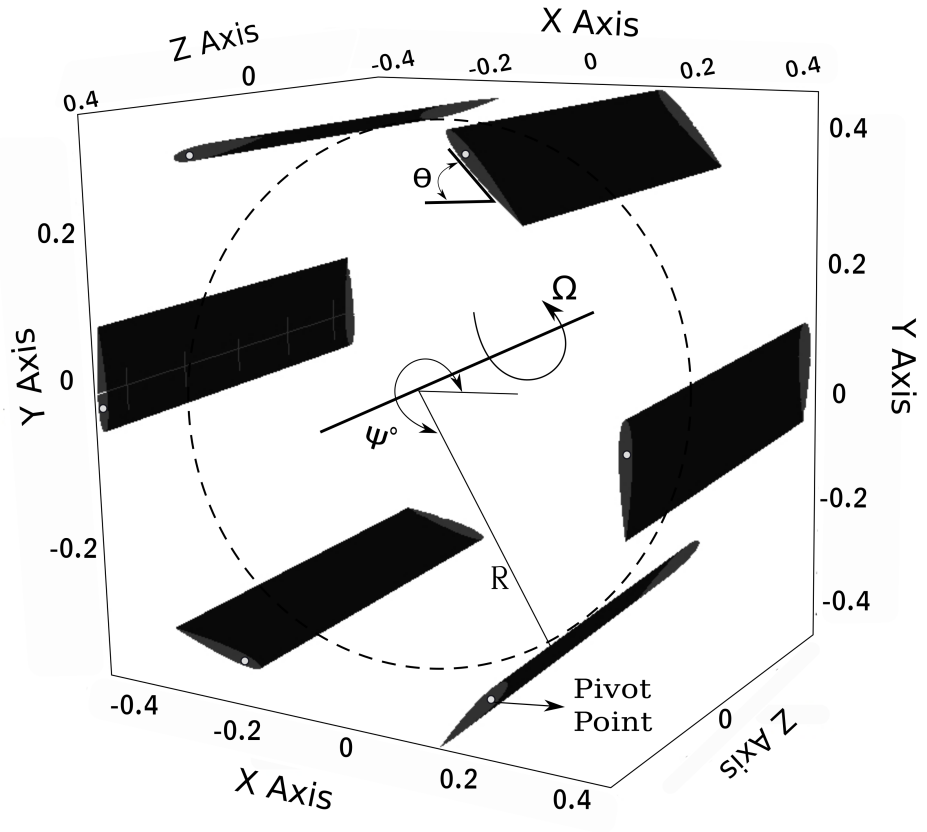

Figure 2.1: Blade arrangement and operating specifications of a typical cycloidal rotor.

A major distinction between this system and conventional propellers in helicopters is the 3D cage-like interior passage, rather than a planar interface through which the flow passes the system. In other words, a cyclorotor operates as an inhaling-exhaling system where the flow is processed within the passing cage. This feature provides the possibility of manipulating the flow stream to the desired exit angle in order to achieve thrust vectoring. The blade motion in a complete revolution is a sinusoidal curve as is shown in Fig.2.2. As discussed in subsequent sections, the blades are generally following a sinusoidal path. These curves are actually attributed to the specific pitching oscillations in which the blades reach a certain maximum pitch angle at the top and bottom of the cycloidal rotor. Thus, according to each defined pitch angle, the blades are following a specific schedule for their angle of attack in all rotating speeds. In the ANN result section the optimized pitching schedules will be presented in full detail.

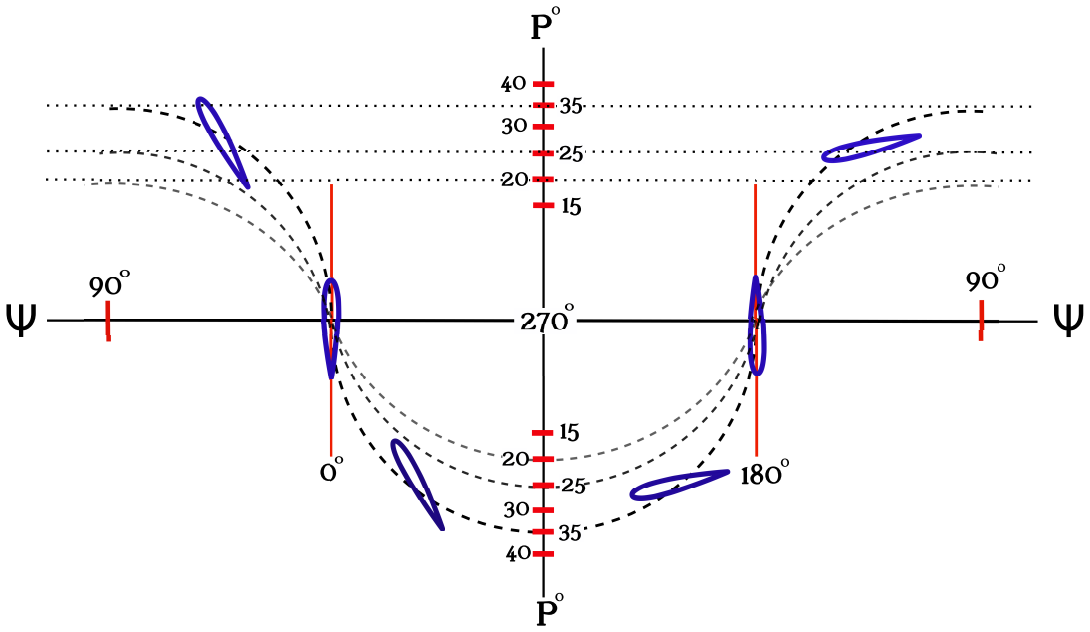

Figure 2.2: Trace of the oscillating blades over a full circular trajectory in cycloidal rotor.

2.2.2 Flow Mechanism

In parallel to a structural design analysis, a better understanding of flow behavior in this thrusting mechanism would potentially lead to efficiency enhancement. In a general sense, as shown in Fig.2.3 from a 2D simulation contour of the flow, there exist three sequential sections for the passing flowfield through a cyclorotor; A) inhaling zone, which is shown using continuous black arc line, B) the in-cage downward flow, and C) the downwash zone, shown with dashed arc line.

As is depicted, the major portion of the circular route belongs to the flow entering the cyclorotor cage. This portion covers the connecting line of $\approx 0^\circ \leq \Psi \leq \approx 200^\circ$ in counterclockwise direction. In a constant rotating speed along the circular trace, the induced flow velocity and its angle differs at each location on the circle. While entering the cyclorotor, the flow assures a downward direction towards the bottom side. This in-cage flow inclines slightly leftward with the α angle. This inclination relates to the rotation direction of the

cyclorotor and affects the operating status of these systems that will be interpreted in the proceeding sections. As the flow reaches the bottom side, it deflects reversely to rightward and sheds out from cyclorotor with β angle. Downwash characteristics are related to different parameters; such as cyclorotor size, blade number, rotating speed and pitching angle. Therefore, in order to find a proper correlation among the involving parameters, to predict downwash angle, a thorough assessment of various sets of tests and simulations is needed. As was discussed earlier, the successive deflection and deformation of the flow in a short fraction of time from entering to exhaling as downwash, leaves the necessity of studying more in detail the flow for clear understanding.

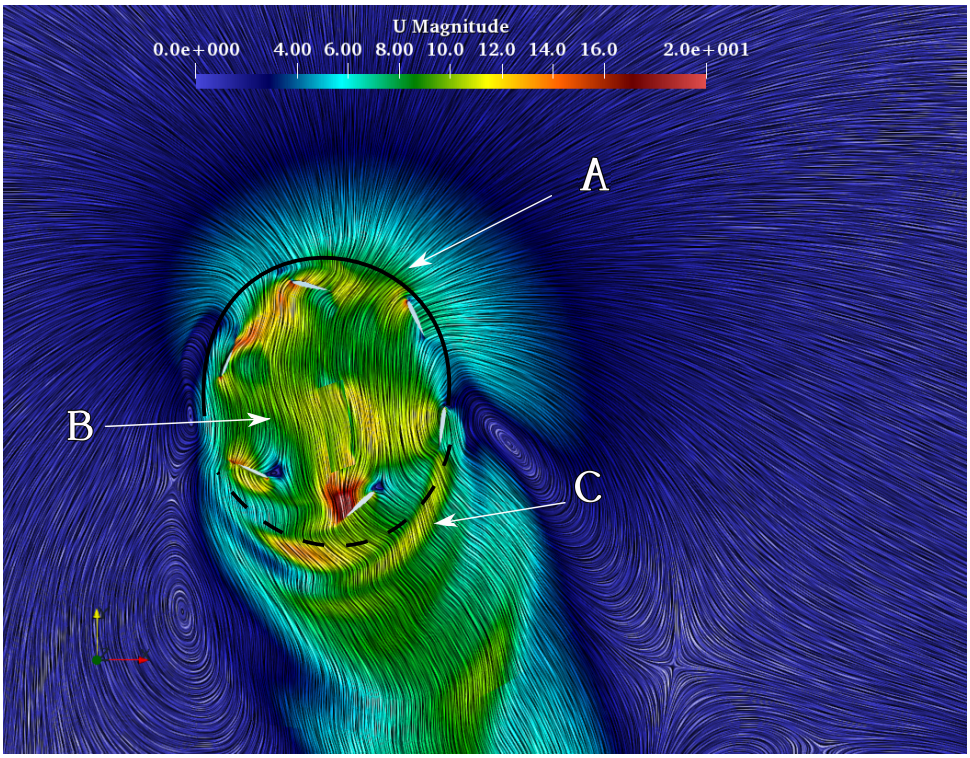

Figure 2.3: The flow pattern of a cycloidal rotor operating in hover state, at 500 rpm and 30° pitch angle.

The contour flow showed in this work is using surface-LIC (Line Integral Convolution) technique which was firstly introduced by Cabral et al.[68] and was subsequently developed by Loring et al.[69] which found to be a beneficial and useful approach in depicting flow traces.

2.2.3 Lift and Thrust on the Circular Trace

The intention in this project is to study and address the thrust mechanism of a cyclorotor at different operating conditions. Here a combination of blade settlement and fluid flow is consequently resulting in thrust outcome. In order be able to design, construct and optimize the functional status of a cyclorotor, here the authors used to obtain a deep conceptual and quantitative knowledge of its operation. Herein, force production is studied for horizontal and vertical axes, at each point on the tracing circle, in order to better perceive the effectiveness of the blade control associated with the pitch schedule. Figure

2.4 illustrates qualitatively the forces produced in each zone of the circle route. By looking at these curves one can view the regions with the highest and lowest force production, at each of the horizontal and vertical elements, in Fig.2.4.a and Fig.2.4.b, respectively.
Figure 2.4 depicts also the schematic of the maximum horizontal and vertical force production in a complete circular revolution. As is seen in Fig.2.4.a, the horizontal force is experiencing a peak production in three regions: 1) $\approx 40^\circ \leq \Psi \leq\approx 90^\circ$, 2) $\approx 170^\circ \leq \Psi \leq\approx 250^\circ$ and 3) $\approx 300^\circ \leq \Psi \leq\approx 350^\circ$. The peak values for the vertical force, as depicted in Fig.2.4.b, correspond to two regions as: 1) $\approx 60^\circ \leq \Psi \leq\approx 120^\circ$ and 2) $\approx 220^\circ \leq \Psi \leq\approx 330^\circ$. The most significant issue is that the reasons and the values of these peak zones are directly attributed to the flow and blade positioning. For each of these forces, the flow state, the angle, the velocity and the projected area of the blade surface are all playing significant roles.
At the upper half of the circle, in the flow suction region, the induced (entering) velocity reaches its highest value by $\Psi \approx 90^\circ$. Here occurs the first vertical force peak and in the first quarter of the circle route is where the blade opens itself till it reaches the maximum pitch angle at the top. As it approaches to the top zone, the first peak of horizontal force occurs in the second half of the first quarter. The peak force values are noticeably higher in the bottom half of the cyclorotor trajectory circle. This fact highlights the significance of the operating state of the bottom side of the cyclorotor.
A clear explanation of this is that the bottom half is responsible for the highest energy extraction from the passing fluid flow, and also loss concerns are increasingly critical in this region. These issues are further discussed in detail in the CFD results section duly supported by plots of computed results.

2.3 Numerical Procedure

2.3.1 CFD Approach and Turbulence Modeling

All the CFD cases are simulated within OpenFOAM [70] package as an open source extensible CFD toolbox. The pimpleDyMFoam solver was found to be the suitable solver for the simulations of a multi-zone moving body in turbulent and incompressible flow, since it benefits from a combination of SIMPLE and PISO algorithms. A bounded first order implicit discretization scheme for time derivatives is used, with a Gaussian integration being chosen for both velocity and pressure derivative terms.
The velocity and pressure residuals are set with 10^{-6} for convergence tolerance criteria. 1500 steps per each rotating cycle is finally selected for time-independent solution convergence. Although the mentioned value corresponds to the main simulations with the final selected grid and turbulence model and with maximum CFL number of 5. Reaching to 10 and 1 percent of the initial residuals, velocity and pressure fields are respectively considered as converged by each iteration.

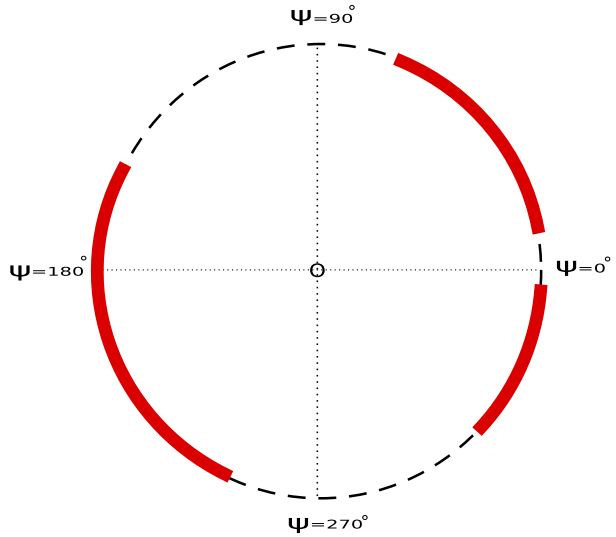

(a) The main regions of horizontal force production.

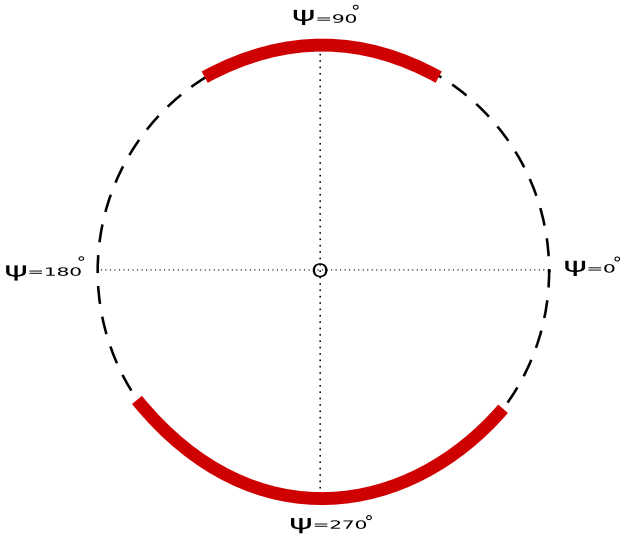

(b) The main regions of vertical force production.

Figure 2.4: The qualitative horizontal and vertical force regions in a complete cycloid trace.

For turbulence modeling, as was also suggested from Yun et al. [1], with whom our CFD results are validated against their experiments, k-ε turbulence model can fairly model the turbulent phenomena for the current simulations. Therefore, in the validation section, the results are all obtained using the k-ε turbulence model. Besides the accuracy of the numerical predictions, since the cases are complicate in terms of blade displacements and also due to the rather large computational domain, high costing turbulence models should be avoided in full unsteady cycloidal rotor computations.

The selection of a suitable turbulence model is a crucial issue to have an accurate simulation. The k-ω-SST method is more suitable to capture flow details and study the internal flow behavior [71, 72]. In terms of airfoil dynamic stall which is highly probable in these systems, the selected turbulence model predicts better accuracies than the results obtained with k-ε and standard k-ω models.

Since the blades are cyclically experiencing up-strokes and down-strokes, flow shedding

and separations are highly affecting the blade surfaces, k-ω-SST model better captures the near-wall effects as well. Pendar and Pascoa [73, 74] simulated a turbulent flow with high rotational speed and provided a thorough understanding of the fluid dynamic characteristics. Their results for those rotational cases were also better obtained by the k-ω-SST model. In fact, this model benefits from a two-equation eddy-viscosity turbulence approach by which it treats the normal free-stream as k-ε, and resolves the shear-layer with k-ω model. The comparisons of the results of k-ε and k-ω-SST at several operational conditions are presented in Fig.2.8. The results show that the k-ω-SST model could predict the results in pretty closer agreements with those of experiments than that of k-ε model. Note that the comparison here is with k-ε and k-ω-SST with same cell densities (12 M).

2.3.2 Definition of the Base Design

Table 2.1 presents base specifications and parameters used for the cyclorotor and the CFD simulations. The $0.8m$ diameter rotor comprises 6 blades with NACA0012 profile and $0.15m$ chord length. The fluid medium is standard air at different rotational speeds and Reynolds numbers as is presented in the table.
By considering a 6-blade cyclorotor system the computational domain is divided into 8 sub-domains in order to keep proper control on each single oscillating and rotating blade. The largest zone belongs to the stationary region, 6 zones are considered for the blade with a combined oscillating and rotating movement, and one goes for the pure rotation of the whole 6-blade assembly which thus construct the rotor. The meshing methodology is based on the BlockMesh utility with an in-house code in Octave to prepare the desired OpenFOAM dictionaries for the cyclorotor base design. A structured mesh procedure is retained for the whole domain of computation as is seen in Fig.2.5. In a 2D planar mesh section, $\approx 170\ k$ cells construct the whole domain with $\approx 45\ k$ cells belonging to all of the 6-blade zone ($\approx 7.6\ k$ cells per each), the pure rotating zone consists of $\approx 47\ k$ and the rest $\approx 76\ k$ cells cover the stationary domain.

Table 2.1: The specifications of the cycloidal rotor baseline model.

Parameter	Value	
Number of blades	6	
Airfoil profile	NACA0012	
Rotor radius	0.4 m	
Blade chord length	0.15 m	
Mesh type	Structured	
CFD simulations	2D, 3D	
Mesh motion	Dynamic oscillating-rotating, AMI	
Turbulence model	k-ε, k-ω-SST	
Inlet Turbulence Intensity	2%	
Fluid	Air	
Re number	300 rpm	9.5×10^4
	400 rpm	1.35×10^5
	500 rpm	1.8×10^5
	600 rpm	2.5×10^5
Aspect ratio	1	

The 3D cases are constructed using the same strategy as is taken for 2D. Symmetry boundary condition is set for the front and the back patches. Over 12 million cells are added to construct the 3D case, by which, the 3D results are presented here. In addition, to study the mesh convergence, three different 3D cases with 8, 12 and 20 million cells were compared at 400 and 600 rpm with 30° and 25° pitch amplitudes, respectively. The results of 12 and 20 million cell cases showed higher accuracy compared with the experiments, and their results were quite close to each other.

The grid study phase was passed through several mesh adaptation steps to ensure the optimal mesh structure for the current simulations. The y^+ value was kept below 1.5 on the wall surfaces. For the moving parts, which comprise 6 blades and the rotating domain (7 in total), the cyclicAMI (Arbitrary Mesh Interface) approach is applied to incorporate the outside and inside regions. The circles shown in Fig.2.5 are presenting the AMI pair-patches. In total, 14 interfaces are created as an AMI patch which are overlapping, in pairs, in order to separate the sliding regions. The matching tolerance between all of the AMI pairs is set to 10^{-6} to maintain a close clearance between the cyclic interfaces. For the connection between the pair interfaces a ”no-ordering” transform method is chosen. This method is appropriate for adjacent sliding patches when they differ in the number of cells.

The region inside the big circle and outside the small circles is assigned to have pure rotating motion about the rotor center. On the other side, the blades and the restricted zones inside the small circles are following oscillating-rotating function in order to achieve a simultaneous coupled motion of pitching oscillations and rotation.

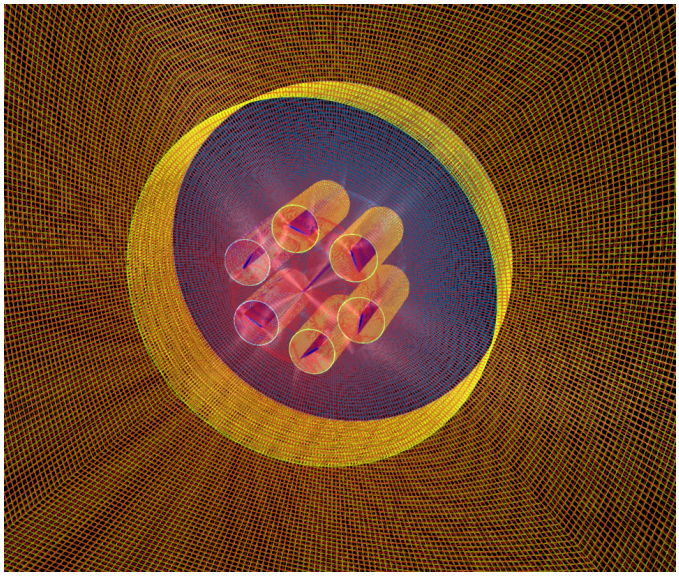

(a) Cycloidal rotor domain mesh

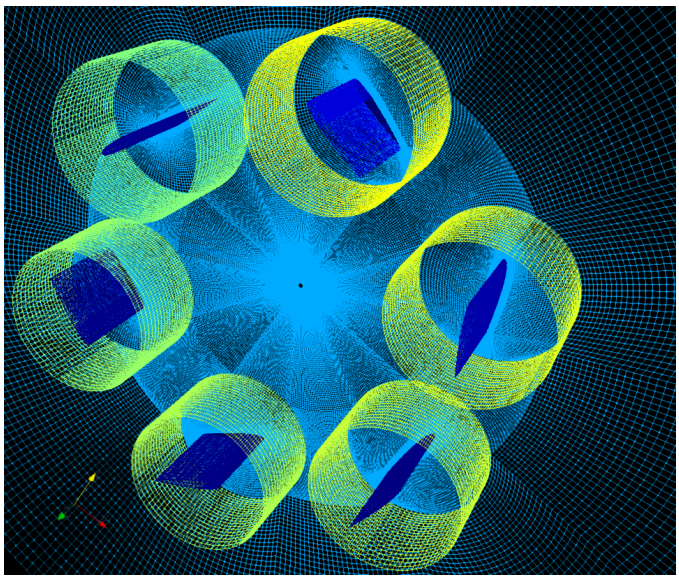

(b) Rotor blades and AMI patches

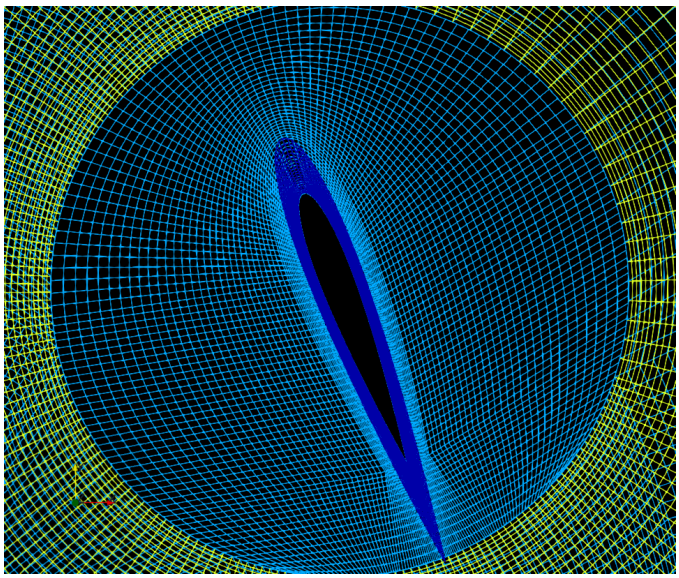

(c) Blade and boundary layer mesh

Figure 2.5: The 3D mesh configurations of a 6-blade cyclorotor and the cyclicAMI patches for the rotor and each of the blades used in the sliding mesh technique.

2.3.3 CFD Code Validations

The current numerical procedure is validated using the experimental results reported by Yun et al. [1] for an unmanned size cyclorotor operating at hover state. Both 2D and 3D results are included in this validation process and reported herein. Therefore, a range of the oscillations and rotating speeds were chosen for the simulations in order to justify their agreement with the experimental peers. The pitching angles include 20°, 25°, 30° and 40°, and the rotating velocity goes from 200 rpm to 600 rpm with 100 rpm intervals. The parameters included to perform validations are the thrust coefficient (Eq.2.1) and power coefficient (Eq.2.2) for each of these 20 cases in both 2D and 3D simulations. The thrust coefficient is defined as:

$$C_T = \frac{T_N}{\rho A (R\Omega)^2}, \quad (2.1)$$

and the power coefficient is:

$$C_P = \frac{P_N}{\rho A (R\Omega)^3}, \quad (2.2)$$

where R refers to rotor radius and A indicates the projected area of the cyclorotor:

$$A = 2Rs \quad (2.3)$$

and P_N, T_N are pointing to net power (eq.5.5) and net thrust (eq.5.6) in the following equations, respectively:

$$P_N = M\Omega, \quad (2.4)$$

$$T_N = \sqrt{T_H^2 + T_V^2}, \quad (2.5)$$

where M and Ω refer to momentum and rotational speeds and T_H and T_V are horizontal and vertical thrusts.
As can be observed in the validation plots (Figures 2.6 and 2.7), the comparison for 2D and 3D cases with the experiments show convincing close agreement. The 3D cases show closer and, in some points, slightly higher values than those of 2D cases. Having confirmed the acceptable accuracy of the numerical approach, the rest of the CFD results are also obtained by conducting the same numerical methodology as well.
Figure 2.8 presents the plots of thrust coefficients from the two mentioned turbulence models and grid structures compared with their approach to experimental data at several

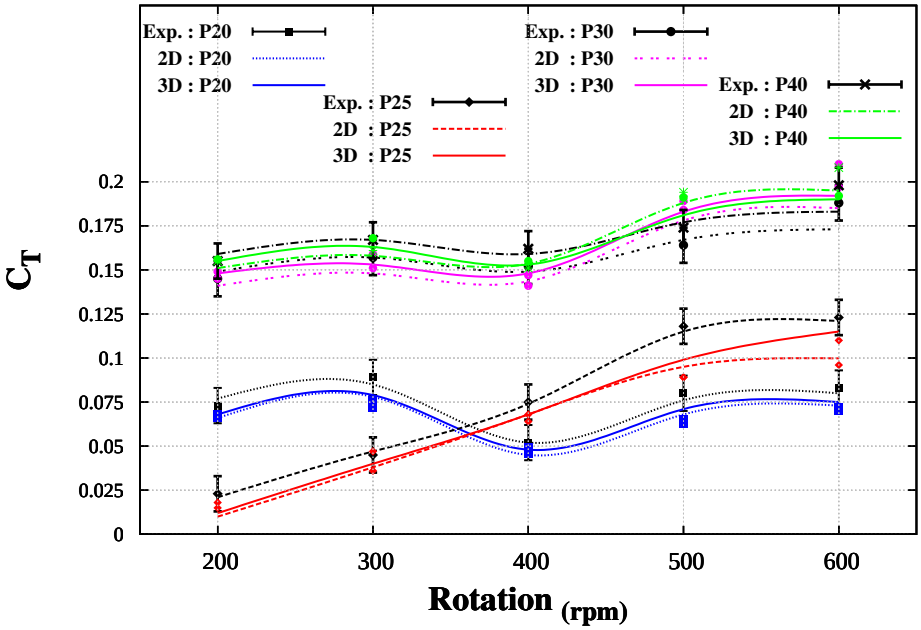

Figure 2.6: Validation using experiments of Yun et al. [1]: thrust coefficient vs. rotation speed.

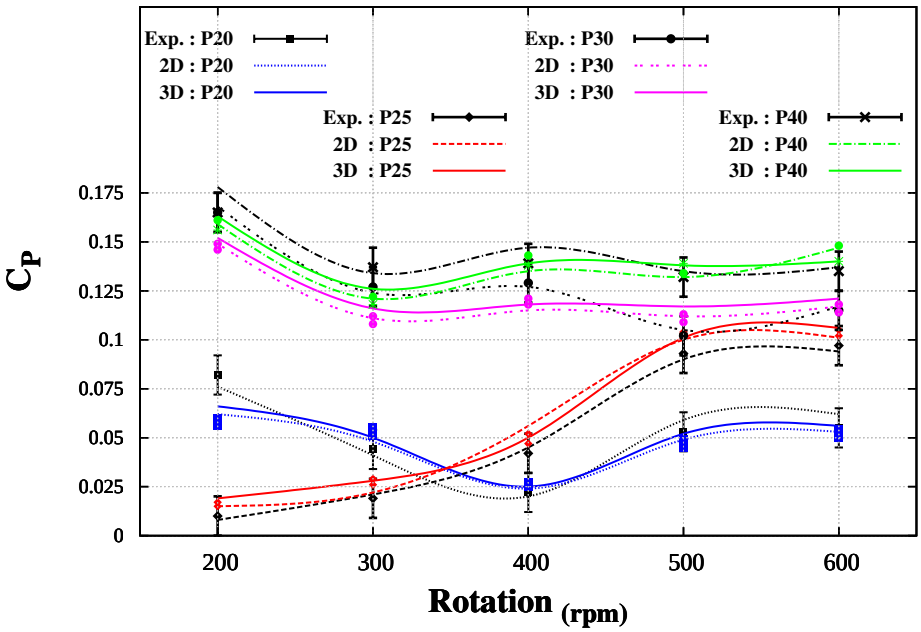

Figure 2.7: Validation using experiments of Yun et al. [1], power coefficient vs. rotation speed.

operating conditions. These conditions consist of two pitching oscillation angles (25° and 40°) at different angular velocities. The grids comparisons for both pitching amplitudes confirm the better agreement of 12 M grid results compared with the 7 M grid structure. These two grids are compared using the same turbulence model as can be seen. On the other side, the results of the two turbulence models of k-ε and k-ω-SST are also determining the higher accuracy of the latter model to the experimental results. This fact is also proven by Wang et al. [75] for the same NACA0012 airfoils operating at oscillating sched-

ules with impending dynamic stall conditions. They confirmed the higher computational efficiency of k-ω-SST in these systems compared with other RANS approaches.

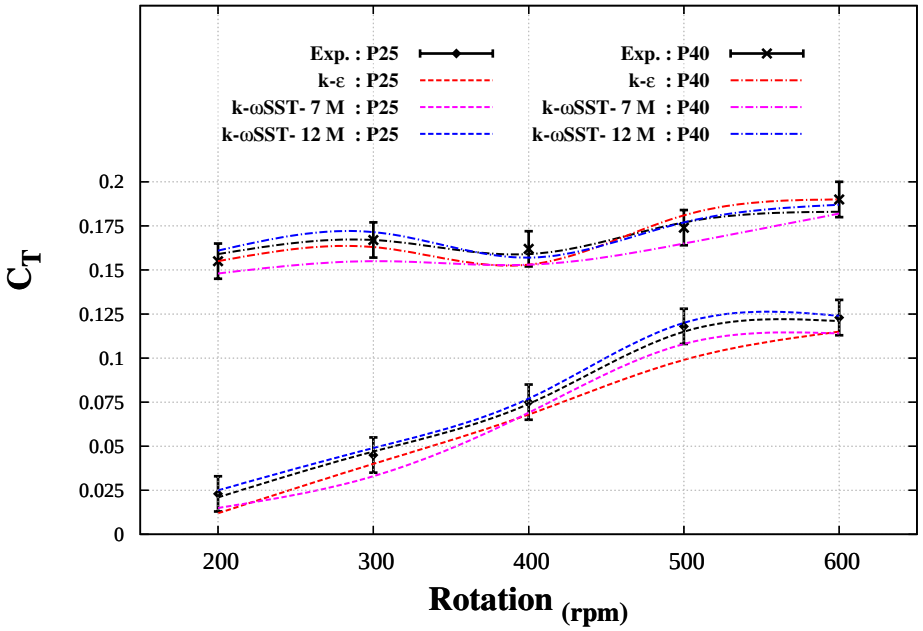

Figure 2.8: Comparison of turbulence models and grids using thrust coefficient values of experiment at pitching amplitudes of 25° and 40°.

2.4 Artificial Neural Network

The practical advantages of using artificial intelligence in various areas of science and technology have sharply arisen in the last decades [76, 77]. In addition to the application of fuzzy-logic and other concepts in several fluid and thermal engineering fields [78, 79, 80], ANNs are currently often more used as a computational analysis methodology for different fluid engineering problems. Some of the significant reasons for this can be: i) Accurate recognition of the inherent relation between all sets of inputs and outputs without the need to realize the physical models. This capability is called pattern recognition, which is achieved as a result of data learning. ii) ANN methodology has also the ability to handle time-varying modeling and adaptive control by use of neuro-controllers. iii) High flexibility in incorporating with other soft-computing approaches, such as fuzzy-logic and genetic algorithms, which provide better efficiency in dealing with higher complexities [81, 82]. On the other hand, in the learning process of ANN, sufficient input data must be provided to more accurately train the algorithms.

This interactive approach provides the possibility to train from a set of data in order to extract the desired information. The target is to find the optimum schedules over a complete cycle in accordance with the achieved database. All of these data is processed in the neural network to obtain the optimum operating schedule by analyzing the values and parameters in a continuous traversing cycle. At the end, the optimum pitching schedules, and their relative optimal efficiencies, are proposed for each of the rotating speeds.

A combined study of experimental tests with numerical simulations accompanied with neural network analysis, has proven to be highly beneficial in problems dealing with diverse conditions and operating states [83, 84, 85]. In the ANN method shown in Fig.2.9, some parameters are chosen to be injected to the input nodes for analysis. The input parameters include the figure of merit ($F.M$), disk loading ($D.L$), power loading ($P.L$), horizontal force (F_X), vertical force (F_Y), thrust (T_N), thrust coefficient (C_T), power coefficient (C_P) and the thrust acting angle (Φ). As is also showed in the diagram, both for 2D and 3D cases that include a range of pitching and rotating speeds are considered in the ANN analysis.

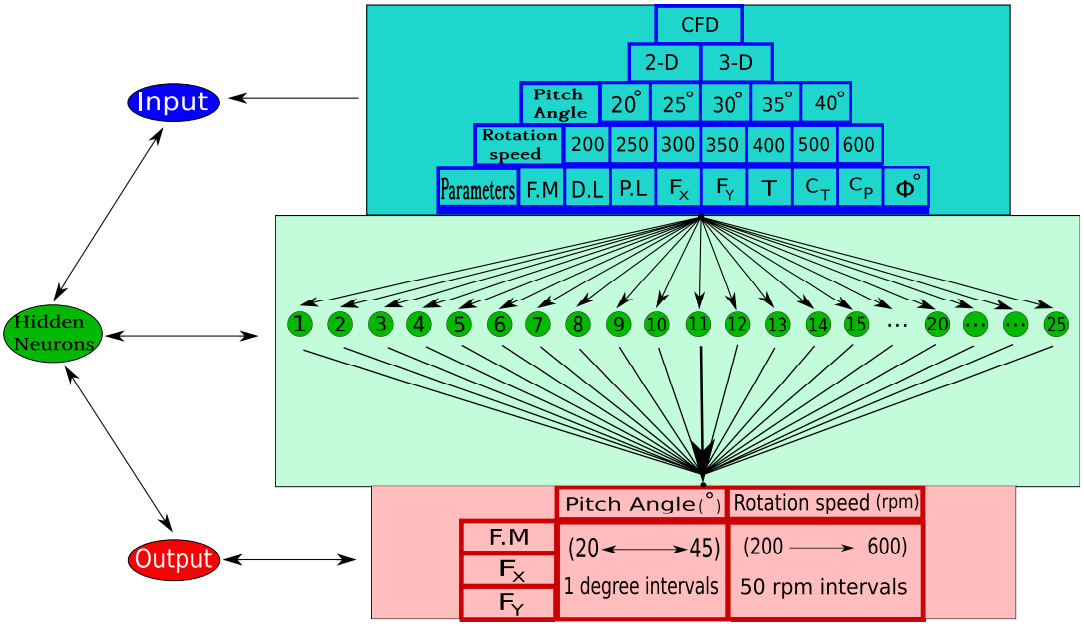

Figure 2.9: Configuration of the optimization model based on the ANN analysis.

The parameters are all provided for different pitching and rotating speeds, and all are achieved in both the 2D and 3D simulations. Thus, a huge number of data is taken as the input for the training process of the ANN algorithm. The desired outputs are $F.M$, F_X and F_Y for a range of pitch angles and rotating speeds that were afterwards used in the subsequent analysis.

2.4.1 Structure of the ANN Analysis

The ANN relies on the real biological neural network that is simulated by its structures. In doing so, it includes numerous nodes, or neurons, which form into layers. Generally, these layers are organized as input and output levels which are all internally connected to the previous and subsequent hidden layers. While the input nodes are considered as the known parameters of the problem, the output layer corresponds to the unknown data space. Error estimations can be computed when the computational information reaches the nodes in the output. In order to reduce the errors to a reasonable level, the computed errors in the competitive process are used to modify the nodes in the whole network, during the learning procedure. Back-propagation is well-known as a feed-forward network

scheme where the biases are treated step-by-step from output to input layers. Clearly, the complete ANN analysis comprise repeating computer-based steps of algebraic and deterministic methods [86].

We configure the layers and nodes in the network, in which a layer is defined by i and the numbers are from $i = 1$, that belongs to the input layer, and the last is $i = I$ which refers to the output layer. Nodes are described by j and they can possibly vary in all layers. Thus, J_i and J_I are defining any random node number of each layer and the output layer node numbers, respectively. Generally speaking, the nodal coordinate of each node will be written as,

$$x_{i,j} = \lambda_{i,j} + \sum_{k=1}^{J_{i-1}} w_{i-1,k}^{i,j} . y_{i-1,k}, \quad (2.6)$$

where $w_{i-1,k}^{i,j}$ refers to synaptic weight, $\lambda_{i,j}$ is the nodal bias at each (i, j) and $y_{i-1,k}$ is the nodal output at the previous layer. $y_{i,j}$ is then derived as a threshold function according to input $x_{i,j}$ as,

$$y_{i,j} = \varphi_{i,j}(x_{i,j}), \quad (2.7)$$

This function is also known as logistic sigmoid function and has continuous derivatives that are beneficial to handle highly nonlinear variable behavior and relations between input and output,

$$\varphi_{i,j}(\zeta) = \begin{Bmatrix} (1 + e^{-\zeta/c})^{-1} & i > 1 \\ \zeta & i = 1 \end{Bmatrix}, \quad (2.8)$$

here c represents the inclination of the function and has a constant value.

Learning, training and determining the errors at the output layer is one of the most significant steps in any ANN methodology with which a specific level of accuracy must be achieved. As was mentioned, one of the most commonly used training algorithm for ANN analysis is the feed-forward back-propagation procedure [81, 86].

The overall error calculations after passing continuous cycles of training and after completing a training phase can be calculated as,

$$E_r = 0.5 \left[\sum_{j=1}^{J_r} (t_{I,j} - y_{I,j})^2 \right], \quad (2.9)$$

where $t_{I,j}$ represents the normalized output for node j in the last layer.

Regarding the evaluation of the accuracy level of the optimal model in ANN, the relation coefficient (R_C) and the mean square error (MSE) are the desired parameters. Through the work of Haykin [86], R_C is defined as,

$$R = \frac{Cov(a, A_p)}{\sqrt{Cov(a,a).Cov(A_p, A_p)}}, \quad (2.10)$$

in which $Cov(a, A_p)$ addresses covariance between the parameters a and A_p as the measured and predicted values,

$$Cov(a, A_p) = E\left[(a - \mu_a)(A_p - \mu_{A_p})\right], \quad (2.11)$$

where E describes the expected value, μ_a and μ_{A_p} are the mean values of a and A_p, respectively. The covariances $Cov(a, a)$ and $Cov(A_p, A_p)$ are described accordingly as,

$$Cov(a, a) = E\left[(a - \mu_a)^2\right], \quad (2.12)$$

$$Cov(A_p, A_p) = E\left[(A_p - \mu_{A_p})^2\right], \quad (2.13)$$

The MSE is represented as:

$$MSE = \frac{1}{n}\sum_{i=1}^{n}(a_i - A_{p_i})^2. \quad (2.14)$$

2.4.2 ANN Performance Evaluation

The forward-feed network approach is taken in the present ANN study. In this method, a series of layers have been used in the input, training, validation and output simulation. There is internal correlation among all successive layers, from the input, until the final output results. By using a number of hidden neurons, the mapping procedure of the input results according to the output values through the training scheme has been accomplished. Approaching higher accuracy is dependent on the model training and testing of the dataset which is applied to the ANN model. As is seen in Fig.2.10, MSE, as an error evaluating parameter, was reduced enough to reach the optimal state at a 25 hidden neuron layer. On the other side, the rising tendency in the R diagram also shows it reached its maximum state after a sharp increase at around 30 layers (see Fig.2.11). Thus, a 25 neuron hidden layer has been chosen for the present ANN analysis. Besides obtaining optimal results through a sufficient number of iterations of the algorithm, the epochs must also ensure to credit the learning rate and training procedures. In doing so, the entire dataset must be passed repeatedly to a number of sufficient rounds, for that a reasonable fitting accuracy be reached, during learning and training sequences.

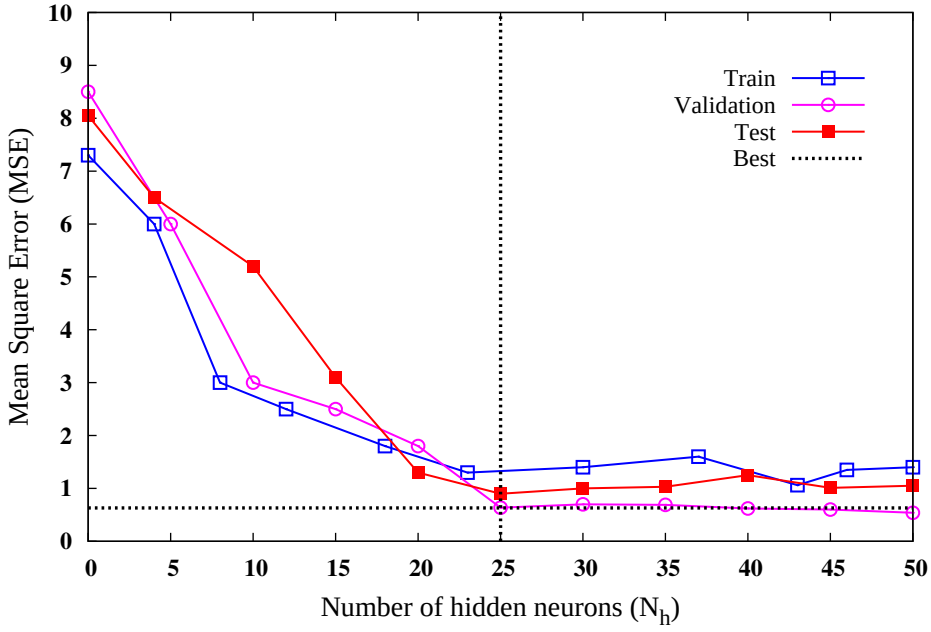

Figure 2.10: Variation and optimal state of mean square error with an increasing the number of hidden neurons.

Figure2.12 illustrates that within the 25 hidden neuron layers, which were diagnosed as the optimum number of neurons, the presented relation coefficient, and the mean square level, converge before a 350 full-round epochs iteration is passed.

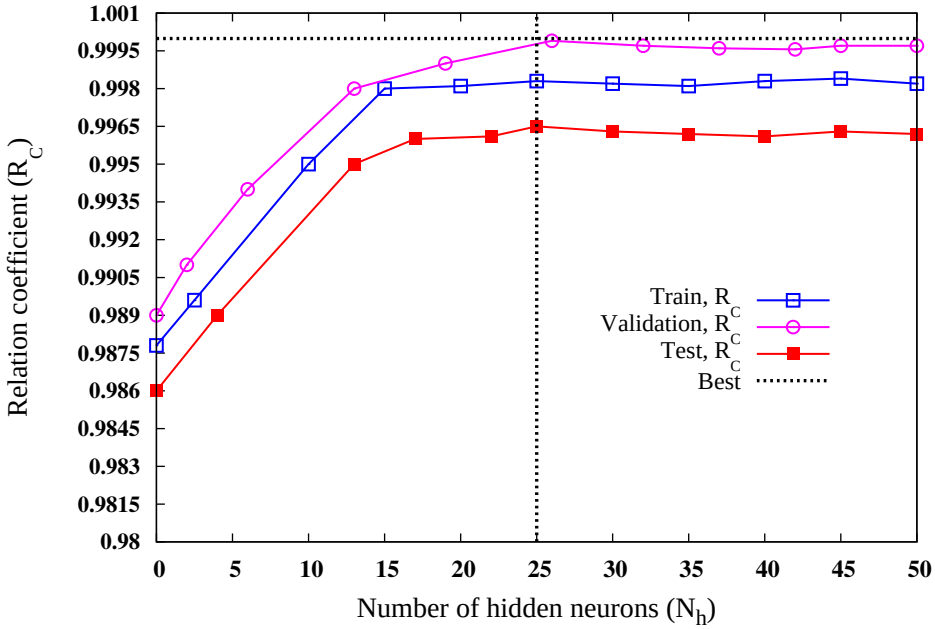

Figure 2.11: Variation and optimal state of the relation coefficient with an increase in the number of hidden neurons.

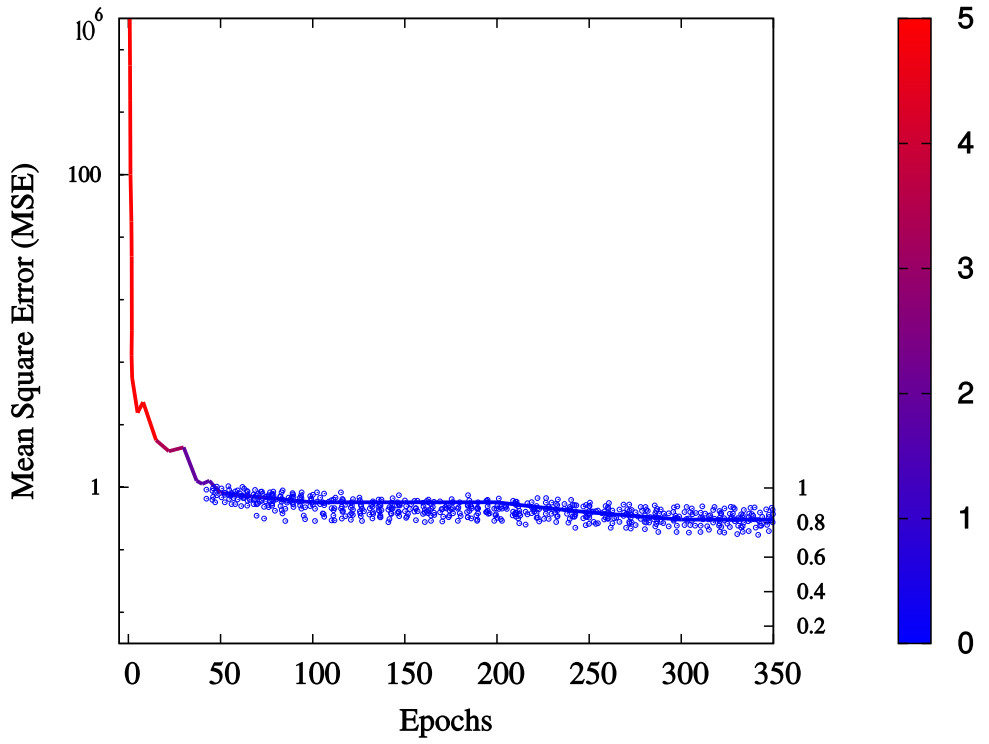

Figure 2.12: Mean square error variation in the optimal neural network model according to the selected neuron number and R_c.

2.4.3 Optimization Design Framework In Active Control

Here is presented the progressive steps (see Fig.3.11) needed to achieve an optimized active control design using the CFD results and the ANN analysis:

1. Define the initial cyclorotor operating states for CFD direct analysis simulations and predictions of flow and operational variables.
2. Validation of the OpenFOAM simulations with experiments.
3. Collecting the database from the various computations using CFD postprocessing.
4. Feeding the database to the ANN algorithm for learning and training progress.
5. Evaluating the trained ANN algorithm to check the accuracy level and CFD data processing.
6. Optimizing the operational conditions using an active control of the pitching angles at diverse rotation speeds.

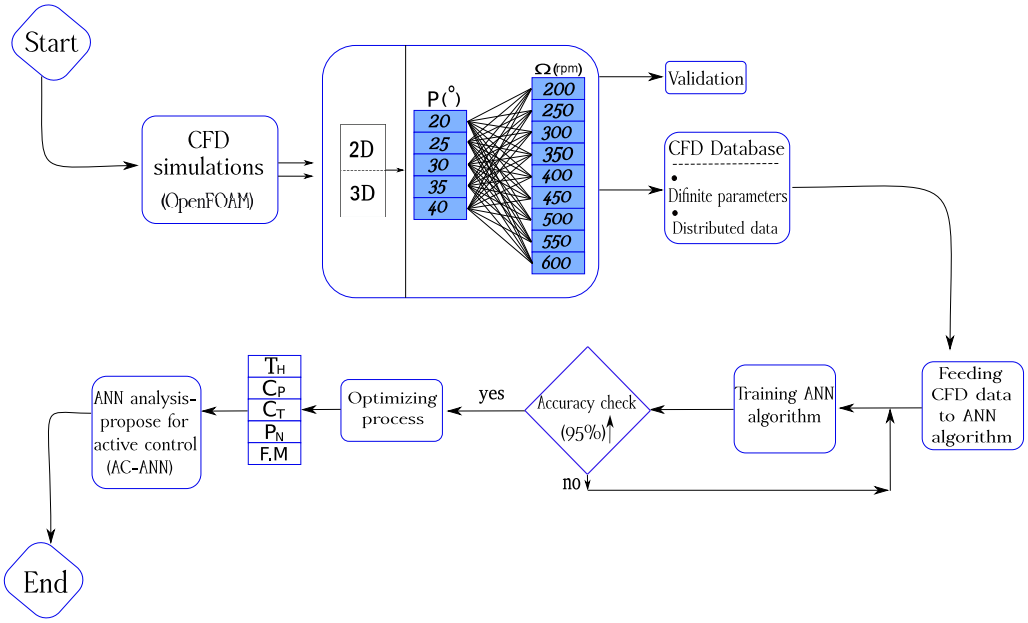

Figure 2.13: Progressive steps used to find the optimized active control modes in order to obtain optimum cyclorotor operation.

In order to compare the relative discrepancies in results of the CFD simulations, and ANN analysis, with those of the experimental tests a parametric study is also shown in tab.2.2.

Table 2.2: Comparison of aerodynamic results of experiments, CFD and ANN optimizations at 30° pitching amplitude, and 450 rpm rotation, in hover state.

Variable	Exp.	2D (CFD)	Error, %	3D (CFD)	Error, %	ANN	Error, %
C_T	0.1582	0.1529	-3.21	0.1552	-1.87	0.1529	-3.32
C_P	0.1196	0.1155	-2.86	0.1203	0.59	11.53	-3.57
D.L	52.81	51.769	-1.97	52.461	-0.66	53.554	1.39
P.L	0.0761	-0.07409	-2.63	0.0749	-1.47	0.0733	-3.65

The values of the aerodynamic variables in each approach are presented and the relative errors are described in order to reveal the reasonable agreement of the current results with those of experiments.

2.5 Results and Discussions

Performance assessments on various parameters that are utilized for the operation of cycloidal rotors have been consistently collected during many years. These parameters include blade numbers, profile types, chord length, rotor size, displacement speeds and oscillations, pitch control strategy and so on, in real tests and also by simulation and analytical studies. In this regard, it has already been proved that cyclorotors are potential candidates to be alternative for conventional propellers in specific situations. Indeed, this fact has been deduced due to the comparative advantages of cyclorotors in certain propulsion and control mechanisms.

In this study a detailed tracking of thrust performance has been assessed over a continuous azimuth trajectory (0° – 360°). Moreover, in order to derive the optimal efficiency

of the operating state, both computational simulations and neural network analysis are conducted. First, a continuous variation of aerodynamic forces and flow behavior is computed through CFD simulation over the continuous circular trace. On the following step, the predicted parameters in all simulations are fed as an input dataset to the ANN code in order to code the optimization process. Using this ANN approach an optimized pitching schedule for each rotating speed is proposed in accordance with the evaluated values of all critical parameters, this will be further discussed in the subsequent sections.

2.5.1 CFD Simulations

The primary phase of the current study was the CFD analysis to understand and predict the detailed behavior of the passing flowfield. Since the dominant flow configures complex flow curvature and deformation while entering (inhale) and exiting (exhale) from the cyclorotor, it is intended to track it over a complete cycloid. In doing so, the lateral and vertical forces of a single operating blade are derived while traverses a circular trajectory. Therefore, several pitch angles and rotational speeds were tested to reveal a logical and comprehensive perception of the flow phenomena. The geometric dimensions are constant for all simulations, with $0.15m$ blade chord and $0.4m$ radius. The Reynolds number for 300, 400, 500 and 600 rpm in hover state were roughly 9.5×10^4 , 1.35×10^5, 1.8×10^5 and 2.5×10^5, respectively. The k-ω-SST is here used following the detailed studies on turbulence model accuracy reported in our previous work [40].
In a cyclorotor operating in hover-state, the majority of the inhale flow enters the cage from the top-half circular path, whereas and the exhale region is addressed to the bottom side of the rotor. The present work is dealing with the study of the flow and rotor blade behaviors including their interaction over a continuous circular trace of azimuth. Therefore, aerodynamic forces, inflow, downwash velocities, and pitching oscillation schedules are all presented continuously over that operating circular trace.
Figure 2.14 depicts the horizontal force coefficient for five pitching oscillation angles from 20° to 40° in four separate rotating speeds from 300 to 600 rpm. As is shown in Figs.2.14(a-d) horizontal force experiences two positive peaks in each cycloid. These peaks sit in the intervals of $30^\circ \leq \Psi \leq 70^\circ$ and $140^\circ \leq \Psi \leq 250^\circ$ of azimuth angles which correspond to the right and left halves of rotor, respectively. Horizontal thrust production is higher in the left half of the rotor as can be seen in all plots of Fig.2.14. It is observable that as the rotational speed increases, the maximum horizontal force occurs in lower pitch angles. The greatest achieved C_{F_X} value, which touches around 0.24, is obtained with 35° maximum pitch angle, rotating at 400 rpm (Fig.2.14.b).

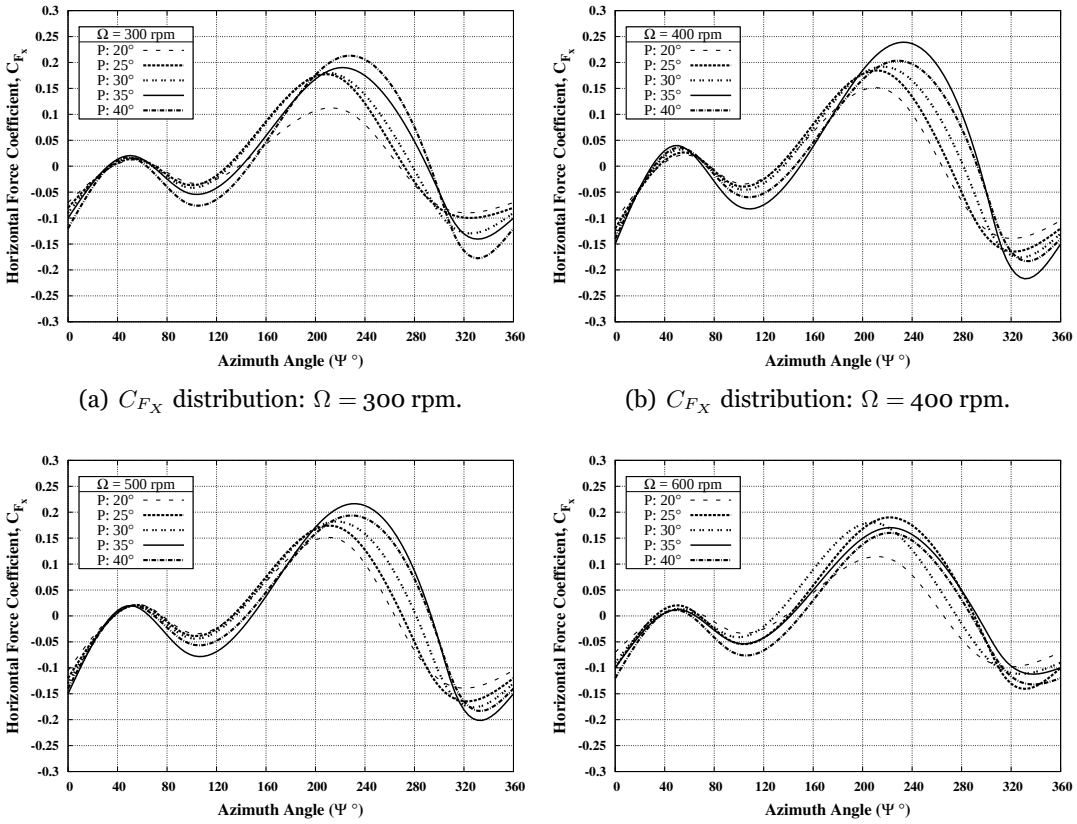

(a) C_{F_X} distribution: $\Omega = 300$ rpm.

(b) C_{F_X} distribution: $\Omega = 400$ rpm.

(c) C_{F_X} distribution: $\Omega = 500$ rpm.

(d) C_{F_X} distribution: $\Omega = 600$ rpm.

Figure 2.14: Horizontal force coefficient distribution over a complete cycloid path at different rotational speeds and maximum pitching amplitudes for a cyclorotor operating in hover.

Three points are valuable to be mentioned while considering the optimum state in here; i) besides the high value regions, it is also essential to obtain the positive thrust zones, ii) it should be noted that the maximum thrust points differ in each single case corresponding to the pitch angles and rotation speeds, and iii) negative thrust zones and the corresponding values have also been noticed when conducting efficiency optimizations.

In addition, vertical force coefficients are also measured for the same operating conditions as shown in Fig.2.15. Likewise the horizontals the vertical forces also exhibit two peaks in a cycle. The contrast here is that the top and bottom halves are mainly responsible for lift production. The highest C_{F_Y} values predicted in the CFD study are related to the 400 and 500 rpm simulations, for a maximum of 40° and 35°, respectively (see Figs.2.15.b and c). The maximum measured C_{F_Y} values are 0.132 and 0.275 in 93°, for the top, and in 262° for the bottom half, respectively, for the 500 rpm case in 35° of maximum pitching angle (Fig.2.15.c). According to the C_{F_Y} plots in Figs.2.15.a-d, it can be noticed that the peak regions do not show significant change while being subjected to different rotational speeds. It also shows that the bottom side of the cyclorotor is producing higher vertical forces compared with the top half. This fact can also be attributed to the virtual camber effect of the blades as was mentioned [87] . The top side actually operates as the main inhaling zone where the air stream is sucked inward from a relatively null velocity. The bottom side, in comparison, experiences a concentrated flow passing with considerably

higher velocity.

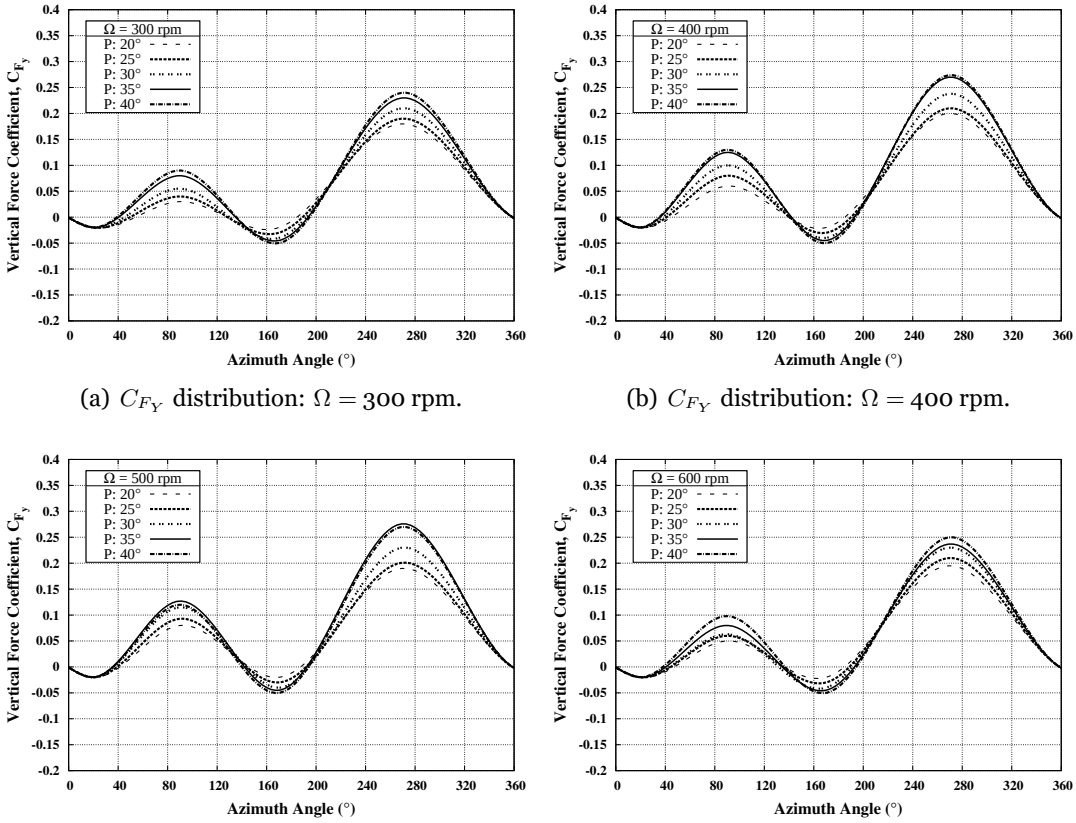

(a) C_{F_Y} distribution: $\Omega = 300$ rpm.

(b) C_{F_Y} distribution: $\Omega = 400$ rpm.

(c) C_{F_Y} distribution: $\Omega = 500$ rpm.

(d) C_{F_Y} distribution: $\Omega = 600$ rpm.

Figure 2.15: Vertical force coefficient distribution over a complete cycloid path at different rotational speeds and pitching angles.

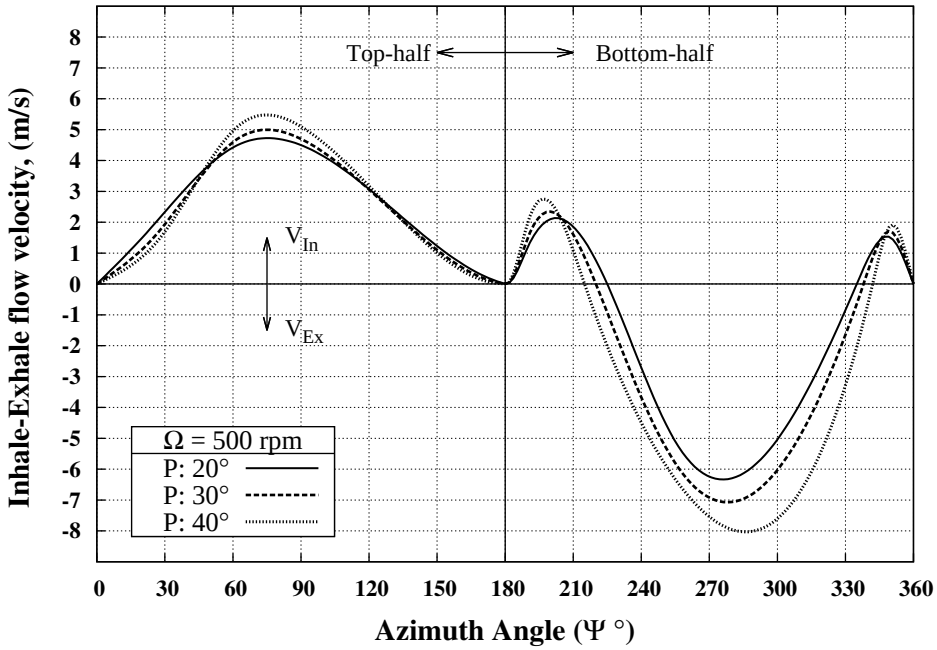

Figure 2.16: Inhale-Exhale flow velocity distribution over a complete cycle.

Another informative measurement regards to the induced flow velocity which, in this paper, has been separately termed as inhaled and exhaled flow. Considering a circular border, except the points of 0° and 180° of Ψ where the flow velocity is assumed zero, the rest regions holds a positive (V_{In}) or negative (V_{Ex}) sign in its velocity. These signs are considered as inhale and exhale velocities, respectively.
We also shown in Fig.2.16 the induced velocity distribution over a complete cycle for the 500 rpm speed and at three maximum pitch amplitudes. Some remarks are: i) the major portion of the circular trace belongs to the inhale flow toward the inside cage ($\approx$ +60%) , ii) by increasing the pitch oscillation angle, the exhale region slightly expands and the velocity peaks also increase. iii) there occurs an inward flow to the cyclorotor cage in the region between $340° \leq \Psi \leq 360°$ which is basically not in favor.

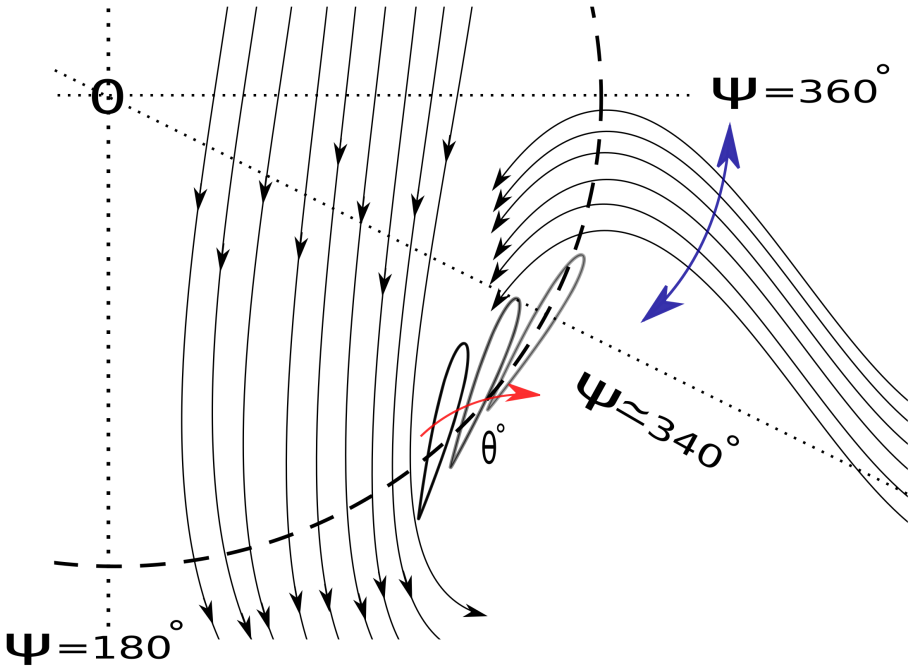

Figure 2.17: Schematic pattern of inward flow in the zone of $\approx 340° \leq \Psi \leq 360°$.

Figure 2.17 depicts a schematic of the flow path within the cage and the above-mentioned inflow entering the cyclorotor. This inflow is also visible in Fig.2.18. This contour is for the 30° pitch and 500 rpm case, but the same phenomenon happens for the rest of cases in all conditions. The possible reason might be strongly related to the pitching motion of the blade in clockwise direction (see Fig.2.17) while passing through this region. As it approaches towards the end point (Ψ=360°), the blade tends to reduce its pitch angle until it reaches 0° at the endpoint, that then becomes completely tangent to the circle path line.
This issue can be physically illustrated as the cause of the up-stroke sequence of the blade, and at the same time, the downward direction of the flow which, in total, induces the flow

inwardly to the cage. The strange horizontal force reduction in the region of about 340° $\leq \Psi \leq$ 360° can also be attributed to this inward flow. This strange behavior of horizontal force was also previous reported from Yun et al. [1] as a complex issue, but it can be attributed to the virtual camber effect of the blades as well [87].

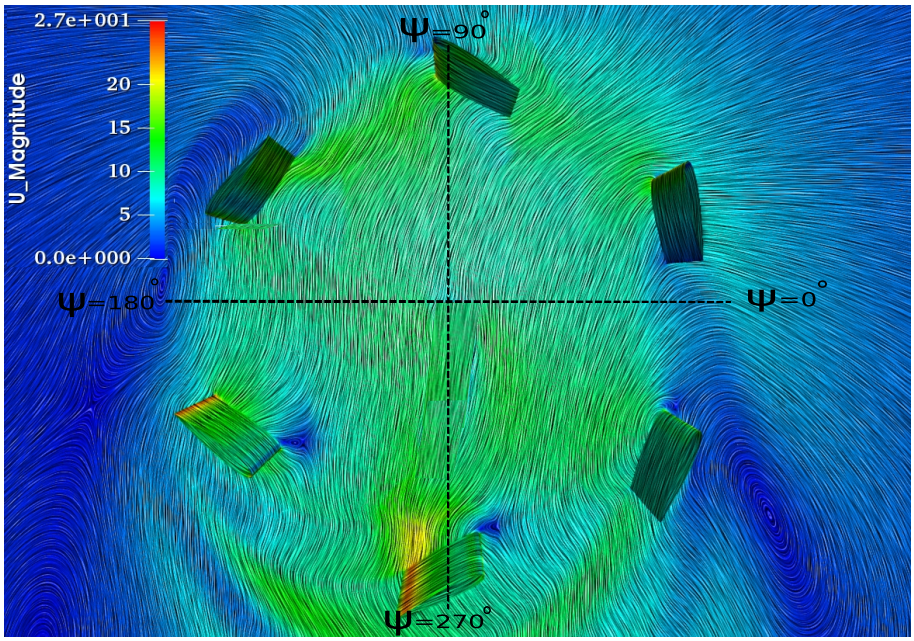

Figure 2.18: Flow contour of the inward and outward pattern in a cyclorotor at 30° pitch angle and 500 rpm rotation speed.

The featuring point is that the inward angle of the inflow imposes reverse horizontal force that subsequently produces the efficiency reduction. Furthermore, it must be noted that the same leakage occurs on the front side at the region of $\approx 180° \leq \Psi \leq 230°$, which is favorable, in accordance with thrust considerations. The more downward the flow goes (from the top to the bottom side of the cage) the higher velocity it takes. This fact causes a pressure gradient inside the cage which reduces in the downward direction and can be defined as the source of this fact, for both sides below the mid-line. This can also be an additional logical reason to implement active control of the rotor motions (both blade pitching and rotation) and this is further discussed in the subsequent sections.

2.5.2 ANN Analysis

Besides the core concept of the present work, related to active control of cycloidal rotor, the use of a neural network analysis appears to be beneficial in this regard. The idea is to go beyond the constant assignment of an oscillating angle while the blades are traversing the circular route. Since each specific position on the circular trace shows a unique behavior while operating, an optimized approach is also needed to take into account the enormous amount of information. In addition, the characteristics of each region also alters in different functioning conditions such as rotating speed, pitching angles and etc.
The blade local angle in a cycloidal rotor can be simply estimated as in reference [49] by knowing the precise position of azimuth (Ψ) and the top and bottom-most positions AOA,

which might be the pitching ultimates at the same time:

$$\theta(\Psi) = \left[\left(\frac{\theta_{(top)} + \theta_{(bottom)}}{2} \right) . \sin(\Psi) + \left(\frac{\theta_{(bottom)} - \theta_{(top)}}{2} \right) \right] \quad (2.15)$$

where $\theta(\Psi)$ refers to the angle of the blade at Ψ°, $\theta_{(top)}$ and $\theta_{(bottom)}$ describe the blade pitch angle while passing through the top and bottom-most locations in the cyclorotor, respectively. This equation can be simplified as $\left[\theta(\Psi) = \theta_{(top)} . \sin(\Psi)\right]$ for the top half ($0^{\circ} \leq \Psi \leq 180^{\circ}$) and $\left[\theta(\Psi) = \theta_{(bottom)} . \sin(\Psi)\right]$ for the bottom half ($180^{\circ} \leq \Psi \leq 360^{\circ}$).
The proposed concept implies to take a novel strategy, by implementing an active control of the blade dynamics in order to enhance the aerodynamic efficiency. Therefore, a comprehensive database of a wide variety of parameters in various operating conditions needs to be collected. This data collection should be done for any application of cyclorotors, for different type, and size which are related to diverse operational intentions. Active control herein, means to assign the local angle schedule, of each pitching oscillation, to the blade. For instance, according to eq.2.15, the blade at the position of Ψ= 60° and with the pitching assignment of 25° has a local angle of -51.65°, whereas the same blade at the exactly the same position, with 40° of pitch angle, has a local angle of -64.64°. Note that the mentioned angles are referred to the rotor origin axis, and not according to the tangent of the circle. So, in the coming discussion, the term pitch angle refers to the local angle of the blade when is subjected to the pitch angle calculated by eq.2.15.

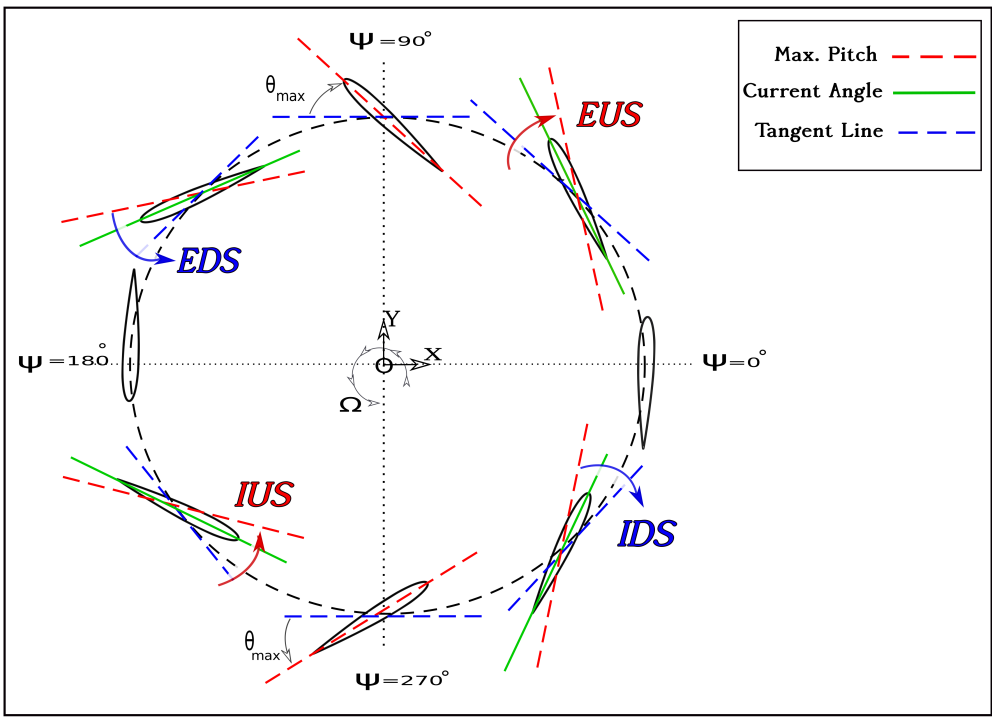

Figure 2.19: Illustration of the blade strokes for a cycloidal rotor in a single route.

The artificial neural network applied to the current UAV-scale cyclorotor to achieve an optimized operation. To this end, a dataset from over fifty simulations in both two and

three dimensional simulations has been included from the CFD results to be used in the algorithm training approach. The collected data is a combined arrangement of over eighteen different parameters which are derived from all the tested operating conditions, for diverse maximum pitching angles and rotational speeds. Force, momentum, vertical and horizontal thrust, net power, power and thrust coefficient, disk and power loading are the included parameters. The intention herein, is not only to provide an overall view of the efficiency scales, but also to track in detail the cyclorotor functionality and fluid flow behavior as the blades traverse.

To actively control the dynamics of the blades in a cyclorotor means to successively alter the pitch angle according to the operating states rather than use a constant pitch oscillation. For more clarity, considering a single blade while passing a single cycle, it reveals different efficiencies at each zone due to the complex flow mechanism acting in this system. This means, at each zone, a specific angle can show better enhancement. Therefore, instead of defining a fixed pitch angle for the complete route, in which normally oscillates constantly from 0° to the defined angle, twice a cycle, the blade can take the angle corresponding to any arbitrary pitch value.

In order to clarify the oscillating conditions, the stroke sequences of the blade while tracing a complete circular path are depicted in Fig.2.19. As is seen, in the first quarter, the blade is in the outward opening phase which is defined as the external up-stroke (EUS), and it continues until it reaches the maximum pitch angle at the topmost position. Approaching to the second quarter, the blade is experiencing the reverse pitching direction, which is here called external down-stroke (EDS). The bottom half of the rotor concerns the inward shifting. The third quarter is oscillating toward the maximum pitch again, which is called internal up-stroke (IUS) and subsequently progresses to internal down-stroke (IDS), in the last quarter.

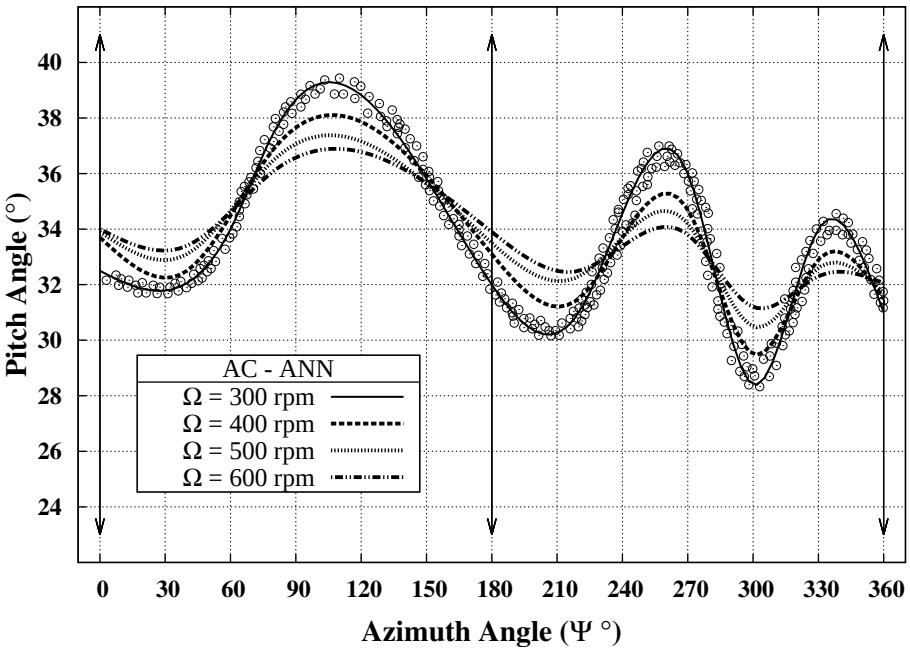

Figure 2.20: Pitching curves proposed by the ANN analysis in order to achieve improved efficiency.

In the ANN phase of this study, by feeding the already predicted and extracted parameters and their values from the current CFD simulations (see Fig.2.9), the algorithm has been trained efficiently for further analysis.
Figure2.20 depicts the ANN active control results from the optimization process. As can be seen in this figure, based on the obtained CFD results, the neural network proposes an optimized pitching oscillation angle on the continuously traversing circular trajectory. These analyses are computed for rotating speeds of 300, 400, 500 and 600 rpm as plotted in Fig.2.20.
The vertical arrowed-lines at Ψ locations of 0°, 180° and 360° in Fig.2.20 are indicating the 0° angle for the blades when passing through these points. Basically, the blades are tangent to the circle circumference at these points.
The following points can be illustrated from the ANN active control result in Fig.2.20:

1. As the blade approaches in the first quarter from 0° to $\Psi \approx 50°$ (where the inhale flow speed (see Fig.2.16) and horizontal force (see Fig.2.14) are both increasing), ANN proposes to decrease the blade angle which means the reduction of the EUS speed.

2. According to figure 2.15 and 2.16, which indicate the maximum lift production and inflow speed are both occurring at $\Psi \approx 90°$ (for the top-half), the ANN proposes continuous rise-up of the blade angle until reaching to $\Psi \approx 115°$. Here the gradual increase in local blade angle implies a lower speed in the EDS. The reason of this, as proposed from the ANN, might be to compensate the lift reduction and the negative horizontal thrust that the blade produces in the zone of $\approx 90° \leq \Psi \leq 120°$ (see Fig.2.14).

3. For the bottom side of the rotor, the ANN proposes to reach the ultimate pitch angle at the location of about $\approx 260°$. This basically means that, the local blade angle at the mentioned position, will be the angle of when the cyclorotor operates with a constant 37° pitch amplitude. The high speed of the downward in-cage flow and momentum achieved, might be the physical justification for this optimization result.

4. Considering $\Psi \approx 90°$ and $\Psi \approx 270°$ for the maximum receiving angle for the top and bottom halves, respectively, ANN provides different values for each of these extremes. Still the max pitch angles in each of the top and bottom halves are happening at the same points, but with different values. For instance, in 300 rpm case, ≈39° is assigned for the top ($\Psi = 90°$), whereas the bottom ($\Psi = 270°$) is showing higher efficiency with ≈36° angle.

5. In the last tracing region, of about $\approx 335° \leq \Psi \leq 360°$, which was previously termed as the undesirable induced flow, the blade is predicted to be more efficient if it experiences a lower IDS speed. That is why the ANN-AC prediction curve in the mentioned region reduces to lower pitch angles in Fig.2.20.

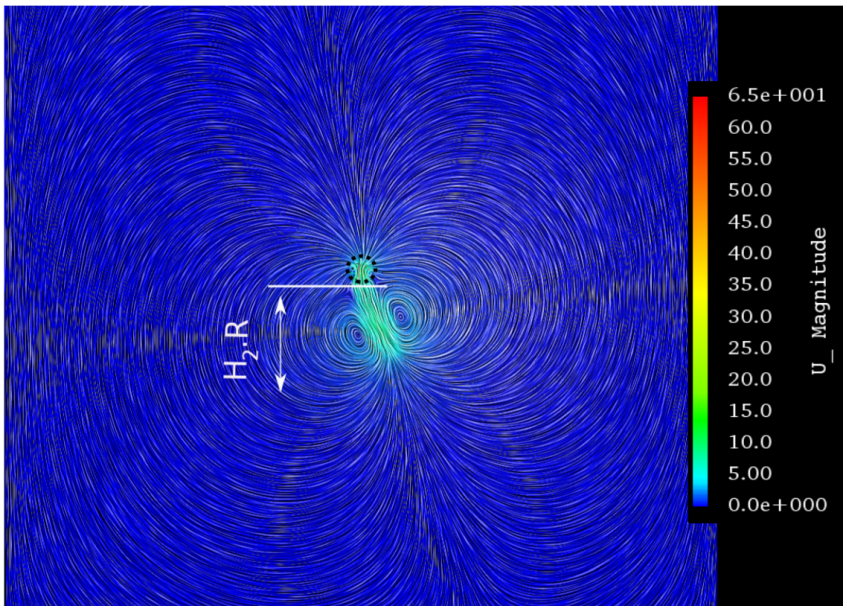

(a) Flow Contour and Downwash for Constant 25° Pitch Angle

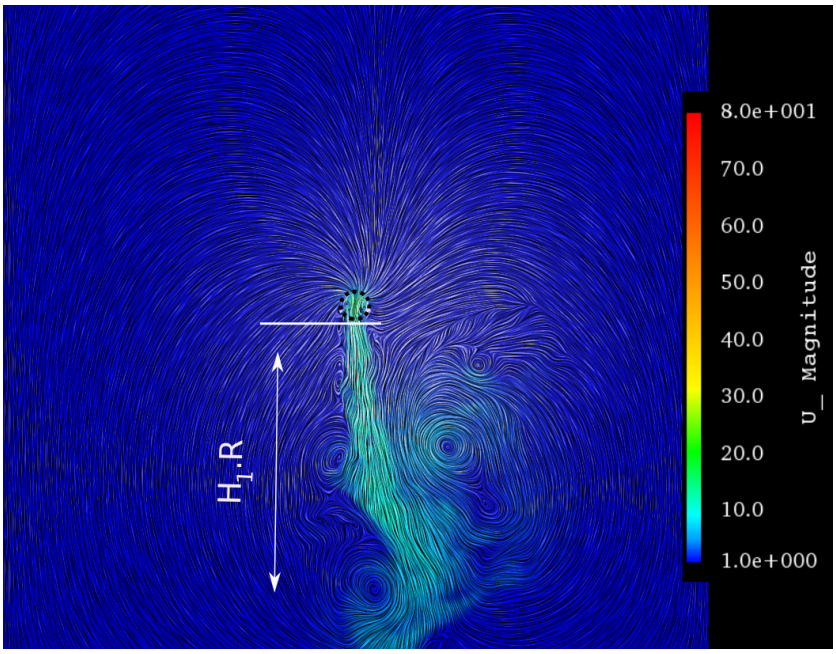

(b) Flow Contour and Downwash for the Optimized Schedule

Figure 2.21: Comparison of the flowfield and downwash jet, for the cycloidal rotor operating at 600 rpm, with different pitching schedules.

According to the optimized pitching schedules, from the ANN analysis, the results are then verified in direct CFD simulations as well. Therefore, the proposed schedules were verified for 7 rotating speeds. Figure 2.21 presents a comparison of the cycloidal rotor operation at 600 rpm rotational speed at two different oscillating schedules. Figure 2.21 is showing the flow LIC contours for a) constant 25° pitch angle and b) an optimized pitching schedule, respectively. An obvious difference between the two simulations are the downwash flow lengths and intensity. A rough estimated measure of these length shows that the downwash length, in the optimized case ($H_1.R$), exceeds $18.R$, whereas the $H_2.R$

length goes around $10.R$. Notice that all geometrical, meshing and other specifications are kept similar in both cyclorotor simulations.
The stream traces of the flow and downwash jet are also shown in Fig.2.22. This figure depicts a 3D view of the flowfield of the optimized operating schedule at 600 rpm speed. The sub-figures herein show the flow traces from different aspects and distances to the rotor. This fact can also be attributed to the virtual camber effect of the blades as was mentioned [87] . The top side actually operates as the main inhaling zone where the air stream is sucked inward from a relatively null velocity. The bottom side, in comparison, experiences a concentrated flow passing with considerably higher velocity.
As a key factor to be considered for flight endurance and hovering efficiency, power loading is considered here to evaluate the performance of the analyzed cyclorotor. Figure 2.23 demonstrates the comparisons of power loading versus disk loading plots with CFD and optimized active control approaches. The plots from numerical results are shown for 20°, 30° and 40° pitching angles. This figure indicates that a pitching oscillation angle of 30° performs better than 40° and 20°, respectively. This fact can also be deduced from the F.M plots shown in Fig.2.24. To achieve higher efficiency and better performance, a higher value of force to power ratio is sought. As is seen, at all constant disk loading values, the moderate pitch angle (30°) shows better efficiency compared with those two pitch angles in producing higher forces and hence higher ratios. Aside from the three fixed pitching oscillations, which are presented in this plot, the optimized oscillating schedule that is proposed from the ANN is also plotted, to compare the performances. On the other side, in order to maximize the power loading, it is critical that the cyclorotor operates at the optimum rotational speed. Furthermore, since net thrust and net power are actually a function of the square and cube of rotating speed respectively, the power loading varies reversely with rotor radius and rotating speed. As is depicted in Fig. 3.20, the optimized schedule is revealing a higher performance ratio (force to power) for all constant disk loadings, as compared with other pitching angles. This fact also demonstrates that proposing optimum pitching schedules will result in an optimum performance ratio, which means a higher power loading for any given disk loading values. This also ensures that the taken approach for the active control of the cyclorotors can be effectively advantageous in aerodynamic performance. The terms power loading (P.L) and disk loading (D.L) are defined as follow:

$$P.L = \frac{T_{_N}}{P_{_N}}, \quad (2.16)$$

and

$$D.L = \frac{T_{_N}}{A}. \quad (2.17)$$

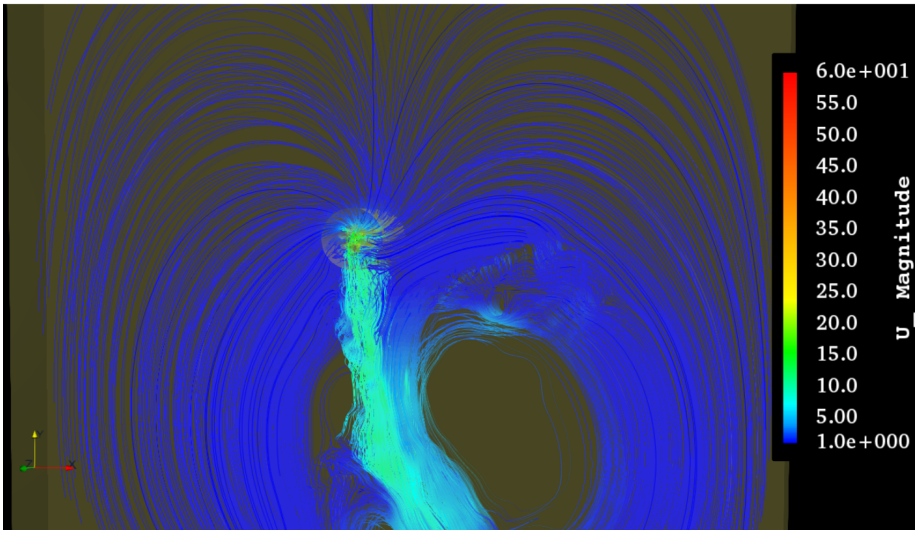

(a)

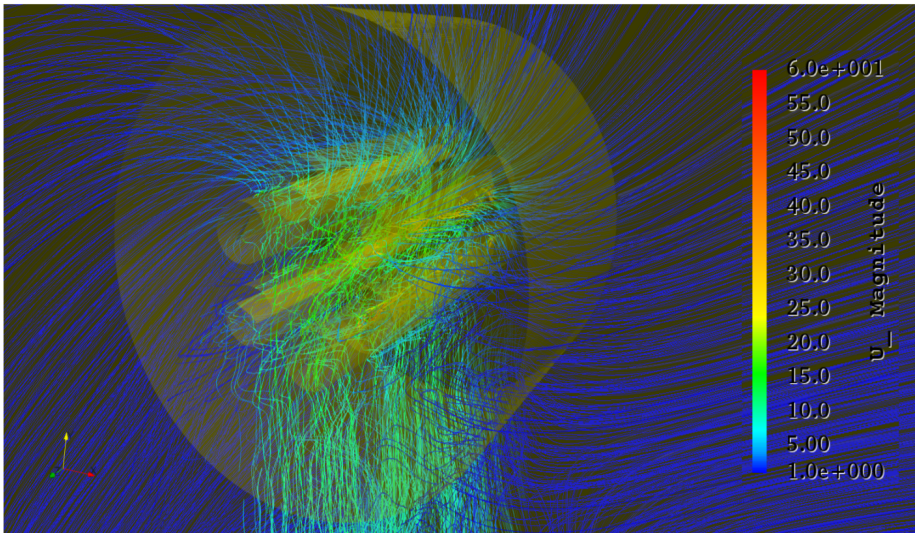

(b)

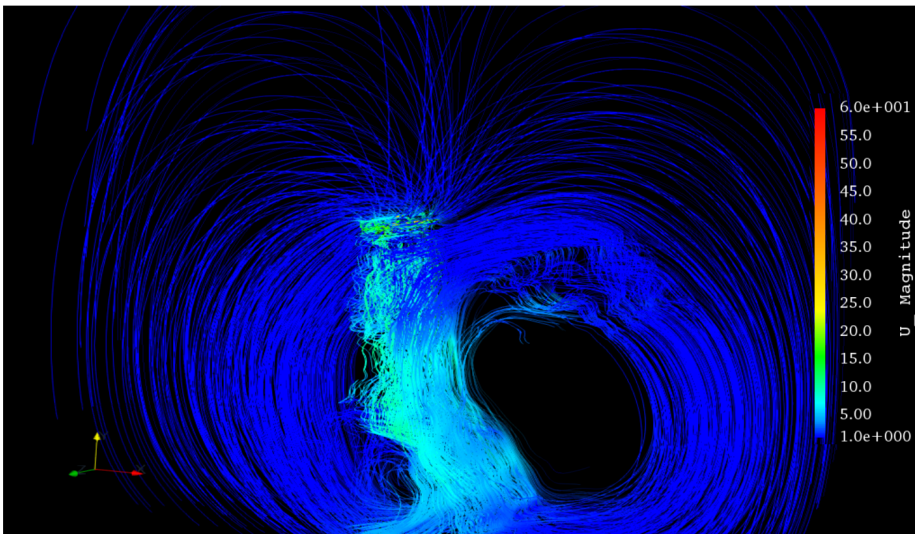

(c)

Figure 2.22: Flow and downwash stream-traces for an operating cycloidal rotor at 600 rpm and optimized oscillating schedule.

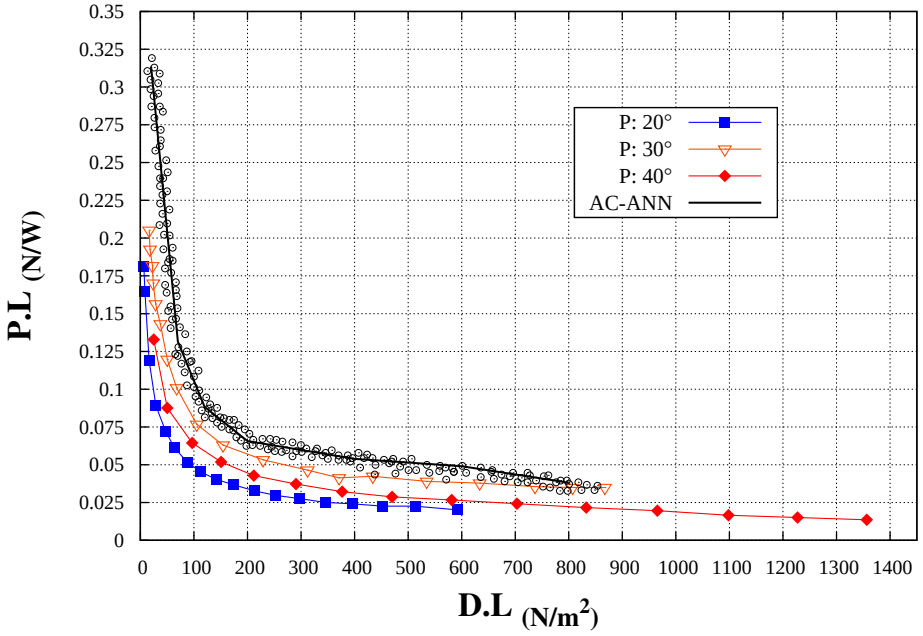

Figure 2.23: Power loading vs. disk loading comparison for different pitch angles in CFD and optimized AC-ANN.

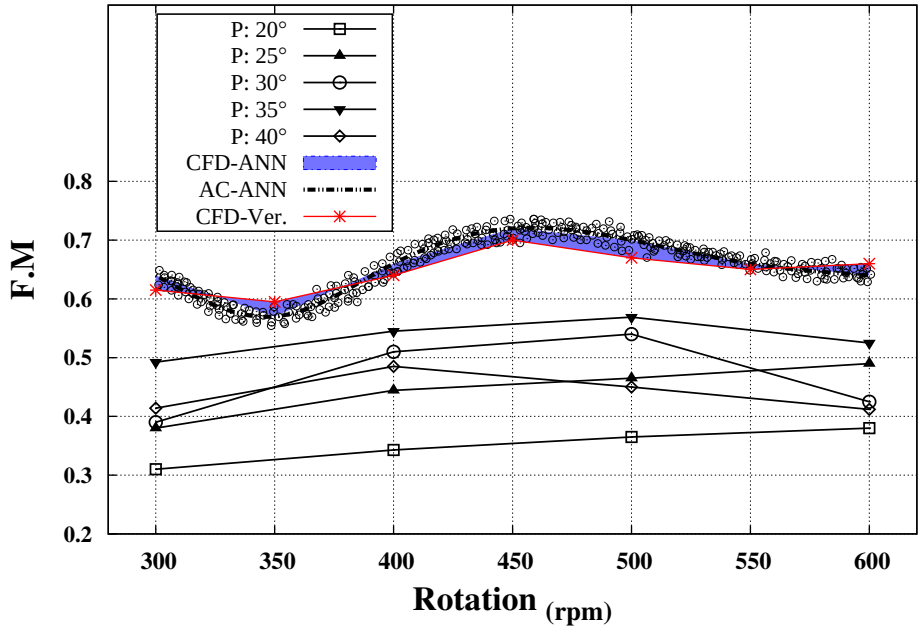

Figure 2.24: Comparison of figure of merit for constant pitch oscillation angle vs. optimized ANN active control pitching curve in different rotation speeds.

2.6 Conclusion

In the present work a detailed analysis of the flowfield produced by the cyclorotor blades over the 360° operating cycle was initially performed. In doing so, the study comprises a combination of the blade attitude while traversing the circular cycle and the correspond-

ing flow behavior accordingly. The concept achieves a comprehensive understanding of the flow dynamics in order to propose an active control approach for the cycloidal rotor. This means that instead of imposing constant pitch angles, the blades follow an optimized oscillation schedule. To this end, the current study was carried out in two phases, namely the CFD simulations and the neural network analysis. The CFD phase is accomplished for a sufficiently wide variety of operating conditions, maximum pitch angles (20°, 25°, 30°, 35° and 40°) and rotating speeds (200–600 rpm with +50 intervals). These CFD predictions led to an appropriate database to be used in the subsequent ANN analyses. The second phase of the present study implies to propose a feasible active oscillating schedule for the operating blades, according to performance analysis. Based on the CFD results, the attained values from various parameters in different conditions were fed to the ANN algorithm for the training procedure. Associated with comparatively high accuracy of ANN approach, the output results are further interpreted and solutions are proposed from the optimization analysis. A summary of the conclusions from both the CFD simulations and ANN analysis are illustrated as follow:

1. The highest efficiency achieved from CFD simulations for the base-reference cyclorotor in hover state was found for the operation at 30° of pitch angle and 500 rpm rotating speed.

2. Although from the theoretical point of view, the top-most and bottom-most locations of the cycloidal rotors are producing the highest lift-up force, there might be some deviations from the defined positions for both vertical and horizontal force productions. This was clearly observed from the plots of forces corresponding to azimuthal angle in diverse conditions.

3. CFD results describe the occurrence of an unfavorable induced flow entering the cage at the location range of approximately 340° to 360°, that can be the source of horizontal force negative sign.

4. At a constant rotating speed, the higher pitch angle is defined, the higher speed the induced flow experiences.

5. According to the ANN approach, which has been taken for the active control concept, the following highlighted comments came noticeable:

   a) Keeping the pitching ultimates at the top and bottom positions of the cyclorotor, the top location experiences comparatively higher pitch angle than the bottom.

   b) ANN has proposed to decrease the speed of the IDS phase in order to minimize the efficiency loss, which is originated from induced flow before reaching the end point of the circular cycle.

   c) ANN proposed a pitch varying schedule of the blades for each defined operation state, based on parametric analysis of variables such as thrust, lift, drag, and aerodynamic efficiency. This approach resulted in improved efficiencies by 12 percent for the cyclorotor operating in hover state.

Overall, the mutual collaboration of the CFD and ANN, resulted in a detailed study of the concept of active control for cycloidal rotors. However, these calculations can be further investigated in real tests to evaluate the performance of the proposed control mechanism of the blades. The way to incorporate the pitch schedule in a real system will constitute a challenge. This includes the use of oscillating frequencies, the feasibility of control at different flight phases, like forward-cruise and vertical lift-up. All these can be studied for future work which might lead to more efficient and even increased performances for a future generation of cycloidal rotors operating at diverse scales.

Chapter 3

3D Effects of The Cyclorotor Endwalls

[1]

3.1 Overview

An aircraft with the capability of vertical take-off and landing, hovering states, and cruise-speed flights fairly comparable with those of fixed-wing is defined as a vertical take-off and landing (VTOL) aircraft [88]. According to this definition a large number of aerial crafts are excluded from the VTOL category, i.e balloons, airships, commercial planes, etc. Technically, the purpose of the VTOL concept can be used for diverse applications and missions which are critically restricted to short runaway terrains and hovering capabilities. Rescue missions, surveillance cameras, fire-fighting missions, short take-off and landing environments such as forests and sea missions, and so on, are just a few examples to mention. Accordingly for VTOL , numerous prospering and also failed propulsion designs have been proposed over the years. Conventional helicopters with planar screw propellers are one the most common systems of this type.
One of the novel concepts for both VTOL applications and naval purposes is the cycloidal rotor (cyclorotor) [2], which was initiated in 1926 by a collaboration between Fredric Kurt Kirsten and Boeing company under the title of "Kirsten-Boeing" propellers [3]. Cycloidal rotor is an arrangement of a couple of blades that are diagonally settled from a circle center, which is considered the rotation center. Moreover, in addition to their rotational displacements, the blades are following a pitching motion schedule that imposes oscillations [43]. Therefore, a pitching center is also allocated on the chord-line of each blade. Compared with conventional propellers, regardless of any operating condition, the aerodynamic features in this system are relatively equal throughout the span-wise direction. However, in the screw propellers, the functional behavior of the flow and the propellers differ from the hub to the tip. Enhanced maneuverability and hovering control and stability, less vortice shedding due to lower tip frequencies, and lower noise, are some of the advantages of cyclorotors [44, 1, 45]. As such the same category rotary device, Darrieus turbine operation is studied under low wind speeds for wind turbine applications. In this regard, Balduzzi et al. [89] performed 2-dimensional unsteady simulations of a Darrieus turbine in order to study the effect of blade designs on the optimal flow curvature for performance criteria in these turbines. By using the blade element method (BEM), and by comparing the two blade designs they proposed an optimum profile which best compen-

[1] Based on the work submitted to Journal of Fluids Engineering, A Coupled Active Control Technique for Oscillating Blades in a Cycloidal Rotor Using CFD and ANN Analysis by Including 3D Endwall Effects, n° pages (21) , 2020

sates the flow effects in order to achieve higher performances. In another parametric study from Castelli and benini [90], the effects of blade incidence angles with various oscillating inclinations at 0°, 30°, 60°, 90° and 120° are evaluated in a helical Darrieus turbine. They could theoretically perform the energy performance estimation with regard to the tip re-circulations of the flow and the induced drag influences on the rotor performance as a function of blade azimuth and longitudinal positions.

Several investigations have been non-continuously reported on structural designs, experimental tests, numerical simulations and also optimization since the advent of cyclorotors. At the Seoul National University, Lee et al. [50] conducted experiments on a UAV multi-cyclorotor design by attaching a payload to test the hovering performance of the aircraft. By implementing the tethered flight tests, they reached to a considerable maneuvering capability of their design and reported efficiency augmentation. Based on the flux-line theory, Adams and Chen [52] performed analytical performance evaluation for cycloturbines. They became capable of predicting the rotor optimization independent of the blade elements. They also proposed their theory for optimization analysis of cycloidal rotors operation in hovering and forward-flight modes. Tang et al. [49] have recently performed a multi-disciplinary optimization analysis using a surrogated model and a genetic algorithm. Based on their proposed methodology, they reported an approximately 20% aerodynamic efficiency increase at hovering-state of a cyclorotor.

Regarding to the flow characteristics in a single pitching blade of a cycloidal rotor, Singh and Pascoa [40] have recently performed a comprehensive and detailed numerical study on its different aspects. Vortices evolution, shedding analysis and the passing flow behavior under deep stall operating conditions at diverse turbulent states by comparing several turbulence models were part of their study. Moreover, they evaluated the blade performance at different angles of attack according the level of dynamic stall and vortex characteristics. Tadjfar and Asgari [91] have performed another similar study by considering turbulence models in predicting the influence of tangential blowing jet while a NACA0012 profile is in dynamic stall at 10^6 Reynolds number. They obtained and reported qualitative and informative flow characteristics of the pitching blade for their lift and drag during peaks and also their down-strokes. To be mentioned that the process of deep dynamic stall for these airfoils under pitching conditions are fairly associated with flow separation from the leading edge and the boundary layer transition from laminar to turbulent flow [92, 93, 94]. It should be noted that due to the adverse pressure gradients the flow becomes extremely sensitive under these conditions and thus an accurate prediction of all these complex behaviors of flow is becoming highly essential in defining the blade behavior under different operating conditions [95].

Using a CFD approach the interaction of the downwash jet flow with the ground, for a UAV cyclorotor, at different take-off and landing altitudes were also investigated [41, 47]. Besides the numerical approach, they also carried optimization analysis of the operating conditions by using neural network analysis. They eventually proposed the optimal rotation speed and pitching oscillation angle for each of the hovering altitudes. In micro aerial vehicles (MAV), Benedict et al. [51] have gone through numerous experimental and nu-

merical tests for the applicability of the cyclorotor for very light VTOL aircraft designs. They have reported numerous informative and detailed studies on different aspects like the rotor size, blade numbers, and different blade profiles.

In a technical report by Gostelow et al. [96] studied the vortex and wake flow formations from two different oscillating blades of a turbine. they demonstrated that in both blunt body and oscillating airfoils the von karman vortex street is impending from the trailing edge of the profile. They performed a comprehensive study regarding the flow structures under various operating conditions, designs and flow speeds.

In addition to the aerial propulsion system, the cycloidal rotors have also been proposed for naval purposes in marine and submarine applications [55, 56]. Similar to the aerial craft, the design, operation, optimization and analysis were pursued and studied with the aim of obtaining higher performances in marine systems [57].

”CROP”, was a major European Union project allocated to further study the different designs and optimizations of the cycloidal rotors. A detailed analytical study on the detection of an optimum mechanical specifications for a UAV-scale cyclorotor was reported by Leger et al. [28, 30, 29]. By using a coupled methodology of CFD simulations and analytical analysis, they proposed optimum blade dynamics and rotor kinematics for different operating conditions in 2D and 3D designs. Approaching to these performance optimizations, Xisto et al. [32, 54] studied more in detail the operating flow while passing through the cyclorotor and the blade interactions with the flowfield. Obtaining higher efficiencies, they proposed the implementation of dielectric barrier discharge (DBD) plasma actuators to enhance the flow control on the oscillating blade profiles. The most significant issue in rotary applications, such as cyclorotors and turbines in general, is the flow losses originating from phenomena like blade stall, shear layer separation, wakes and vortices which induce an overall reduction in the system performance [58, 59]. As a novel concept in flow control in different stationary or even multi-motion physics and applications, plasma actuators have been widely proposed in recent years [63, 64]. Scientists in this field have proven considerable advances in both aerospace and mechanical systems with the performance augmentation in flow control, and avoidance of boundary layer separation [65, 66, 67].

The quantification of the unsteady aerodynamic loading for oscillating airfoils was the subject of the theoretical and numerical study of Corral and Vega [97]. In the first phase, based on a perturbation analysis of the linearized Navier–Stokes equations, they deduced that a new parameter namely unsteady loading should be essentially introduced for the study of the unsteady pressure caused by oscillating airfoils. By this, they managed to straightly predict the airfoil performance according to the steady flowfield at each vibration mode. This theory was then further confirmed [98] in a numerical assessment of different airfoil profiles and under various operating modes. They could possibly prove their theory to be an assistant in comparing the flutter characteristics of airfoil types quantitatively.

Although the investigations on cyclorotors had some halts in some decades, the researchers in this field are obtaining a good progress on this topic in the most recent years. As is

above-mentioned, the researchers are finding and proposing more efficient designs for this propulsion system in different applications. There include aerial and naval systems cyclorotor structural design and specification, rotor sizes and blade numbers, blade profiles and sizes, various operational conditions, different flight modes, dynamic control and optimization, flow pattern etc., are all featured issues that have been partly investigated. The positive claim is that during the recent years, more novel designs, patents and practical applications, especially in aerospace field, are being reported.
A novel propulsion design using a coupled utilization of two cycloidal rotors combined with an adjustable pair-wing system is recently submitted as an international patent by the current authors of this study. This newly patented propulsion system provides VTOL and higher speed forward-flights and the possibility of take-off and landing from/on both ground and marine surfaces. Furthermore, we have already conducted some numerical and optimization analysis on UAV-scale cyclorotors focusing on different issues. The interaction of the cyclorotor downwash jet flow with the ground surface in take-off and landing phases, optimization and performance analysis at hovering state operation, lift-up and forward-flight simulations and efficiency assessments are the investigated issues accordingly.
In the present work, the authors are about to study and illustrate the effectiveness of endwall design on a UAV-scale cycloidal rotor in hovering mode. The use of endwall designs with an optimization analysis is the focus of this study. The three main designs are sides-free, single endwall, and double endwalls. In the initial phase, the designs have gone through CFD simulations under various operating conditions. Then, a database is collected with the main parameters to be used in the artificial neural network analysis. The other novelty of the present work is to address the computed parameters in a continuous azimuthal trajectory for precise performance analysis. Aside from the comparisons of the three designs at different operating conditions, an active-control methodology is taken and proposed for each of the designs to operate at the corresponding optimal condition. The main focus is to reveal the optimum pitching schedule at each rotational speed rather than assigning a constant pitching angle to the blades. As was also declared in our previous studies [47], the mutual collaboration of CFD and ANN has provided remarkable insight and efficiency enhancements for a cyclorotor at different operating modes and conditions. Therefore, the active-control methodology is currently performed for different type of endwall designs and the optimal operating efficiencies are also obtained for each operating condition according to the continuous circular trace of the blades.

3.2 Cycloidal Rotor Definition

3.2.1 Operational Design

In principle cycloidal rotors are a combination of diagonally arranged blades in circle, where the center of this circle is the rotation center. In addition, the blades are oscillating simultaneously while traversing the circular route. According to each design the pitching center varies along the chord line. For instance, in the current simulations, all the blades

pitching centers are positioned at the front quarter length from the leading edge. These rotors have shown their potential in various applications such as in naval thrusters, wind energy, and aerospace for propulsion purposes.

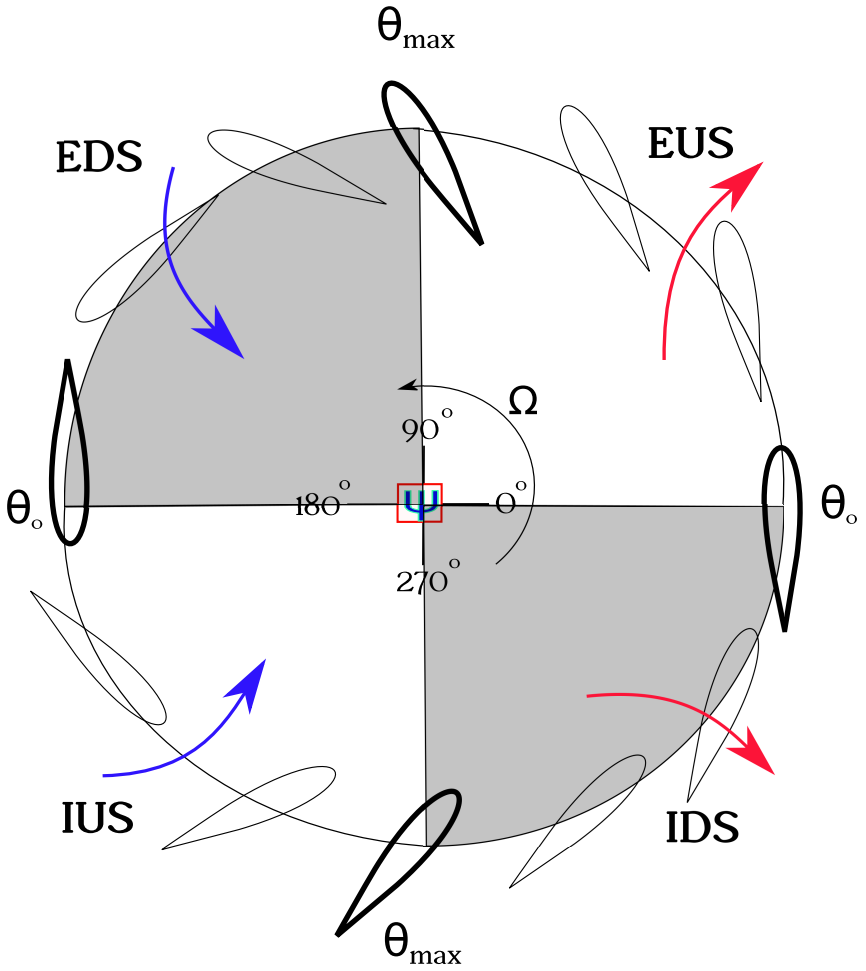

Figure 3.1: Schematic of blade settlement and operating procedure in a typical cyclorotor.

The schematic of the blade settlement and operating procedure is depicted in Fig.3.1. The orbital location of the blades on the circle is defined by the azimuth angle (Ψ) which is shown in the center. For the current design, each blade experiences two rounds of reciprocal oscillations in each cycle. The rotating direction is counter-clockwise in here, and the pitching extremes happen at $\Psi = 90°$ and $270°$ per cycle.
To further clarify the pitching-rotating mechanism, each stroke of oscillation is given as internal or external sign. The first quarter where the blade passes between $\Psi = 0°$ to $90°$ is called EUS which implies the external up-stroke of the blade, towards the maximum external angle. In the second quarter, the blade tends to retreat back to its initial angle which is simply called EDS, for external down-stroke. The lower half corresponds to the same procedure with the difference that there is an internal approach of the blade to reach its maximum pitching angle. Thus, those two are called IUS and IDS for internal up-stroke and down-stroke, respectively.

3.2.2 Active Flow Procedure

The acting flowfield through the cycloidal rotor experiences several deformations and curvatures until passing out from the system. Considering it as an inhaling-exhaling cage-like system, the flow passes through 3 stages. It is worth to mention that the flow behaves differently for each functional purpose. This means even as a propulsion system in aerial crafts, it depends onto which flight mode is operating. Forward-flight, take-off phase or hovering state all result in different flow mechanisms, correspondingly.
A general view of the flowfield in a cyclorotor operating in hovering mode is presented in Fig. 3.2. As is depicted, the three sequential stages which the flow passes through are identified as: 1) Inhaling region, 2) the downward flow inside the rotor cage, and 3) the downwash jet flow at the bottom zone of the cyclorotor.
It can be noticed that for the most part of the circular path refers to the inhaling region. This zone varies approximately from $\approx 0^\circ \leq \Psi \leq \approx 200^\circ$ in CCW direction. At each constant rotational velocity along the circular trace, the velocity, and angle of the induced flow changes at each location. As the flow enters to the interior passage, it moves downward by keeping a slight leftward inclination. While passing out through the bottom-side of the rotor cage, the flow condenses and flushes out by deflecting rightward as the downwash jet flow. To be noted that the downwash flow angle and velocity also alters with different designs (rotor size, blade numbers, etc.) and different operational conditions (rotating speed and pitching angle).

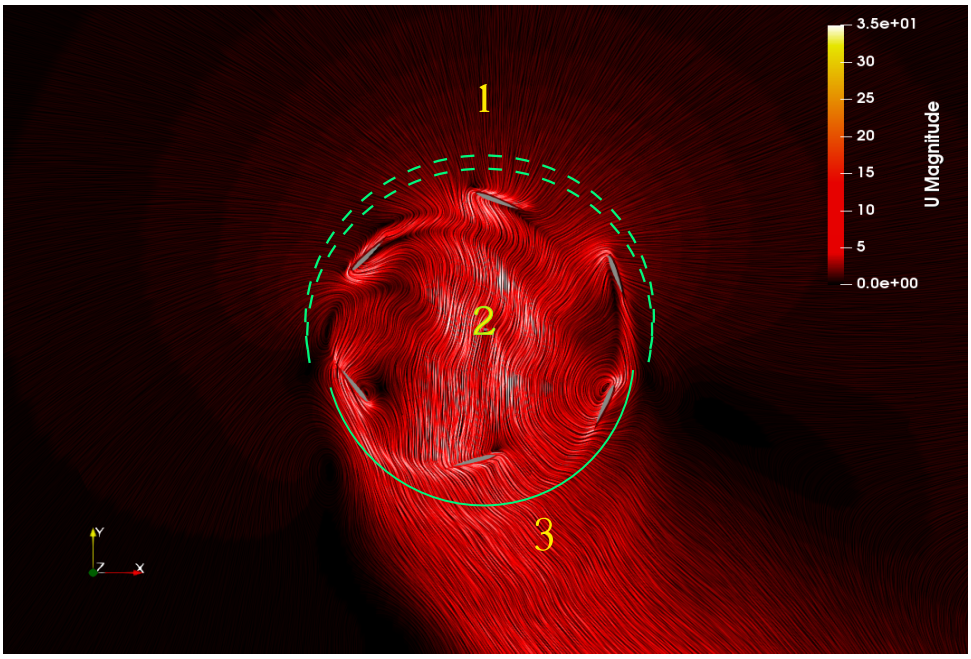

Figure 3.2: The flow structure in a hovering cycloidal rotor at 300 rpm and 20° pitch angle.

As is mentioned, the flow is subjected to consecutive deformations in a short time-pace while entering into exit zone as a downwash jet flow. Thus, an appropriate understanding of the flow mechanism is essentially required to reach higher efficiency and thrust performance. In order to reach a better operational state or a reasonable outcome, different

research approaches are needed. This covers a vast range of experiments, CFD simulations, analytics and optimizations to reach the optimal operation.

3.2.3 Side Endwalls

The subject of restricting the flow passages in turbomachinery applications always raised questions related to loss issues and efficiency levels. The main target is to gain higher control on the flow behavior and further enhance the system operations. One of the main concerns while manipulating the flow over diverse passage designs, especially in rotary devices such as gas turbines or cycloidal rotors, are flow losses, separations, wake and vortices, stall occurrence, flow leakage and secondary flow, which can strongly impact on the outcome of the operations.

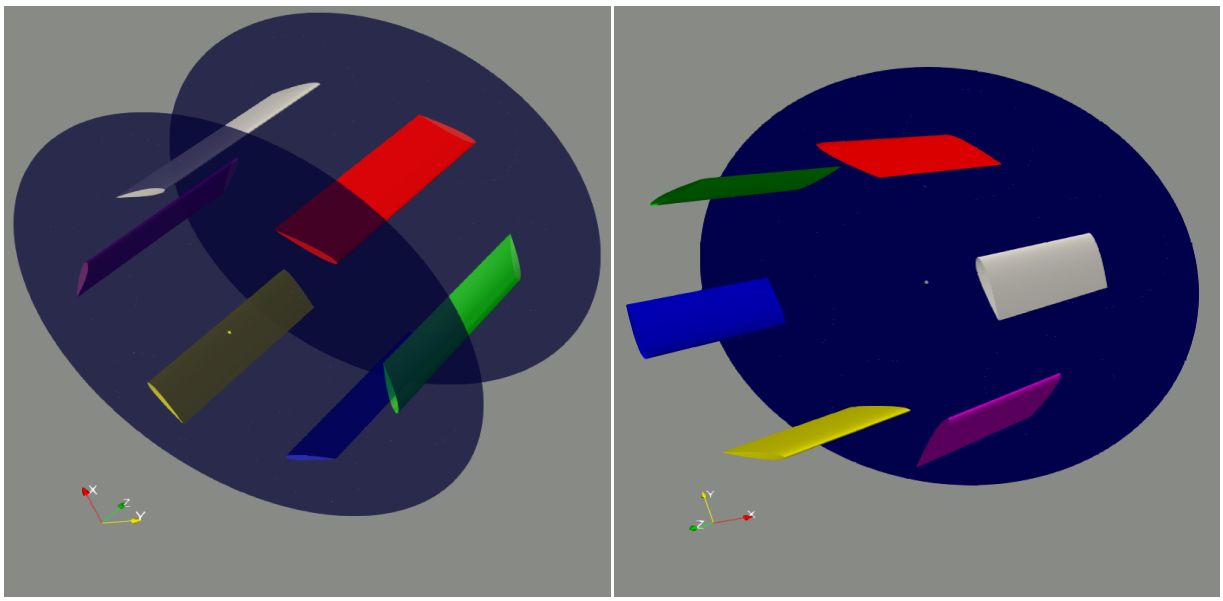

(a) Double-Side Endwalls (DE) in cyclorotor (b) Single-Side Endwalls (SE) in cyclorotor

Figure 3.3: Schematic of the side endwalls in cycloidal rotor.

Different from those of our previous studies [41, 47], the current work deals with the operational analysis of a cycloidal rotor operating in hover with 3 designs of endplates. The first is the sides-free (SF) where no endwalls are attached, and the second and third belong to single-endwall (SE) and double-endwall (DE), respectively. Both numerical and ANN studies are carried out to analyze the performance and optimal operating conditions, of each of these models correspondingly. Since cycloidal rotors are operating under various conditions such as different flight modes, and different combinations of rotating velocities and pitching oscillation angles, and each of these operating conditions result in different performances, it is important to study the endwall effect for these devices. It should be taken into consideration that this work describes the operation and evaluation analysis in all hovering modes of the rotor operations.

3.3 Numerical Simulation Methodology

3.3.1 Base Design Characterization

The test model of the UAV size cycloidal rotor which is under the subject of the present work consists of a 6-bladed rotor with a diameter of $0.8m$. The main characteristics of the base design are illustrated in tab.6.1. The blades airfoil shapes are comprised of NACA0012 profiles with $0.15m$ chord length. The pitching center is also positioned at 0.25 chord portion distance from the leading edge.
Three designs of rotor were also modeled in terms of the endwall presence. First is free sides where no endwall is employed, and the remaining two designs are with single and double-sides endwall, respectively. Aside from achieving the optimal pitching schedule for each of the rotational conditions, the endwall flowfield effect is also the other goal of this study.
Th blades are settled diagonally around the center with an aspect ratio of 1. Standard air is considered as the fluid medium in this study, and according to different operating conditions the active Reynolds number varies as is presented in the mentioned table. The rotor is assumed to function under null incoming velocity which represents the hovering operational state. More details are also seen in the table, and are further discussed in subsequent sections.

Table 3.1: The specifications of the base model of cycloidal rotor.

Parameter	Value	
Blade Numbers	6	
Airfoil profile	NACA0012	
Rotor radius	0.4 m	
Blade chord	0.15 m	
Grid type	Structured	
CFD simulations	3D	
Mesh motion	Dynamic oscillating-rotating, AMI	
Turbulence model	k-ε, k-ω-SST	
Inlet Turbulence Intensity	2%	
Fluid	Air	
Re number	300 rpm	9.5×10^4
	400 rpm	1.35×10^5
	500 rpm	1.8×10^5
	600 rpm	2.5×10^5
Aspect ratio	1	

3.3.2 CFD Approach and Turbulence Modeling

The OpenFOAM CFD toolbox is used for the simulations in the present project [70]. This simulation package is open source and actively extensible with the available base codes to be suitable for a variety of numerical computations. The most appropriate solver which best suits the application of cycloidal rotor is pimpleDyMFoam which can basically deal with multi-moving bodies with incompressible flows and turbulent conditions. This solver utilizes a combination of PISO and PIMPLE algorithms as well. Furthermore, in ap-

proaching to time-derivatives, a first-order bounded implicit discretization scheme, and, for pressure and velocity derivation terms the Gaussian integration has been employed. In order to deal with convergence criteria the computational residuals are made to reach 10^{-6} for both velocity and pressure equations. For the finalized turbulent computations under a Courant number of 5, the simulations were fairly passing 1500 loops/steps per each rotation of the rotor in order to save a time-dependent solution.
The selected turbulence model for the current simulations is k-ω-SST which was also approved to be the optimal choice, as was reported before from our previous work [47] and also for a deep comparison study by Singh and Pascoa [40]. Moreover, since the present study focuses on the 3D effects of endwalls, the flow structures are thus more affected by the surfaces while traversing the rotor blades and endwalls. Hence a more accurate modeling than k-ε method would be requested, which was previously performed by [1]. On the other side, due to the relatively large computational domain and the complicated procedure of blades oscillation, turbulence models such as Large Eddy Simulation (LES) result in extremely high cost in computations and were thus avoided. As a matter of fact, k-ω-SST model gains the advantage of a two-equation eddy-viscosity turbulence approach where it can resolve the free stream as such in k-ε and also treat adequately the shear-layer regions with k-ω model component.

3.3.3 Computational Domain and Code Validation Module

Since all the blades are displacing individually according to each of their specific pitching schedule, and the rotational movement is parallel to the oscillations, the computational domain is then sub-divided into 8 separate regions to comply with the 6-bladed structure. The majority of the domain includes the base mesh that models the stationary region which is the full region outside the outer (big) circle. The second mesh zone is the inner part of this big circle which dominates the rotational movement. Ultimately, 6 zones are also allocated for each of the operating blades with their dual displacement at the same time with rotation and pitching oscillations.
The grids are all constructed using the BlockMesh utility, with extra coding in Octave to perform the proper OpenFOAM libraries for the meshing procedure. It is worth to mention that all parts of the mesh domain, comprising the rotor and the blade boundary layers are prepared in structured-mesh format. Different aspects of the mesh structure for the whole cycloidal rotor are also presented in Fig.3.4. Considering a planar section of the mesh, the whole domain consists of $\approx 170\ k$ grids nodes, with approximately $\approx 45\ k$ cells belong to the blade zones (6 inner regions with $\approx 7.6\ k$ cells per each), and the rotating region out of the blade zones is comprised of about $\approx 47\ k$ cells, and thus the remaining $\approx 76\ k$ cells belong to the full stationary region.

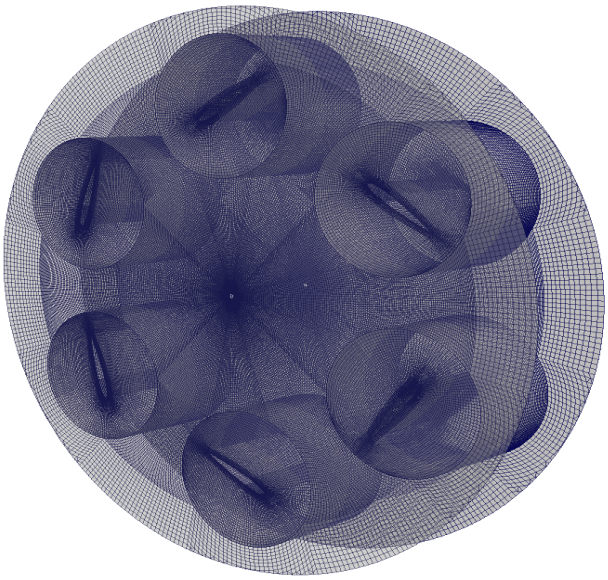

(a) Single-Side Endwalls (SE) in cyclorotor

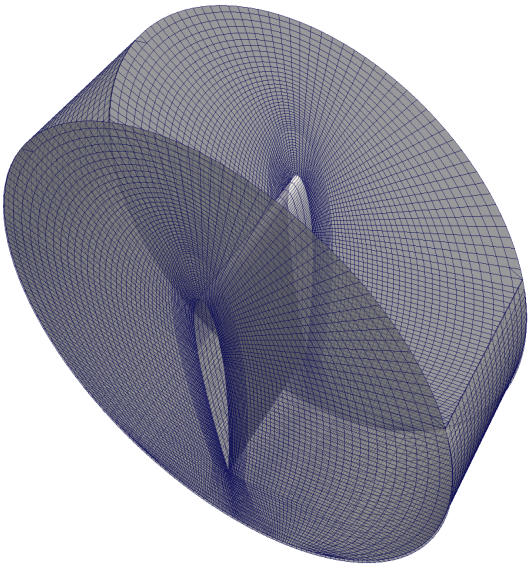

(b) Single-Side Endwalls (SE) in cyclorotor

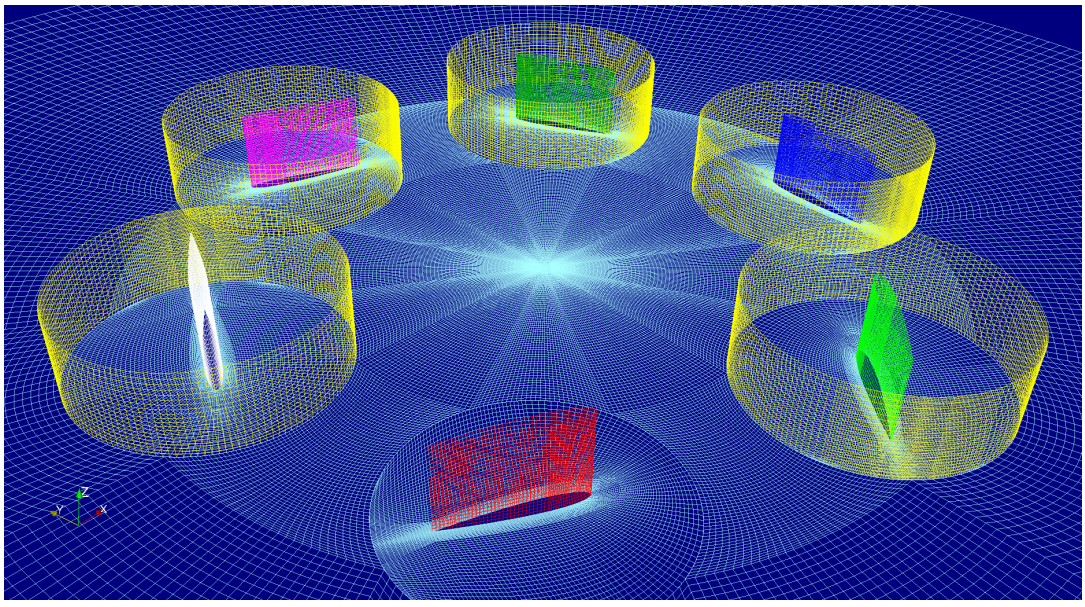

(c) Double-Side Endwalls (DE) in cyclorotor

Figure 3.4: Schematics of the side Endwalls in the cycloidal rotor model.

The grid independence phase is done by successive mesh adaptations in OpenFOAM in order to reach the optimum mesh. In addition, the value of the y^+ is kept less than 1.5 on all the rigid surfaces. The challenge for the moving parts are overcome by using the cyclicAMI (Arbitrary Mesh Interface) technique for all of the sliding interfaces between the moving zones. Therefore, 14 separate AMI patches are identified for the 7 moving zones, by which each zone is surrounded by 2 pair-patches to incorporate the inner and outer regions. To ensure the high accuracy of the AMI patches, the merge tolerances are all set to 10^{-6} between the coupled interfaces, and the transform methods are set as ”noOrdering”. The final three-dimensional grids indeed configure the same mesh mechanism that was

illustrated above. The front and rear interfaces are set as symmetry BCs accordingly. Grid convergence study is also accomplished by three different mesh numbers with 8, 12 and 20 million cells. The optimum results are obtained for the 12 M case to which we name as mesh-2, and the 8 M mesh is called the mesh-1 in the presented plots for validation. The comparison of results is presented for 4 different pitching angles and at 5 consecutive rotational speeds. The results for the 20 M structure were fairly close to what the mesh-2 obtained, and thus they are not provided in the plots for more clarity of the comparisons. The validation procedure of the present work has been accomplished using the experimental results reported by Yun et al. [1] for a UAV-scale cycloidal rotor at hovering state. In doing so, several operating conditions are therefore selected to be numerically predicted and compared with those of the test data. For this purpose a range of rotational velocity and pitch oscillation angles is accordingly presented. The rotational velocity ranges from 200 rpm to 600 rpm with a 100 interval increase, and the pitching angle values are obtained 20°, 25°, 30° and 40°.
The main parameters in the validation assssment are the thrust coefficient (Eq.5.3) and power coefficient (Eq.5.2). The thrust coefficient is defined as:

$$C_T = \frac{T_N}{\rho A (R\Omega)^2}, \quad (3.1)$$

and the power coefficient is:

$$C_P = \frac{P_N}{\rho A (R\Omega)^3}, \quad (3.2)$$

where R refers to rotor radius and A indicates the projected area of the cyclorotor:

$$A = 2Rs \quad (3.3)$$

and P_N, T_N are pointing to net power (eq.5.5) and net thrust (eq.5.6) in the following equations, respectively:

$$P_N = M\Omega, \quad (3.4)$$

$$T_N = \sqrt{T_H^2 + T_V^2}, \quad (3.5)$$

where M and Ω refer to momentum and rotational speeds and T_H and T_V are horizontal and vertical thrusts.
As is seen in the validation plots (Figures 3.5 and 3.6), the results are showing reasonable agreement with the experiment data. The comparison of the grid structures is also pre-

sented in Fig.3.6. By confirming the granted accuracy of the numerical methodology, the exact same numerical approach is taken for the remaining CFD simulations.

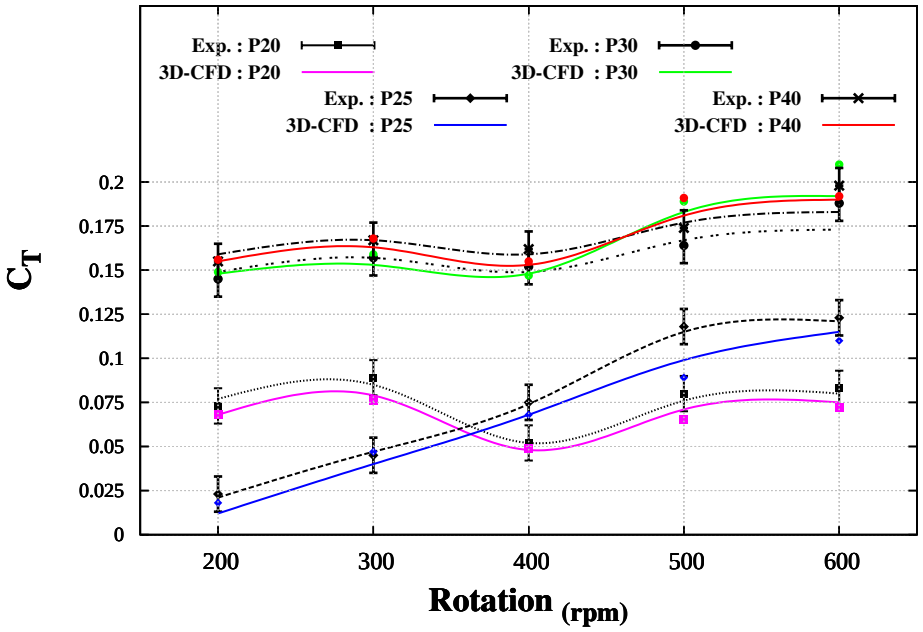

Figure 3.5: Validation using the experiments of Yun et al. [1]: thrust coefficient vs. rotation speed.

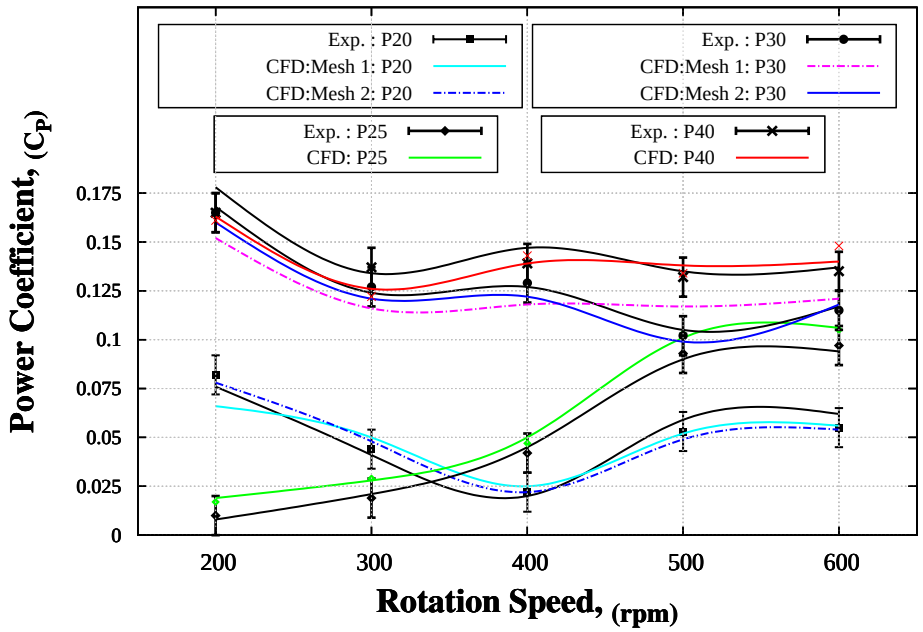

Figure 3.6: Validation using the experiments of Yun et al. [1]: power coefficient vs. rotation speed.

3.4 Artificial Neural Network

The artificial intelligence emerged every day as more practical for a wider range of applications, for different sciences and technologies, in the recent decades [77]. ANNs are

gradually finding more space in computational analysis fields in fluids, thermal and other engineering issues [78]. The concern for this enhancement of ANN in recent engineering applications can be due to: i) this methodology provides fast assessment of the data with no need of digesting the physical or real model, which is called pattern recognition and data learning. ii) with the assistance of neuro-controllers, this approach is capable of dealing with time-varying and adaptive controls. iii) ANNs are fairly adaptable with various soft-computing approaches (like fuzzy-logics and genetic algorithms) which makes it more efficient in treating complex problems.

In principle, ANN uses an interactive method to receive a dataset as an input, and get trained for the subsequent desired processes. For instance, the target in the present study is to look for the optimal pitching schedules for a complete round trace for all blades in different rotational speeds. This is feasible by training the data achieved from the numerical part in the simulations. Through this study, the optimum pitching schedule of the blades and the overall efficiency of the cycloidal rotor for different operating conditions and designs are presented. It has been demonstrated that the combination of experimental tests and numerical simulations with neural network analysis can be highly advantageous in problems with various operating conditions [84].

As is shown in Fig.3.7, parameters such as power loading ($P.L$), disk loading ($D.L$), thrust (T_N), figure of merit ($F.M$), horizontal force (F_X), vertical force (F_Y), thrust coefficient (C_T), power coefficient (C_P) define all of the data herein used as the input for the ANN algorithm.

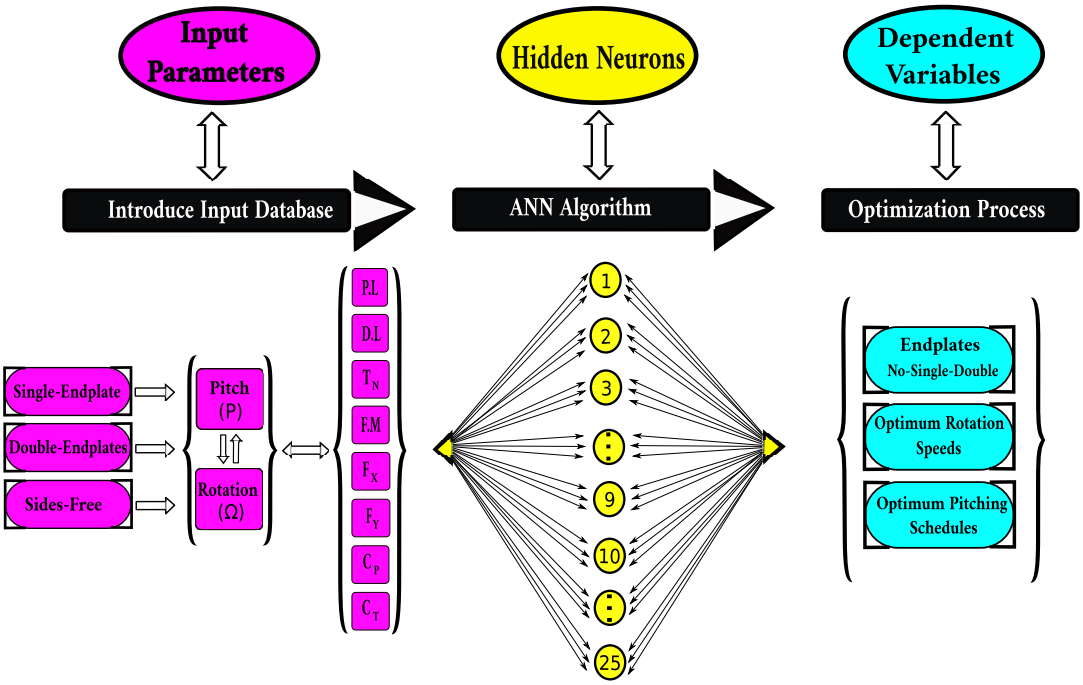

Figure 3.7: The structure of the optimization procedure based on the ANN analysis.

A combination of all the mentioned values at different operating conditions of pitching and rotation is injected separately to the input neurons for all the three endwalls types. Based on the comparatively large database, the ANN algorithm passes through the train-

ing procedure to reach the accuracy level for further optimizations. In the current work, the desired output data are the pitching angles, F_X and F_Y and $F.M$ for the main designs with different endwall structures, at various operating conditions.

3.4.1 Neural Network Structure

As like any biological neural network, the ANN structure also include numerous neurons in the form of layers. These layers configure the input and output stages which are interconnecting all hidden layers. The data space is divided into known (input) and unknown (output) parameters.
One of the most important parts of the ANN analysis is the error estimations while the computations reach to the output nodes. Along the learning process, the estimated errors in the computations are interactively modifying the nodes in the network domain to decrease the errors to a reasonable level. As a known feed-forward network scheme, the back-propagation method treats the biases of the layers from the output to input reversely. Thus, the complete ANN methodology includes repeatable algebraic loops in the deterministically.
The layers are defined by i and their numbers start from $i = 1$, which relates to the input layer, and the last is $i = I$ which corresponds to the output. The nodes are described by j symbol and they vary in all the layers. Moreover, J_i and J_I are expressing any random node number for each of the layers and the output node, respectively. In general, the nodal coordinates of each node is defined by,

$$x_{i,j} = \lambda_{i,j} + \sum_{k=1}^{J_{i-1}} w_{i-1,k}^{i,j} . y_{i-1,k}, \quad (3.6)$$

$w_{i-1,k}^{i,j}$ denotes the synaptic weight, $\lambda_{i,j}$ refers the nodal bias at (i, j) and $y_{i-1,k}$ expresses the nodal output for the previous layer. $y_{i,j}$ can be derived as a threshold function according to the input $x_{i,j}$ as,

$$y_{i,j} = \varphi_{i,j}(x_{i,j}), \quad (3.7)$$

This is called logistic sigmoid function and has continuous derivatives for a highly nonlinear behavior of variables at input and output,

$$\varphi_{i,j}(\zeta) = \begin{Bmatrix} (1 + e^{-\zeta/c})^{-1} & i > 1 \\ \zeta & i = 1 \end{Bmatrix}, \quad (3.8)$$

here c represents the inclination of the function and has a constant value. One of the essential steps in all kind of ANN methodologies is the error estimation in learning and training the data at the final layer. As was aforementioned, feed-forward back-propagation procedure is considered as one of the most commonly used training algorithm for ANN analysis

[86].
The final error computation after continuous loops of training can be presented as,

$$E_r = 0.5 \left[\sum_{j=1}^{J_r} (t_{I,j} - y_{I,j})^2 \right], \quad (3.9)$$

in which $t_{I,j}$ refers to the normalized output for node j in the final layer.
The relation coefficient ($R_{_C}$) and the mean square error (MSE) are included as parameters regarding the accuracy evaluation for the optimal ANN model. Through the work of Haykin [86], $R_{_C}$ is defined as,

$$R = \frac{Cov(a, A_{_p})}{\sqrt{Cov(a,a).Cov(A_{_p}, A_{_p})}}, \quad (3.10)$$

where $Cov(a, A_{_p})$ describes the covariance between the parameters a and $A_{_p}$, as the measured and predicted values,

$$Cov(a, A_{_p}) = E\left[(a - \mu_a)(A_{_p} - \mu_{A_{_p}})\right], \quad (3.11)$$

here E addresses the expected value, μ_a and $\mu_{A_{_p}}$ are the mean values of a and $A_{_p}$, respectively. The covariances $Cov(a,a)$ and $Cov(A_{_p}, A_{_p})$ are defined as,

$$Cov(a,a) = E\left[(a - \mu_a)^2\right], \quad (3.12)$$

$$Cov(A_{_p}, A_{_p}) = E\left[(A_{_p} - \mu_{A_{_p}})^2\right], \quad (3.13)$$

The MSE is finally correlated as:

$$MSE = \frac{1}{n} \sum_{i=1}^{n} (a_i - A_{_{p_i}})^2. \quad (3.14)$$

3.4.2 ANN Performance

In the present approach of forward-feed network, a series of layers are utilized as the input for training and validation in order to reach the output results. All the layers are thus internally correlated as well. The mapping procedure of the input results is performed accordingly with the output values through the training scheme by using a number of hidden neurons. Reaching higher accuracies is related to the testing and training the applied dataset in the ANN algorithm. It can be observed from Fig.3.8 that the MSE value stabilizes at around 25 neurons.

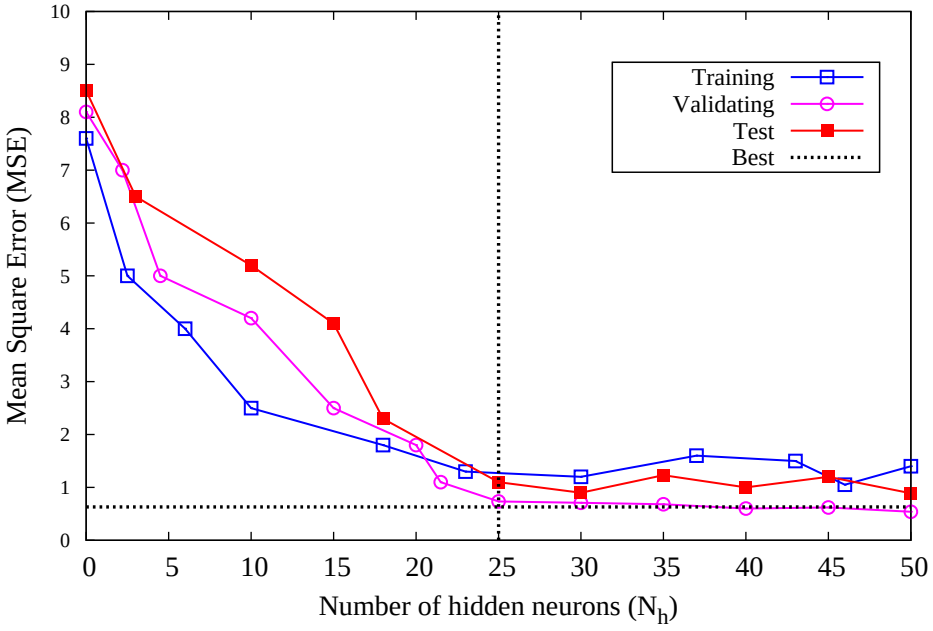

Figure 3.8: The optimal state of mean square error variation while increasing the number of hidden neurons.

Figure 3.9 presents the rapid increase of the R_C at the stated neuron number, here assumed as the optimal state for the current ANN optimizations.

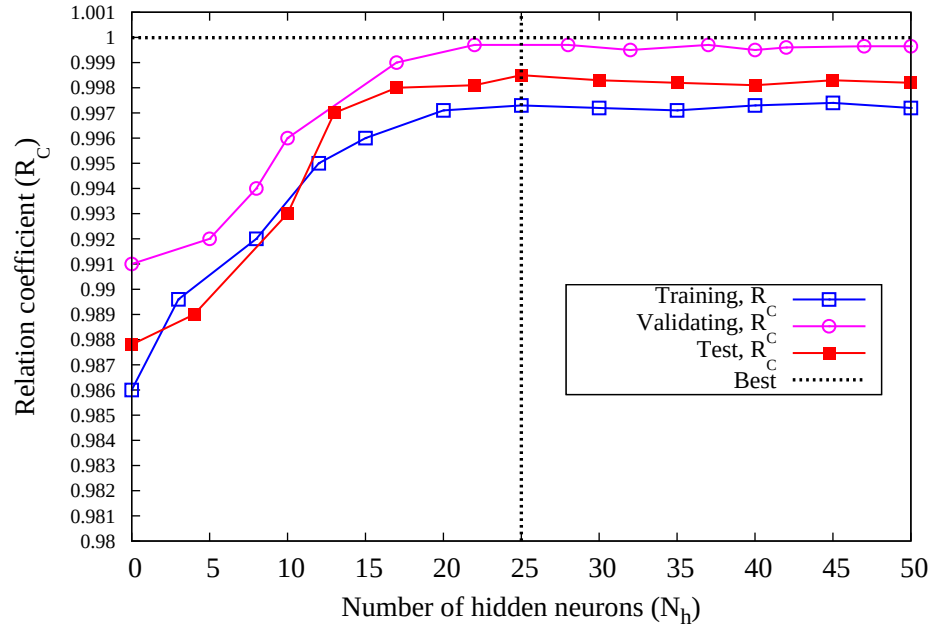

Figure 3.9: The optimal state of the relation coefficient variation with an increase in the number of hidden neurons.

Monitoring the epochs can also be the other criteria to accredit the training procedure for the algorithm. Therefore, to achieve the desired fitting accuracy, the whole dataset is passed through the learning and training loops in a sufficient number of cycles.

Figure3.10 demonstrates that at the optimum hidden neuron layers, the mean square error, and the presented relation coefficient converge by performing iterations of less than 300 epochs rounds.

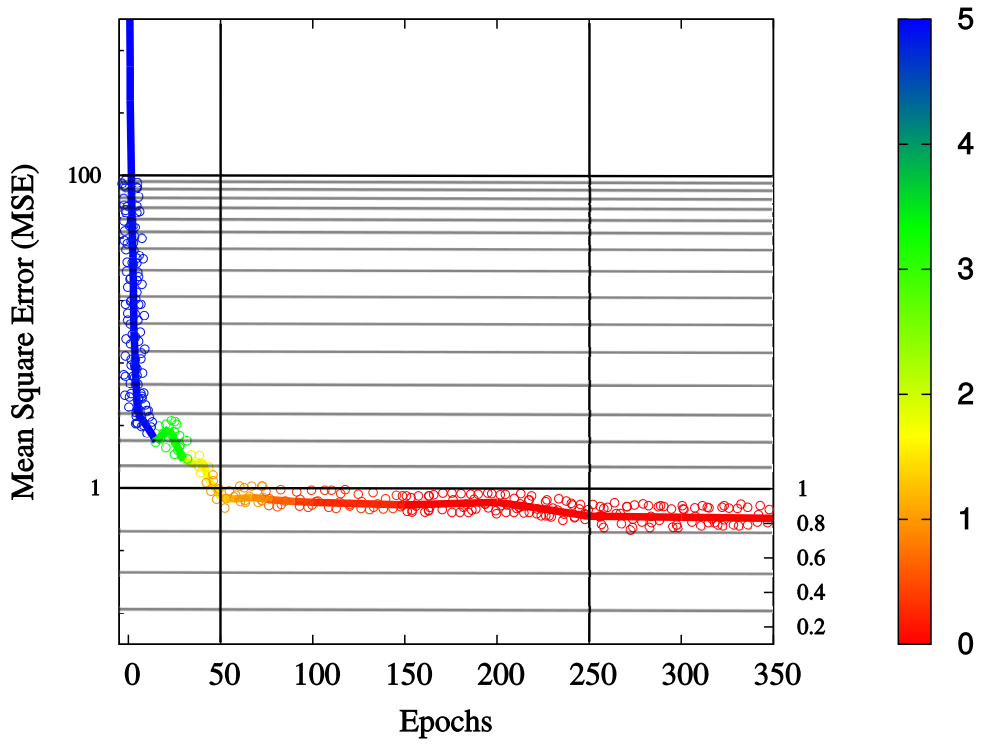

Figure 3.10: Variation mean square error in the optimal neural network model according to the neuron number and R_c.

3.4.3 Optimization Framework in Active Control

The progressive steps for deriving the optimized active control as result of coupled analysis with CFD and ANN are illustrated in Fig.3.11,

1. Defining the base cycloidal rotor operating conditions used for CFD simulations and predictions of operational variables for all three endwall designs.
2. Validating the numerical methodology, simulations and codes with experiments.
3. Building a database from the various simulations, from all the designs and operating conditions, using CFD post-processing.
4. Feeding the database to the ANN algorithm for learning, training, and error estimating progress.
5. Evaluation of the trained algorithm by checking the data processing and accuracy levels.
6. Optimization of the operational conditions for an active-control on the pitching oscillation schedule for several rotation speeds and designs.

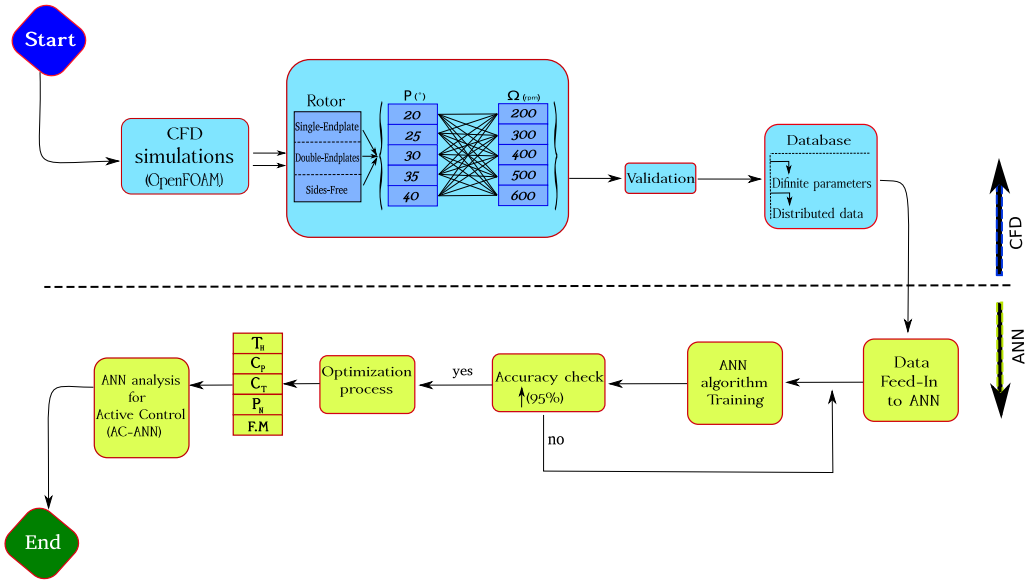

Figure 3.11: Progressive steps used to find the optimized active control modes in order to obtain optimum cyclorotor operation

Technically, one of the main processes which has to be organized is the interactive comparison of the numerical results for the included parameters with those of experimental values. These are essential in gaining higher accuracy while feeding the data to the neural network and reaching to higher accuracies for the optimization results. An example of the comparisons of the two and three-dimensional results for the values of four parameters at a 30° pitching amplitude, and 450 rpm rotational velocity, is presented in tab.6.2. We tried to illustrate the errors from the CFD and ANN approaches in relation to the real tests in experiments.

Table 3.2: Aerodynamic parameters obtained from experiments, CFD and ANN optimizations at 450 rpm rotation and 30° pitching amplitude, in hovering mode.

Variable	Exp.	3D (CFD)	Error, %	ANN	Error, %
D.L	52.81	52.461	-0.66	53.554	1.39
P.L	0.0761	0.0749	-1.47	0.0733	-3.65
C_P	0.1196	0.1203	0.59	11.53	-3.57
C_T	0.1582	0.1552	-1.87	0.1529	-3.32

3.5 Discussions

The performance of cycloidal rotors under various operating conditions has been assessed and studied by numerous parameters over the recent years. The featuring parameters are blade profiles, number of the blades, blade size and chord length, rotor radius, angular velocity, pitching oscillation angle, and the different type of rotor applications. As a matter of fact, cyclorotors are proposed as an alternative propulsion system instead of screw propellers for the VTOL aircraft.

Unlike all of the reported studies, even the previous study of the present authors [47], this work deals with the presence of the side-endwalls over the rotor cage. A comparison of the

side-wall effect and performance is provided for all three designs with S-F, S-E, and D-E. In addition, the optimum operating performance of each of these designs is presented in terms of the pitching schedules. In doing so, the thrust performance and the overall efficiency of each design is tracked continuously over the complete 360° azimuthal trajectory. This study is conducted based on a coupled approach of numerical simulations and neural network optimizations for the proposed active-control schedules for the cyclorotor operation. The continuous variation of the vertical and horizontal thrust in parallel with flow behavior is derived from the CFD prediction over the full circular trace. Subsequently, the collected CFD database for all designs and parameters, at various operating conditions, is fed into the ANN algorithm. The output of the ANN method is the optimized and proposed pitching schedule of the cyclorotor at different rotational speeds for each of the endwall design type.

3.5.1 CFD Results

The initial phase of this work is to numerically simulate the cycloidal rotor with the three endwall designs, and to derive all the parameters and values regarding all the aforementioned operating conditions, with diverse pitching oscillations and rotational speeds. As was discussed in the early sections of the current chapter, the dominant flow streams behave in a complex manner while entering and passing through the cyclorotor. This fact is different for all operating conditions and designs, such as forward-flight, up-lift phase, hovering mode and for different applications of the rotor. Thus, information was extracted related to the blades forces and loadings over the continuous circular path, to gain a better vision of the blade strokes and lift and thrust performances.

In order to approach the functional behavior of the rotor, the vertical and horizontal forces of a single blade while starting from $\Psi = 0^\circ$ and traversing the circle to the endpoint ($\Psi = 360^\circ$) is fully considered. The flight mode is the hovering state, and the blade forces are calculated for the three endwall design cases in accordance to different operating conditions. The operating conditions include five successive pitching angles from 20 to 40 degrees and 5 rotating speeds from 200 to 600 rpm, as was declared previously.

The base geometrical specification for the current cycloidal rotor is a 6-blade arrangement with $0.15m$ chord and a rotor radius of $0.4m$. All the operating conditions are similarly simulated for the three endwall designs as well. In principle, in a hovering state operating condition, the cycloidal rotor inhales the air flow from the top half of the cage and directs it downward to the bottom side to exhale it out as downwash jet.This can be accepted as a general flow stream, but the effective local behavior of the passing flow at each significant point on the circle path is quite unique. This means that each zone of the trajectory has different flow velocity and angle at each operating condition, which result in different behavior and, hence, different efficiency and performance of the rotor.

Figure 3.12 shows the horizontal force coefficient plots for the three S-E, D-E, and S-F designs operating at 35° pitching oscillation and two rotating speeds of 400 (Fig. 3.12.a) and 600 rpm (Fig. 3.12.b).

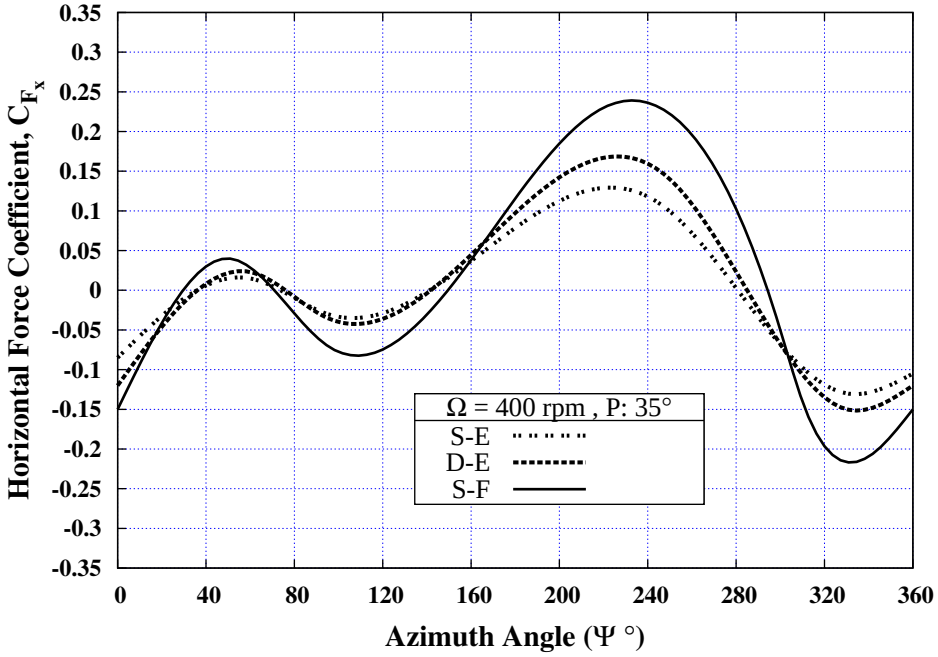

(a) C_{F_X} distribution: $\Omega = 400$ rpm.

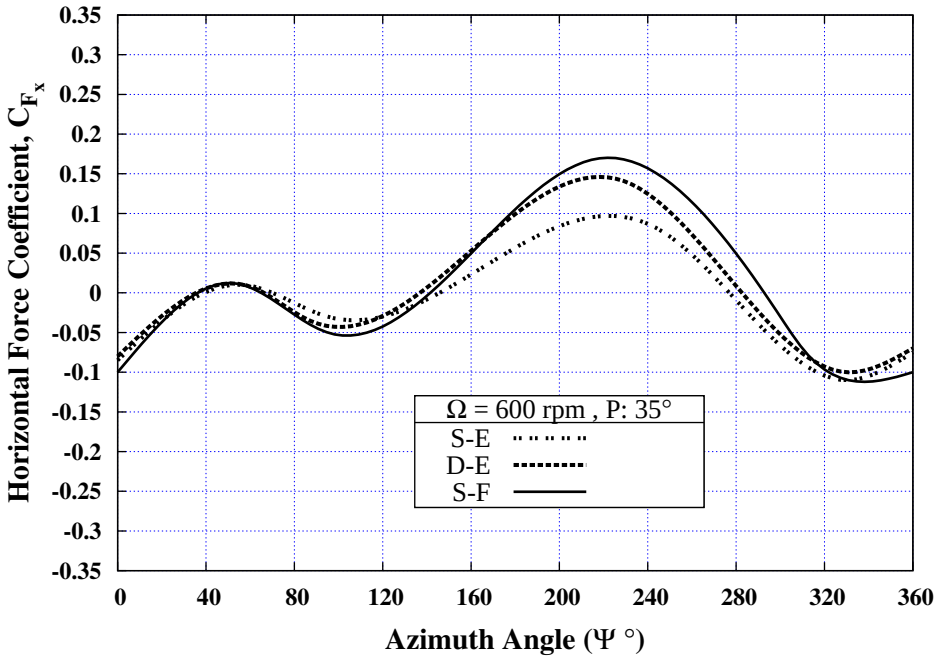

(b) C_{F_X} distribution: $\Omega = 600$ rpm.

Figure 3.12: Distribution of horizontal force coefficient over the circular trajectory at different operating conditions, for a hovering cyclorotor with and without endwalls.

According to Fig.3.12, the horizontal force coefficient passes through two peaks in the azimuth zones of $30° \leq \Psi \leq 70°$ and $140° \leq \Psi \leq 250°$. These regions are pointing to the left and right sides of the rotor cycle. As is clearly seen, the higher horizontal force belongs to the sides-free geometry with no endwall in the rotor, and the D-E and S-E are coming after. This order is similar for both figures of 3.12.a and b which are for 400 and 600 rpm speeds. The difference between the Fig.3.12.a and b is the lower horizontal force

production by increasing the rotational speed. This fact is also observed for all these three endwall designs.

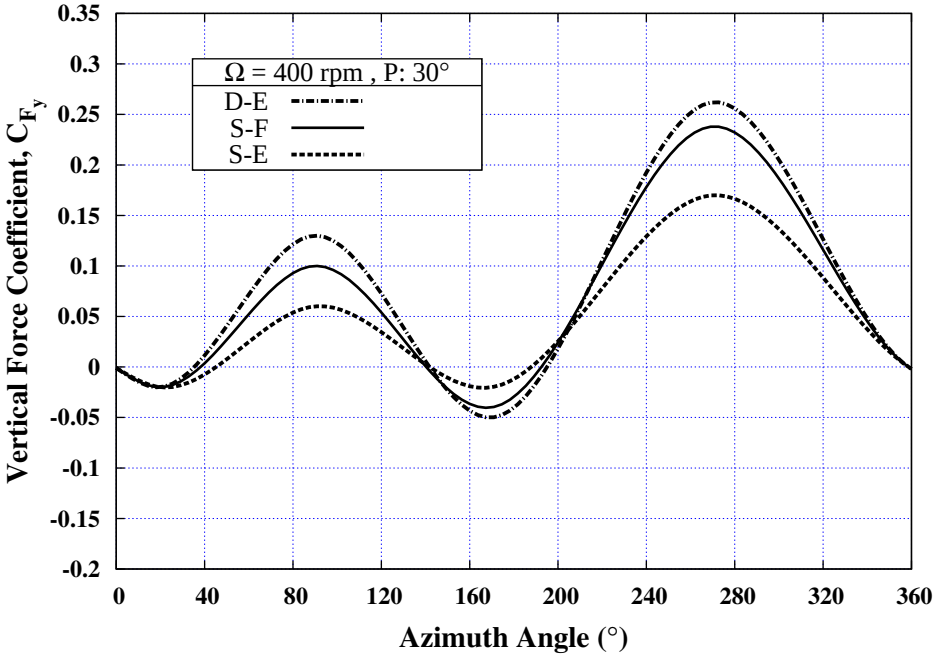

(a) C_{F_Y} distribution: $\Omega = 400$ rpm.

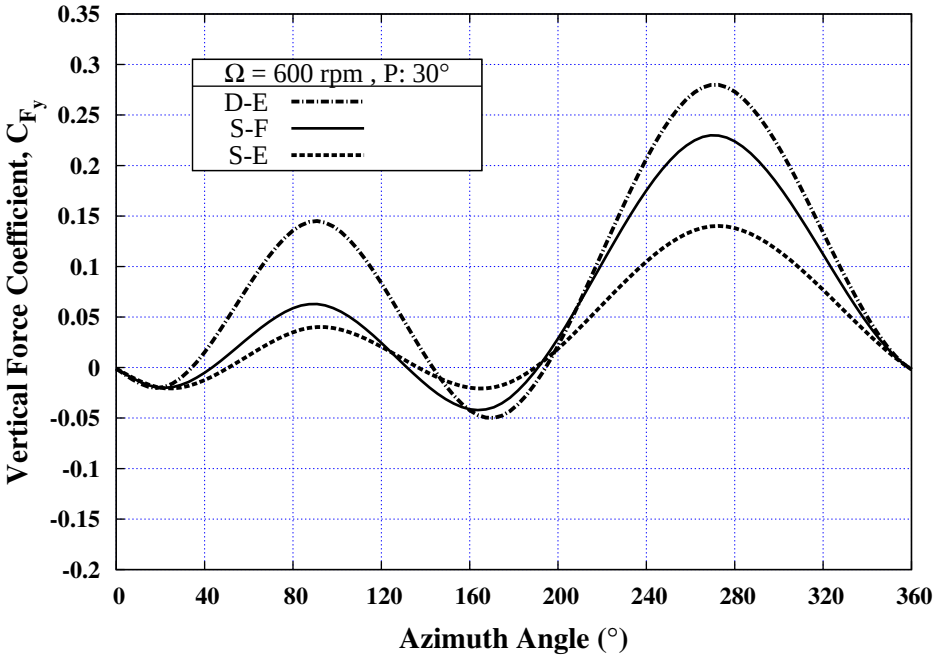

(b) C_{F_Y} distribution: $\Omega = 600$ rpm.

Figure 3.13: Distribution of vertical force coefficient over the circular trajectory at different operating conditions for a hovering cyclorotor with and without endwalls.

Vertical force distribution is also presented for the same three designs and rotational speeds, but for 30° of pitching oscillations in Fig.3.13. Similar to those in horizontal, the vertical forces are also experiencing two extremes per each round. Comparing to the hori-

zontal, one of the major discrepancies of the vertical force is the peak regions which shows to happen in the top and bottom sides of the rotor. As is seen in both figures 3.13.a and b, at each constant pitching oscillation angles, the D-E design produces higher vertical thrust than the other two designs with S-F and S-E coming afterwards. Other than that, the comparison between each design curves at different rotation speeds, the D-E design shows a higher vertical thrust production at a higher angular velocity, whereas, the other two are decreasing at 600 rpm. In terms of horizontal force, the free-sided model generates 8% and 11% higher values by average compared with the double-endwall and single-endwall, respectively. However, in accordance with the computed values for vertical force, the double-endwall design produces 7% and 16% higher force by average compared with sides-free and single-endwall design, respectively. This fact implies that, aside from what the measurements are declaring about the total efficiency, one can select the appropriate design according to the application and the purpose of their aircraft designs.

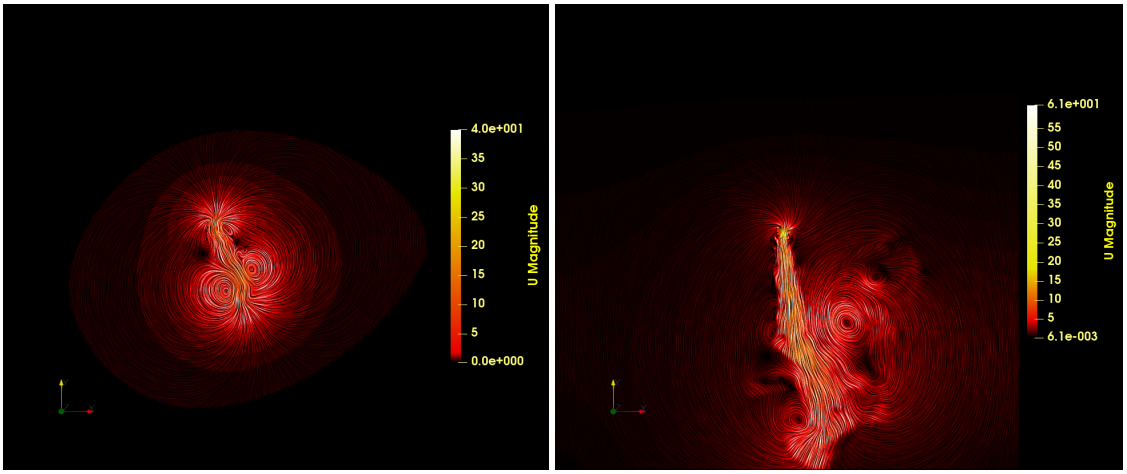

(a) LIC contour flow in S-E.

(b) LIC contour flow in D-E.

Figure 3.14: Velocity contour and downwash jet flow for S-E and D-E designs at: $\Omega = 500$ rpm, $P = 35°$ using surface line integral convolution.

Furthermore, it is obviously seen that the bottom side of the cyclorotor contributes with th major amount of lift force than the top side, but the point is that both are occurring while the blades are passing through the maximum angles per each cycle. In principle, at the hovering state operation under null incoming velocity, the top-side of the cyclorotor is where the air-stream is inhaled to the inside cage, and the lower half is where the flow exhales in a more condensed pile-like downwash jet.

A comparison of the flow mechanism between the single and double endwall designs is shown in Fig.3.14. As can be observed, the downwash jet strength and the length in the D-E (Fig.3.14.b) design at fairly constant operating speed and pitching angle is comparatively 2.5 times higher than the downwash in the S-E (Fig.3.14.a). These comparisons are depicted after 15 cycles of run which corresponds to the same time-sequences for both simulations. A side view of the flow glyph and surface line integral convolution (LIC) contour for both SE and D-E cases at different operating conditions is also depicted in Fig.3.15.

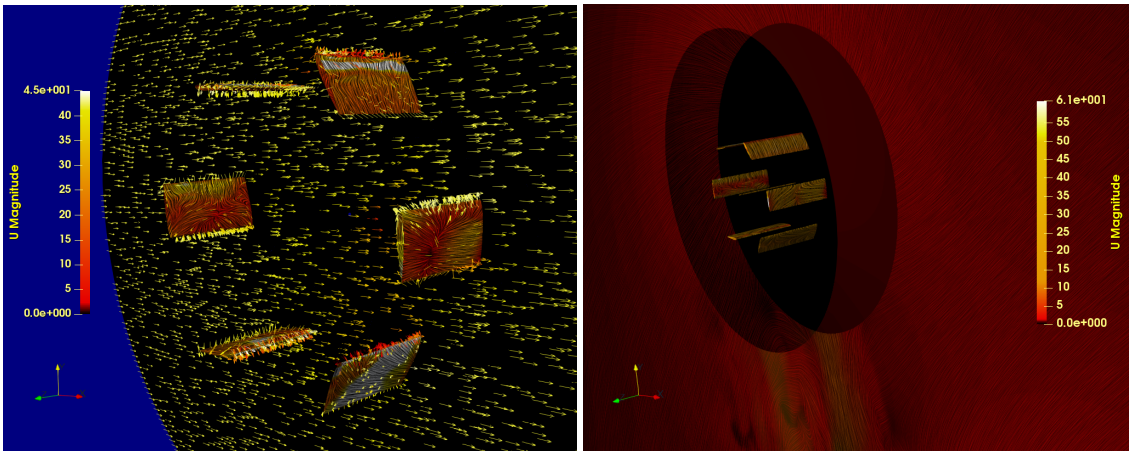

(a) S-E Glyph and surface-LIC contour: $\Omega = 600$ rpm, $P = 30°$.

(b) D-E surface-LIC contour with endwalls: $\Omega = 500$ rpm, $P = 35°$.

Figure 3.15: A side endwall view of the glyph and surface-LIC contours of the S-E and D-E at different operating conditions.

Likewise plots in figures 3.12 and 3.13, all the aforementioned parameters are collected for all ranges of pitching oscillations and rotational speeds over a continuous 360° trajectory. This was done to have the appropriate and sufficient database for the optimizations and analysis.

Figure.3.16 shows the flow structure on the blade surfaces at different azimuth angles in the cyclorotor. A cross section of the rotor is here presented to better visualize the flow behavior with the presence of the side wall at the $\Omega = 500$ rpm, $P = 30°$ operating condition. As is shown, the uniformity of flow stream is disturbed with the endwall effect, and vortex structures are shedding from the tip of the blades in the spanwise direction. The in-cage side (pressure surface) of the blade at Ψ =230°, and the external view of the suction surface flow at Ψ =110° are depicted in Fig.3.16.c and d, respectively. In order to present more clearly the flow structure, the surface-LIC contours of the flow on the shear layer are depicted. The leg horseshoe vortices structures are visible in Fig.3.16.d on the suction surface of the passing blade at relatively the top-side of the cycloidal rotor rout. The effect of the flow behavior like separation, vortex shedding, secondary and cross flow, at the presence of the endwall is influencing the whole rotor system efficiency. Therefore, we are using the parameters like power and disk loadings and figure of merit to evaluate the efficiency and performance of the current cyclorotor models in the present study in both CFD and ANN methodologies.

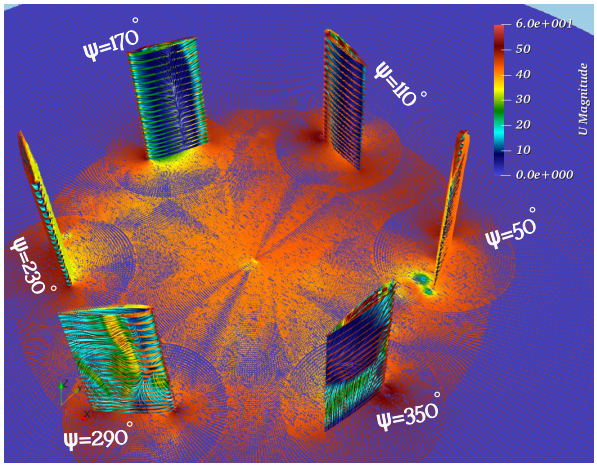

(a) LIC contour of the side-wall flow in the rotor.

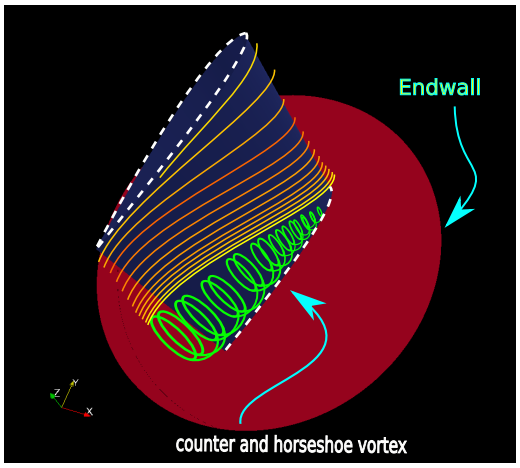

(b) Endwall vortx pattern of Sharma and Butler [99].

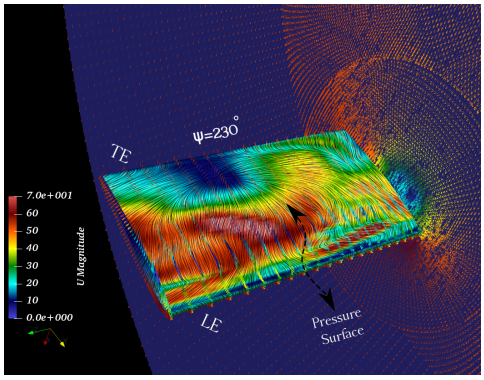

(c) LIC contour of Crossflow view on the pressure-side of the blade at Ψ =230°.

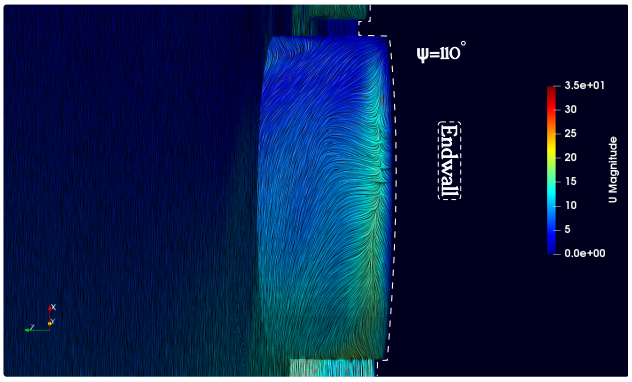

(d) Shear flow structure and the side-wall effect view on the suction-side at Ψ =110° .

Figure 3.16: Three-dimensional boundary layer with the vortex generation and secondary flow occurring in the presence of side endwall in a cycloidal rotor at $\Omega = 500$ rpm, $P = 30°$.

3.5.2 ANN Analysis

Considering the current work on the performance analysis of three different sidewalls for a UAV-scale cycloidal rotor, the principal effort has been assigned to actively control the pitching schedules for each design and each specific operating condition. This active control procedure is actually targeting the pitching oscillation schedules at each point on the circular trace. That means, based upon the dataset obtained from all the operating arrangements with rotating speeds and pitching angles for each of those designs, an approach with neural network methodology will be proposed to actively modify the pitching schedule of the blades at each location on the azimuthal trajectory. Therefore, instead of assigning fixed pitching angles for each specific operation, we can actively apply this methodology to obtain the optimized state at each rotational speed. By this, since each zone on the circular trace has a significant characteristic in terms of flow angle, blade speed, flow velocity, etc., by actively controlling the pitching oscillation can result highly effective in achieving efficiency increase.

Technically the local angle of the blade (the blade AOA at each azimuth angle) in cyclorotor

is calculated through [49], where the top and bottom-most positions at $\Psi = 90°$ and 270°, respectively, are defined as the pitching extremes:

$$\theta(\Psi) = \left[\left(\frac{\theta_{(top)} + \theta_{(bottom)}}{2}\right).\sin(\Psi) + \left(\frac{\theta_{(bottom)} - \theta_{(top)}}{2}\right)\right] \quad (3.15)$$

in which $\theta(\Psi)$ expresses the blade angle at $\Psi°$, $\theta_{(bottom)}$ and $\theta_{(top)}$ are defining the pitching angles when traversing through the top and bottom locations, respectively. This simple form of the previous correlation can be shown as $\left[\theta(\Psi) = \theta_{(top)}.\sin(\Psi)\right]$ for the top (0° $\leq \Psi \leq$ 180°) and $\left[\theta(\Psi) = \theta_{(bottom)}.\sin(\Psi)\right]$ for the bottom half (180° $\leq \Psi \leq$ 360°).
Here, the concept is to actively control the dynamics of the blades in order to keep them operating at the optimum aerodynamic performance. As was mentioned, active-control implies the assignment of the optimum angle to the blades at their corresponding location on the azimuthal trace. This is possible only when a comprehensive database is already in-hand from the experiments and the CFD predictions from numerous operating conditions. For instance, from what is presented in eq.4.11, at the azimuth location of Ψ= 60°, the blade is expected to achieve -51.65° AOA with the pitching oscillation of 25°. But the same blade at the same location will get -64.64° AOA if is assigned to 40° of pitching oscillation. To be mentioned, these angles are all computed and presented from the rotor center as the origin axis. This illustration was to clarify the relation between the local AOA and the pitching angle of the blades when the cyclorotor is running. Thus, in the upcoming discussions, the local AOA of the blades at each pitching angle is referred to the eq.4.11.
In the present study, in order to train the artificial neural network algorithm, a database from over seventy-five simulations from all the three endwall designs is collected. A combination of various parameters from each of the simulations are then processed and computed, accordingly. Net power, net thrust, momentum, power loading and disk loading, horizontal and vertical thrusts, power and thrust coefficients are all part of included parameters in all simulations with pitching angles and rotation speeds. As was previously stated, we intent to track the values of each of the parameters according to the azimuthal location of the blades on the circular route, to obtain a detailed vision of the parameters and flow behavior. Therefore, the concept is to continuously modify the blade angle according to the optimum local pitching oscillations, rather than holding them at a specific constant pitch.
To better demonstrate the blade dynamics in the following discussions, the initially defined strokes (EUS, EDS, IUS and IDS) (Sec.3.2.1) for each of the four quarters are used to simplify the descriptions.

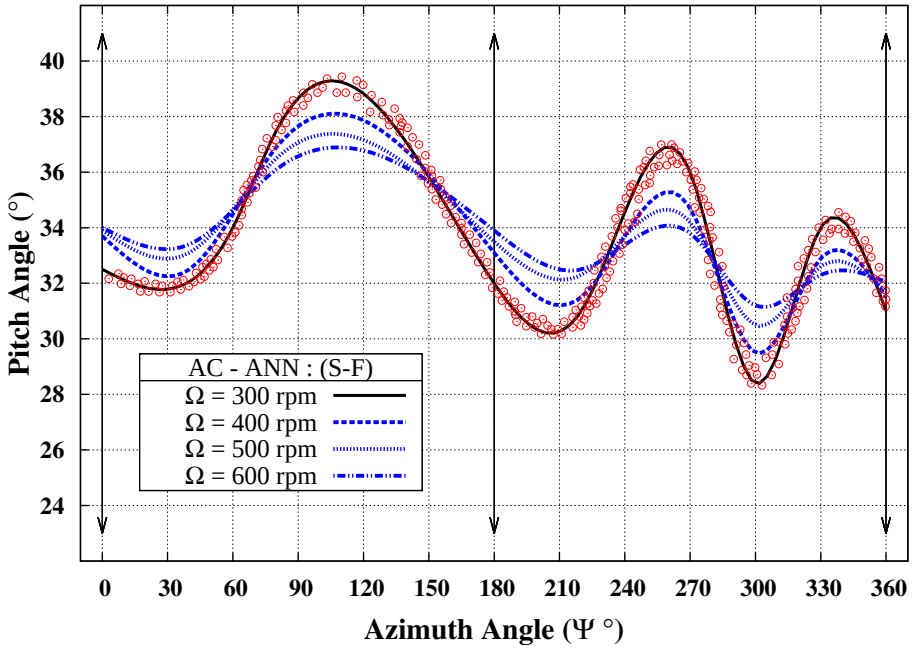

Figure 3.17: The pitching curves from the ANN analysis at different rotating speeds for the sides free design.

The optimized oscillating schedules from the ANN process is depicted for a range of rotation speeds in Figs.3.17, 3.18, 3.19. These plots are presenting the optimum ANN proposed pitching curves over the continuous circular trace for four rotational speeds in S-F, S-E and D-E, respectively. Each of these plots contain three vertical arrows at Ψ=0°, 180° and 360°, shows that the blade AOA is fully tangent to the circle line at any pitching angle, when passing through these locations.
The qualitative and quantitative illustrations from the ANN results are pointed out in Figs.3.17, 3.18, 3.19:

1. S-F (Fig.3.17)

   EUS) While starting at 32.5°, the ANN proposes a decrease in EUS speed by the mid-curve, and an increase in the speed until the blade reaches the top position. The maximum pitch angle at the topmost position is 39°.
   EDS) It is proposed to slightly continue the rise-up the angle while it reaches 105° of azimuth (that indicates a decrease in EDS speed), and then an increase on EDS speed is suggested (which implies a faster down-stroke). A convincing reason for this behavior which the ANN has proposed might be to compensate the vertical thrust decrease and also the negative lateral force that is produced by the blade in the region between $90° \leq \Psi \leq 120°$ (see Fig.3.12).
   IUS) The increase in the IUS is proposed until it reaches 260° of azimuth with about 37 degree of pitch. The lower part of the cage is more responsible for the downward flow (inside the cage) and this can be to compensate the lift and momentum behavior.
   IDS) The region between 330° and 360° on the azimuth trace is subjected to an in-

ward flow to the cage. This fact is also clear in the C_{F_X} plots. The ANN has proposed a reduction in the IDS speed for a higher performance of the blade in this region.

2. S-E (Fig.3.18)

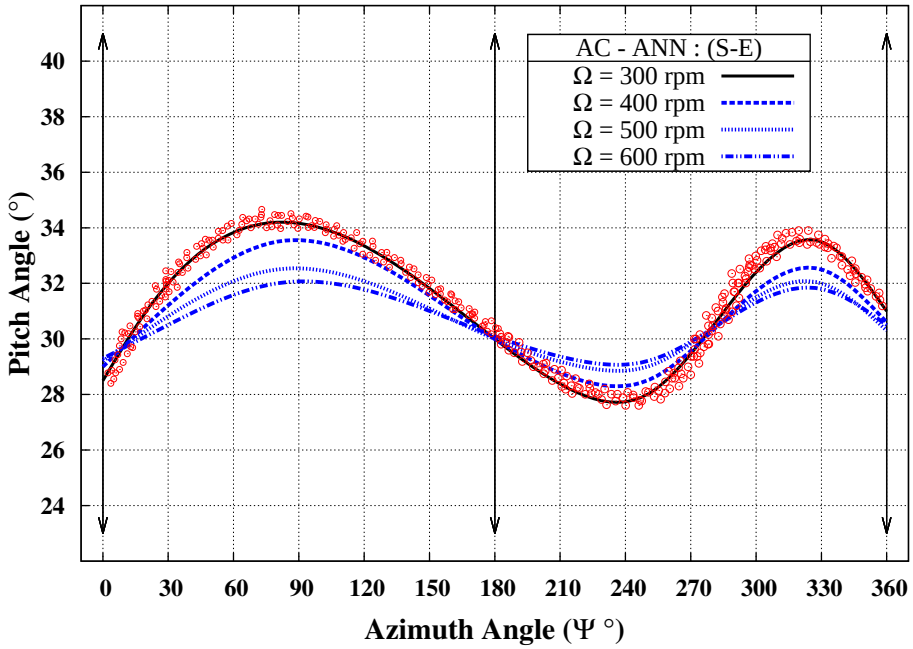

Figure 3.18: The pitching curves from the ANN analysis at different rotating speeds for the single side endwall design.

EUS) The EUS quarter in the this model proposes to gradually increase the angle, which basically corresponds to a faster EUS motion. Although the maximum pitch occurs at the location of 90°, yet the region between 70°–80° receives the maximum AOA with about 34.2°.
EDS) The EDS part is continuously dropping, which indicates a lower speed in the downward stroke to reach the tangent (0°) of AOA.
IUS) While approaching the third quarter, the blade is defined to oscillate slowly to reach the bottom-most location. Moreover, the lowest pitching angle regards to about 240° of azimuth. The prescribed pitch for the 270° location is about 29.5°, which is almost 5° less than what is assigned at the top position.
IDS) The last quarter in S-E design is also an increasing-decreasing rate in the IDS speed.

3. D-E (Fig.3.19)

EUS) Increase in the EUS phase by reaching the maximum pitch at 90° with 38.4° in the doubled endwalls. This might be due to the inhale section of the design which

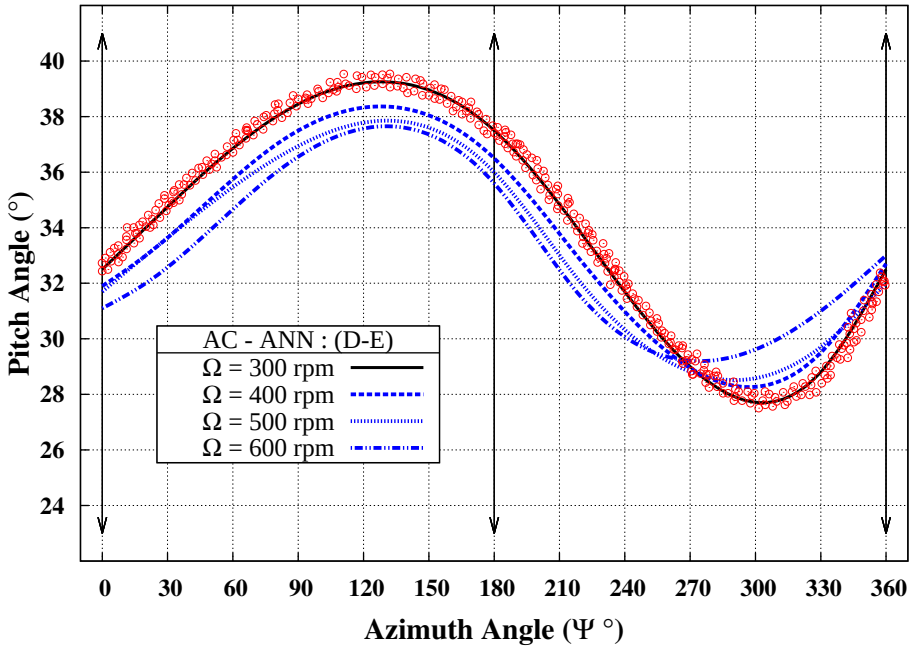

Figure 3.19: The pitching curves from the ANN analysis at different rotating speeds for the double side endwall design.

contributes to an increased volume of flow intake.

EDS) The second stroke passes at almost stable state between 39° to 39.5° until it reaches the left side of the rotor.

IUS) A gradual reduction in IUS speed is prescribed with the maximum 29° AOA at the bottom-most location.

IDS) The IDS motion is proposed in an increasing speed until the blade reaches the initial point of the cycle.

Power loading is one of the main parameters which is considered for flight efficiency and endurance. This actually correlates to the net thrust per net power, for the operating mechanism.

$$P.L = \frac{T_N}{P_N}, \quad (3.16)$$

The other important parameter in performance evaluation is the disk loading which corresponds to the produced thrust over the effective operating area.

$$D.L = \frac{T_N}{A}. \quad (3.17)$$

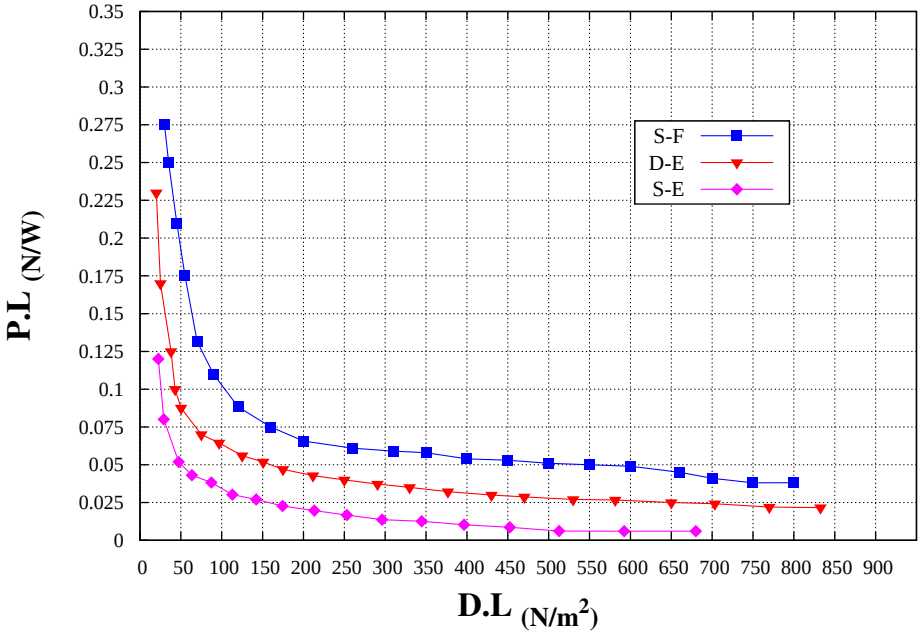

Figure 3.20: Comparison of power loading vs. disk loading for different endwall designs: $\Omega = 500rpm$, P=30°.

Figure 3.20 presents a comparison of the power loading (P.L) versus disk loading (D.L) for the three designs at a typical operating condition. As is clear, the free side-wall design performs with higher power loading at each constant disk loading compared with the other two designs. Moreover, it is the D-E case that after S-F, operates at comparatively higher efficiency than the S-E. In order to gain higher efficiencies, it is desired to achieve higher force to power ratios. On the other hand, to maximize the power loading values, an optimum rotation speed of the cycloidal rotor must be taken. Furthermore, the optimum operating state is not only dependent on the angular velocity, but also on the pitching oscillations that are the other key factor to achieve better performances. Thus, the importance of ANN optimizations in proposing the optimum pitching schedule at each rotational speed is more bold in this study. Therefore, it is expected that for each of the designs which are plotted in Fig. 3.20, the active control blade dynamics be implemented in order to obtain higher force to power ratios.

As an aerodynamic performance parameter, figure of merit (F.M) is actually the most important scale known to evaluate the operating efficiency in the cyclorotors. That is because the F.M encompasses all the parameters from aerodynamic power and thrust, to disk and power loadings.

$$F.M = \frac{(C_T)^{\frac{3}{2}}}{\sqrt{2}C_P} \quad (3.18)$$

In figures 3.21, 3.22, 3.23, a comparison of the F.M values at different rotating speeds and pitching as obtained from CFD simulations is presented, and the optimized active control proposed from the ANN analysis for each of the S-F, S-E and D-E is depicted. As is obvious

from what is achieved from ANN optimizations for the oscillating schedules of the blades, all of the three designs are revealing higher performances when running using optimized schedules are employed.

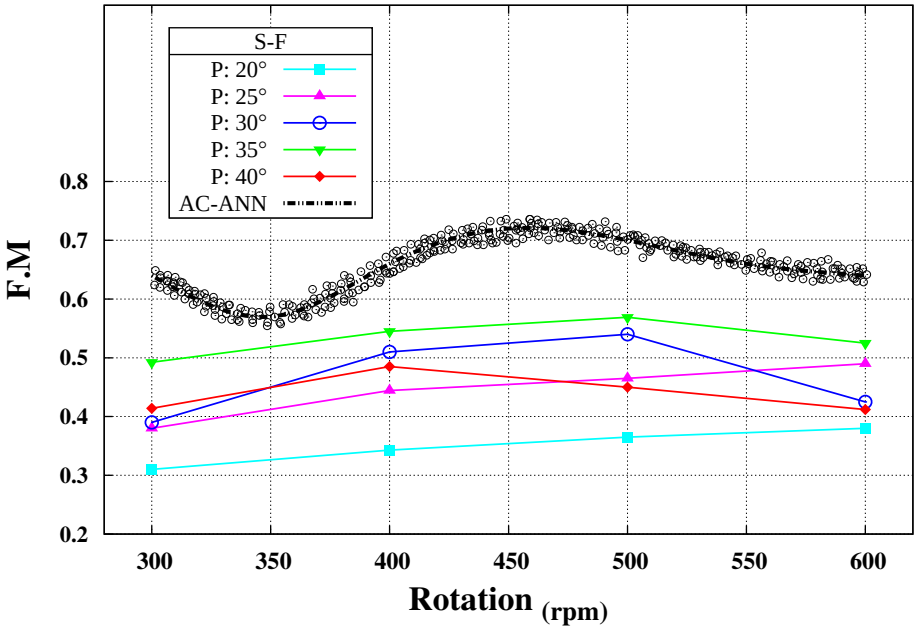

Figure 3.21: Comparison of figure of merit for constant pitch oscillation angle vs. optimized ANN active control pitching curve at different rotation speeds.

For the S-F model in Fig.3.21, the optimum state regards to the Ω of 500 rpm and 35° of pitch, whereas a higher efficiency is performed by ANN at about 450 rpm with the prescribed pitching schedule, which reaches to about 0.73 of F.M value.
The F.M measurements for S-E case in Fig.3.22 is also presented for both CFD and ANN approaches. The maximum F.M value predicted from the numerical simulations belongs to the 400 rpm and 30° of pitch angle, and the ANN has similarly proposed the best pitching schedule at 400 rpm rotational speed. The maximum proposed F.M value for the optimum state of the S-E case is predicted to be around 0.58, which is still 0.08 units higher than the best achieved from the CFD simulations. This value (0.58) is 18.8% less than the proposed F.M value for the free sides model rotor.

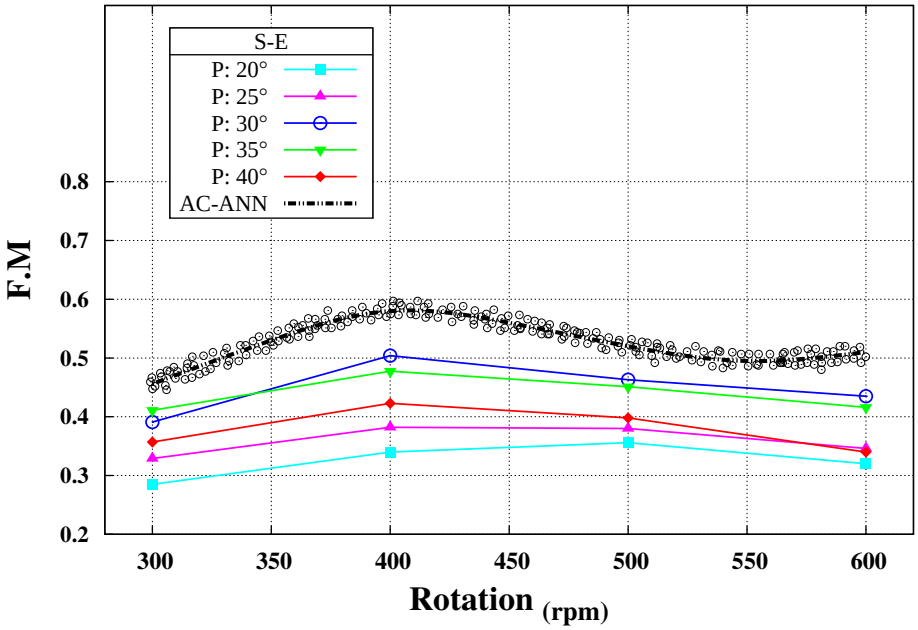

Figure 3.22: Comparison of figure of merit for constant pitch oscillation angle vs. optimized ANN active control pitching curve at different rotation speeds.

The last F.M plot (Fig.3.23) belongs to the D-E model which has shown to be more efficient than the single endwall. The CFD has predicted the 550 rpm and 40° as the maximum F.M value condition that reaches 0.53. The ANN, on the other hand, proposed the 420 rpm and 600 rpm to be operating at the optimal state. The maximum proposed F.M in ANN is about 0.61 for the D-E case at 420 rpm. The doubled endwall case at the optimum operating state lacks by 13.6% efficiency and aerodynamic performance from the sides free cyclorotor

It worths to mention that all the computations, simulations and analysis are merely based on the responses from flow behaviors and the rotor specifications in the current work. This means that the mechanical structure of the designs for each of the endwall models must be separately surveyed and studied. Obviously assembling endwalls on the cycloidal rotors impose higher loads and complexities to the design. In addition, cyclorotors are all utilizing a combination of different mechanical means for the blade controls and rotating operations. The effect of these mechanical means where also neglected in the studies which were performed.

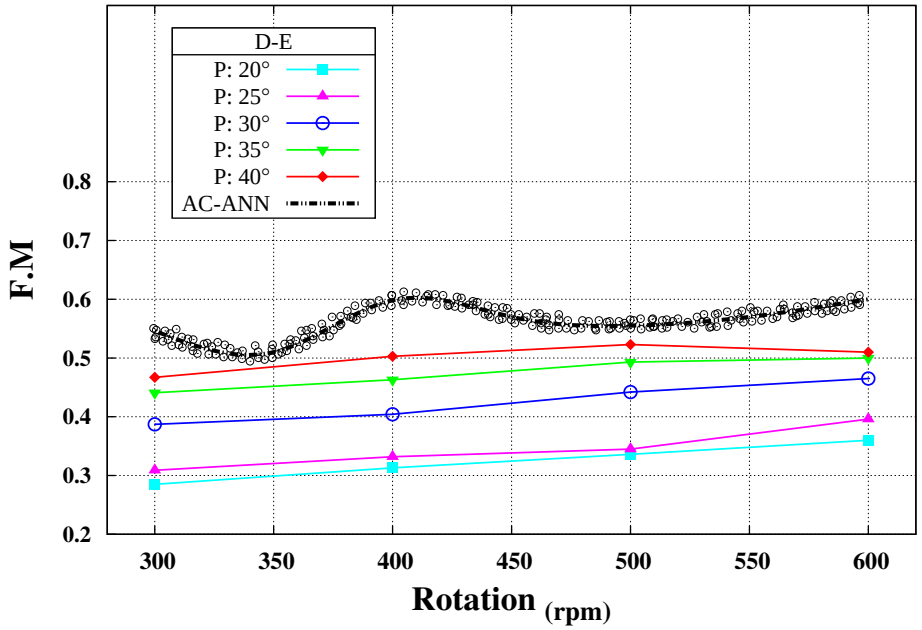

Figure 3.23: Comparison of figure of merit for constant pitch oscillation angle vs. optimized ANN active control pitching curve at different rotation speeds.

3.6 Conclusion

A detailed analysis of the endwalls effect in cycloidal rotors is presented using a coupled methodology based on CFD and ANN optimization. Three different designs of hovering-mode cyclorotor with free sides (SF), single-endwall (SE) and double-endwalls (DE) have been simulated and analyzed at various operating conditions. This study features in calculating the blade aerodynamic parameters over the 360° circular trace continuously. According to the complexity of the flow interactions while the blades are subjected to a combination of rotational and pitching oscillations, the cyclorotor characteristics are all extracted through the four mentioned EUS, EDS, IUS and IDS quarters. A huge database is collected from numerous simulations by considering a representative number of parameters. The database is then used for the learning and training of the ANN algorithm for further optimization analysis. The novel concept in the current work is to propose the optimum pitching schedule for the blades at each corresponding rotational speed, instead of assigning a constant pitch angle to the operations. In this approach, all the three endwall designs are simulated, predicted and optimized for higher performances, and the main contribution of the work is the active control mechanism which is proposed for the operation of the cyclorotor at different rotational speeds. According to the performed CFD and ANN analysis, the single side endwall design results in about 18.8%, and the doubled design at about 13.6% lower efficiencies than the free sided cyclorotor. However, it has computed that regardless of the overall efficiency, the SE model generates 8% and 11% higher horizontal force values compared with those of DE and SE, respectively. On the other side, the vertical force production has been estimated to be by average 7% and 16%

higher in values for DE design compared with the SF and SE models. These features can strongly influence the selection of which design to employ for different applications and purposes in aircraft designs.

Chapter 4

Forward-Flight and Lift-up Phases

[1]

4.1 Overview

Cycloidal rotors have shown high potential to be utilized as propulsion mechanism for various sizes of vertical take-off and landing (VTOL) aircrafts [2]. Since these rotors have a three-dimensional (3D) operating strategy, they benefit from several advantages compared with the conventional screw propellers in helicopters. This 3D operations refers to the the relatively constant flow velocity over the entire spanwise direction of the blade. Relatively low noise pollution, more efficient maneuverability, higher stability at hovering-state it desirable to be utilized in different sizes of aerial crafts and for complex and critical missions as well.

In recent years the number of applications of VTOL-capable aircrafts has sharply increased. These applications include a wide range of industrial operation areas such as surveillance, monitoring, and environmental missions like natural disasters, traffic and road concerns, payload transmission, firefighters in rescue occasions and so on. A similar necessity in most of the mentioned missions is the high level of controllability which is required. Thus, the need to employ efficient propulsion systems to provide a better flight conditions emerges as urgent.

The present work deals with cycloidal rotor (cyclorotor) which was first proposed as a new rotor designed by Fredric Kurt Kirsten in 1926 [3]. Up until 1940s there were a number of surveys on this mechanism but there was a halt of about 50 years on their development. In 1998, BOSCH Aerospace Incorporation tested a cyclorotor at UAV scale which led to the report of comparatively low-noise operation characteristic for these rotors [100]. Some more investigations in numerical simulations and experimental tests were also done for light scale crafts such as airships and those which are known as lighter-than-air (LTA) vehicles by Onda and his colleagues in Japan [5, 3, 9]

Hwang et al. [11, 12] conducted a parametric optimization of cyclorotors in order to obtain optimum states of operations in terms of sizing, blade numbers, rotor radius, and by employing spar joined with blades. They used genetic algorithm as well as numerical and experimental tests for their optimization process. In one of their real tests, they used a 4-cyclorotor configuration operating in 2 pairs in their VTOL design. Their design reached $\approx$ 160 newton thrust with improved stability at hover-state operations. On the control

[1] Based on the work submitted to Journal of Aerospace Engineering, Performance Optimization of Forward-Flight and Lift-Up Phases in a Cycloidal rotor Using an Active Control Mechanism, n° pages (57) , 2020

mechanism and the structural behavior of the blades [101, 102] performed studies by pursuing the rotational effects. They proposed a robust control methodology to enhance the blade performance while subjected to high rotational speeds. In cycloidal rotors also the stall, separations and efficiency reductions might be as a result of vibrations and flapping issues. Further studies on vibration problems is also reported [103] for circular cylindrical applications where indeed high pressurized liquids are the result of oscillations rather than the air instead.

In an analytic study carried out by Yun et al. [13], they intended to study the thrust vectoring analysis in cyclorotors. They also performed more detailed and complementary investigations for UAV scale cyclorotor using numerical, experimental and analytics approaches to reveal a better understanding on the dominant flow, rotor properties and design specifications[14, 1]. The first stream-tube model, which was developed to accurately model the cyclorotor was designed in 1975 for Darrieus wind turbines [15].

Ilieva et al. [2, 16] conducted on overview of the diverse propulsion systems proposed over the years for airship type vehicles. They clarified the positive and negative points of such propulsion systems from different aspects like power sourcing, efficiency, concerns in functionality and etc. MAAT project was also introduced by them as a major FP7 European Union effort to perform research on high-altitude airships. A recent comprehensive study by [104] demonstrates a novel technique and concept in unconventional airships in which facilitates some granted methodologies and guidelines for the airship or aircraft designers.

Boirum et al. [19] conducted a historical survey with review of documentation on design, application and analysis of cyclorotors since their very early inception. Benedict et al. [21] carried out a detailed research on MAV-scale aircrafts using cyclorotors as their main thrusters. They conducted both experimental tests and numerical predictions as well. They demonstrated a fairly light MAV craft flying with two counter-rotating cyclorotor, with 3 blades each, and a net weight of 290 g.

The environmental restrictions have also been surveyed by Kocer et al. [38] for UAV-operating quad-rotor. They considered the effects of flying at close-ceiling regions on the efficiency of UAV-size propellers. They compensated the ceiling effects by proposing a centralized predictive controller that minimizes those effects. On the other hand, the effects of ground surface has also been investigated in several studies [33]. In those works, the researchers attempted to understand the static and dynamic effects from ground on the propulsion and flight mechanism. For instance, [33] considered a combination of wings and tail while operating at close-ground heights. In a numerical work carried by Rami and Pascoa [41], they also simulated a UAV size cyclorotor at its lift-up phase, at close levels of the ground surface. They could predict the best operating conditions for different effective heights above the surface. The same authors, in [47], used both CFD simulations and neural network analysis (ANN) to effectively propose the optimized pitching oscillations at each rotation speed. They simulated cyclorotor operations at various conditions and using the database achieved from the CFD computations, they trained the neural network algorithm and went through an optimization process. They concluded that

different efficiencies could be gained when a cyclorotor operates as a propulsion system for a VTOL aircraft in different heights.

CROP [27] was a project under European union FR7 framework license which held cyclorotors as the optimizing target. Leger et al. [28, 29] studied the different operating principles of cyclorotor at hovering state using an analytic approach. Furthermore, in another numerical work, they predicted the presence of three-dimensional effects, tip leakage and main flow structure considerations while being equipped with endplates. All these efforts led to the CROP report [31]. Under other titles like BOSCH and IAT21 also a comprehensive research was carried out on different aspects of design, optimization, sizing and efficiency levels for cyclorotors. Xisto et al. [54, 32] assessed the feasibility of applying plasma actuators of dielectric barrier discharge (DBD) on blades in cyclorotors. They were targeting to compensate the stall conditions where large efficiency losses are expected. They reported that no effective stall avoidance or even delay could be achieved using DBD, but they reached higher thrust levels during downstroke phases. In rotary blades as such in turbines and cyclorotors, the flow on the blade surfaces, is highly sensitive to the instant oscillating-rotating motions. The flow structure complexity varies with flow separation, wakes, and stall phenomena which must be noticed when analyzing performance issues and flow losses [58, 59]. Quite recently, novel approaches based on applying plasma actuators for flow control, separation avoidance and boundary-layer flow enhancement, are proposed which had resulted in efficiency enhancements on blade applications [64, 65, 66].

Some studies have been done on several rotors in VTOL crafts [17], where they mentioned that blade interaction was also playing a significant role on the efficiency of aircraft and that happens in cycloidal rotors as well. Yu et al. [39] investigated the main variables which affect the aerodynamic efficiency of a cyclorotor in forward-flight. Advance ratio and the number of blades were the two mentioned parameters which affected it most. They concluded that more blades will result in higher efficiency and lower vibration while operating. On the other side, using higher advance ratio leads to less blade vortex interaction (BIV) effects.

Singh and Pascoa [40] considered pitching oscillations of a single airfoil as representative of a blade in cycloidal rotor. They tried several turbulence models in order to compare them while capturing the flow phenomena during oscillations and strokes. The SST-SAS and also SAS models were the ones which could better capture the flow effects at pre-stall, stall and post-stall situations. National aeronautics and space administration (NASA) claimed in a report [42] that the cyclorotor mechanism convects a massive pile-like flow, as downwash, which significantly affects the efficiency of the cyclorotor. Thus, flow characteristics at all flight regimes must be taken into concern in order to obtain the optimum operating conditions of cyclorotors.

In the present study the forward-flight and vertical lift-up phases of a UAV scale cyclorotor is investigated through numerical CFD simulations and neural network analysis. First, various operating conditions for pitching oscillations at relative rotational speeds are simulated, for each of the forward and vertical speeds in forward-flight and lift-up mode, re-

spectively. This was done after obtaining a sufficient database of parameters and after post-processing from CFD predictions, the ANN algorithm was then trained for further optimization analysis. Consequently, the optimum pitching schedules are proposed for each rotation speed of each flight speed in both phases. This was the result of tracking the blade sequentially while traversing the circular trace in one complete revolution. To the best of the authors' knowledge, this work is the first study carried on CFD simulations accompanied with ANN analysis for further optimizations of cyclorotors operating in forward-flight and vertical lift-up phases using on-board techniques [105]. Different flight speeds in both phases are considered at each specific operating condition of pitching oscillations and rotational speeds to obtain the optimum oscillating schedules under the required operating conditions.

4.2 Cycloidal Rotor System

4.2.1 Design Principles

Cycloidal rotor is termed to a group of blades sitting diagonally about a center with a defined arrangement. In this system (see Fig.5.1), blades experience two simultaneous displacements: one is rotating (with Ω rad/s) around the rotating center, and the other is pitching oscillation about their pivot point. These rotors can be utilized in various applications like wind turbine, ships, aircrafts and LTA airships. In the present work the design is aimed for a UAV-size aircraft and to be used as of VTOL propulsion system.
Considering the front face of Fig.5.1, blades which are positioned on the right and left sides at Ψ=0° and Ψ=180°, respectively, are in tangent with the circular route which causes the 0° pitch angle. The locations of Ψ=90° and Ψ=270° of azimuth angles (top and bottom extremities) are described to gain the maximum pitch angle. While traversing a complete cycloid, the blade experiences 4 strokes in which occurs two by two inward and outward. These strokes are here defined as external up-stroke (EUS), external down-stroke (EDS), internal up-stroke (IUS) and internal down-stroke (IDS) (as is shown in Fig.5.1).
Operating at a cyclic rotation and pitching oscillations according the theme given here, the system functions as an inhaling-exhaling rotary device which processes the flow unlike the planar fans and propellers traditionally used in helicopters. This three-dimensional movement of the blades brings higher efficiency of acting on the fluid medium, resulting in low-noise operations and higher flow controllability, due to comparatively equal flow velocity over the whole span of the blade. The specifications of the current cyclorotor configuration is presented in Tab. 4.1.

Table 4.1: Specifications of the UAV-scale cycloidal rotor configuration.

Blade Number(s)	Blade Profile	Chord (C)	Pitching Center	Rotor Radius	Span
6	NACA0012	0.15 m	0.35$*$ C	0.4 m	0.8 m

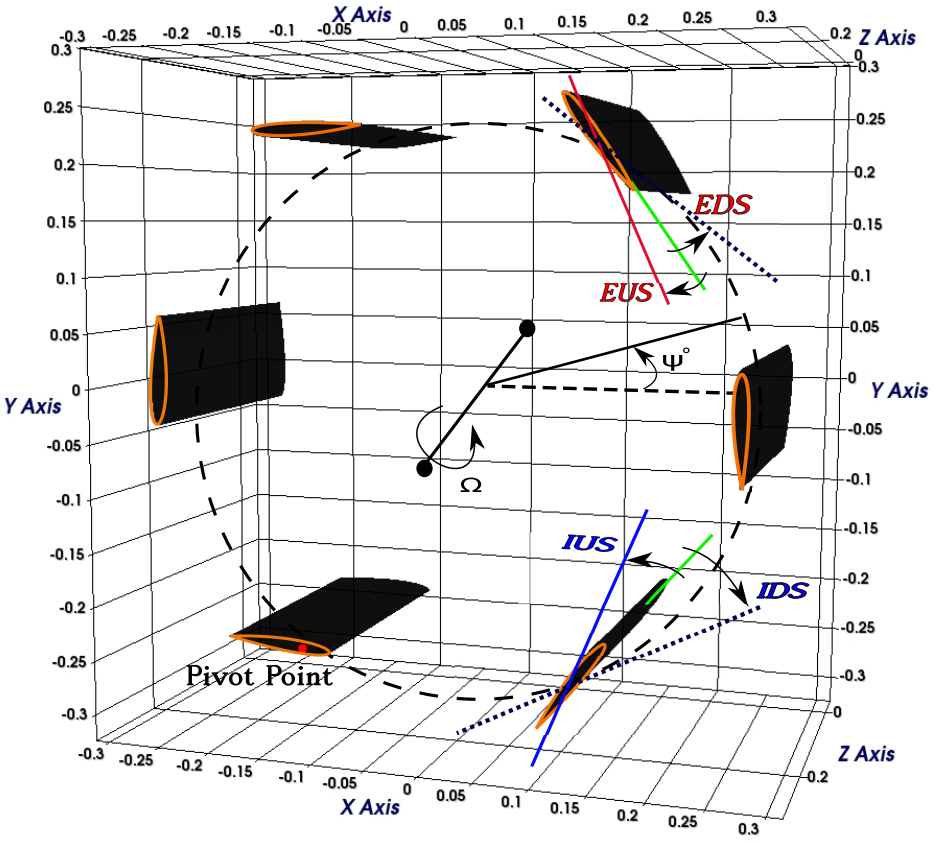

Figure 4.1: Schematics of blade arrangement and operating principles in a typical cycloidal rotor.

4.2.2 Hover-State

Prior to dealing with forward-flight and lift-up phases, a comprehensive illustration of the operating state and flow mechanism in a hover-state mode would be indispensable to better understand the concept. From the entrance until exiting the cyclorotor, flow passes through three successive stages. First is the inhaling region where the cyclorotor sucks the air-stream from the top-half, to the in-cage area. The major portion of the circle belongs to inhaling region. As the flow gets inside the cage, it goes vertically downward (with a slight inclination to left) and reaches the exit region of the rotor. In the third step, a rightward inclination to the flow happens as it leaves the cage, which here is called downwash jet flow.

The importance of studying in detail the flow structures and operating states is to obtain accurate computations of the thrusting mechanism. Figure 4.2 shows the high force production regions in a complete circle. The blue arcs in the top and bottom sides are the regions of vertical force and the red arcs represent the horizontal force production regions.

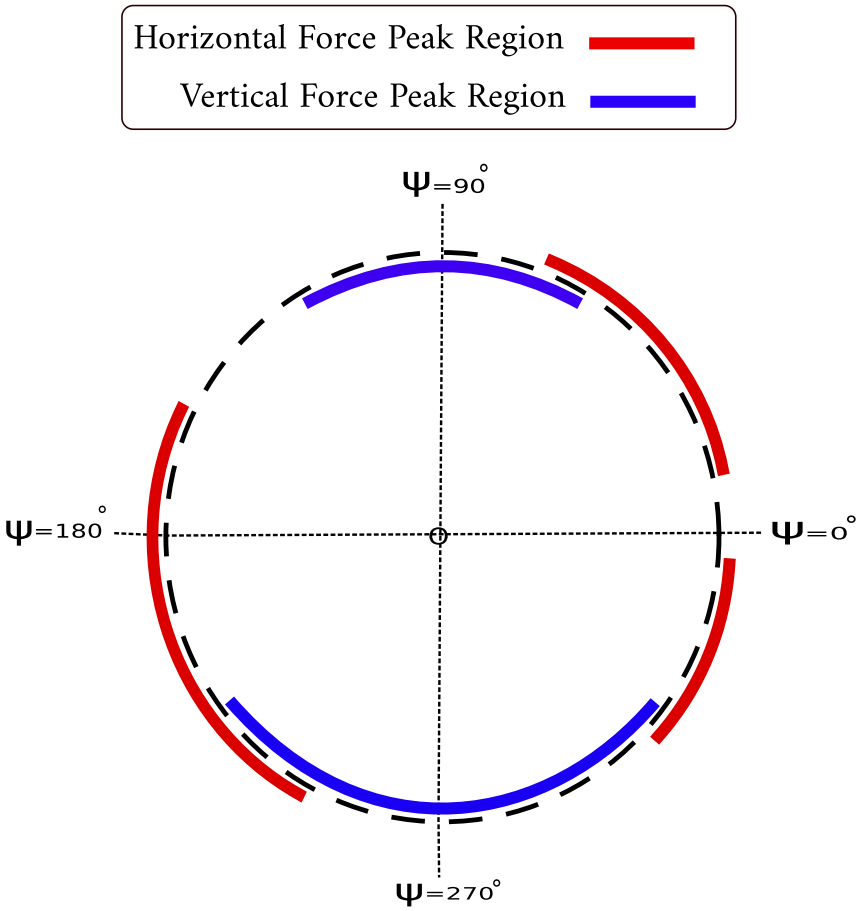

Figure 4.2: Horizontal and vertical force peak regions in a complete cycloid trace.

These peak regions are obtained by tracking a single blade in a complete round in numerical computations which will be further illustrated in subsequent sections.

4.2.3 Forward-Flight

As a means of propulsion system for aircraft, here the forward-flight operation of a UAV-scale cyclorotor is studied under various conditions. Forward speeds of 10, 15, 20 and 25 m/s are selected to collect an inclusive database while operating in different operating conditions. These conditions consist of pitching angles of 20°, 25°, 30°, 35° and 40° with all individually in 9 different rotating speeds from 200 to 600 with 50 rpm intervals. This could effectively result in collecting a numerical database obtained from CFD simulations for the chosen forward speed of operation.

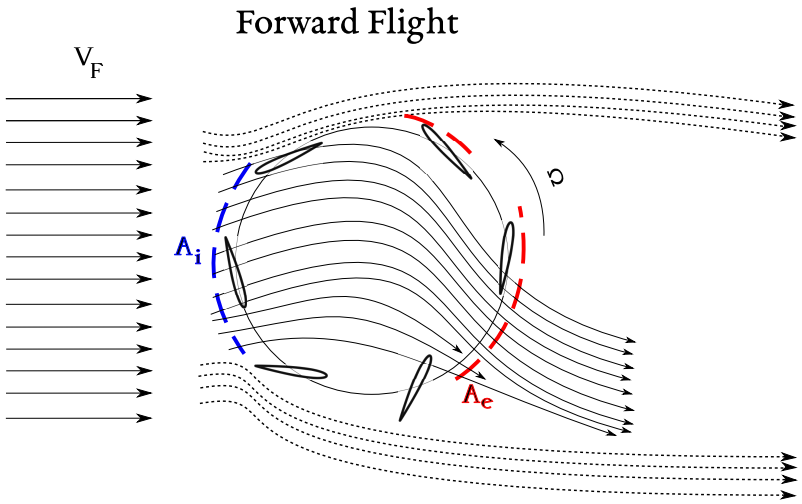

Figure 4.3: Schematic of the forward-flight pattern in an operating cyclorotor.

Figure 4.3 shows a schematic of flow pattern while a cyclorotor operates at forward or in cruise mode flight. The blue dashed-arc defined with A_i refers to inhaling, and the red arc with A_e indicates the exhaling areas. This might be of high importance to observe the in-out regions of flow in order to reach better design strategies and hence more efficient operating modes.

4.2.4 Lift-Up Phase

The other aspect of this chapter deals with the lift-up characteristics of an operating cyclorotor. As is seen in Fig.4.4, inhaling (A_i) and exhaling (A_e) regions in lift-up phase are very similar to what it experiences in hovering state [47] which will be further discussed in numerical results section.

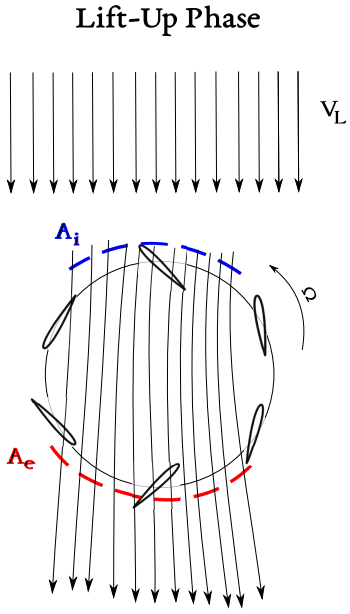

Figure 4.4: Schematic of the vertical lift-up pattern in an operating cyclorotor.

Vertical velocities of 4, 6 and 8 $m/_S$ are applied for the lift-up simulations under the same

operating conditions of pitching angles (5 modes) and rotating speeds (9 modes) as was considered for forward-flight. This collection of data for both forward-flight and lift-up phase became essential for the neural network approach and the optimization process which is also carried out later in this study.

4.3 Numerical Approach

4.3.1 CFD Simulation and Turbulence Modeling

Numerical simulations in this study are done using a CFD approach based on OpenFOAM package (Weller et al. 1998) which is known as an open source and extensible toolbox. In choosing the appropriate solver for current case which is a multi-zone displacing construction, pimpleDyMFoam is selected as an incompressible solver which is capable of dealing with turbulent predictions. The advantage of this solver is the coupling of both PISO and SIMPLE algorithms. For velocity and pressure derivative terms, a Gaussian integration discretization is chosen and for time derivatives, a bounded first order implicit discretization is set for the simulation, in $fvScheme$ and $fvSolustion$ dictionaries inside OpenFOAM.
The selected turbulence model for current simulations is k-ω-SST (Shear Stress Transport). This turbulence model uses two-equation eddy-viscosity approach which is capable of treating the normal free-stream with k-ε and resolving the shear layer with k-ω approach.
A complex displacement of blades is faced in cyclorotors during simultaneous rotating and pitching oscillations. Besides, the trend of the flow while passing through the cyclorotor is also illustrated to be highly complex, experiencing sharp curves and inclinations in a short pace of time and distance. Stall, up- and down-strokes, blade-flow interactions and flow separation are all the impending phenomena which are not beyond expectations in such instant altering rotary mechanism. Thus, as was also suggested in [40, 41], the optimum turbulence model in terms of computation costs and accuracy in predicting flow structures would be k-ω-SST which is used here as well.

4.3.2 Computational Domain

The geometry definition and the meshing processes are all done using blockMesh utility within OpenFOAM. Using Octave coding, we were capable of generating the desired dictionary for the mesh. As is seen in Fig.4.5, the meshing methodology is fully structured on computational domain.
Since there exist separate displacements of different regions in this type of rotor, as rotating and pitching zones, hence these regions require to be in separate interfaces in order to be able to introduce distinctive movements to each zone. Thus, the geometry herein (Fig.4.5) is comprised of eight individual areas of i) stationary domain (the area outside of rotor (big dashed-circle)), ii) rotating region (the whole region of inside big dashed-circle) and iii) pitching motion regions (regions inside the 6 small-dashed circles) which

are for the six blades. Therefore, the inner small dashed-circle regions that displace with rotation and pitching oscillations simultaneously.

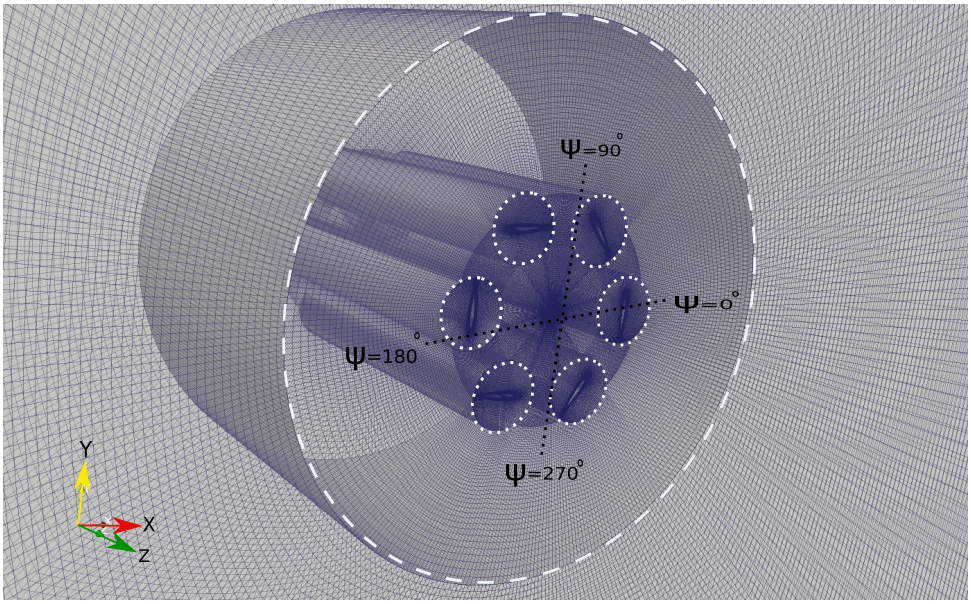

Figure 4.5: Mesh configuration of cyclorotor and defining cyclic-AMI regions for rotor and blades using sliding mesh technique.

For such combination of 7 split regions, we created 14 cyclicAMI (arbitrary mesh interface) patches to be able to slide on each other in pairs. Each 2D inside surface of small-dashed circles consists of 7.5 k grids which brings 45 k cells for 6 blades in total. The region outside the small-dashed, and inside the big-dashed, which merely rotates, consists of about 45 k cells and almost the same number of grids are constructing the stationary domain. Around 20 million grids are used for the 3D cases in the current simulations.

4.3.3 Validation of CFD Approach

The validation of current numerical simulations is done using the experimental data as were reported by Yun et al. [1] for a UAV cycloidal rotor. To this end, a range of pitching oscillations and rotating speeds values are selected in simulations and experiments for the validating comparisons. The pitch values include 20°, 25°, 30° and 40° and the rotating speed values are 200, 300, 400, 500 and 600 rpm.
The chosen parameters are thrust and power loadings which are reported as two principal parameters in validations so far.
Power coefficient is defined as:

$$C_P = \frac{P_N}{\rho A (R\Omega)^3}, \quad (4.1)$$

and the thrust coefficient is:

$$C_T = \frac{T_N}{\rho A (R\Omega)^2}, \quad (4.2)$$

in which R indicates to the radius of cyclorotor and A refers the projected area of the rotor:

$$A = 2Rs, \quad (4.3)$$

and P_N, T_N are describing net power and net thrust in the following equations, respectively:

$$P_N = M\Omega, \quad (4.4)$$

$$T_N = \sqrt{T_H^2 + T_V^2}, \quad (4.5)$$

where M and Ω refer to momentum and rotational speeds and T_H and T_V are horizontal and vertical thrusts.

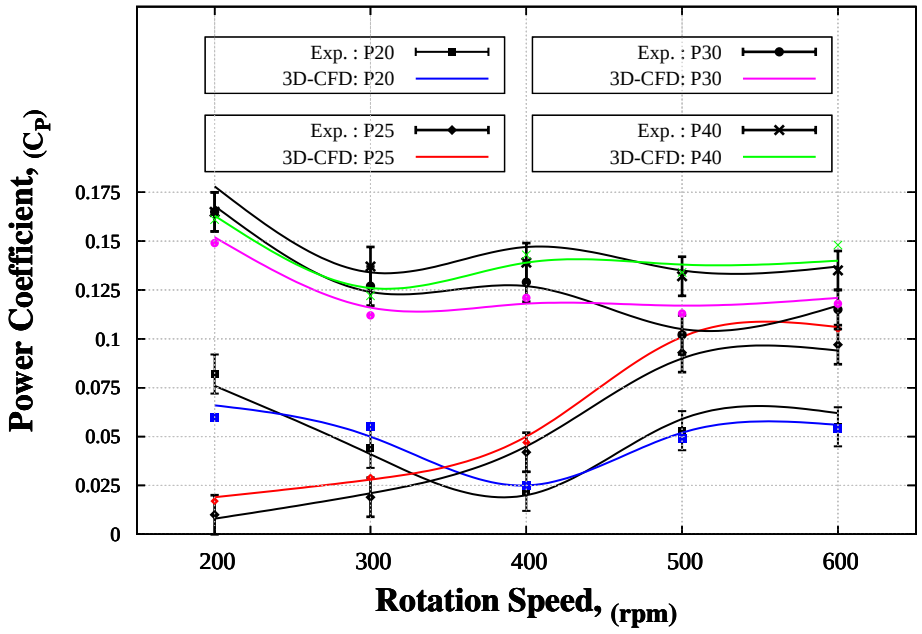

Figure 4.6: CFD validation with data of Yun et al.[1] using power coefficient at different rotation speed. The corresponding error bars are presented.

Figures 5.7 and 5.6 for power and thrust coefficients, respectively, depict the plots that compare CFD simulations and experiments. A convincing agreement is revealed from these plots with the results of experimental tests from (Yun et al. 2007).

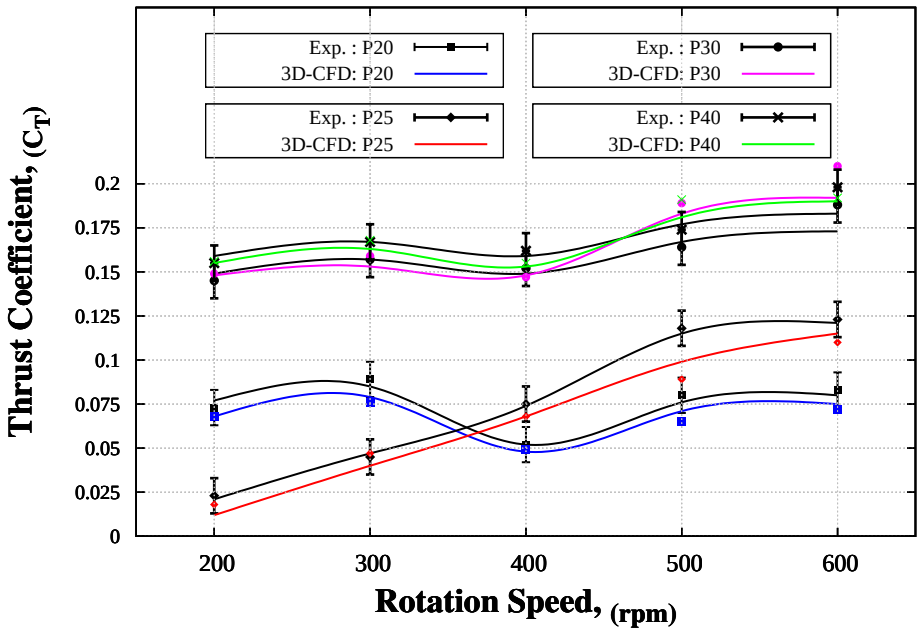

Figure 4.7: CFD validation with data of Yun et al. [1] using thrust coefficient at different rotation speed. The corresponding error bars are presented.

4.4 Neural Network Methodology

Artificial neural network (ANN) has widely shown its practical usage in numerous fields of science and technology and hence it is getting more involved in recent fast-going global industry. This approach is proposed to be able to dynamically analyze the optimum efficiency of cyclorotor in different operating states [47]. Therefore, it has been declared in [83] that ANN can play a significant role while a combination of data-sets in real tests and numerical predictions are going to decide the optimum state of operation.

In the current study 8 parameters are selected as the primary values to be fed into the input nodes, as is depicted in Fig.4.8. These parameters include vertical force (F_Y), horizontal force (F_X), total (net) thrust (T_N), power and thrust coefficients (C_P and C_T), power and disk loadings ($P.L$ and $D.L$) and figure of merit ($F.M$).

It is to be noted that all of the mentioned parameters, and their corresponding values, are inserted for each single combination of rotation speed (Ω) and pitching oscillations angle (P°), for each flight speed of forward and lift-up as were derived from numerical simulations. Thus, the ANN algorithm is trained using a sufficient number of parameters and values collected through the CFD database. The targeting parameters are the force coefficients (C_{F_X} and C_{F_Y}) and $F.M$ for various range of Ω and P°, for each operating mode in forward and lift-up speeds (V_F and V_L).

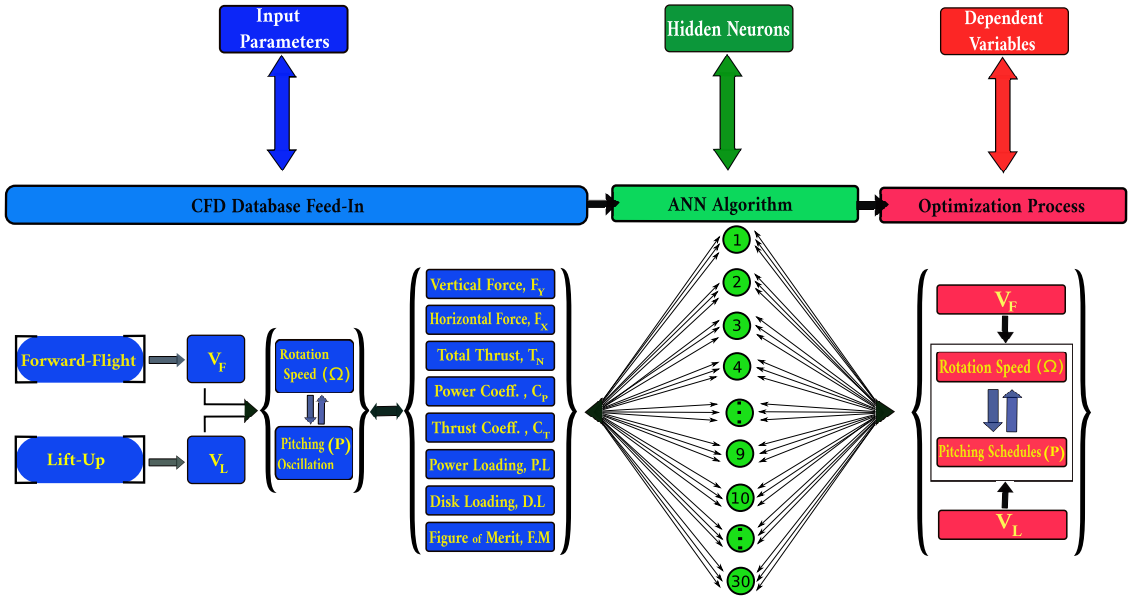

Figure 4.8: Diagram of the optimization procedure proposed, by using neural network analysis.

4.4.1 ANN Structure

The relation coefficient (R_C) and mean square error (MSE) are the selected parameters in estimating accuracy and evaluation of the ANN model.
R_C is described through the work of Haykin [86] as:

$$R = \frac{Cov(a, A_p)}{\sqrt{Cov(a,a).Cov(A_p, A_p)}}, \quad (4.6)$$

where $Cov(a, A_p)$ indicates covariance between the measured and predicted values a and A_p ,respectively:

$$Cov(a, A_p) = E\left[(a - \mu_a)(A_p - \mu_{A_p})\right], \quad (4.7)$$

that E defines the expected value, μ_a and μ_{A_p} are the mean values of a and A_p, respectively. The covariances $Cov(a, a)$ and $Cov(A_p, A_p)$ are according to:

$$Cov(a, a) = E\left[(a - \mu_a)^2\right], \quad (4.8)$$

$$Cov(A_p, A_p) = E\left[(A_p - \mu_{A_p})^2\right], \quad (4.9)$$

and MSE is formulated as:

$$MSE = \frac{1}{n}\sum_{i=1}^{n}(a_i - A_{p_i})^2. \quad (4.10)$$

4.4.2 ANN Performance Analysis

For the current ANN analysis, the approach of forward-feed is chosen, and this demands for a series of layers in order to be able to pursue the entire data-input, training procedure, model validation and desired output. In doing so, the progress of data mapping among the values of input data and outputs has been accomplished by using hidden neurons for training the scheme.

Figure 4.9 reveals the evaluation of errors which has reduced sufficiently at a 30 hidden neuron layer. Noteworthy that reaching to higher levels of accuracy is highly dependent to testing and training the database through the ANN model.

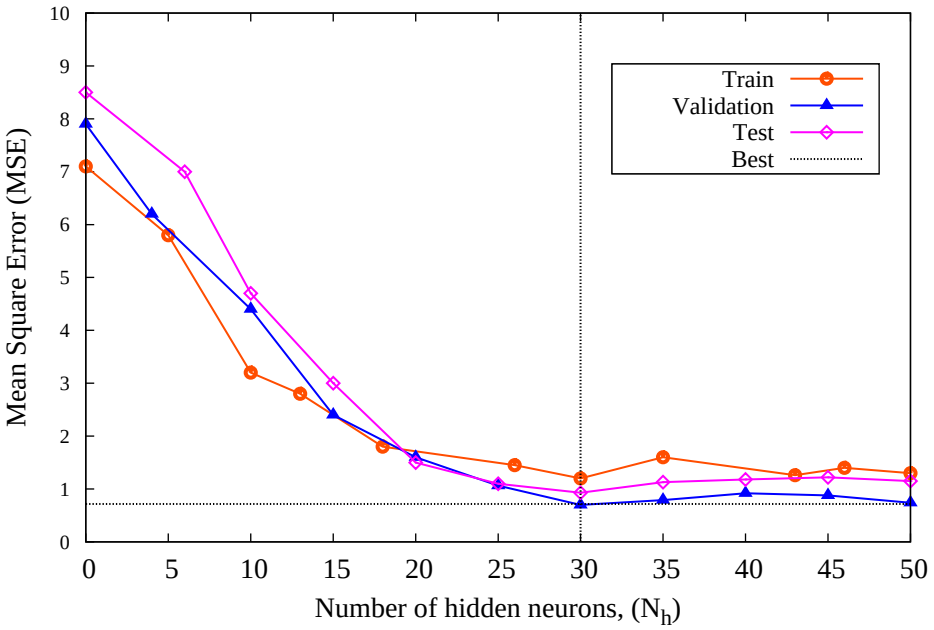

Figure 4.9: Mean square error variation and optimal state vs. number of hidden neurons.

Furthermore, it is shown in Fig.4.10 that R_C plot tends to rise-up to the maximum level nearly at 30 layers. Therefore, the optimal hidden layer for the current ANN analysis is chosen at 30 which resulted in convenient convergence.

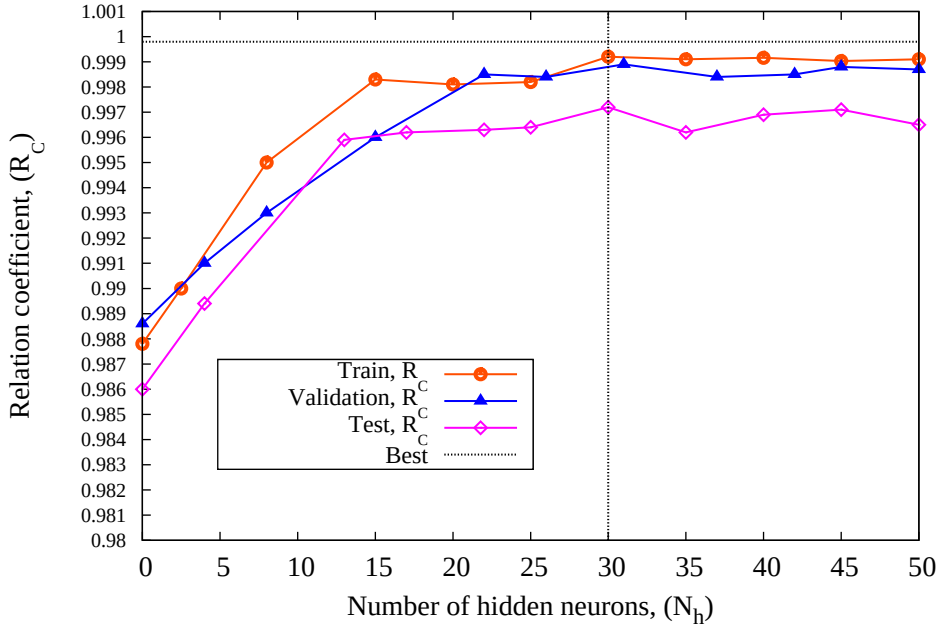

Figure 4.10: Relation coefficient and optimal state vs. number of hidden neurons.

4.4.3 Active-Control Methodology

A progressive flowchart of the current optimization process for active control methodology is shown in Fig.4.11. Following is the illustrative points of the flowchart:

1. Selecting operating conditions for simulations and predictions in all modes of forward-flight, lift-up and hover states.
2. Validation of numerical codings, simulations and results with those of experiments with the defined parameters.
3. Database collection of all computations and postprocessings for further data analysis at each operating condition.
4. Training the ANN algorithm using the assessed database from numerical simulations.
5. Estimating the accuracy and error levels of the ANN model after feeding-in the data and training.
6. Optimizing the values and parameters for each of the flight modes and conditions which are considered herein.
7. Proposing the optimum operating schedules of cyclorotor for both lift-up and forward phases in a range of pitching oscillation angles and rotating speeds.

Table 4.2: Aerodynamic results comparison between experiments, CFD and ANN optimizations at 25° pitch angle and 600 rpm.

Parameter	Exp.	2D–(Err. %)	3D–(Err. %)	ANN–(Err. %)
$D.L$	48.36	46.26–(-4.17)	47.75–(-1.26)	46.81–(-3.20)
$P.L$	0.0632	0.0598–(-6.82)	0.0648–(2.53)	0.0631–(-1.74)
C_T	0.1283	0.1197–(-6.41)	0.1253–(-3.2)	0.1249–(-2.65)
C_P	0.1062	0.1024–(-5.80)	0.1079–(1.6)	0.1039–(-2.16)

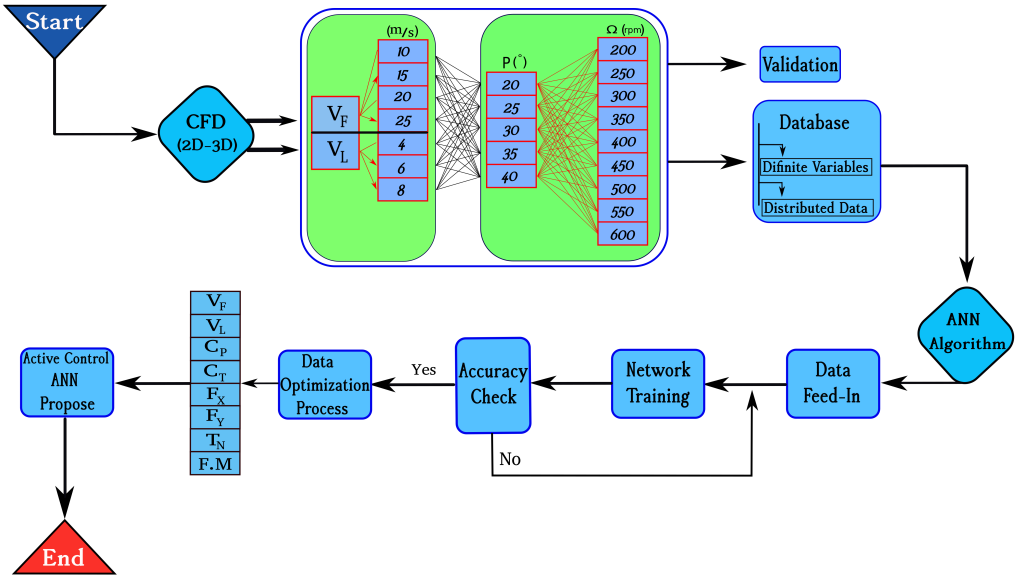

Figure 4.11: Active control flowchart for optimization analysis of ANN and numerical data.

A parametric study of the values of disk loading ($D.L$) (eq.4.12), power loading ($P.L$) (eq.4.13), C_T and C_P at 600 rpm and 25° is shown in table4.2. This is to obtain better vision of the deviations among real tests, numerical predictions and the ANN analysis. The exact value of each parameter, with the corresponding error percentage, as a sign of deviating from experimental tests are all compared in this table.

4.5 Results and Discussions

Parametric studies have been carried out on cyclorotors in various scales, in different operating conditions, and for diverse applications all over the years. These studies consist on a variety of experimental and numerical surveys for parameters such as rotor size, specific applications, number of blades, airfoil profiles, pitching and rotating considerations, controlling systems, etc. In terms of propulsion system for aerial crafts, cyclorotors are claimed to be beneficial and a good candidate compared with conventional screw pro-

pellers. However, more studies are imperatively required to justifying the credibility and feasibility of cyclorotors as a means of propulsion system for aircraft in terms of efficiently. The operational characteristics of a UAV-scale cyclorotor is studied while functioning at forward-flight and lift-up phases. In doing so, a wide range of parameters and values are included to cover thoroughly and with sufficient detail for operating modes. The computations in several speeds and with each operating condition are also carried out, accordingly. Moreover, a sequential tracking of the operating blade is covered over the azimuthal revolution from $\Psi = 0^\circ$ to $\Psi = 360^\circ$. This was done in order to assess detailed thrusting performance over the whole circular trajectory in a complete cycloid. Thus, the subsequent optimizations through ANN approach would be more reliable since they are considering continuous displacement of blades.

4.5.1 Numerical Simulations

Typically, in cyclorotors, the passing flow experiences complex structures and curvatures during inhaling and exhaling from the system. The point is that the flow characteristics, curvatures, behavior and effects alters, while cyclorotor is operating at different conditions. These conditions include hovering-state, forward flying mode and lift-up phase, aside from other variable operating conditions, which were mentioned before. Thus, technically the most proper way of measuring the properties would be to track the flow while the blade traverses over the circular trajectory. This technique was done for the hover phase of exactly the same size cyclorotor in [47].
Currently, the forward-flight and lift-up is targeted to explore the flow behavior and the resulting effects on the overall efficiency. Therefore, in addition to the hover-state operating conditions, here different pitching oscillation angles and rotating speeds were included, diverse flying speeds are also separately investigated in each of the mentioned operating conditions.

4.5.1.1 Forward-Flight

In forward mode, as was schematically depicted in Fig.4.3, simulations were carried as though the rotor is passing leftward flow at different forward speeds. In this flight phase, cyclorotor functions considerably different as compared with the hover state. Inhaling and exhaling regions, in-cage flow and even the downwash jet behaves in comparatively different style. Figure 4.12 presents the forward operating mode at 10 $m/_S$ with 200 rpm and 30° rotating speed and pitching angle, respectively. The flow shows to accelerate high from the top (Ψ=90°) and bottom (Ψ=270°) positions as the flow sheds in wake streams from these two peaks with relatively high velocities.

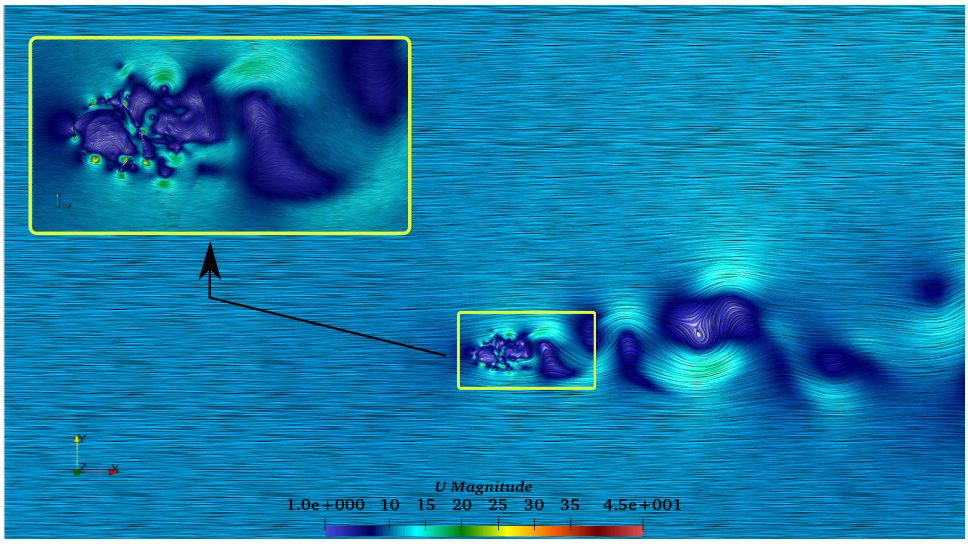

Figure 4.12: Flow contour of cyclorotor with 10 $m/_S$ forward speed simulation, at 30° pitch angle, and 200 rpm.

For the induced flow inward and outward the circular cage, the positive and negative signs are attributed to inhale and exhale flows, respectively. Figure 4.13 presents the flow passing through the cyclorotor at 10 $m/_S$ forward speed. The black and blue plots are for rotations of 400 and 600 rpm, respectively. In each of these, lines are for 20°, dashed-lines are for 30° and dotted-lines are for 40° pitch angles.
As is seen, the region between $\Psi \approx 90°$ and $\Psi \approx 280°$ is the inhale arc in forward mode operation. The passing lines below the zero-velocity horizontal line are addressing the exhale flow areas (Fig.4.13). At constant rotating speed it is shown that the higher pitching angle results in higher induced flow, in both inhale and exhale regions. On the other hand, the higher rotating speed induces higher speeds at both regions accordingly. The other note from this plot is that the bottom-side exhaling region ($\approx 180° \leq \Psi \leq \approx 280°$) experiences higher velocities in all conditions, which might source from the inclination of the blade compared with while it passes through the top-side inhaling region, that sort of obstructs the inflow.

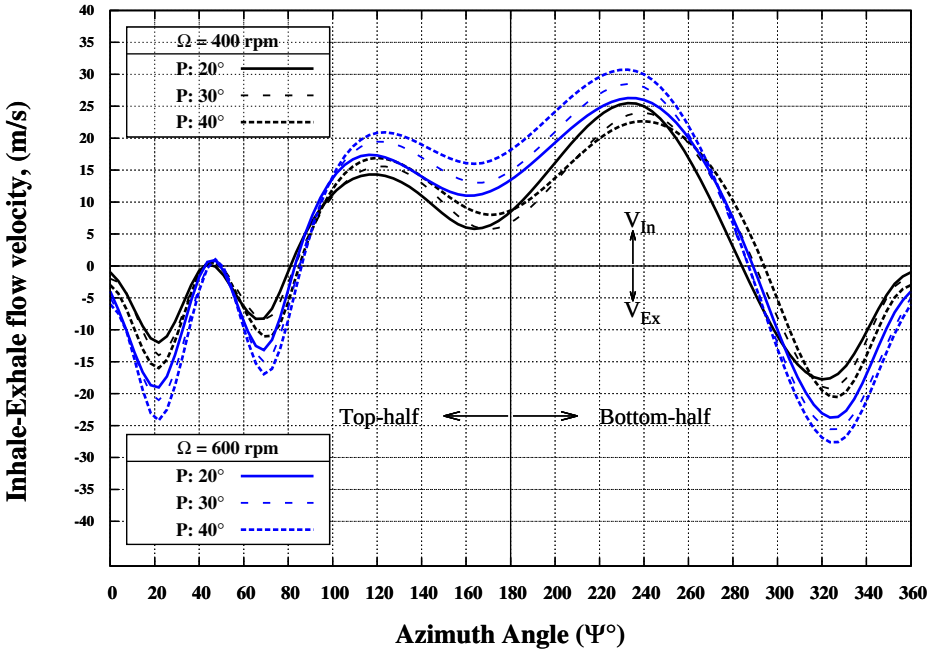

Figure 4.13: Comparison of inhale-exhale flow velocity distribution over a complete trajectory at a constant forward speed of 10 $m/_S$ under different operating conditions.

Furthermore, the induced flow velocities in different forward speeds are also plotted in Fig.4.14. This is to get a comparison of forward speed effects on the acting flow in cyclorotor. As is noticed, the inhale and exhale regions are somewhat analogous, but the major distinction is in the intensity of the induced flow while being subjected to different forward speeds. Increase in forward speed shows to result in also increased induced flow in every region.

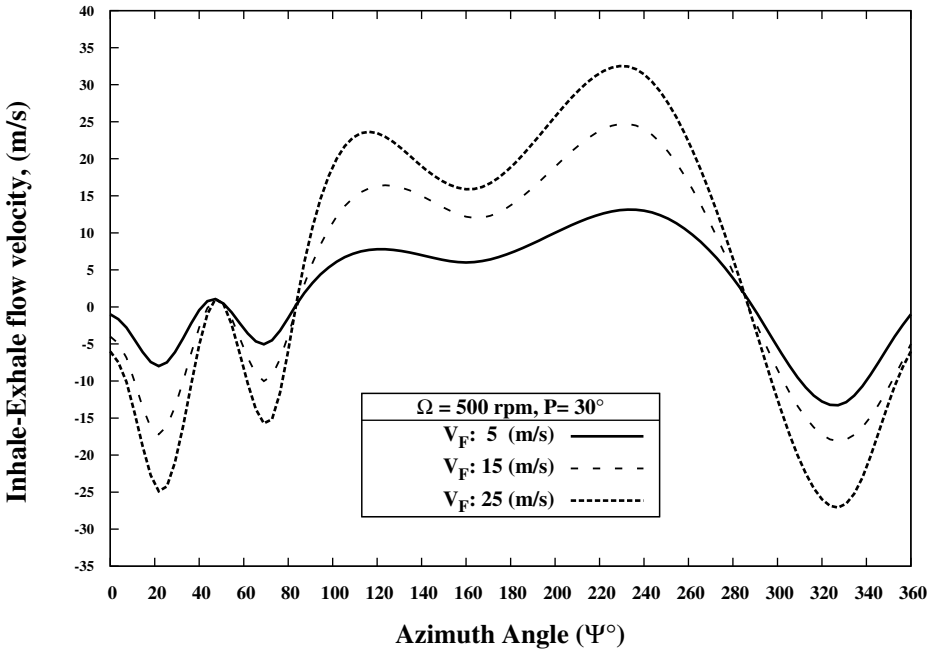

Figure 4.14: Comparison of inhale-exhale flow velocity distribution over a complete trajectory at 500 rpm and 30° under different forward speeds.

4.5.1.2 Lift-Up

For lift-up phase, as was schematically depicted in Fig.4.4, simulations are carried as though the rotor is passing upward in different speeds. In this flight phase the cyclorotor functions considerably similar as the hover state. Inhaling and exhaling regions, in-cage flow and even the downwash jet behave in almost similar trend. Figure 4.16 presents lift-up operating phase at 6 $m/_S$ with 300 rpm and 25° rotating speed and pitching angle, respectively.

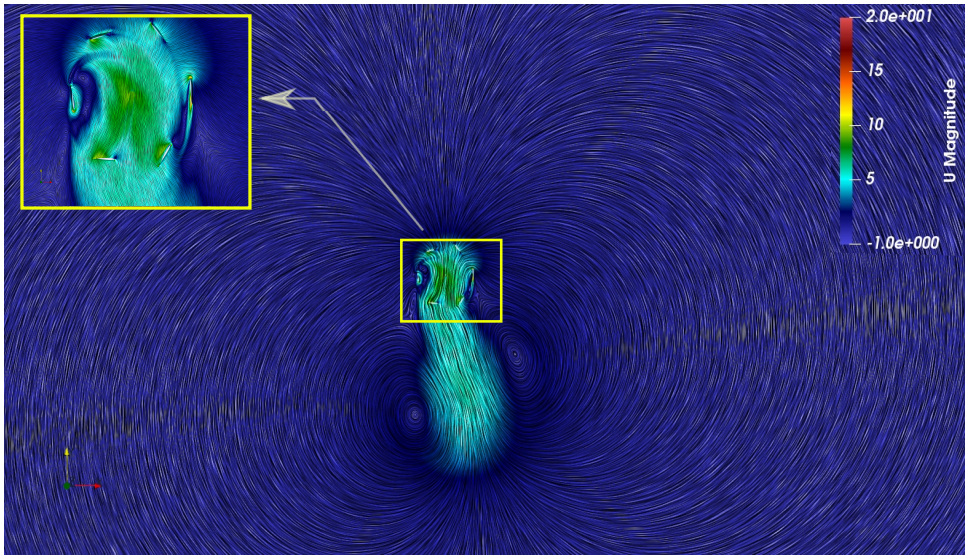

Figure 4.15: Flow contour of cyclorotor with 6 $m/_S$ lift-up speed simulation at 25° pitch angle and 300 rpm.

Likewise, in forward mode, the positive and negative signs are also attributed to inhale and exhale flows, respectively. Figure 4.16 presents the flow passing through the cyclorotor at 4 $m/_S$ lift-up speed. The black and blue plots are for rotations of 400 and 600 rpm, respectively. In each of these, lines are for 20°, dashed-lines are for 30° and dotted-lines are for 40° pitch angles.
From this figure, it is visible that roughly one third of the circular route is covered with exhale flow (≈210° ≤ Ψ ≤ ≈ 330°). Therefore, the rest portion belongs to the inhaling region which is even larger than the hover-state operating condition [47]. It is also noticeable that the higher pitch angles induce higher velocities at each constant rotating speed. The complicating point is that the induced flow velocities do not obey a straight rule at each operating condition. For instance, the velocities at 30° and 40° pitching angles in 400 rpm result in higher velocities than 20° and 600 rpm. These are the situations that a higher controllable mechanism like ANN can give us necessary help in order to actively choose the optimum operating states which is illustrated in the subsequent sections.

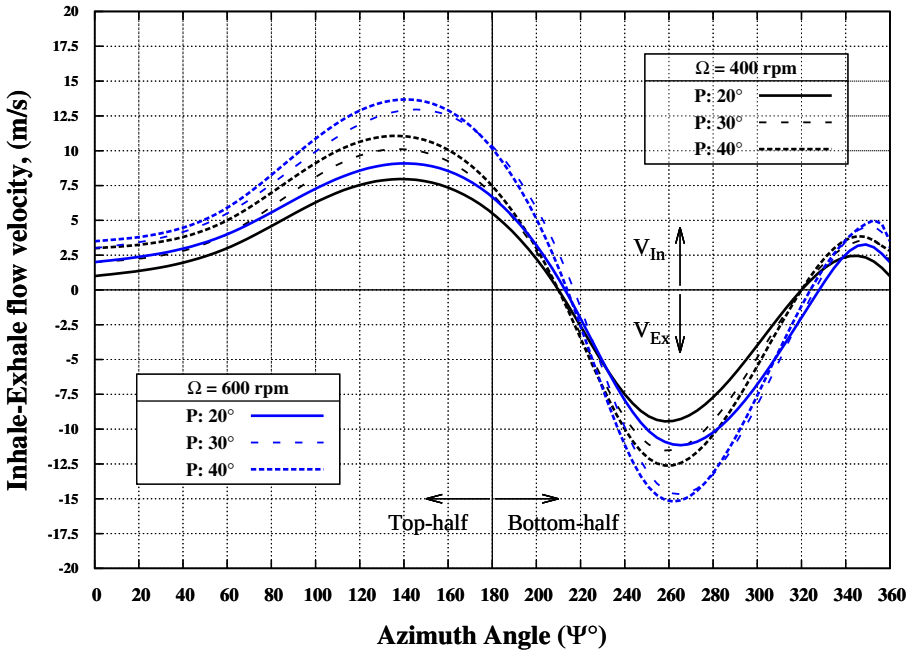

Figure 4.16: Comparison of inhale-exhale flow velocity distribution over a complete trajectory at a constant lift-up speed of 4 $m/_S$ under different operating conditions.

Moreover, the induced flow velocities in different lift-up speeds are also plotted in Fig.4.17. This is to get a comparison of lift-up speed effects on the dominant flow in cyclorotor. As is noticed, the inhale and exhale regions are somehow similar, but the significant difference is in the values of the induced flow while being subjected to different upward speeds. The comparisons declare that, likewise the forward mode, the higher speeds will induce higher velocities in flow.

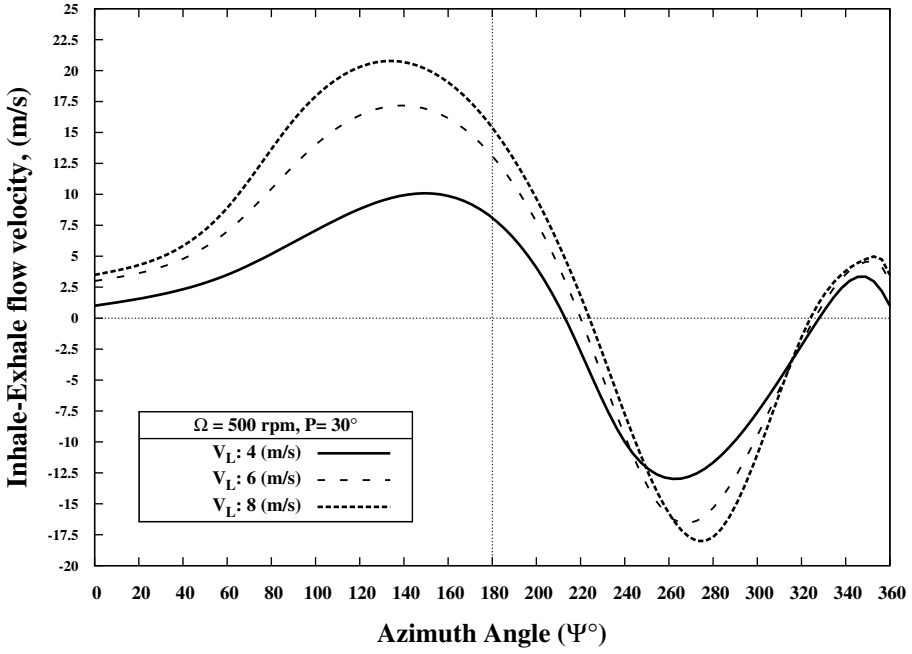

Figure 4.17: Comparison of inhale-exhale flow velocity distribution over a complete trajectory at 500 rpm and 30° under different lift-up speeds.

4.5.1.3 Thrusting Mechanism

In order to evaluate the thrust mechanism at each of the operating conditions, the resultant of horizontal and vertical forces must be calculated at each of these conditions, correspondingly. A distinctive module of the current study is the continuously tracking procedure of blades and flow on the whole circular trajectory. In fact, this method gives a clear vision of where might be the possible regions of minimum and maximum force productions. These precise point to point data measurement will play the decision making role in ANN analysis for proposing optimum states of operation.
Figure 4.18 reveals a comparison of horizontal force distribution of a cyclorotor operating at three different phases. At a constant condition of 30° and 600 rpm, the horizontal force distribution of hovering-state, forward speed of 10 $m/_S$ and lift-up speed of 4 $m/_S$ are illustrated herein. In principle, hovering state distribution gives a base definition to interpret the other two phases. The profiles of forces in this plot (Fig.4.18) express an important issue in force peaks in different flight modes. Indeed, it declares that the most Significant distinction is the lead or lag of peaks while comparing different states. Although there exist variations in their magnitudes, the peaks are following similar approaches. As is seen, the hover-state horizontal force peaks happen, roughly, at $\approx 30^\circ \leq \Psi \leq \approx 70^\circ$ and $\approx 140^\circ \leq \Psi \leq \approx 250^\circ$, whereas the peak distributions for forward mode occurs at regions of $\approx 20^\circ \leq \Psi \leq \approx 60^\circ$ and $\approx 260^\circ \leq \Psi \leq \approx 350^\circ$ and the same profile for lift-up mode sits between $\approx 20^\circ \leq \Psi \leq \approx 80^\circ$ and $\approx 200^\circ \leq \Psi \leq \approx 320^\circ$.

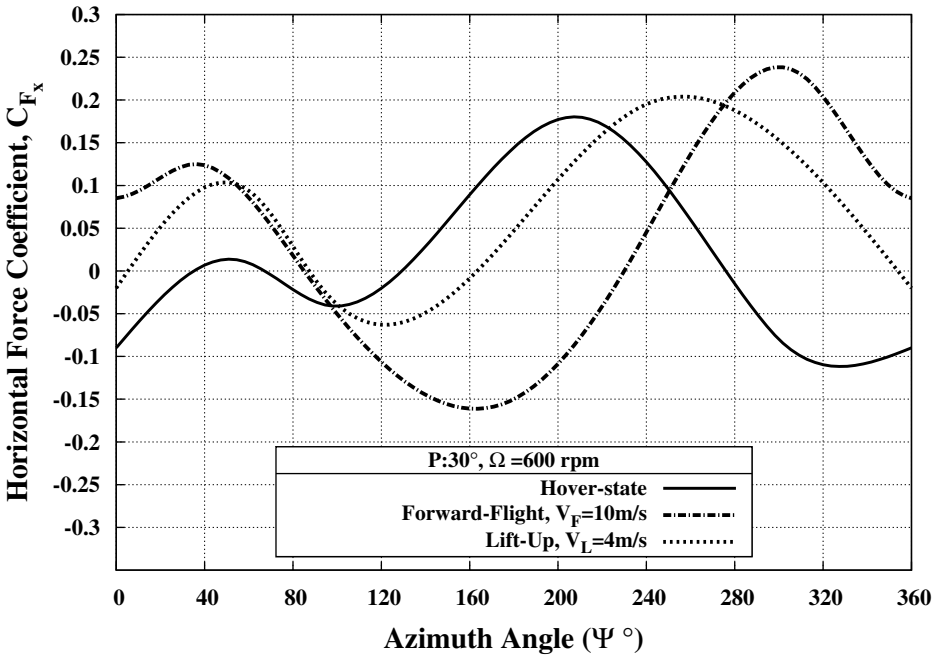

Figure 4.18: Comparison of horizontal force coefficient distribution over a complete revolution in different flight phases of hovering, forward-flight and lift-up phase at constant rotating and pitching conditions.

Comparing vertical force distribution (see Fig.4.19) of the cyclorotor while operating in different modes but modeled the same conditions as illustrated for Fig.4.18, again it is visible that the principal discrepancy, among the force distribution in different modes,

are the lead and lag of force productions according to the azimuthal angle. For instance, the hover-state vertical force peaks occurs at $\approx 60^\circ \leq \Psi \leq \approx 100^\circ$ and $\approx 210^\circ \leq \Psi \leq \approx 330^\circ$, whereas the peaks for forward mode occurs at regions of $\approx 40^\circ \leq \Psi \leq \approx 140^\circ$ and $\approx 300^\circ \leq \Psi \leq \approx 360^\circ$ and the same profile for lift-up mode lays between $\approx 50^\circ \leq \Psi \leq \approx 130^\circ$ and $\approx 220^\circ \leq \Psi \leq \approx 350^\circ$.

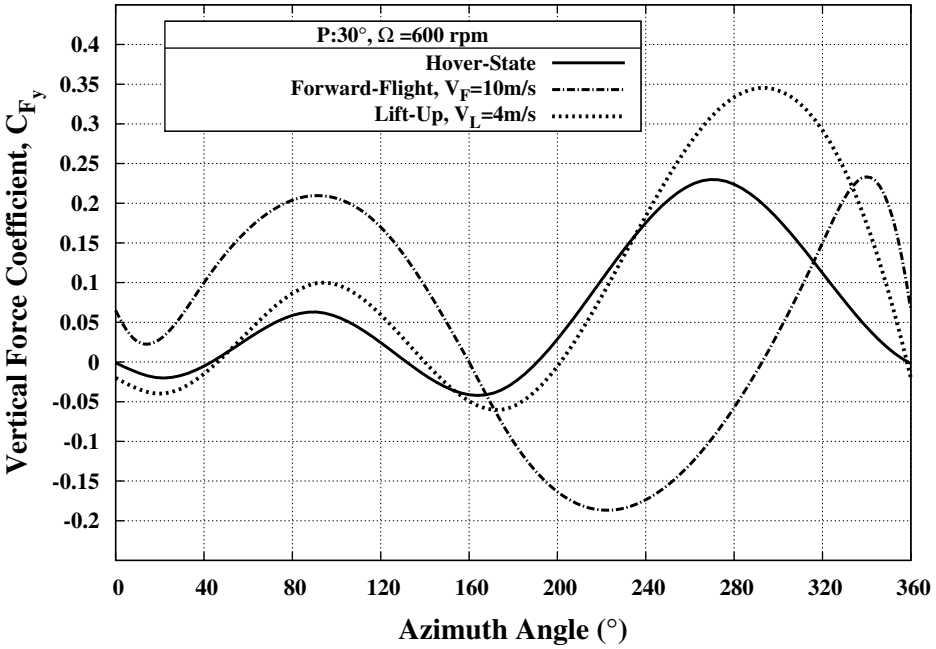

Figure 4.19: Comparison of vertical force coefficient distribution over a complete revolution in different flight phases of hovering, forward-flight and lift-up phase at constant rotating and pitching conditions.

These were a constant operating condition comparison for three different modes of flight, just to give a better insight on the differences in force production regions while being subjected to different flight modes in cyclorotor. Consequently, the whole computations and database from all operating conditions, and flight phases, are considered for the ANN analysis in order to obtain optimum operating states.

4.5.2 AC-ANN Analysis

Regarding to the core concept of the present work which is to actively control the dynamics of cycloidal rotors, the artificial neural network methodology is utilized for the data analysis and optimization process. The main attempt is to move beyond the restrictions of constant pitching assignments, in each cycling revolution ($0^\circ \leq \Psi \leq 360^\circ$), in order to achieve higher efficiencies and controllability. As it became clear from previous section, each single traversing point has its unique behavior at each operating condition. Thus, an active optimizing procedure would be beneficial in order to run the rotor at its optimum efficiency at all times.

According to the exact azimuthal location of the blade in cycloidal rotor, its angle of attack (AOA) could be extracted from Eq.4.11 as was presented by Tang et al.(Tang et al. 2015):

$$\theta(\Psi) = \left[\left(\frac{\theta_{(top)} + \theta_{(bottom)}}{2}\right).\sin(\Psi) + \left(\frac{\theta_{(top)} - \theta_{(bottom)}}{2}\right)\right] \quad (4.11)$$

that $\theta(\Psi)$ presents to the local AOA, $\theta_{(top)}$ and $\theta_{(bottom)}$ describe the AOA of blades when traversing through the top- and bottom-most positions in cyclorotor as Ψ=90° and Ψ=270°, respectively.

The novelty of present work is the ANN contribution to increase the operational efficiency, by actively controlling the dynamics of blade pitching oscillations. The ANN approach, for current UAV-size cycloidal rotor, is employed for operational optimizations. Therefore, a vast dataset is involved from the numerical postprocessed results to be used in algorithm training approach.

To better illustrate the oscillating strokes, all the cycling sequences of the blade in a complete route are clearly shown in Fig.5.1. As is depicted, the blade is opening outwardly in the first quarter, which is abbreviated as EUS (external up-stroke) and it lasts up to the top-most location at Ψ= 90°. Approaching to the left quarter in the top half, the blade is downwardly reversing the cycle direction which is shown as EDS (external down-stroke). The blades experience inward shifting while passing through the bottom half of rotor. The quarter between Ψ= 180° to Ψ= 270° in counter-clockwise direction is called internal up-stroke region which is assigned with IUS and, eventually approaching to the last quarter (bottom-right quarter), the blades follow back to their initial state with an internal down-stroke calling IDS.

To actively control the oscillating dynamics of blades in cyclorotor means to potentially alter the blades pitch angle in accordance with the different operation states. Obviously, considering a single blade as traversing a single cycloid revolution, it shows different efficiencies at each point of azimuth angle, due to the complicated flow phenomena acting in this propulsion system. This fact particularly clarifies that at each specific position, a certain angle can provide higher enhancements during operations. Thus, instead of assigning constant pitching angle for the operations where the blades normally oscillate twice per a cycle, the blade can actively operate at angles corresponding to best performing pitching oscillation.

So, a combination of data from various parameters and values was derived and assessed in different arrangements of operating conditions, in pitching angles, and in rotating speeds for each of these two flight modes. Generally it is intended to not only provide a view of the efficiency scales, but also to track in detail the blades during the whole circular trajectory, and gain a better insight on the flow behavior.

4.5.2.1 Forward-Flight

In accordance with the illustrations given on the ANN approach, and the methodology of actively controlling the pitching oscillations, the optimization process is accomplished on both forward state and lift-up phase of the operating cyclorotor. An optimized oscillating schedule of blade, in a complete tracing 360° azimuth route, is presented in Fig.4.20. This

plot typically shows the proposed active control pitching oscillations for 10 and 20 $m/_S$ forward speeds, including 500 and 600 rpm rotational speeds for each. At the locations of Ψ=0°, 180° and 360°, the vertical lines are addressing the 0 degree AOA while passing through these points.

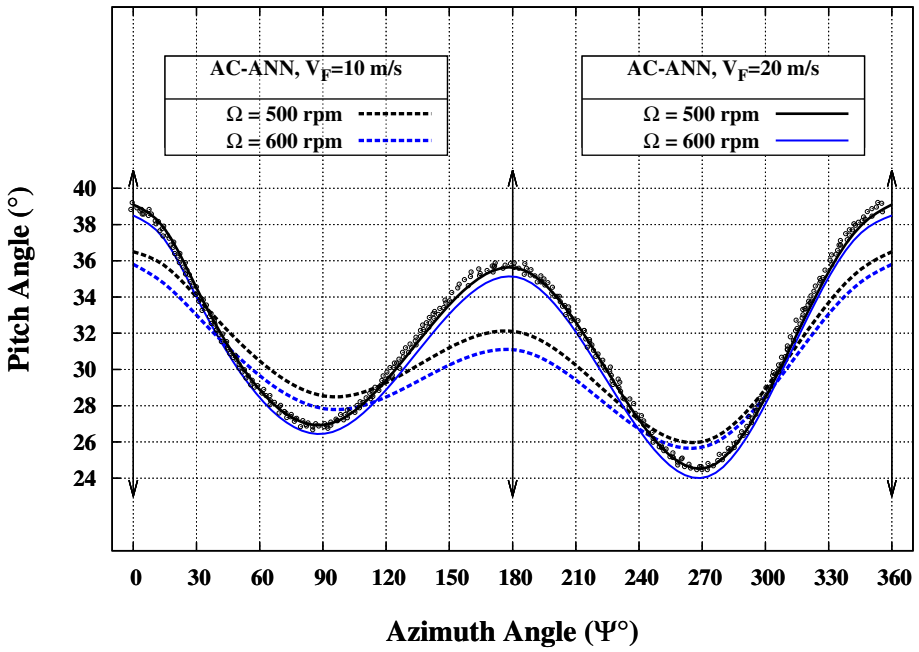

Figure 4.20: Optimized pitching curves proposed in ANN active control analysis for forward-flight mode in two different velocities and rotation speeds.

In the following we highlight from this diagram the forward-flight optimization process:

1. The quarters and strokes that the blade experiences in forward-flight mode can be cyclically sub-divided as:

   i) A continuous slow-down of EUS and IUS speeds are proposed from ANN as the blade moves through the first and third quarters, between $0° \leq \Psi \leq 90°$ and $180° \leq \Psi \leq 270°$, respectively.

   ii) While approaching toward Ψ= 180°, in the second quarter, and also between $270° \leq \Psi \leq 360°$ in the forth quarter, speed-up for EDS and IDS speeds are proposed from the ANN active control.

2. For both forward speeds in Fig.4.20, the lower rotation speed is proposed to operate at a slightly higher pitching angle compared with the higher rotation speed.

3. Higher forward speed is subjected to sharper incident changes and operate at higher oscillation values.

4. In all operating conditions the blades are proposed to experience roughly 2° lower AOA at bottom-side ($\Psi \approx 270°$) as compared with the top-side point at Ψ=90°.

As one the primary parameters in efficiency measurements is the figure of merit (F.M)

which comprises in evaluating both disk loading (D.L) and power loading (P.L) as follow:

$$D.L = \frac{T_N}{A}, \quad (4.12)$$

and

$$P.L = \frac{T_N}{P_N}, \quad (4.13)$$

and F.M is described as a function of both D.L and P.L in accordance with the following relation:

$$F.M = \frac{PL\sqrt{DL}}{\sqrt{2\rho}}, \quad (4.14)$$

where ρ is the air density. As an important scale of evaluating the aerodynamic efficiency of the cyclorotor, F.M plots are depicted in Fig.4.21 for forward-flight operating mode at three speeds of 10, 20 and 30 $m/_S$. These F.M values are the optimized values after ANN analysis and proposing active schedule for pitching oscillation.

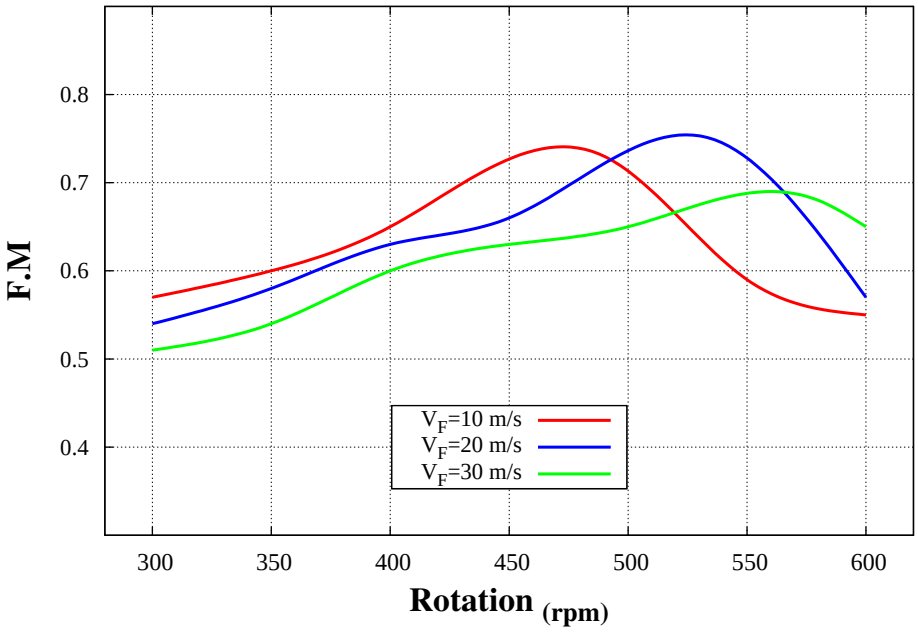

Figure 4.21: Figure of merit (F.M) for forward-flight operation, at a constant pitch oscillation angle of 35°, and in a range of rotation speeds proposed by the AC-ANN for different forward speeds.

It can be concluded from Fig.4.21 that at 10 $m/_S$ speed, the optimum reachable F.M value, according to the optimized pitching oscillations from ANN, can be nearly 0.74 at 475 rpm rotational speed, whereas, for 20 and 30 $m/_S$ the maximum F.M values are 0.77 and 0.69 at 530 and 570 rpm, respectively. It is also depicted that by increasing the forward speed more than 20 $m/_S$ causes a reduction in operating efficiency. As a matter of fact, ANN analysis is merely proposing higher efficient operating states according to the database

analysis and optimizations.
It must be noted that all current numerical predictions, ANN analysis and optimizations proposed here, are for a specific UAV-type cyclorotor with the properties which are defined in Tab.4.1.

4.5.2.2 Lift-Up

Lift-up phase operations are also analyzed using an ANN approach similar to the optimizations discussed in forward-flight mode. The continuous pitching schedules over a complete circular route is also proposed by ANN for two lift-up speeds in Fig.4.22. The local pitching oscillations for a single blade operating at two rotation speeds of 400 and 500 rpm, at each of 4 and 6 $m/_S$, are plotted in this figure.

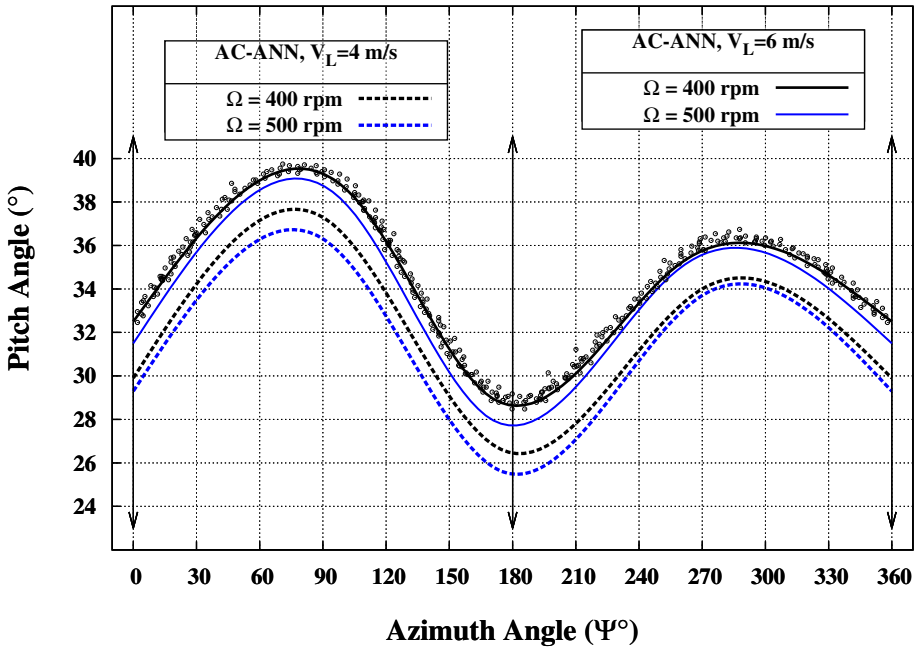

Figure 4.22: Optimized pitching curves proposed in ANN active control analysis for lift-up mode in two different velocities and rotation speeds.

Here are the most important points interpreting from Fig.4.22:

1. Likewise in forward-flight mode, the blade strokes can be distinctive in four quarters:

   i) A continuous increase in the rate of up-stroke speeds are visible for the first and third quarters in EUS and IUS. This increase in the first quarter continues to $\Psi \approx 80^\circ$ and for the third it continues up to $\Psi \approx 290^\circ$, respectively.

   ii) The second and forth quarters are proposed to decelerate the rates in EDS and IDS speeds in active control optimizations.

2. For both lift-up speeds in Fig.4.22, the lower rotation speed is proposed to operate at higher pitching angles compared with the higher rotation speed which was the same for forward speeds.

3. Higher lift-up speed is subjected to higher rate changes in oscillations and is proposed to operate at higher pitch values.

4. At all operating conditions, the blades are experiencing ≈3° higher pitching peak at the top point compared with bottom-side position.

According to the F.M plot showing in Fig.4.23, the efficiency comparisons for three lift-up speeds of 4, 6 and 8 $m/_S$ are illustrated. A wide range of rotational speeds from 300 to 600 with 50 rpm intervals is considered as well. So, in accordance with the optimized pitching schedules corresponding to rotational and lift-up speeds, the F.M is the estimated aerodynamic efficiency of the cyclorotor while operating in the proposed schedules in active control.

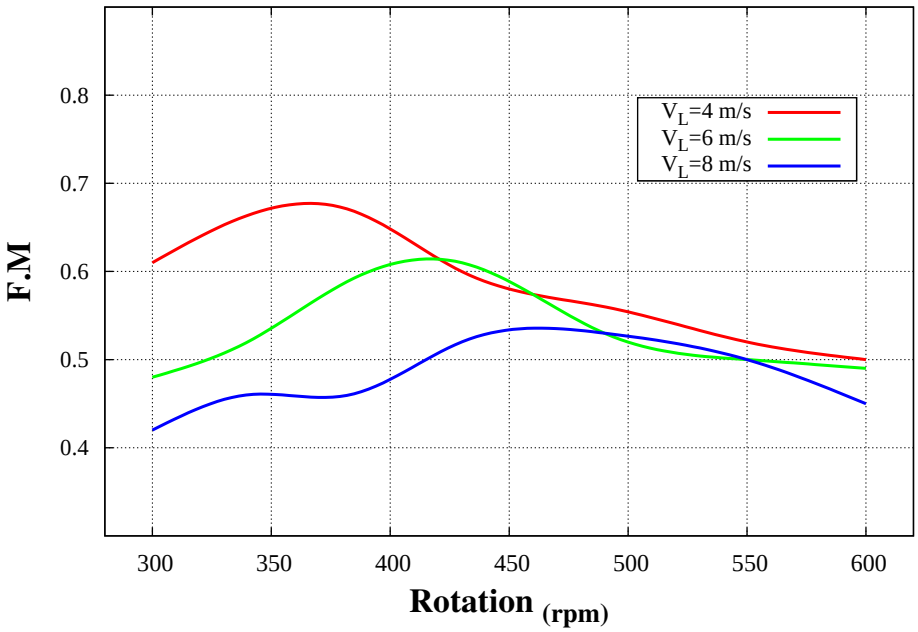

Figure 4.23: Figure of merit (F.M) for lift-up mode at a constant pitch oscillation angle of 35° and in a range of rotation speeds proposed by AC-ANN for different forward speeds.

The higher efficiency of the cyclorotor operating at 4 $m/_S$ lift-up speed with 370 rpm rotation is clearly visible in Fig.4.23. It is also seen in this plot that increasing the lift-up speed causes considerable reduction in the operating efficiency. By the way, as the lift-up speed increases, the optimum rotational speed also goes higher correspondingly. The optimum rotating speeds, for 6 and 8 $m/_S$ lift-up speeds, are proposed to be respectively at 420 and 470 rpm as presented in Fig.4.23.

4.6 Conclusion

A combined collaboration of numerical simulations joined with neural network analysis is illustrated in present chapter. The study is conducted with the aim of optimizing the operating states in a UAV-size cyclorotor for lift-up and forward flight phases. The procedure herein undertaken is to sequentially track the blade and flow in a complete route of

360° trajectory. In doing so, CFD predictions have been accomplished for a range of operating conditions (pitching angles and rotation speeds) in both forward-flight and lift-up modes with different horizontal and vertical speeds, respectively. Subsequently, using the achieved database from CFD post-processing, to train the ANN algorithm, active control optimization analysis was proposed on the second phase. A list of findings from both CFD results and ANN analysis are summarized here:

1. CFD;

    i) Forward-Flight:

    a) The arc between $\Psi \approx 90^\circ$ and $\Psi \approx 280^\circ$ is predicted for the inhale region, and the rest belongs to the exhaling part. These regions do not significantly change for different horizontal speeds.

    b) Higher pitching angles induce higher flow velocities at constant rotational speed. Likewise, higher forward speed causes higher values of the induced flow velocity.

    c) In both horizontal and vertical force distributions, forward-flight shows more deviation from those of hover-state force curves. However, they follow the same peaks and oscillations as the hover mode does.

    ii) Lift-up:

    a) This phase has shown very similar behavior as hover-state operation. It was presented that merely one third ($210^\circ \leq \Psi \leq 330^\circ$) of the circular trajectory belongs to the exhale arc and from the rest area the flow is inhaled by the cyclorotor.

    b) Higher pitching angles induce higher flow velocities at constant rotational speed. Also, same as forward mode, higher lift-up speeds result in higher values of the induced flow velocity.

    c) Force distributions in this phase is much closer to the hover-state force curves. Furthermore, they follow the same peaks but with a small variation in the values and a lag in azimuth angle.

2. AC-ANN;

    On the basis of the attained results, and collected database from CFD simulations, the neural network proposed the following items to active control the operating mechanism, in order to achieve higher efficiency levels:

    i) Forward-Flight:

    a) The strokes of EUS and IUS are assigned to happen with decreased rates, whereas the EDS and IDS are proposed to speed-up while passing the strokes in forward-flight. Top-side point is experiencing about +2° higher AOA compared with the bottom-side position.

    b) At constant forward speed, the lower rotation speed is proposed to operate at higher pitching angles and vice versa. Furthermore, higher forward speeds are subjected to sharper incidents of strokes while traversing.

c) The optimum state for forward-flight is assumed to be with 20 $m/_S$ at 570 rpm and active pitching schedule using ANN which results in 0.77 F.M value.

ii) Lift-up:

a) The strokes rates is proposed to happen conversely of in lift-up phase. Meaning that the strokes of EDS and IDS are assigned to pass with decreased rates, while EUS and IUS are proposed to speed-up. Top-side point is experiencing about +3° higher AOA compared with the bottom-side position.

b) Likewise in forward-flight, the lower rotation speed is proposed to operate at higher pitching angles at constant lift-up speeds. Moreover, higher forward speeds are subjected to sharper incidents of strokes while traversing.

c) For lift-up phase, the optimum operating state among three vertical speeds is proposed with 4 $m/_S$ at 370 rpm which brings 0.67 of F.M value.

This study is suggesting the mutual collaboration of CFD simulations and neural network analysis in order to reach higher operating efficiencies in cyclorotors. The active control concept can be further investigated for future real tests to reveal a detailed understanding of the controlling needs, the feasibility of mechanical means to actively change the oscillation schedules and to obtain a practical insight while the cyclorotor is functioning as a thruster for VTOL aircraft in forward-flight and lift-up phases are yet to be fully developed.

Chapter 5

Vertical Take-off and Landing Performance at Near-Ground Levels

[1]

5.1 Overview

The tendency to equip aircraft with cycloidal rotors as means of Vertical Take-Off and Landing (VTOL) propulsors has increased in recent years [2]. Considerably lower noise production and more stable hover and vertical displacements in comparison with those of conventional screw propellers, as used in helicopters, are the main reasons to witness this tendency.

Aircraft being capable of VTOL and hover are increasingly emerging in various critical and routine applications. Rescue missions in roads and environmental disasters, observance and monitoring-based carriers, surveillance cameras, payload carriage in situations like transmitting forest tree are, just to mention a few examples. Within VTOL category, numerous designs have been proposed along the years. Helicopters are the most typical crafts in this kind, but concerning the thrusting mechanism, several alternatives are yet in hand. Nevertheless, each of them has their own strength and weakness points, thus, one should select a design to utilize it toward the desired output and try to overcome the drawbacks and sophistication in this regard.

This chapter deals with the cycloidal rotor which was initially introduced as a novel conceptual design of propellers by a German origin researcher Fredric Kurt Kirsten. His collaboration with Boeing company then led to Kirsten-Boeing propellers reported in 1926 [3]. This was considered as the onset of a new practical generation of blades operating in a cage-like assemble which was totally different from those of conventional propellers, in terms of exerting all sections of blades in span-wise direction a fairly equal action into the fluid. There exist some research reports concerning cyclorotors within the first two starting decades until 1940s. It was by then the subject of many research that was afterwards lost for a long period of about 50 years. In an effort from BOSCH Aerospace incorporation in 1998, the operational efficiency of a UAV size cyclorotor was examined and built using modern methods and knowledge. With their full-scale design, the most astonishing feature of their report was the considerably low noise-pollution characteristic of the current operating mechanism [4]. The advent of more efficient coding and computing resources made the numerical investigations on this state of the art complicated mechanism more

[1] Based on the work published in the Journal of Aerospace Science and Technology, https://doi.org/10.1016/j.ast.2019.105495, and, SAE International Journal of Advances and Current Practices in Mobility, doi:10.4271/2019-01-1872

feasible since the era of late 20th century. In Japan, Onda et al. [5] whose work was mainly on Lighter Than Air (LTA) vehicles, like airships, have also started to utilize the cycloidal rotors in their configurations instead of conventional propeller-type thrusters. It actually was a modified prototype of ACROSTAT airship design which was previously reported [6]. Fast functioning and better control-ability due to employing these rotors were the attained enhancements observed in their design from what they have declared with conventional propellers [7, 8, 9].

Parametric optimization of cyclorotor is being pursued by Hwang et al. [10, 11]. They intended to track the optimizing steps from the very basic parameters like number of blades, sizes, radius, spar positioning within blades, number of plies by which the blades are coated, weight, etc, all considered simultaneously in their survey. Experimental tests, CFD approach and Genetic algorithm were some methods they worked with. In another work, which is being conducted both experimentally and numerically, the authors introduced a somewhat new design of the operating cyclocopter [12]. They have equipped the craft with four functioning rotors acting in two pairs, with each of these running on opposite directions to counteract the resultant undesired torque. Their design intended to provide up to 166 N thrust. Their experiment showed up about 15 percent higher power consumption than the design expectations. In spite of unstable vertical flight control, they have indicated that a praising achievement was attained in hovering regime.

In an article in 2005, Yun et al.[13] performed a predominantly analytic study in order to reveal a clear insight of how to determine the thrust vectoring in cycloidal rotors. They applied ”eccentricity” in both terms of magnitude and phase angle in their parametric designs. Applying eccentricity to the operational process enables the controlling mechanism to actively shift the resultant thrust vector to the desired direction. One of the main studies can be attributed to [1] and a complementary in [14], which was accompanied by experimental, numerical and analytical investigation on a typical UAV type cyclocopter. Prior to carrying out the tests, they have gone through analytics to identify the rotor specifications which would best fit in terms of performance for a UAV by using a modified version of Stream-tube model for a more accurate response in cyclorotors, this was initially developed for Darrieus wind turbines [15]. Thus, they have manifested the following five major results drawn from their study pertinent to the dominant flow acting through the rotor:

1. The inflow velocity at 0° and 180° of azimuthal angles is about zero.

2. The inflow moves vertically downward when passing the top half circle, and deflects towards the rotation direction as it passes the bottom half circle path.

3. If considering counter-clockwise direction and giving positive and negative signs to the inflow and outflow, respectively, the arc between 0° to 270° in azimuth is positive and from the latter up to 360° consists predominantly of negative sign.

4. The occurrence of tilted downwash while exiting the rotor stems from the inherent

flow behavior from within the rotor itself.

5. Another very important finding was that the curvilinear pattern of the exerted flow, to the cyclorotor, results a cambered-like behavior in the blades whereas in fact, they are all symmetrical. This issue is assumed as the key source of higher lifting force attained from bottom half of rotor compared to the top one.

Ilieva et al. [2, 16] have surveyed an overview on the diverse propulsion mechanism being proposed over the years, especially on airships till recent modern innovations. They came to clarify the benefits and drawbacks of these propelling systems in terms of functionality, operating efficiency, power feeding and so on. They also introduced the MAAT project being held in European Union, a major project on high altitudes airships. Several studies indeed have been applied on different rotor-thrusters in aircraft [17, 18] which the interactions of blades or propellers are making significant impact on the overall efficiency of the crafts, like what also happens in cycloidal rotors.
A historical review of the publications and reports specifically on cyclorotors or cyclogyro designs has been filed in 2009 by Curtis et al. [19]. Further, Benedict et al. [20, 21] in university of Maryland conducted extensive research on MAV scale cycloidal rotor crafts both experimentally and numerically. In one of their studies they have presented a relatively light MAV design flying with double-counter rotating 3-bladed cycloidal rotors in sides, with a total 290 g craft net weight. They performed detailed tests while considering various parameters such as different blade profiles, blade thicknesses and different sizes in further investigations.
Gagnon et al. [22, 23, 24, 25] have also conducted detailed investigations from an aerodynamic and aeroelastic point of view. In their former referred article, they conducted that a 50 percent input power reduction will be achieved if the cycloidal rotor is replaced with conventional tail rotor of a helicopter. They effectively used different approaches as CFD, analytical models and theory to deeply study numerous featuring parameters in cylorotors. Blade number, rotation speed, rotor sizing, blade flexibility and pitching schedule were brought into consideration as variables to study. In terms of flexibility of blade profiles, they stated that it can not lead to better aerodynamic improvements, to reduce the rigidity of profiles since blades deform, their effective AOAs change accordingly and, thus, efficiency drop is evident in their analyses as well. Stability analysis of a modeled rotor was also the topic of a joined numerical and analytical work from Navazi and Hojjati [26]. Under CROP title, a European Union project [27] was developed on cyclorotors, Leger et al. [28, 29] attempted to analytically evaluate and study different working principles of a cyclorotor in hover state. Study and calculations of mechanical means for pitching motions, eccentricity variations, optimum mechanical dimensions, angular velocities and efficiency comparisons of their optimum design has been performed for BOSCH, IAT21 and Seoul National University design. In a further numerical modeling [30], Leger and his colleagues targeted 3D effects presence, specifically in the region between the endplates and the propeller tip, where flow leakage is more imminent. CROP project report was then issued by [31]. Within the same project, Xisto et al. [32] brought to study the feasibility

assessment of employing Dielectric Barrier Discharge (DBD) plasma actuators in cyclorotors. They aimed to consider the stall conditions where pitching amplitudes exceed a critical value and separations occurs and thus flow losses become inevitable. They reported that applying DBD was not an effective method to delay stall occurrence but showed great performance in resulting into a higher level of lift coefficient in the downstroke portion phase. DBD plasma actuators are still susceptible to be the subject of further detailed study, although a much better understanding of the existing complexity in cyclorotor flow behavior is vitally important.

The issue of ground effect has been the target of some researchers as are presented in [33, 34, 35, 36, 37]. The attempt was to study the effects of ground hight level (static and dynamic) on the flight means. These articles have been conducted in several approaches of experimental, analytical and numerical simulations to study the ground effects on different geometries from canard, wings and different airfoils. These studies are definitely important since the subject of the current study also concerns the ground effect in several operating conditions and heights to predict the optimum functionality of a typical UAV cyclorotor. In [33], they studied the operating status of a combination of wings and and tail, concerning the ground effect and their relative positions. They proposed a mathematical model by which the aerodynamic optimization of wing-in-ground (WIG) craft could be possibly predictable.

Important to mention that the environmental effects are that essential in some essence that even the ceiling effects are also becoming the target of investigations like the study of Kocer et al. [38] in a VTOL UAV quadrotor.

In a comprehensive study carried out both experimentally and numerically from Yu et al. [39], forward flight efficiency has been the main research subject. They featured the effects of advance ratio and blade numbers as the influential parameters. The authors indicate that reaching the same efficiency as the screw propellers is feasible in cyclorotors for flights. 3 and 4-bladed cyclorotors showed the best obtained efficiency in terms of blade numbers. As they have declared, the more blade numbers, the less vibrations and better mechanical efficiency. They achieved higher efficiencies with moderate to high advance ratios. Moreover, the blade vortex interactions (BVI) become less in higher advance ratios.

The performance of seven turbulence models were studied by Singh and Pascoa [40] on a single blade oscillations of a cycloidal rotor. The authors the accuracy of the results obtained and performed a comparison among all with the experimental results. They have stated that SST-SAS and SAS were the two models being capable of better capturing and predicting the flow. Their attempt was to study a single oscillating blade under pre-stall, stall and post-stall conditions. In a numerical analysis conucted by Rami an Pascoa [41] , they considered various oprating condition with pitching angles and rotating speed. In addition, their concern was to simulate and predict the optimum state of operating condition while in close distance with ground-surface level. They concluded different efficiencie could obtain while the cycorotor operates in different altitudes as a propulsion system of a VTOL aircraft.

The main focus has been laid on the operating traits of a cyclorotor-thruster aircraft in its vertical take-off and landing phases. Technically, these phases are always considered as critical modes in flying aircraft regardless of their type, whether are happening horizontally like in normal airplanes or vertically in helicopters.
As was indicated in a technical report from National Aeronautics and Space Administration (NASA) [42], cyclorotors are propulsors in which the downwash flow convects in a pile-like flow, shedding out from the bottom side of rotor. This concentrated massive volume of flow can undoubtedly play significant role on the overall functionality of a cyclorotor aircraft, especially in its close-ground level flying operations.
To the best of our knowledge, this is the first study conducted on cyclorotors that focuses on the taking-off and landing phases of an aircraft. A comprehensive numerical research enlightening the effects of a considerably wide range of parameters is involved in assuring its performances under these conditions. Six sets of vertical distances from the ground, three sets of pitching maximum oscillations and all each in three different rotational speeds of the cycloidal rotor are explored, in order to reveal a fairly appropriate understanding of downwash flow impact, in the case when the aircraft levels up its altitude, or vice versa, under ground effects.

5.2 The Cyclorotor System

5.2.1 Base Configuration

In a cycloidal rotor it is intended to rotate a group of blades (preferably located diagonally in pairs) about two different centers; One is the rotation about the rotor center, indicating the rotor rotation, and the other relates to the rotation of blades about their own pivot point or pitching center, which is termed as pitching oscillation. The centers in both axes are parallel to the blade span. The blades experience a repeated sequence while traversing a complete rotation, hence the current system is termed cycloidal rotor or shortly cyclorotor.
A typical view of the working principles in a cyclorotor is depicted in Fig.5.1. As is simply previewed, the principal concept is to rotate each propeller about the O and P centers, simultaneously. This harmony eventually exposes a sinusoidal cycloid curve in each blade while experiencing a complete round route. This fact can be clearly revealed while the top and bottom halves of the rotor are detached and sitting along each other as is shown in Fig.5.2. This statement is valid for rotors similar to the considered herein, in which the diagonally fronting pairs are precisely in the same certain angle of attack toward their passing direction. In the rotor sketch (Fig.5.1), the rotating direction is considered counter-clockwise and the maximum pitching angle is set to happen at the top and bottom extremes (azimuthal angles of 90 and 270 degrees). Noteworthy that these angles are not at all constant and may vary along a cyclorotor design. The directions, signs, blading styles and all arrows are just to lay a comprehensive pattern of the functioning procedure.

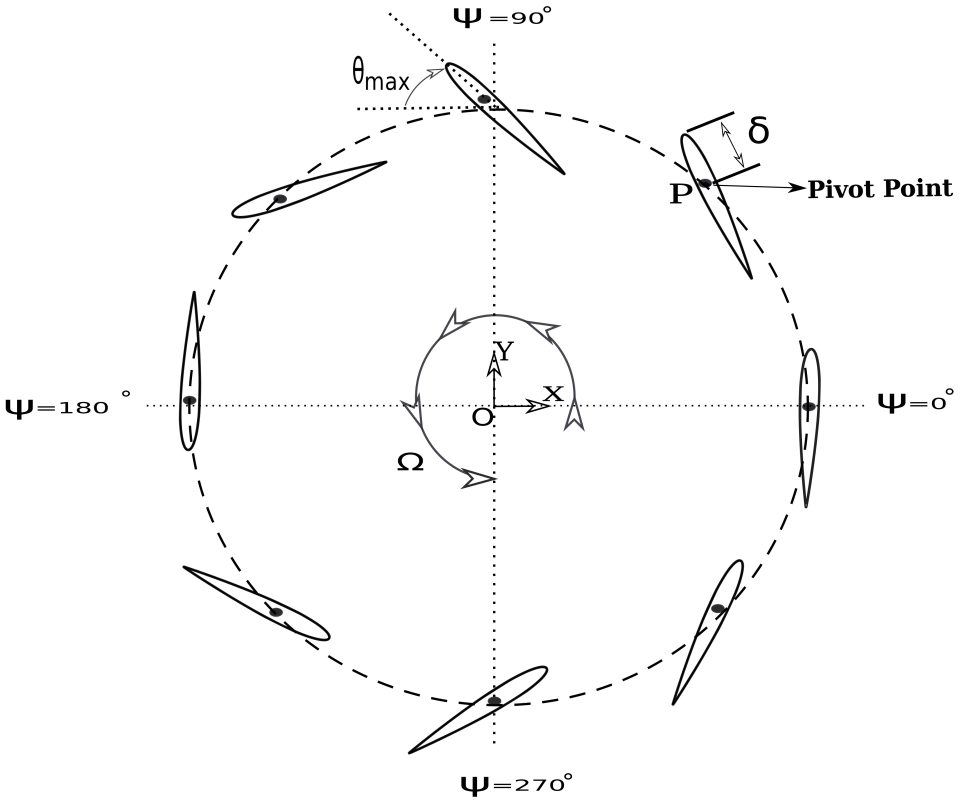

Figure 5.1: Schematic of the operating principles in a typical cyclorotor.

The specifications of the cyclorotor used in the current study include a rotor radius of 0.4 m, blade chord length of 0.15 m, pitching axis distance to blade trailing edge of 0.0525 m, span of 0.05 m, blade-chord to rotor-radius of $c/R = 0.375$, and the 6 blades (with NACA0012 profile) are equally positioned by 60° intervals roundly, and the solidity value is 0.3582. Solidity is a non-dimensional parameter showing what fraction of the rotor projected area is occupied with the presence of blades as is expressed in eq.5.1:

$$\sigma = \frac{N_b\, c}{2\,\pi\, R}, \quad (5.1)$$

where N_b refers to number of blades, c is the blade chord and R shows the rotor radius. Properties such as rotating speed, pitching altitudes and vertical distance of the rotor from the ground level are all variables through the simulations and are discussed in later sections.

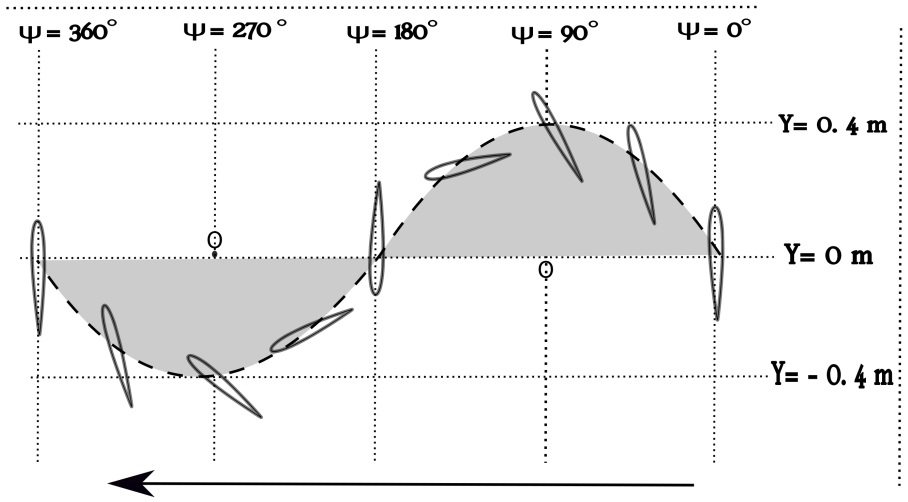

Figure 5.2: Sinusoidal trajectory of a single blade in one complete revolution.

Based upon the different traits appearing specifically in lift and drag, while an airfoil profile is changed, the use of camber on the propellers was also the subject of surveys in several reports. It is well substantiated that cambered profiles improve classical propellers efficiency through numerous applications, such as jet engines. However, cyclorotors are inherently disclosing an operation type in which each propeller experiences movements toward upward and downward, intermittently, per revolution. The airfoil top surface, while traversing the upper half cage region, changes to bottom surface in the bottom half and vice versa, but the existing criteria is maintaining positive AOA during the entire route. This fact consequently restricts the possibility of employing cambered airfoils in cyclorotors. A possible solution could be an active camber system, by which the desired curve can be applied and distort, in order for that the airfoils appropriately gain benefit from cambered characteristics.

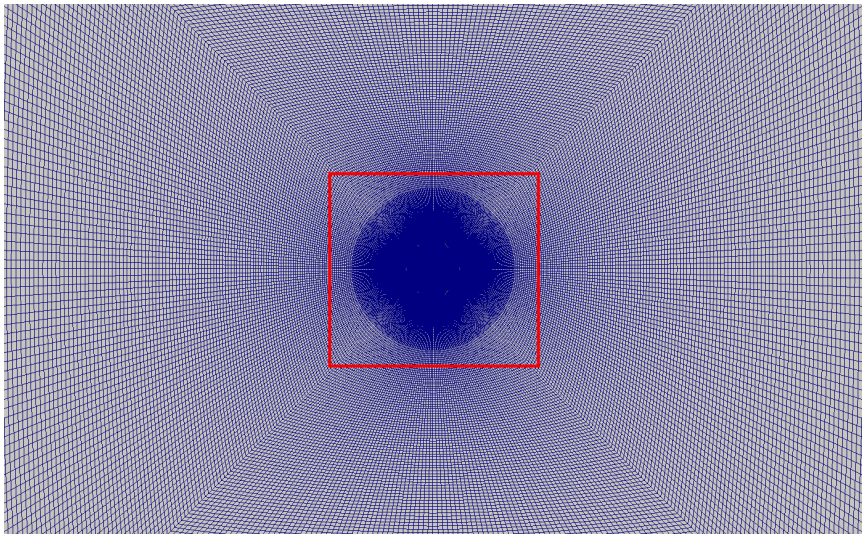

(a) Domain-Mesh View

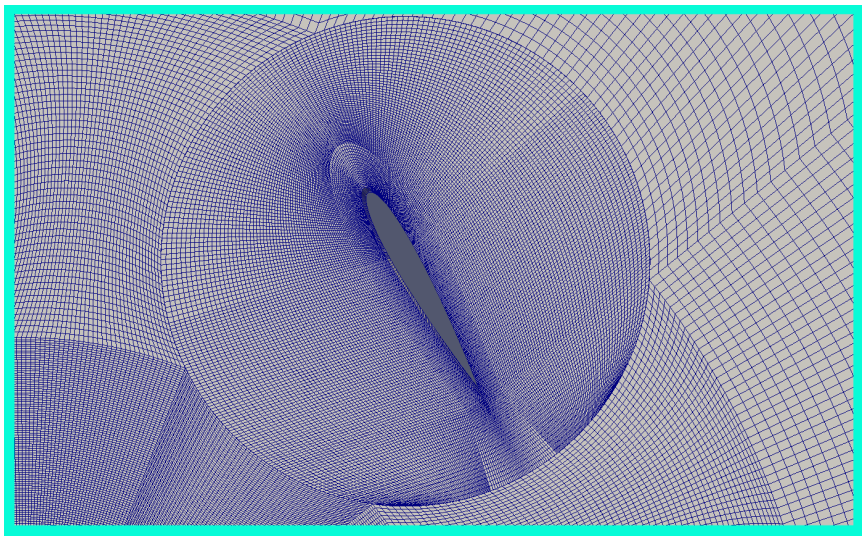

(b) Blade-Mesh View

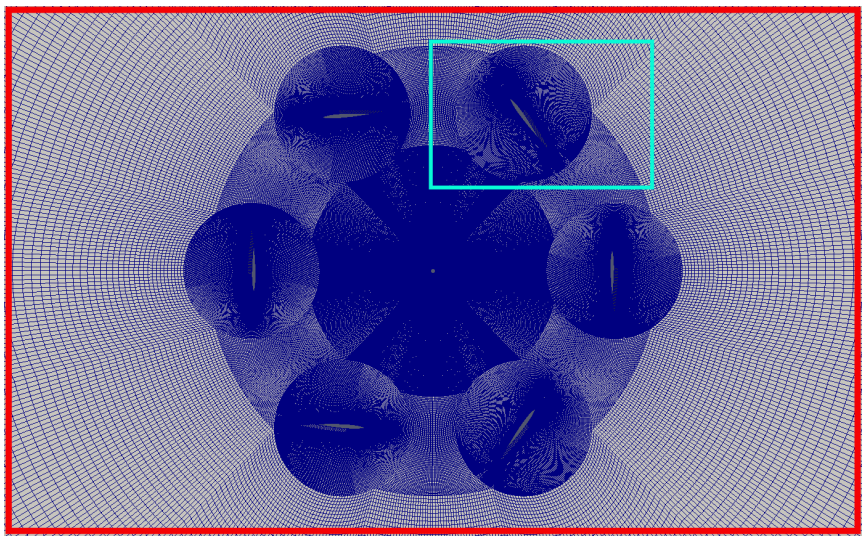

(c) Rotor-Mesh view

Figure 5.3: Mesh Configuration of the 6-bladed cycloidal rotor.

5.2.2 Thrusting Mechanism

Proceeding with the above-mentioned illustrations of the typical cycloidal rotor, the thrust mechanism, which is a critical component, should be revised. Thrust is a result of the contribution between rotating and pitching motions of the blades in this system. Zero AOA refers to when the blade chord-line is tangentially aligned to the circular rotation path and any deviation imposes a positive or negative value. This behavior has so far been controlled using mechanical means by defining an "eccentricity" so that pitching oscillations in desired magnitude and direction can be assigned. This happens by offsetting two variables: phase angle (ε) and magnitude (e) of eccentricity. According to this procedure, fairly instant shifts can easily be applied to the thrust vector direction, as is also declared by most related authors. It is recognized that there is a need for a much more efficient pitching mechanism, from dynamic control point of view, it sounds indispensable that a better active control be obtained and a considerably lighter mechanical load be imposed on the overall system.
The analyses presented herein are done in null velocity, the hover state of the aircraft is thus considered.

5.3 Numerical Methodology

5.3.1 CFD Solver Definition

The CFD solver being used in the current simulations is pimpleDyMFoam which comprises both PISO and SIMPLE algorithms using a finite volume method in OpenFOAM [70]. This solver can deal with mesh displacements and multi-moving regions in computational simulations. For the derivative terms of both velocity and pressure, Gaussian integration is used and for time derivatives a bounded first order implicit discretization scheme is chosen as well. The residuals are reached well below 10^{-5} confirming the convergence accordingly.

5.3.2 Turbulence Modeling

By benchmarking with the assessed experimental work [1], k-ε is able to fairly predict the overall operating state of the cyclorotor in terms of thrust, power and efficiency parameters. Thus, the same turbulence model was used for the validation part of current work as was suggested by the mentioned experiment study [1]. Concerning the comparatively large computational domain, besides accuracy, one should mindfully select the most efficient turbulence model, and consider the difficulties of performing a real Direct Numerical Simulation (DNS) or even Large-Eddy Simulations (LES) which might lead to huge computational costs. On the other hand, to better capture the wall effects the best solution is to use the k-ω-SST (Shear Stress Transport) turbulence model.
In principle, k-ω-SST features from its bi-functional merit. This two-equation eddy-viscosity turbulence model acts as k-ε model in normal free stream, however, it benefits from k-ω

model when resolving boundary layer and shear layer regions quite adjacent the wall surface.
Since the current study deals with a relatively large domain and it also simultaneously focuses the influences streaming from ground effects, k-ω-SST model is herein chosen which results in both lower computational run time and better accuracy.

5.3.3 Mesh Configuration

The computational domain is composed of 8 split sub-domains in order to separately simulate each of the 6 blades, the pure rotating region, and the huge stationary part, which constitute the majority of the whole domain.
The meshing methodology is fundamentally based on blockMesh utility within OpenFOAM. Due to the rather complex geometry, in terms of meshing a complete rotor, the Octave coding was exploited in order to construct the base blockMesh dictionary structure. Considering a two-dimensional plane, the geometry consists of about 750000 grid cells. Mesh adaptation is sequentially applied in order to reach an optimal mesh arrangement in terms of the results accuracy.
The resulting mesh configuration is such that the mesh density in the pitching-rotating region, around each blade, is nearly 90000 cells and about 6 percent of the cells belong to the stationary part, therefore the rest goes to the pure-rotating region of the rotor cage. As depicted in Fig.6.8, the configuration is composed of fully Hexahedral structured grids with the highest concentration around the moving parts, to efficiently resolve and capture the flow phenomena as the rotor operates. The value of y^+ is kept well below 0.15 on the blades surfaces.

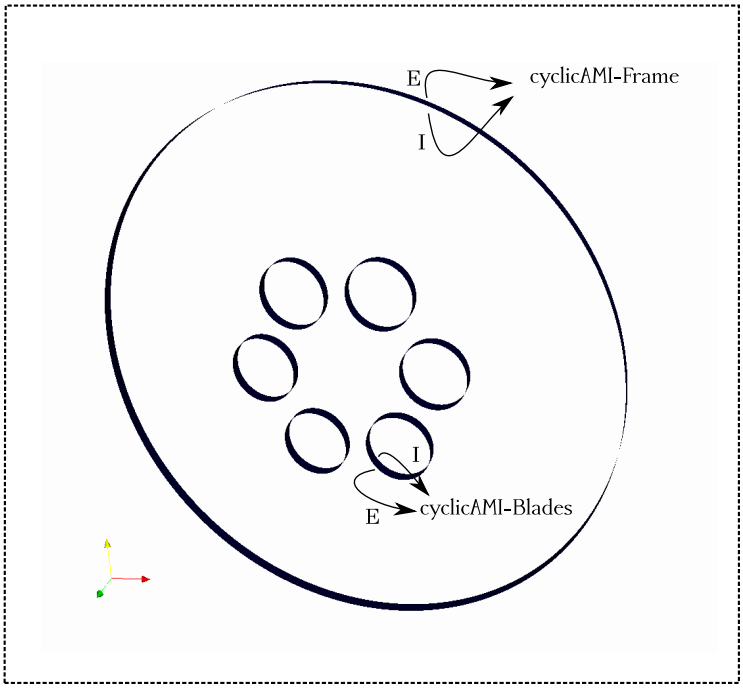

Figure 5.4: Sliding mesh interfaces in computational domain.

The element that separates each blade region part from the pure rotation domain is their

pitching motion in addition to that of rotation. Hence, to reasonably correlate and incorporate the regions, 14 cyclicAMI (Arbitrary Mesh Interface) [106] patches are defined accordingly by pairs among regions as shown in Fig.5.4 in such a way that the flow can pass in a logic manner through the whole domain. In this figure 7 circular interfaces are perspectively shown, each of them holds a pair at their corresponding boundary internally (I) and externally (E), where a very close distance ($2 \times 10^{-4}\ m$) is set as coincident gap between each pair (which is obviously impossible to distinguish from this shot (Fig.5.4)), with minimum matching tolerance of 1×10^{-8} which provides sufficiently accurate data transmission among sliding interfaces. The big circle, which circumferentially wraps the other circles is responsible for the pure rotational motion of the whole remaining cells inside this portion, while the outside domain is completely stationary, and the inner small circles introduce the pitching oscillations along with the rotation so that they provide pitching-rotating displacement. The distinction between the outer big circle with the inner small ones is that the former has just a single direction in clock-wise, or reverse, while operating. Whereas the latter experiences heading to both directions in each revolution, or cycle, which describes the inherent behavior of cyclorotors.
The domain covers about 15 times the rotor size in both positive and negative directions. This also happened toward the rotor upward direction in vertical plane, whereas the downward distance differs for several paces of taking-off and landing altitudes(see Fig.5.5). It is believed that the mesh configuration is extended large enough from all relevant sides so that trustful numerical results are obtained. The shortest length from floor level is 2.5 m which equates almost 2.5 times the rotor size. This length was considered as the landing level of the aircraft.

5.4 Vertical Take-Off and Landing

Since all turbomachinery systems are designed for specific applications, their design targets also differ. For instance in conventional propellers, used in helicopters, each spanwise position acts differently as approaching toward the tip with its maximum tangential speed. This actually sweeps the flow and disperse it out radially, whereas the functionality in cyclorotors is remarkably different from those of conventional propellers, since in these systems they exert fairly similar influence through the entire span. This key fact, accompanied with the specific operating fashion in cyclorotors lead to development the of a relatively concentrated outflow, rather than to dissipate it.

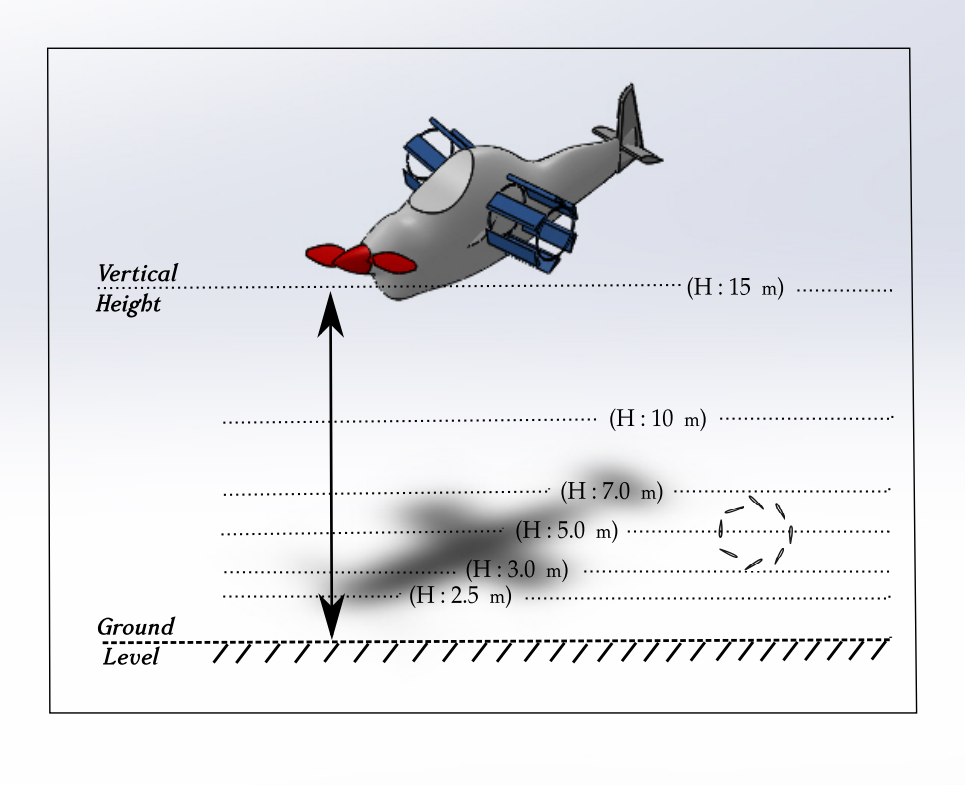

Figure 5.5: Cyclorotor altitudes in a typical aircraft.

To this end, it is worthy to identify the decisive influence of the resulted downwash outflow, particularly in cyclorotors. This issue has not been surveyed yet, especially in Take-off and landing modes of a cyclorotor-thruster aircraft to investigate the downwash impact, when craft is at a close and influential distance to the ground.
In this regard, the ground effect in the VTOL phase of a cyclorotor at 2.5, 3, 5, 7, 10 and 15 meter altitudes is studied as is exhibited in Fig.5.5. Furthermore, the effect of rotational speed and pitching variations were also considered for 200, 400 and 600 rpm and 20, 30 and 40 degrees, respectively, in each single set of altitude level.

5.5 Results and Discussion

5.5.1 Validation

To approach the desired properties as illustrated in the preceding sections, the first step was the validation of the CFD models with the relevant experimental tests. This part has been successfully done, by comparing the numerical results with those of Yun et al.[1]. These are experimental test results for 12 different simulations. These simulations cover 3 sets of pitching amplitudes for 20, 25 and 30 degrees and include 4 rotational speeds as 200, 300, 400 and 500 rpm successively in each pitching category. The results of the validation are shown and compared using the power coefficient (Eq.5.2) and thrust coefficient (Eq.5.3) as follow:

$$C_P = \frac{P_N}{\rho A (R\sigma)^3}, \quad (5.2)$$

$$C_T = \frac{T_N}{\rho A (R\sigma)^2}, \quad (5.3)$$

in which A indicates the projected area of the cyclorotor, defined as,

$$A = 2Rs, \quad (5.4)$$

where P_N, T_N are introducing net power and net thrust using correlations 5.5 and 5.6 respectively :

$$P_N = M\sigma, \quad (5.5)$$

$$T_N = \sqrt{T_H^2 + T_V^2} \quad (5.6)$$

where M and σ refer to momentum and rotational speeds and T_H and T_V are horizontal and vertical thrusts.

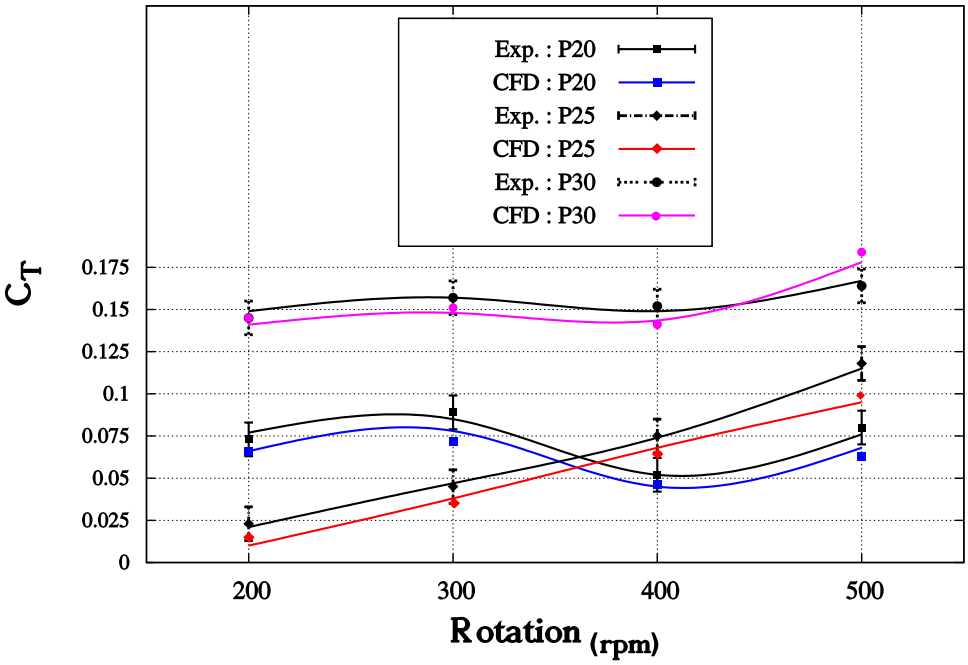

Figure 5.6: Validation using experiments of [1]: thrust coefficient vs. rotation speed.

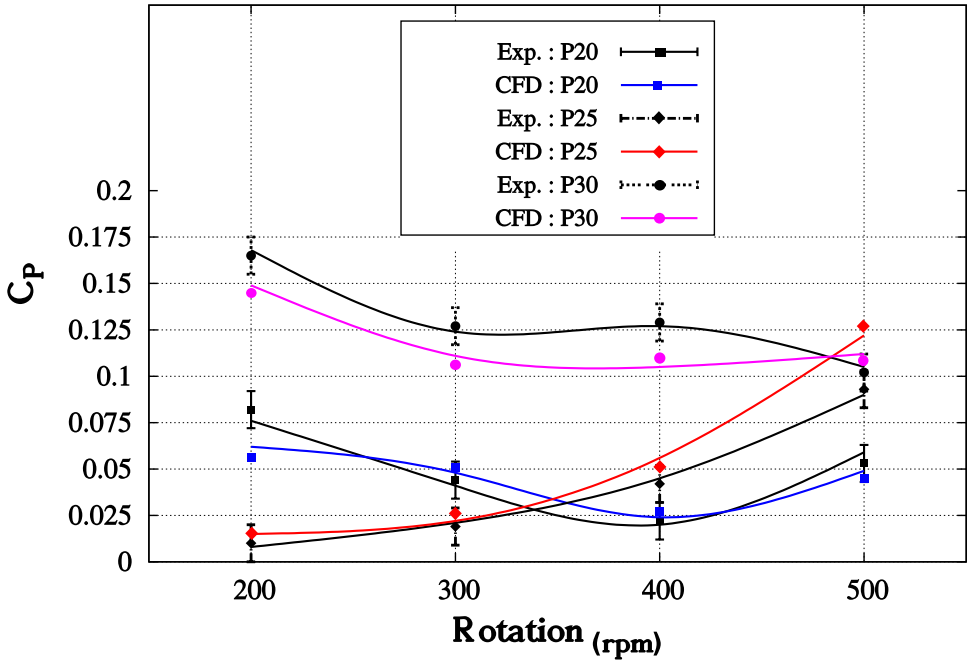

Figure 5.7: Validation using experiments of [1]: power coefficient vs. rotation speed.

As can be seen in figures 5.6 and 5.7, the comparisons reveal a considerably fair agreement between the experiments and the numerical results within the error margins. Even though the empirical correction factor k_{emp} has not been applied, the values derived from CFD predictions are noticeably close with real tests, specially in the thrust coefficient plot. The confirmation attained from these two plots, and other parameters, indicate that the models are accurate and other simulations can be freely conducted based on the same numerical solution methodology.

5.5.2 CFD Simulations of Cyclorotor-Ground interactions

The nature of the downwash flow through a cyclorotor is a pile-like stream, which significantly affects its functionality while in close distance to the ground. Through this work, an attempt is made to study the rotor behavior in several working conditions according to their relative distance from the ground level. Six height levels are chosen for the simulations with 2.5, 3, 5, 7, 10 and 15 meters, from the center of the rotors to the ground. Subtracting the rotor radius ($0.4m$) out of the altitudes gives us the actual distance from the bottommost point of the rotor to the ground surface. Thus, $2.5m$ actually corresponds to $2.1m$ distance to the ground level.
In the numerical tests, pitch angles of 20°, 30° and 40° were selected with 200, 400 and 600 rpm rotating speeds, and this whole combination have undergone simulations for each single vertical distance declared above. This could effectively clarify which strategy proposes a better operational outcome in these flight modes, especially in VTOL phases. Rotating speeds represent frequency values of $3.\overline{33}$, $6.\overline{66}$ and 10 Hertz, respectively.

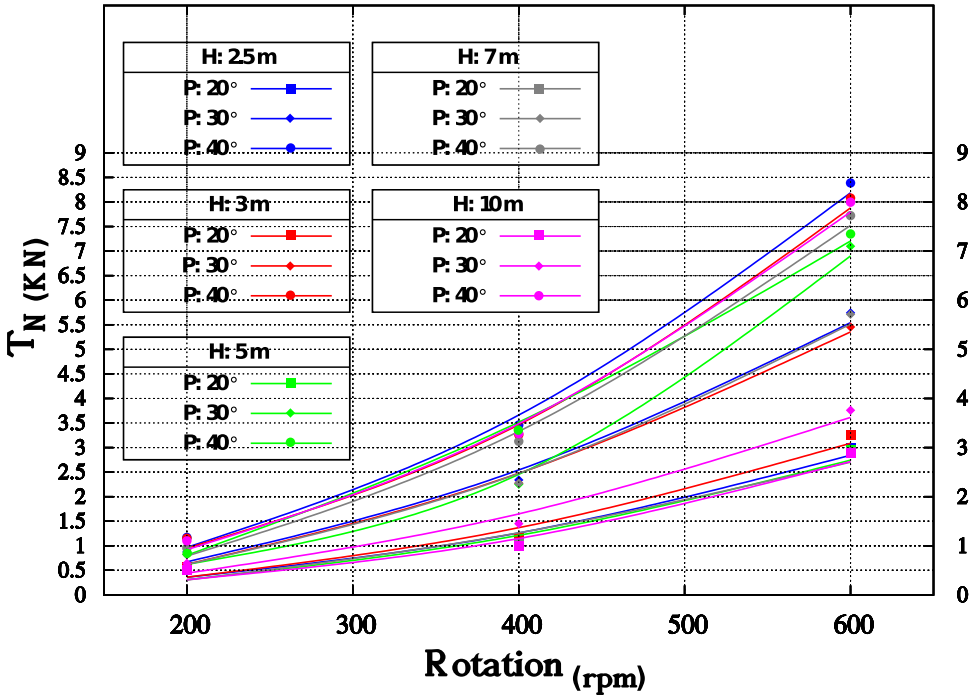

Figure 5.8: CFD Predicted net thrust vs. rotation speed for different altitudes and pitching angles.

As the cyclorotor ascends to higher altitudes since its take-off, the behavior of the downwash coincident with ground surface alters from two-sided bounced, to single inclined mass flow. In case of a counter-clockwise rotation (as is herein considered), the downwash flow tends to shift and incline rightward for all cases (see Fig.5.10). Furthermore, the strength of the downwash bounced flow is comparatively visible in Fig.5.10.b, where the up-bounced jet velocity in region "A" reaches fairly to $16m/s$, which is close to the in-cage maximum velocity of $\approx 20m/s$. The coordinates of point "A" measured from the origin center of the cyclorotor is $\approx (+6, +2)$, therefore, in vertical axis, that point is positioned at $5m$ altitude from the ground. Such assessment gives a comprehensive understanding of what level of impact the downwash shedding might lay on the overall functionality of the cyclorotor.

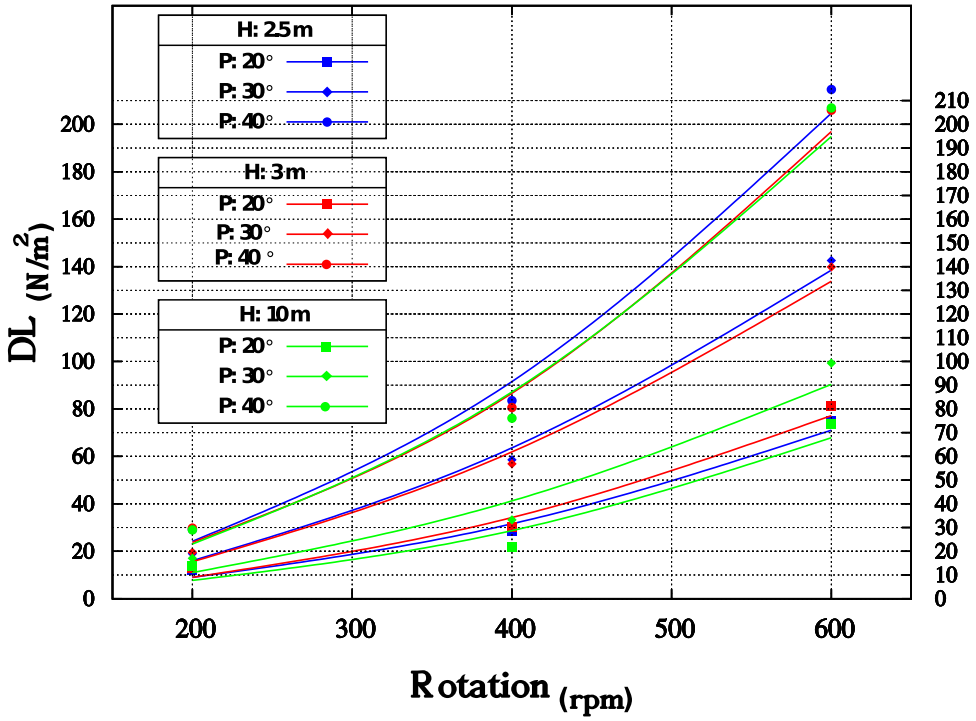

Figure 5.9: CFD Predicted disk loading vs. rotation speed for different altitudes and pitching angles.

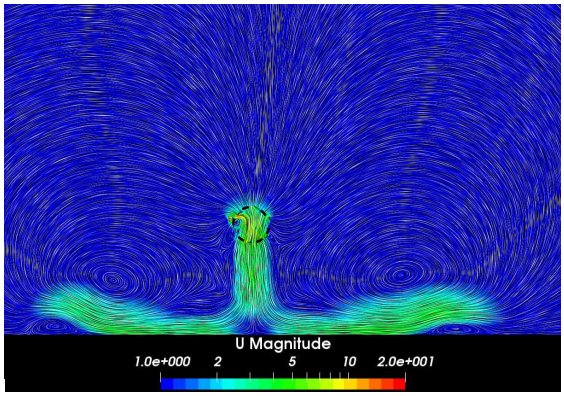

(a) 2.5m - 200rpm - 20° Pitch angle

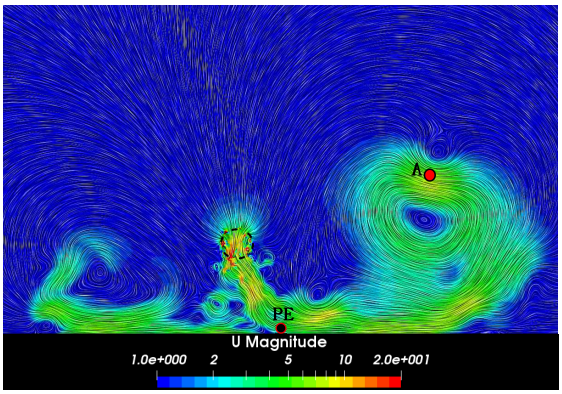

(b) 2.5m - 500rpm - 30° Pitch angle

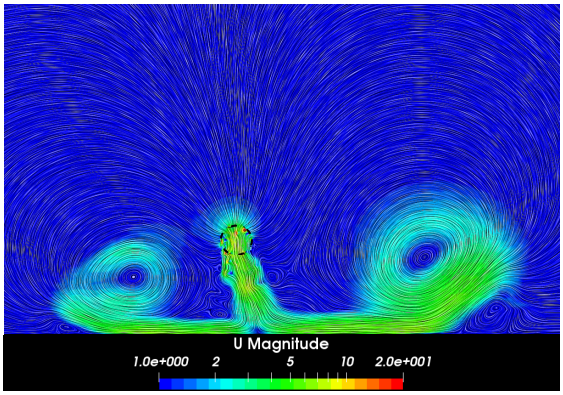

(c) 2.5m - 200rpm - 40° Pitch angle

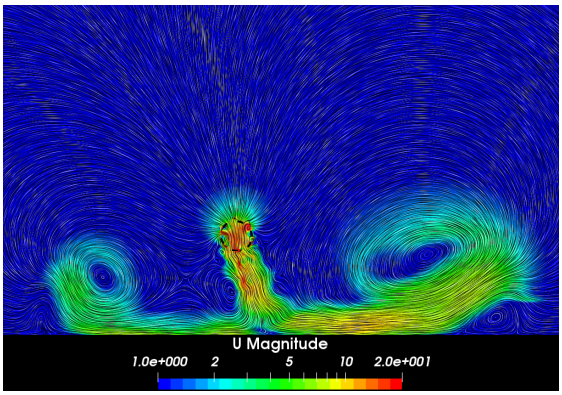

(d) 2.5m - 600rpm - 40° Pitch angle

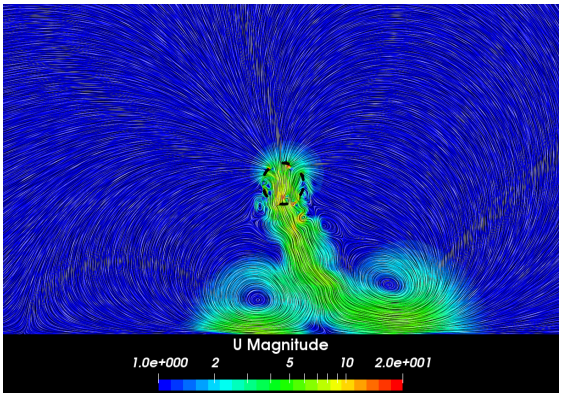

(e) 5m - 200rpm - 40° Pitch angle

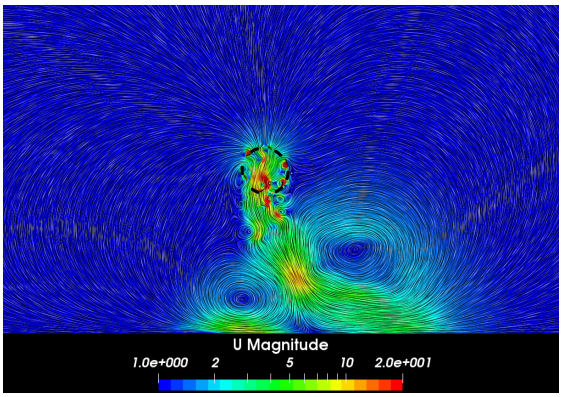

(f) 5m - 600rpm - 40° Pitch angle

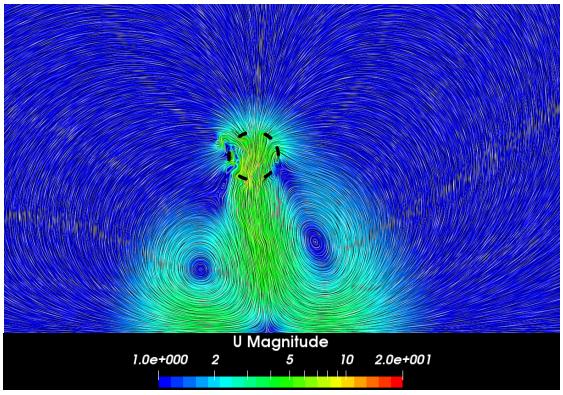

(g) 3m - 200rpm - 20° Pitch angle

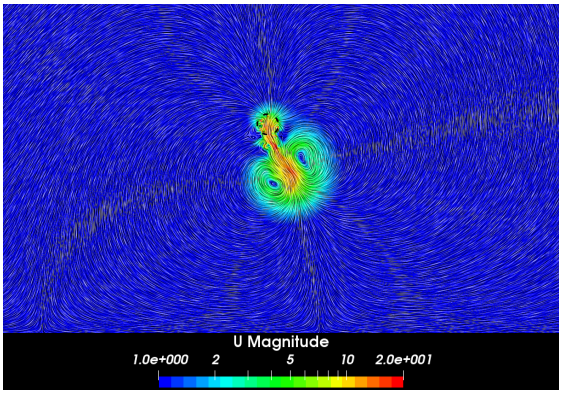

(h) 10m - 600rpm - 40° Pitch angle

Figure 5.10: Pitching oscillations and rotations of the cyclorotor to achieve cyclic convergence in time history of the downwash flow.

Accordingly, the term Point of Effect (PE) is here introduced to define the location of the collision center, where the downwash flow has the core interaction with ground surface (typically shown in Fig.5.10b), in each of these cases from $2.5m$ up to $7m$ vertical distance, and for which the surface interactions have not yet been vanished. These distances are thus divided by the rotor diameter ($0.8m$) in order to show them in non-dimensional (H/D) format. For the same desire, the horizontal distances of PE are also divided to their related altitudes (X/H). The exact locations of the PEs are measured from the vertical origin of the rotor center (as is shown in Fig.5.10c,d) and are presented in Table5.1. This provides PE positions, and the relative flow velocities, adjacent to the ground surface in each operational altitude, including all pitching angles and rotation speeds being simulated through this study.

Regardless of any altitude level, the primary reason of the efficiency augmentation relates to the reverse pressure which is induced from the downwash flow collision with ground surface. As was previously mentioned, the higher the vertical distance, the less dispersing the downwash experiences. That is the reason why we observe a downwash fork in the lower altitudes near the ground surface, as is depicted in Fig.5.10a-g. A region of pressure-bubble is also visible in the mid-fork position, fairly adjacent to the ground, which also displaces rightward as the downwash core column inclines more, at higher altitudes.

It should be noticed that cyclorotor simulations showed similar behavior for both 10 and 15 meters heights, which indicates that the ground effect became negligible at these altitudes, so in the next plots the latter is excluded.

Take into account that the velocity contours shown in Fig.5.10 are in surface-LIC (Line Integral Convolution) format, which was first introduced by [68] which uses image vector field algorithm techniques. This algorithms were gradually extended in several softwares and applications like paraview [69] to show the flow traces more efficiently.

Although the flowfield from the rotor cage is unsteady, the average velocity fields are depicted in Fig.5.10. The fields are obtained after sufficient cycles are passed to ascertain the downwash flow has become fairly developed up to quasi-steady state. The comparisons shown in Fig.5.10c,d and Fig.5.10e,f for cases at the same height but different rotation speeds, confirms that aside the unsteady behavior of (in-cage) flow, downwash jet characteristics does not show significant changes and can be fairly interpreted after passing numerous cycles.

Table 5.1: Horizontal locations of Point of Effect (PE) from cyclorotor center.

Altitude (H/D)	Pitch Angle (°)	Rotation Velocity (rpm)	Position (X/H)	Velocity (m/s)
		200	0.12	3.6
		400	0.2	7.8
		600	0.24	10
		200	0.16	5.1
		400	0.24	9.7
		600	0.3	17
		200	0.52	6.4
		400	0.68	13
		600	0.88	18
		200	0.1	2.4
		400	0.116	4
		600	0.133	6
		200	0.133	4.3
		400	0.166	10
		600	0.2	15
		200	0.336	6.2
		400	0.533	12
		600	0.63	15
		200	0.1	0.5
		400	0.12	0.8
		600	0.14	0.9
		200	0.12	1
		400	0.16	1.8
		600	0.19	2
		200	0.13	1.7
		400	0.166	1.9
		600	0.196	2.1
		200	0.357	0.1
		400	0.428	0.2
		600	0.457	0.3
		200	0.414	0.2
		400	0.442	0.6
		600	0.471	0.7
		200	0.428	0.28
		400	0.442	0.83
		600	0.442	1

As is seen in Figures 5.8 and 5.9, in a constant rotor size, net thrust and disk loading (DL)are both showing incremental behavior by increasing pitch angles at each rotation speed. Nonetheless, the distance between each disk loading values, in pitch angles, also gets enlarged by increasing the rotation speeds. Reversely, the power loadings (PL) are larger in lower rotating speeds, as is depicted in Fig.5.11. More important, PL values in 20° and 30° pitching angles are showing at considerably higher values, by doubling the values at 40°.

DL is defined as follows:

$$DL = \frac{T_N}{A}, \quad (5.7)$$

and PL as:

$$PL = \frac{T_N}{M\,\sigma}. \quad (5.8)$$

A primary parameter considered herein, which significantly outlines the operating efficiencies is the Figure of Merit (FM). As is defined in the following correlation (eq.5.9), the two major factors controlling the FM are PL and DL with the major effect being played by the former parameter.

$$FM = \frac{PL\sqrt{DL}}{\sqrt{2\,\rho}}. \quad (5.9)$$

The results of FM for all altitude levels and rotating speeds are shown in Figures 5.12, 5.13 and 5.14, in each individual pitching angle. The ground effect showed to be considerably influential on the functionality and efficiency of the cyclorotor, as can be seen from the high values that have been achieved for the FM during take-off and landing phases. Results demonstrated in Fig.5.13 confirm that applying 30° for pitching oscillations accompanied with 200 rpm rotational speed lead to FM values close to 1, and even above.

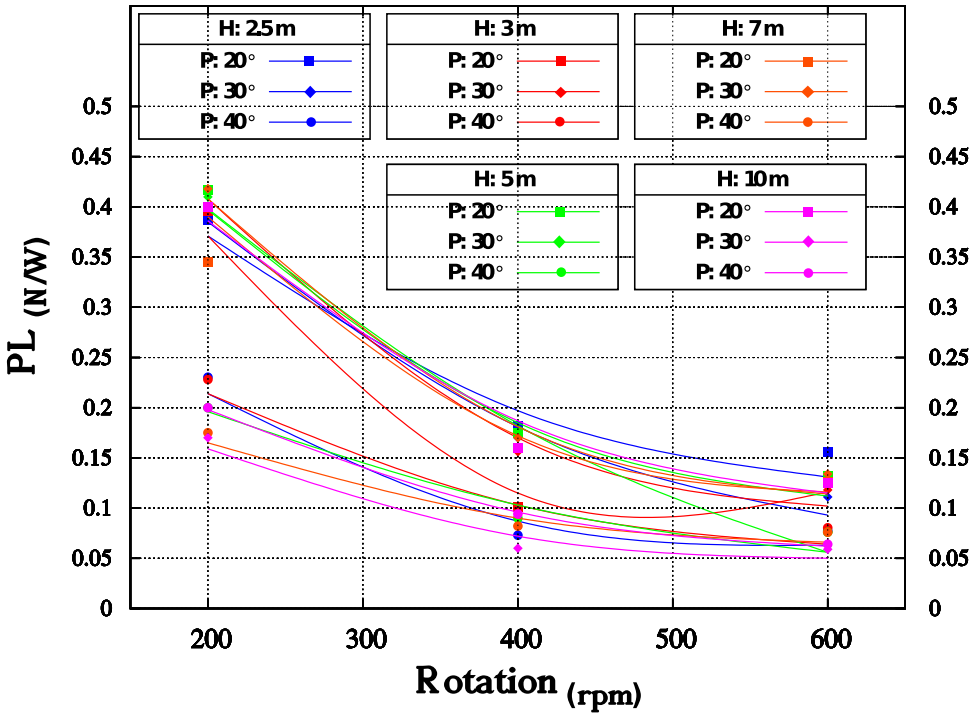

Figure 5.11: CFD Predicted power loading vs. rotation speed for different altitudes and pitching angles.

This fact has been proved in Fig.5.13 for the first 4 sets of altitude levels. Moreover, as the flight altitude increases above $7m$, different strategies to select between rotation speeds in 20° and 40° angles are available as the more desirable, since they provide higher FM values rather than 30°.

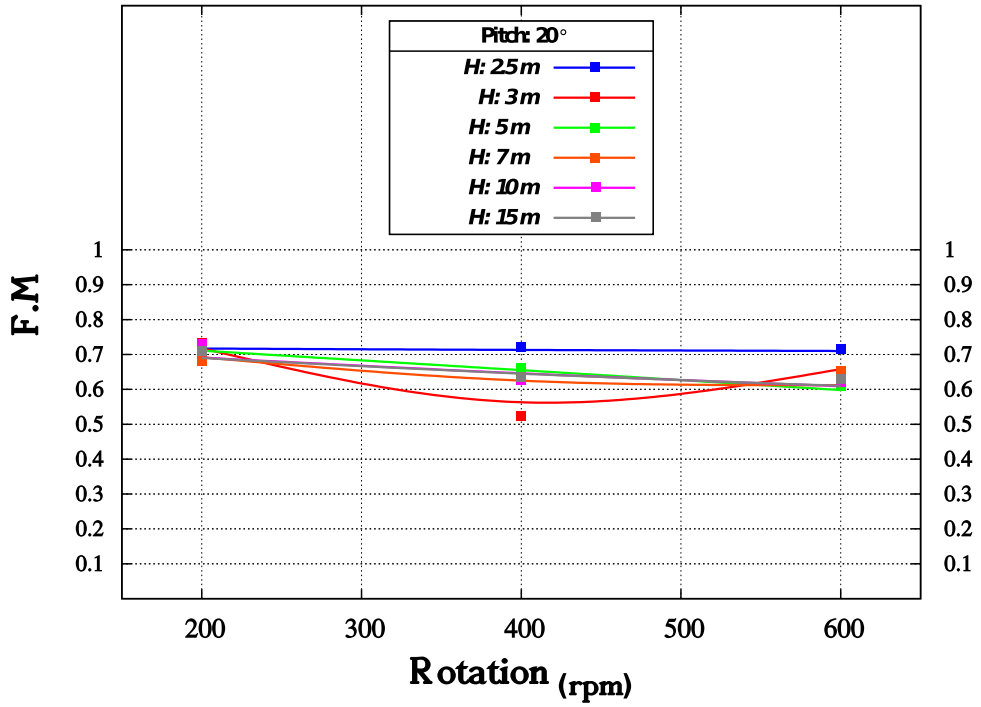

Figure 5.12: CFD Predicted figure of merit vs. rotation speed for 20° pitch angle in different altitudes.

Then, regarding the assessed results for net thrust, DL and Pl in Figures 5.8, 5.9 and 5.11, it is possible to choose the operational set according to the flight expectations.

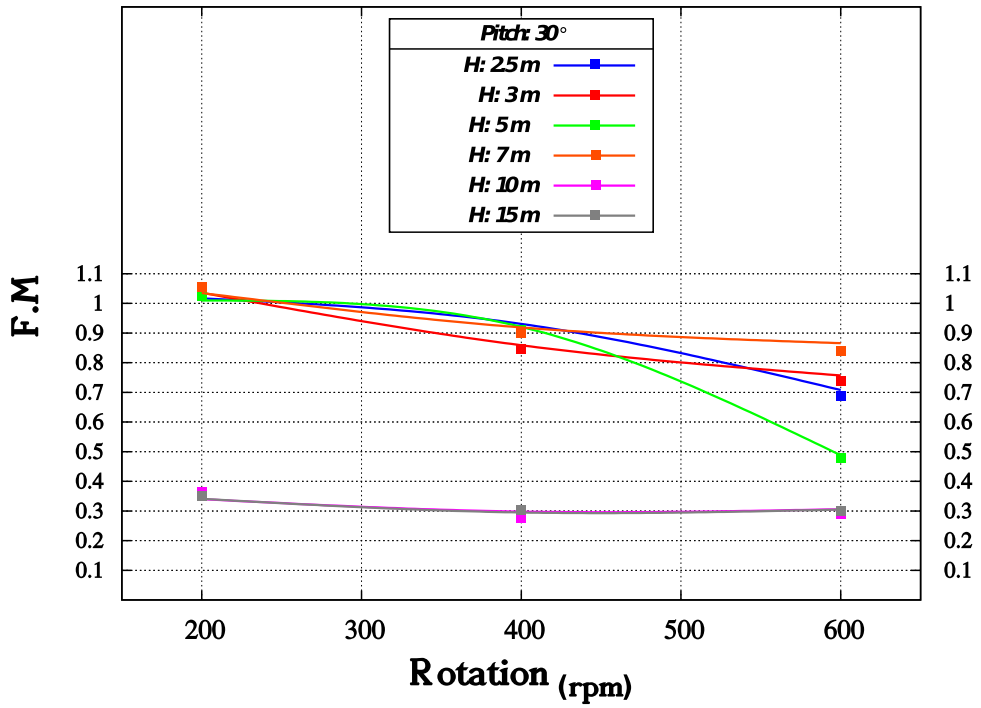

Figure 5.13: CFD Predicted figure of merit vs. rotation speed for 30° pitch angle in different altitudes.

Although higher rotational speeds lead to lower PL values it is probable that during cruise flight higher thrust and speeds are achieved, this is evident in Fig.5.8.

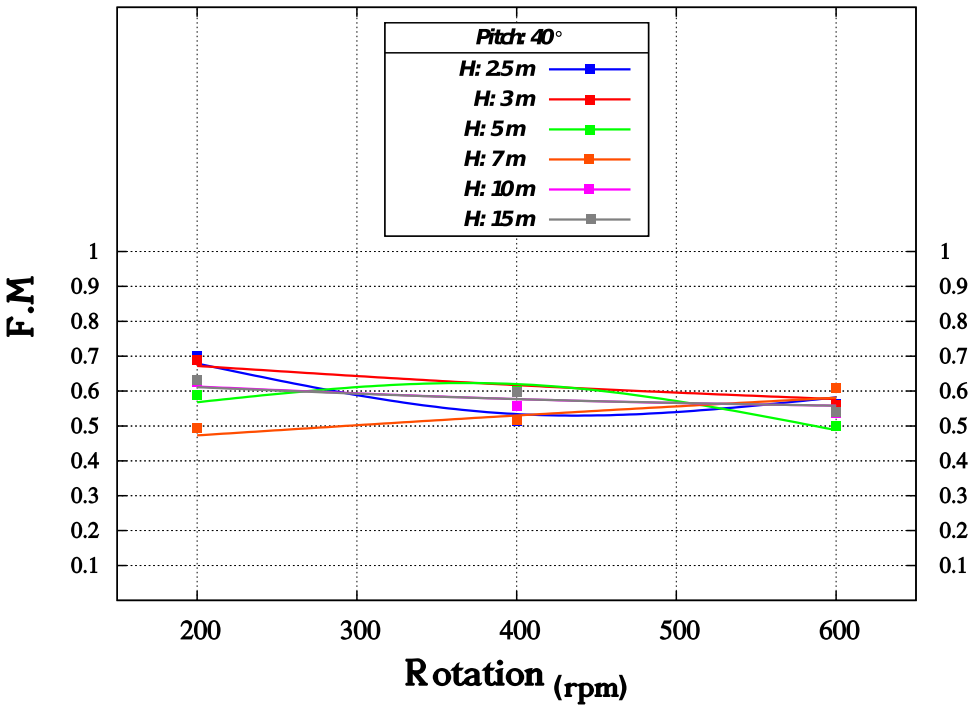

Figure 5.14: CFD Predicted figure of merit vs. rotation speed for 40° pitch angle in different altitudes.

The issues being pursued in this study are crucially essential in take-off and landing phases, since these are the most critical phases for aircraft. In these particular type of cyclorotors, which are mostly concerned in carrying payloads or even manned crafts for several specific missions, it is of high concern to uprise their capability for each flying mode [107].

5.5.3 Machine Learning and Data Processing

5.5.3.1 Artificial Neural Network Analysis

In order to explore a wider variety of VTOL conditions, an extra study has been conducted using ANN analysis on the pre-obtained CFD results [76, 77]. A combination of CFD and experimental analysis in ANN has also effectively been studied in a featured work from Naphon et al. [83]. The authors clearly pointed to the relatively high accuracy and efficient predictions from the neural network analysis. The neural network coding part consists of three distinct steps as is seen in Fig. 5.15: 1) loading and reading the whole CFD database, 2) Algorithm to train the data and 3) Data analysis and accuracy tests followed by exporting the processed data. This comprises a combination of over 540 values in database, which have been obtained from the CFD simulations in previous section.

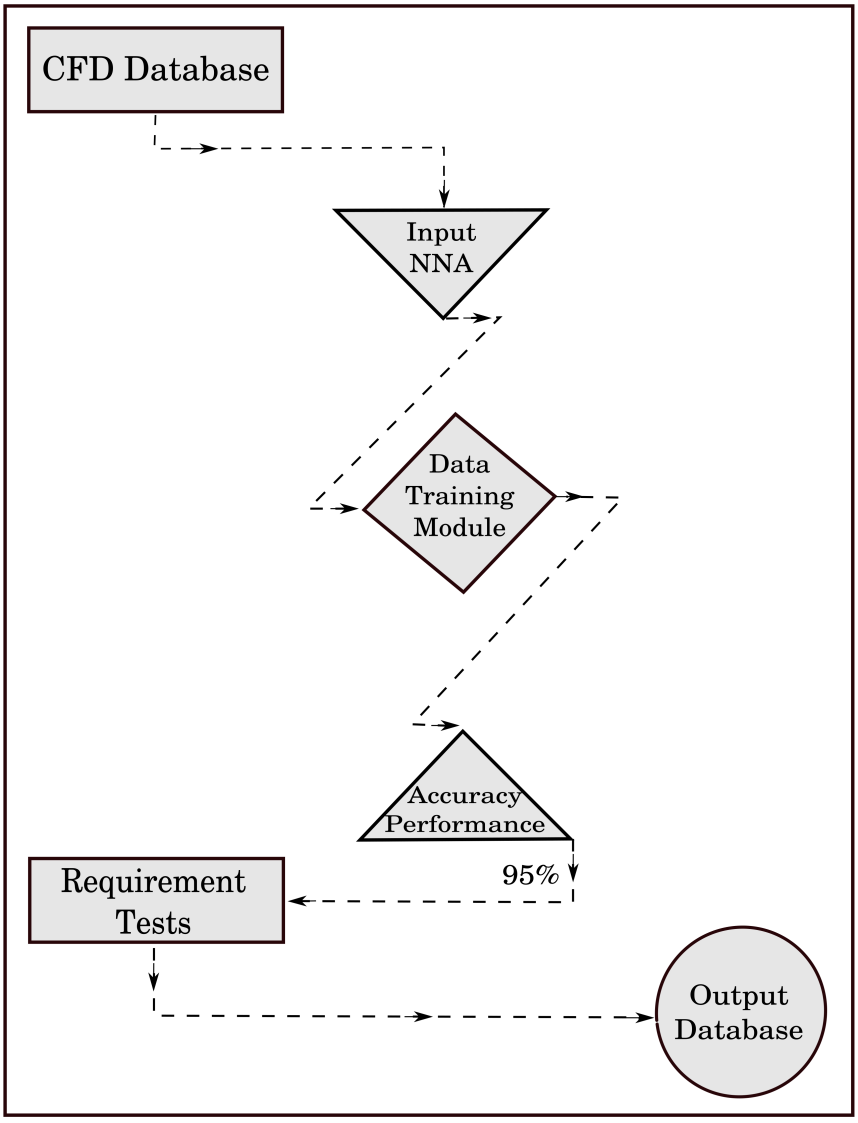

Figure 5.15: Neural network data acquisition diagram.

The neural network currently used is coded on a 10-layer algorithm which is capable of data analyzing with an accuracy of approximately ≈ 95 percent. As the initial CFD database is loaded to the neural network, the training and adaptation process starts to be operated in further estimations. While the algorithm is precisely trained, it goes for compilation and iterative sequences to match up the output assigned variables. Then an accuracy monitoring loop initiate in parallel with new data generation. The performance plots are provided through Figures 5.16 and 5.17.

The training method being used in this study is feedforward network. Feedforward actually consists of a series of layers. The first layer has a connection from the network input. Each subsequent layer has a connection from the previous layer. The final layer produces the network's output. Feedforward networks can be used for any kind of input to output mapping. A feedforward network with one hidden layer and enough neurons in the hidden layers, can fit any finite input-output mapping problem. Specialized versions of the feedforward network include fitting (fitnet) and pattern recognition (patternnet) networks. A variation on the feedforward network is the cascade forward network (cascadeforward-

net) which has additional connections from the input to every layer, and from each layer to all following layers.

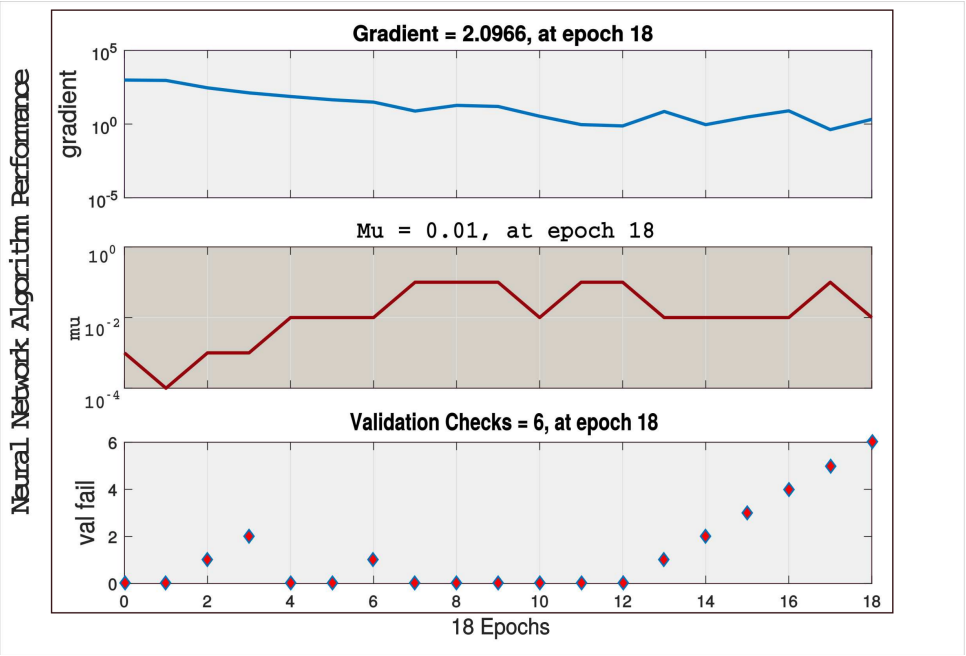

Figure 5.16: Performance plots of neural network analysis.

The desired outcome was including closer altitude intervals (each 0.5m), 10 rotation speeds from 200 to 650 rpm in intervals of 50, and covering the whole pitching oscillation degrees from 20 to 40.

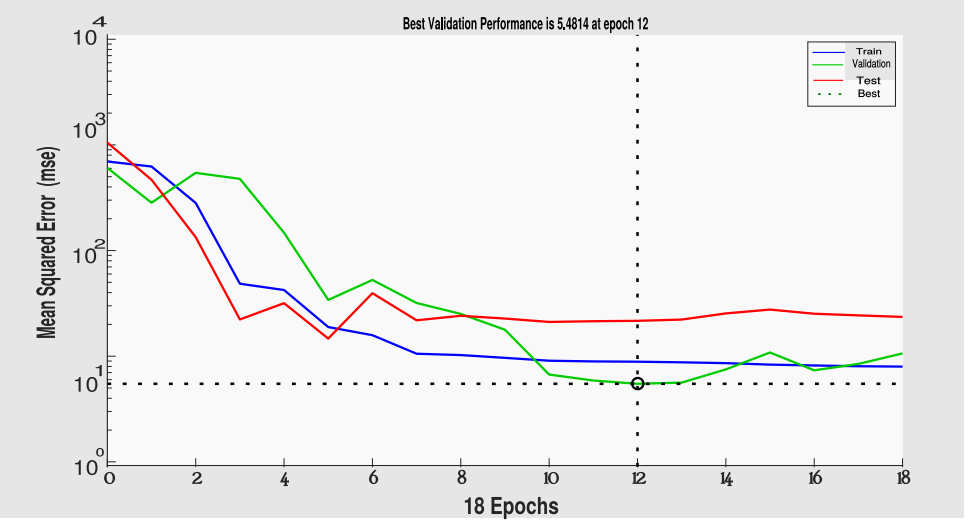

Figure 5.17: Optimum reached point in neural network training sequence as the lowest error is achieved per iterations.

Through these, a huge database of over 150 million values resulted from this neural network analyses that was processed. It is decided to focus on FM parameter which reveals the overall efficiency of the selected operating condition.
Since the obtained results from neural networks are of analytic and estimation types, they

are mostly considered to be qualitatively evaluated and discussed to capture an understanding of the logics and an overview of the phenomena.
The plots of 5.18–5.21 are shown to compare how the efficiency of the rotor alters in terms of pitching oscillations and distance to ground level. Moreover, it is prohibited to include the results of the altitudes higher than 10 m, since the operating mechanisms and principles are gradually becoming independent of ground distance while ascending.
As is seen in Fig. 5.18, and just for this altitude, most of the rotation results are presented, but the subsequent plots have been eliminated and limited to 4 speeds to reveal a better view for the comparisons.
For the cyclorotor operating at 2.5 m, it can clearly be seen in Fig. 5.18 that the optimum operation happens with 200rpm, at the pitching range of 24° to 28°, which exceeds the value of 1.1 in FM.

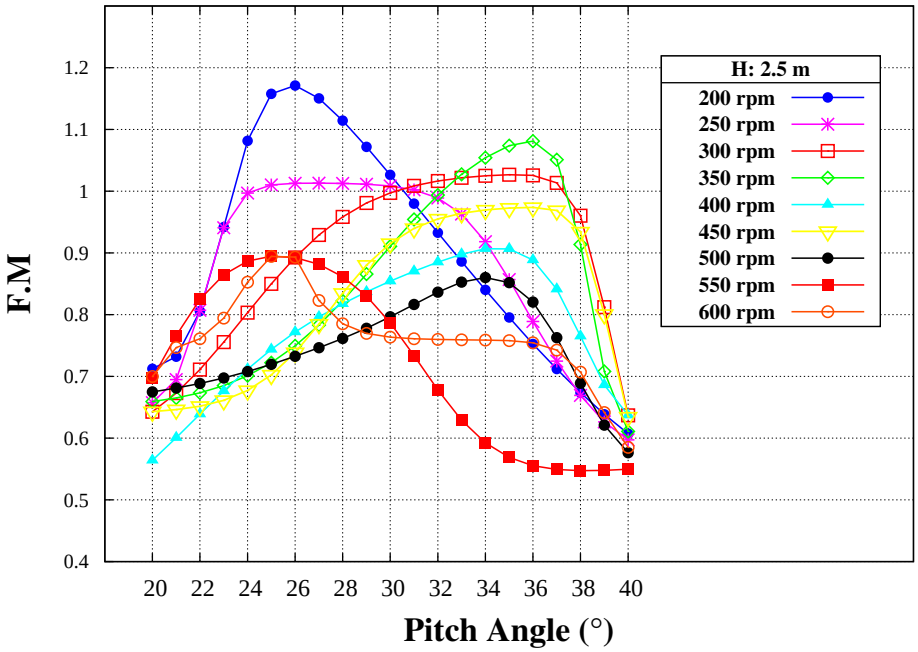

Figure 5.18: Figure of Merit vs. Pitching degree in different Rotation speeds for 2.5 m level.

From Fig. 5.19, the best result is obtained at 350 rpm in the range of 33° to 37° pitch angles, at 3 m altitude level.

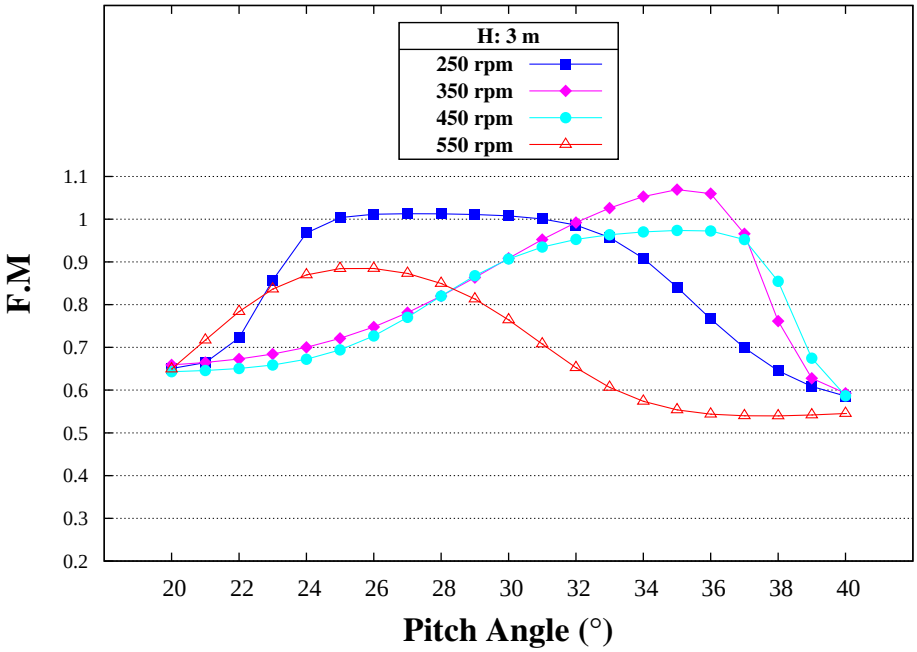

Figure 5.19: Figure of Merit vs. Pitching degree in different Rotation speeds for 3 m level.

As the rotor reaches the altitude of 5 m, it is seen in Fig. 5.20 that the rotation speeds between 350 to 450 rpm, in the pitch range of 31° to 35°, provides better efficiency. The reason of neglecting 250 rpm stems from the higher thrust being achieved in higher rotation speeds rather than the lower ones, as was discussed earlier in this study with CFD results.

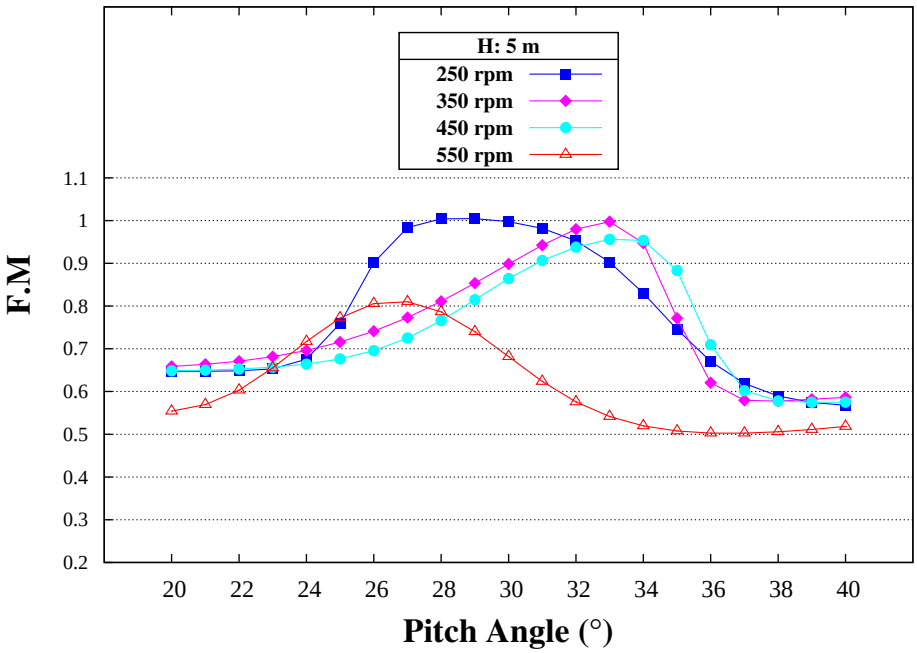

Figure 5.20: Figure of Merit vs. Pitching degree in different Rotation speeds for 5 m level.

While approaching altitudes up to 10 m, already considered as independent operating conditions in what regards to ground effects, the plot in Fig. 5.21 assures optimum con-

dition occurs in the range of 350 to 450 rpm speed (more shifted toward the latter), in between 20 to 28 degrees of pitching oscillations.

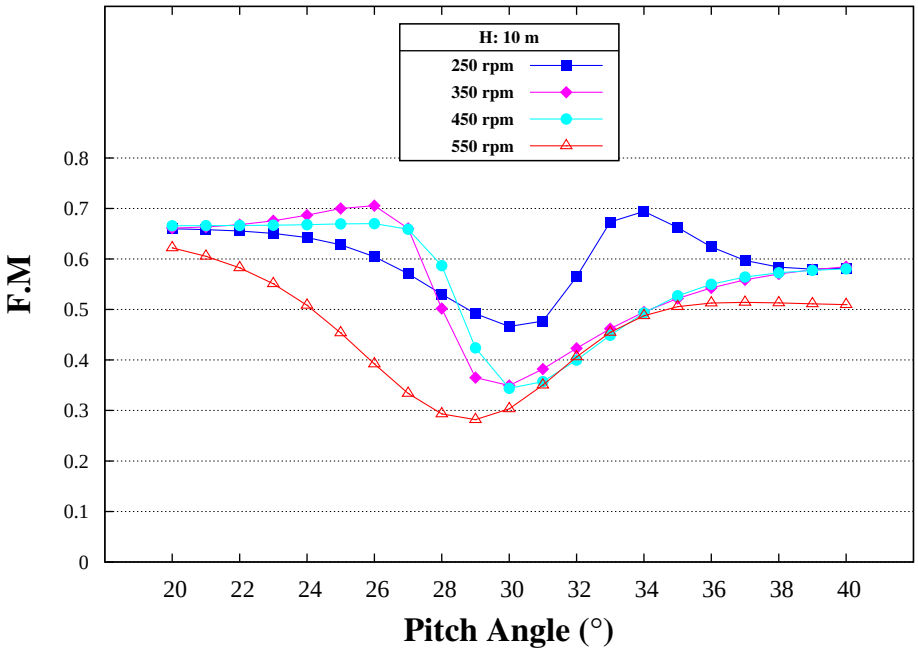

Figure 5.21: Figure of Merit vs. Pitching degree in different Rotation speeds for 10 m level.

5.6 Conclusion

A numerical study of the operating status of a typical cyclorotor which was previously proposed for unmanned aircraft is investigated through this phase. The focus was laid to study the role of ground effects on ascending and descending of a typical unmanned size cyclorotor in VTOL phases. The aim was to clearly predict and propose the optimum conditions using the most influential parameters such as operational altitude, rotation speed and pitching oscillation angle. Furthermore, a neural network field was included as the second phase of this study to obtain better estimative predictions from the already assessed CFD results.

Training the CFD results using neural network analysis truly provided further predictions of the cyclorotor performance in various conditions. CFD results revealed that the optimum operational performance for the close-ground levels is achieved by 30° and 200 rpm for pitching and rotating speed, respectively. Evaluations from ANN also admit that the optimum operational performances are highly dependent to ground distance of the working cyclorotor. This necessitate active control of pitching oscillation angles and rotation speeds to have the cyclorotor operate at its optimum condition at different situations. Active control of cyclorotors can be the subject of future investigations which has not been the point of concern yet.

Chapter 6

Novel Flight Propulsion System for VTOL/STOL Aircraft

[1]

This chapter is based on the submission of our international patent application N/Ref.: PPP 2020/9959 which is presenting a novel propulsion mechanism for VTOL-capable aircraft by using two cycloidal rotors, a pair-wing system and DBD plasma actuators.

6.1 Cycloidal Rotors and Pair-Wing System Definition

The invention is related to a flight propulsion system, mainly designed for Vertical/Short Take-Off and Landing (VTOL)/(STOL) aircraft, which comprises a front cyclorotor (1), pair-wings mechanism involving top wing (2) and bottom wing (3), 3-DOF adjusting mechanism for pair-wings (4), dielectric barrier discharge (DBD) plasma actuators (5), bar mechanism for pitching oscillation and rotation speed controls (6) and rear cyclorotor (7), a yawing mechanism for rear cyclorotor (8), all on each side of the flight vehicle. This propulsion system is particularly useful for VTOL aircraft. The main features of this invention are: high controllability and maneuverability, low noise and environmental pollution, VTOL, STOL, hover state flights, marine and ground take-off and landing, high safety, suitable for different aircraft scales and for different missions and purposes, instant altering the flight direction.

6.2 Description

6.2.1 Technical Domain

The present invention is related to flight propulsion system for vertical take-off and landing aircraft using two cyclorotors at front and rear portions and pair-wings in the middle of the rotors and DBD plasma actuators on the bottom wing, all on both sides of the aircraft providing extremely high controllability and take-off and landing phases to occur on both marine and ground surfaces.

6.2.2 Summary

This invention is regarded to a flight propulsion system for vertical/short take-off and landing (V/STOL) aircraft, mainly consisting in two cyclorotors namely front and rear cy-

[1]Based on the work published in the Proceedings of Fluids Engineering Division Summer Meeting, FEDSM2020, 10.1115/FEDSM2020-20292, and, Proceedings of the Canadian Society for Mechanical Engineering International Congress CSME-2020 , doi: 10.32393/csme.2020.55

clorotors and pair-wings positioning in between the cyclorotors. The concept is to benefit more efficiently from the downwash airflow of the cyclorotors and process the airstream in order to design an effectively enhanced propulsion system, providing vertical take-off and landing phases for aircraft in various scales. In this invention, the pair-wings function as a nozzle-like cascade to inhale a desired portion of the downwash airflow from the front cyclorotor and convect properly the channeled airflow toward the rear cyclorotor. This invention is employing on both sides of the aircraft. The DBD plasma actuators on the aft-portion of the suction surface of the bottom wing prevents any flow separations and minimize flow perturbations convecting to rear cyclorotor. The front cyclorotor is in larger size compared to the rear cyclorotor. In addition, the rear cyclorotor operates at considerably higher rotational speeds in contrast with the front cyclorotor. Using a control mechanism, the rear cyclorotor is yawing from its mid-span and thus provides instant flight direction shifting in all working conditions. This propulsion system provides both short and vertical take-off and landing flights for the aircraft. Since the principal working medium is airflow, highly less environmental pollution will be produced. The design of this invention is such that considerably low noise is made and an extremely high maneuverability and instant controllability is attained using this flight propulsion system. With this invention, the aircraft can take-off and land from/on both marine and ground surfaces in all conditions especially in urgent cases. This invention allows the aircraft to glide in circumstances of any failure in any section and thus the safety factor is also noticeably enhanced.

6.2.3 Prior Art

The invention described herein is based on a flight propulsion system that performs vertical short take-off and landing with improved efficiency.

US005265827A [108], discloses an aircraft with vertical take-off and landing capability having at least two laterally paddle wheels rotatable on a central axis. Each of the paddle wheels has a plurality of blades pivoted by a system to obtain a determined blade pitch angle. In one embodiment the aircraft comprises only a pair of paddle wheels which provide lift, thrust, roll and yaw control of the aircraft while the pitch of the aircraft is controlled through a vertical axis rotor. In another embodiment the aircraft comprises two paddle wheel pairs in which the separate pitch control rotor is unnecessary. Although, this invention may comprise two or more paddle wheels, it does not makes use of wings neither a pair-wing nozzle mechanism to optimize the lift and maneuverability. In the said invention, the use of plasma actuators is not considered too.

US4194707A [109], discloses a lift augmenting device to provide a vertical take-off capability in aircraft. This device includes a pair of rotor assemblies with independently individually pivoted rotor vanes so that the position of the vanes can be changed. This invention does not make use of a pair of rotors working together, neither a pair-wing system. Also, does not allow to change the position of the rotors in order to improve the yaw movement. In addition, the said device does not include plasma actuators.

US20160376003A [110], discloses an aircraft with high propulsion efficiency abilities to

perform short take-off and landing and having cruise speed up to subsonic limit. Although the propulsion of the said aircraft is based on a cycloidal rotor scheme, this aircraft does only perform short take-off and landing and does not allow to perform vertical take-off and landing. Moreover, the said aircraft makes use of improved cycloidal rotor thrusters but does not consider the use of pair-wings for increase propulsion efficiency. The use of plasma actuators is not considered in the said invention.

US1754977 [111], discloses a vertical rising airplane providing the combining advantages of the helicopter with those of the airplane. The said vertical rising airplane includes oppositely rotating frames revolving about axes substantially transverse to the horizontal of flight of the machine. Although, the said airplane makes use of rotatory propelling devices, the said invention does not consider the use of a pair-wing nozzle, neither a pair of cycloidal rotors with a size relation. The rotary propeller devices operate along the same and can't be moved in such a way they allow to improve the aircraft yaw control. Also, it does not contain plasma actuators for improved efficiency.

US 4482110 [112], discloses a composite aircraft comprising a system of airfoils rotating about a horizontal axis providing lift and thrust in combination with a lighter-than-air gas containment bag providing buoyant lift, so than the said aircraft is capable of lifting and transporting loads. Although the said aircraft makes use of a rotating blade system, it needs an additional gas containment bag to provide the required lift. Moreover, it does not consider the use of wings, neither a pair-wing system which works also as a nozzle. Also, it is not considered the use of plasma actuators.

US 2507657 [113], discloses an aircraft with mixed type propulsion. The aircraft includes, on either side of the fuselage, rotors fixed to a common horizontal and transverse shaft which work as paddle wheels. These rotors include a plurality of blades and are controlled in such manner that the resultant aerodynamic force acting on said blades is directed either vertically or obliquely. This allows to obtain either a lifting or lifting and propelling actions. Although the said invention makes use of rotors with a plurality of blades, it does not consider the implementation of a pair-wing system. Furthermore, in the said invention the rotors are mounted in a common shaft and they are not movable. Moreover it does not includes plasma actuator devices to improve the efficiency of the system.

US 6231004B1 [114], US6527229B1 [115], and US8448905B2 [115], disclose lift generation devices and aircraft with aerodynamic lift generating device. The devices disclosed use a tangential flow rotor positioned in place of the leading edge of a wing-like body and rotating such that the part of the fan rotor at the top of the wing-like body is moving backwardly, towards the trailing edge of the wing-like body, whereas the lower part is shrouded and in various of the embodiment of that earlier device the shroud terminates in a lip which helps to form and locate a vortex within the rotor when the rotor is in motion. The lift generation devices are intended for short take-off and landing aircraft, and they don't perform vertical take-off and landing. The aircraft disclosed in US8448905B2 [115], which uses the said aerodynamic lift generators, is able to perform vertical take-off and landing. However, the said aircraft generates the vertical thrust by means of a vertical axis fan, instead of doing it by means of cycloidal rotor thrusters as disclosed in our invention.

Moreover, the lift generating devices comprise only one rotor and one wing, it does not combine two cycloidal rotor thrusters with a size relation, and it does not use a pair-wing nozzle system. Moreover, the said aircraft and lift generating systems does not consider the use of plasma actuators for improved efficiency.

US1432700 [116], discloses a propeller embodying a plurality of vane or blade members mounted so as to rotate upon their own axes while selves rotate about a common axis.

US2580428 [117], constitutes an improvement of the patent US1432700 [116], and it relates to aircraft and more particularly to cyclogiro aircraft and cycloidal propellers in which a combination of lift and propulsion forces are exerted by cycloidal motion of airfoil members or blades. In these documents the propulsion is only provided by cycloidal rotors and they do not consider the use of pair-wings combined with cycloidal rotors. Besides, the cycloidal rotor system it is not movable, and the implementation of more than two cycloidal rotors does not consider the use of cycloidal rotors with size relation. Moreover, the implementation of plasma actuator devices is not considered.

US5100080 [118], discloses an improved rotor assembly comprising at least one profiled wing an intended to be caused to rotate in a fluid in order to develop sustaining and/or propelling forces. The said invention does not contain a pair-wing nozzle combined with cycloidal rotors thrusters. The use of plasma actuators is not considered too.

WO 2018/140199 A2 [119], discloses a cycloidal rotor air vehicle including a cycloidal rotor assembly supported by the air-frame and configured to rotate about an axis of rotation relative to the air-frame. The cycloidal rotor assembly includes a plurality of blades having a longitudinal axis connected to a motor to rotate about the axis of the cycloidal rotor and a servo to adjust the pitch of the blade. The said invention is particularly intended for micro-air vehicles. The said invention does not comprise a pair wing system. Also, it does not makes use of a system with two cycloidal rotors with a size relation between them. The use o plasma actuators to optimize the system is also not considered. The said invention is only intended for air vehicles with very low mass and cannot be used in aircraft intend for load transport.

6.3 General Description

The tendency to equip aircraft with cycloidal rotors (shortly say, cyclorotors) as means of Vertical Take-Off and Landing (VTOL) propulsors has increased in recent years [2]. Considerably lower noise production and more stable hover and vertical displacements in comparison with those of conventional screw propellers, as used in helicopters, are the main reasons to witness this tendency. aircraft being capable of VTOL and hover are increasingly emerging in various critical and routine applications. Rescue missions in roads and environmental disasters, observance and monitoring-based carriers, surveillance cameras, payload carriage in situations like transmitting forest tree are, just to mention a few examples. Within VTOL category, numerous designs have been proposed along the years. Helicopters are the most typical crafts in this kind, but concerning the thrusting mechanism, several alternatives are yet in hand. Nevertheless, each of them has their

own strength and weakness points, thus, one should select a design to utilize it toward the desired output and try to overcome the drawbacks and sophistication in this regard. The cycloidal rotor which was initially introduced as a novel conceptual design of propellers by a German origin researcher Fredric Kurt Kirsten. His collaboration with Boeing company then led to Kirsten-Boeing propellers reported in 1926 [120]. This was considered as the onset of a new practical generation of blades operating in a cage-like assemble which was totally different from those of conventional propellers, in terms of exerting all sections of blades in span-wise direction a fairly equal action into the fluid. There exist some research reports concerning cyclorotors within the first two starting decades until 1940s. It was by then the subject of many research that was afterwards lost for a long period of almost 50 years. In an effort from BOSCH Aerospace incorporation in 1998, the operational efficiency of a UAV size cyclorotor was examined and built using modern methods and knowledge. With their full-scale design, the most astonishing feature of their report was the considerably low noise-pollution characteristic of the current operating mechanism [100]. In Japan, Onda et al. [121] whose work was mainly on Lighter Than Air (LTA) vehicles, like airships, have also started to utilize the cycloidal rotors in their configurations instead of conventional propeller-type thrusters. It actually was a modified prototype of ACROSTAT airship design which was previously reported [122]. Fast functioning and better controllability due to employing these rotors were the attained enhancements observed in their design from what they have declared with conventional propellers [123, 124, 9]. One of the main studies can be attributed to [125] and a complementary in [14], which was accompanied by experimental, 3numerical and analytical investigation on a typical UAV type cyclocopter. Prior to carrying out the tests, they have gone through analytic to identify the rotor specifications which would best fit in terms of performance for a UAV by using a modified version of Stream-tube model for a more accurate response in cyclorotors, this was initially developed for Darrieus wind turbines [15]. Thus, they have manifested the following five major results drawn from their study pertinent to the dominant flow acting through the rotor: (1) The inflow velocity at 0 ◦ and 180 ◦ of azimuthal angles is about zero. (2) The inflow moves vertically downward when passing the top half circle, and deflects towards the rotation direction as it passes the bottom half circle path. (3) If considering counter-clockwise direction and giving positive and negative signs to the inflow and outflow, respectively, the arc between 0 ◦ to 270 ◦ in azimuth is positive and from the latter up to 360 ◦ consists predominantly of negative sign. (4) The occurrence of tilted downwash while exiting the rotor stems from the inherent flow behavior from within the rotor itself. (5) Another very important finding was that the curvilinear pattern of the exerted flow, to the cyclorotor, results a cambered-like behavior in the blades whereas in fact, they are all symmetrical. This issue is assumed as the key source of higher lifting force attained from bottom half of rotor compared to the top one. In a comprehensive study carried out both experimentally and numerically from Yu et al. [126], forward flight efficiency has been the main research subject. They featured the effects of advance ratio and blade numbers as the influential parameters. The authors indicate that reaching the same efficiency as the screw propellers is feasible in cyclorotors for flights. As was indicated in

a technical report from National Aeronautics and Space Administration (NASA) [42], cyclorotors are propulsors in which the downwash flow convects in a pile-like flow, shedding out from the bottom side of rotor. This concentrated massive volume of flow can undoubtedly play significant role on the overall functionality of a cyclorotor aircraft, especially in its close-ground level flying operations. Herein, for the proposed flight propulsion system, it is tried to benefit from the terminology of the cyclorotors or cycloidal rotors but to use in a systematic arrangement in order to enhance the flight characteristics. In doing so, two sets of cyclorotors are placed on each side of the aircraft. These cyclorotors are configured in different specifications since they are holding different tasks and missions. A double wing assembly is designed to place in between the two cyclorotors on each side of the aircraft. The bottom wing is to divide the flow in two separate portions through the downwash region of the front cyclorotor. These two portions can possibly be controlled using the control systems to displace the wings in three different motions. The top wing thus, provides a channel-like passage in nozzle-shape to work on the passing airstream to enhance its properties for a better thrust and lift forces. As the nature of the cyclorotors are the more efficient controllability and maneuverability, using a yawing system for the rear cyclorotors on each side of the aircraft propulsion system gives a highly instantaneous direction-altering capability. The other important characteristic of the proposed flight propulsion system in the current invention is that this system can provide the vertical take-off and landing phases on both ground and marine surfaces. Both the cyclorotors and the wings arrangements are admitting a safe and efficient functional status of the proposed propulsion system. This characteristic actually increases the safety factor of the aircraft while in emergency conditions and requires to glide and even land in any possible surface. Another important feature of this invention is the use of DBD plasma actuators on the bottom wing. Employing DBD plasma actuators can efficiently improve the overall functionality of this flight propulsion system in several operating aspects. Plasma actuators are electronic devices with proven ability for active flow control. These devices, when operated, produce a body force which pulls the adjacent air toward the surface, in which they are applied, and accelerates it downstream, in a tangential direction to the surface. Due to this phenomenon, these devices are effective for many applications within the active flow control field, such as separation control, wake control, aircraft noise reduction, modification of velocity fluctuations or boundary layer control [127]. These devices are very attractive because they present very low mass and are fully electronic. Therefore, they allow to manipulate the flow field by electronic means, reducing the need of mechanical components which would increase the weight of the aircraft. Moreover, they present fast response time meaning that, accordingly with the flight conditions, they may be instantaneously enable or disable. In addition, although they require a high voltage signal to operate, the current is very small, in the order of milliamps. Therefore, these devices present low power consumption. The effectiveness of these devices for flow reattachment and separation delay has already been proved in many studies [128, 129]. Therefore, in the present invention plasma actuators are applied on the top surface of the bottom wing in order to attach the flow to surface and delay its separation. By this the losses are re-

duced and the efficiency of the propulsion system is increased. In other embodiment, plasma actuators may be also applied in the cycloidal rotor blades in order to enhance the lift and thus increase the efficiency of the flight propulsion system. Since, plasma actuators present proven ability for deicing and ice prevention [130], they may also be used to prevent the accumulation of ice in the components of the flight propulsion system. According with this, the plasma actuators may operate as flow control and anti-icing devices, which turns the proposed propulsion system suitable for aircraft intend to fly under ice formation conditions.

6.4 Description of the Drawings

Figure 6.1: A schematic of flight propulsion system with a combination of cycloidal rotors and lateral wings and DBD plasma actuators on the wing surface where (1) represents the front cyclorotor, (2) represents pair-wings, (3) represents the top wing, (4) represents the bottom wing, (5) represents the 3-DOF control mechanism fro the pair-wings, (6) represents the DBD plasma actuator strip tapes, (7) represents the bar-mechanism for pitching oscillation controls of the cyclorotors, (8) represents the rear cyclorotor, (9) represents the yawing control mechanism of the rear cyclorotors.
Figure 6.2: The specifications of the flight propulsion system with the details of operation where (10) represents the blade profile of the cyclorotor, (11) represents the maximum pitching oscillation angle of cyclorotor, (12) represents the rotation speed of cyclorotor, (13) represents the distance between pivot point and leading edge of the blade in cyclorotor, (14) represents the pivot point of the blade in cyclorotor, (15) represents the radius of cyclorotor, (16) represents the center location of cyclorotor, (17) represents the inlet patch of the pair-wings cascade, (18) represents the outlet patch of the pair-wings cascade, (19) represents the chord length of the top wing, (20) represents the angle of the top wing, (21) represents the aerodynamic control center of the top wing, (22) represents the chord length of the bottom wing, (23) represents the angle of the bottom wing, (24) represents the aerodynamic control center of the bottom wing, (25) represents the reference center point.
Figure 6.3: The airflow sections functioning in the flight propulsion system where (26) represents the airflow inhale region of the cyclorotor, (27) represents the in-cage flow, (28) represents the downwash region of cyclorotor, (29) represents the free-downwash flow of the cyclorotor, (30) represents the flow portion entering the pair-wing cascade, (31) represents the induced flow from DBD plasma actuators.
Figure 6.4 6.5: The yawing rotation of the rear cyclorotors on each side of the aircraft and the resulting downwash inclination where, (32) represents the yaw angle of the left-side rear cyclorotor, (33) represents the yaw angle of the right-side rear cyclorotor, (34) represents the inclined angle of the downwash flow from left-side rear cyclorotor, (35) represents the inclined angle of the downwash flow from right-side rear cyclorotor.

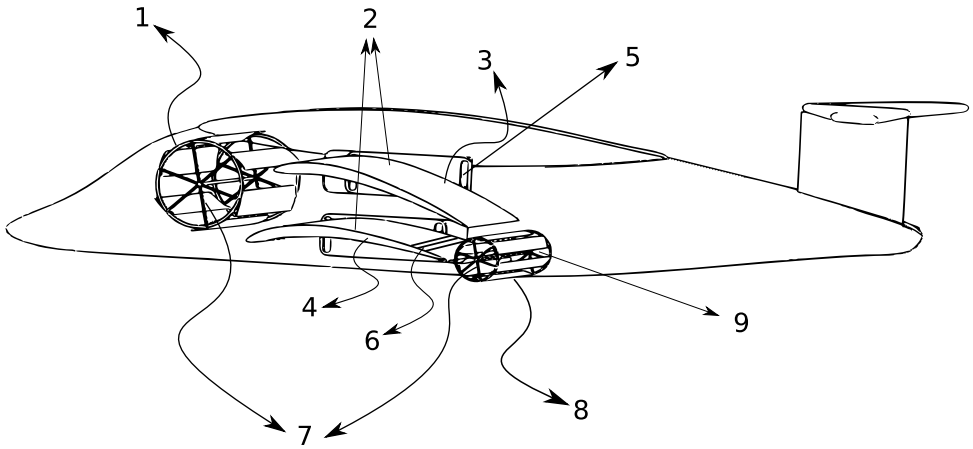

Figure 6.1: Main Components 3D view.

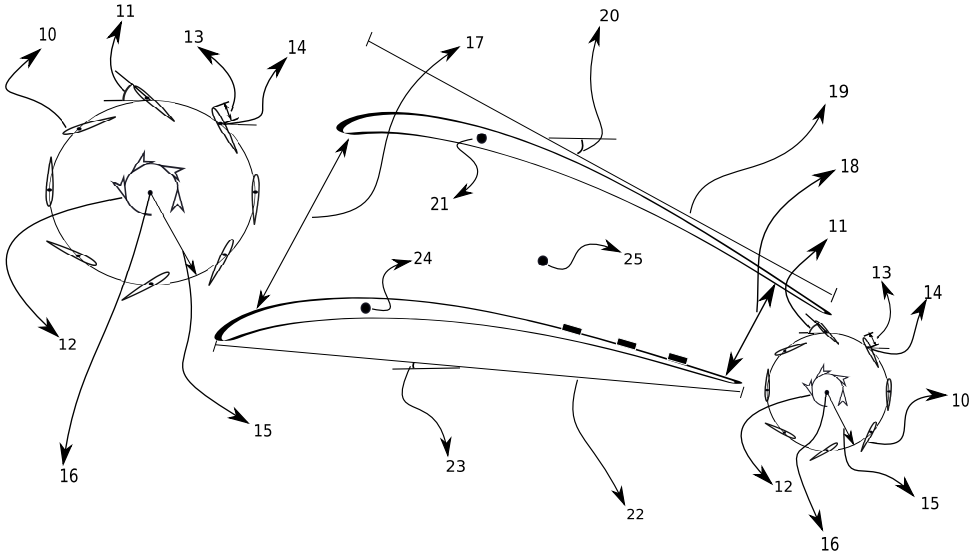

Figure 6.2: Cyclo Wing Configure.

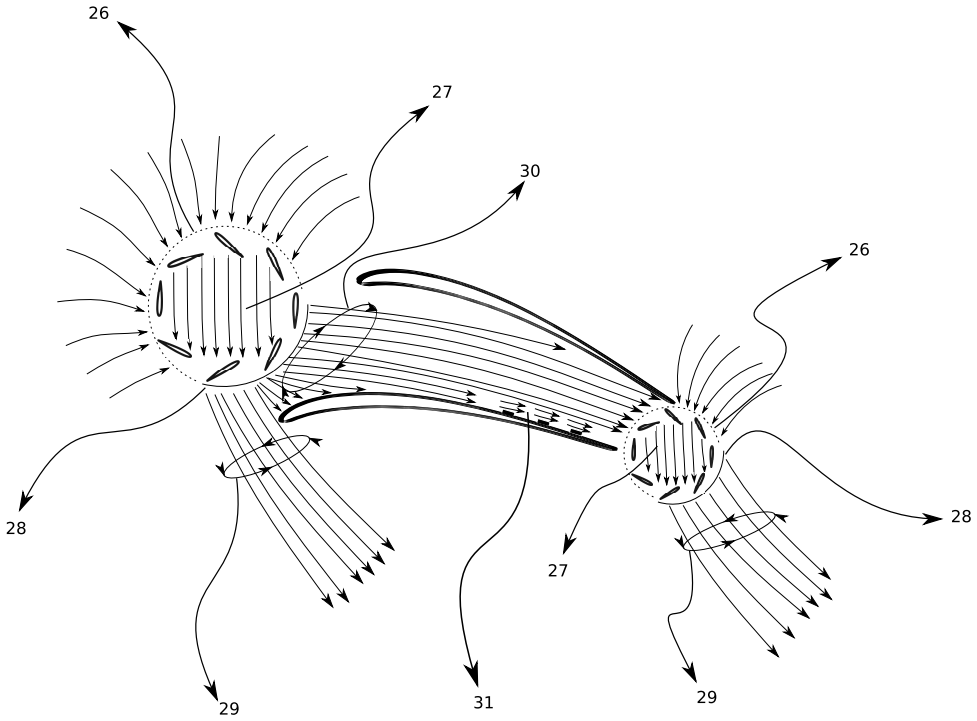

Figure 6.3: Flow Streams.

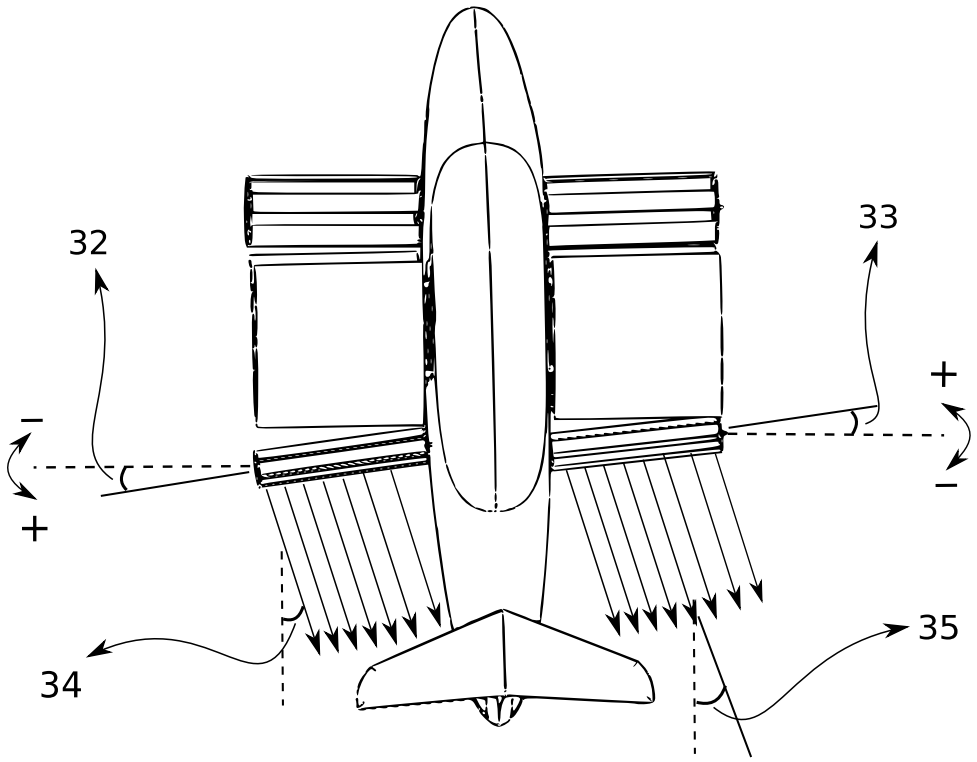

Figure 6.4: TopView-a.

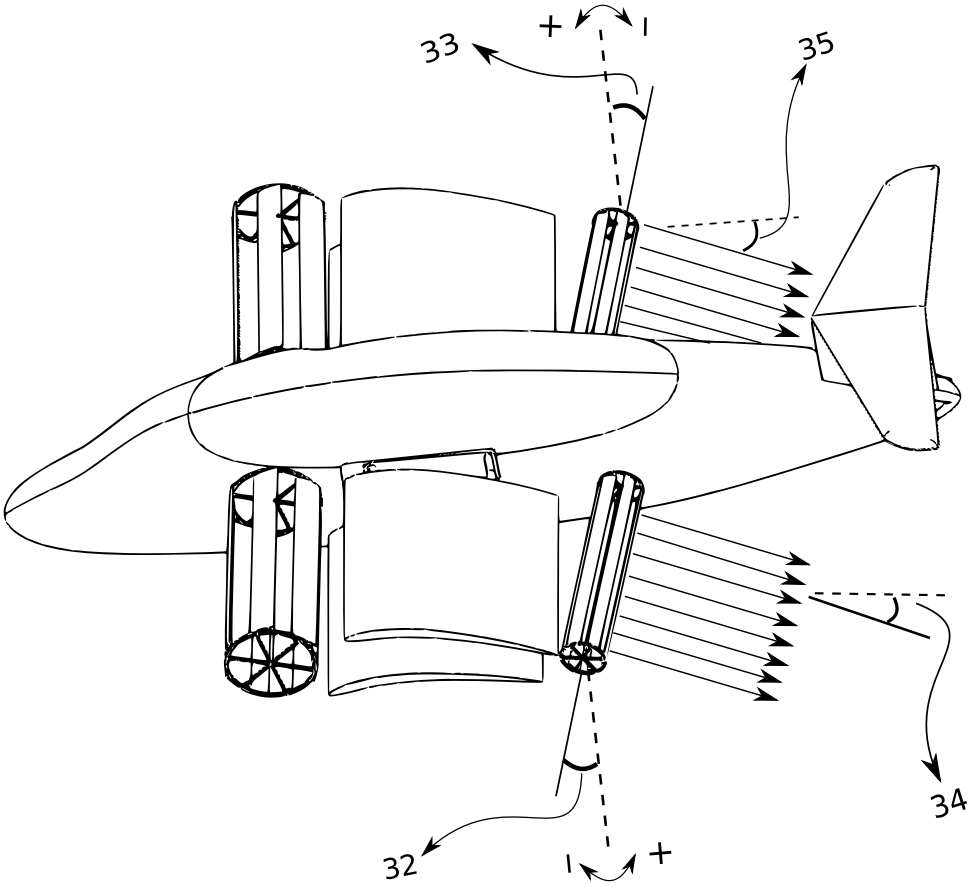

Figure 6.5: TopView-b.

6.5 Matching numbers

1. : represents the front cyclorotor.
2. : represents the pair-wings.
3. : represents the top wing.
4. : represents the bottom wing.
5. : represents the 3-DOF control mechanism for pair-wings.
6. : represents the DBD plasma actuators.
7. : represents the bar-mechanism for pitching oscillation controls of cyclorotors.

8. : represents the rear cyclorotor.

9. : represents the yawing control mechanism of the rear cyclorotors.

10. : represents the blade profile of the cyclorotor.

11. : represents the maximum pitching oscillation angle of cyclorotor.

12. : represents the rotation speed of cyclorotor.

13. : represents the distance between pivot point and leading edge of the blade in cyclorotor.

14. : represents the pivot point of the blade in cyclorotor.

15. : represents the radius of cyclorotor.

16. : represents the center location of cyclorotor.

17. : represents the inlet patch of the pair-wings cascade.

18. : represents the outlet patch of the pair-wings cascade.

19. : represents the chord length of the top wing.

20. : represents the angle of the top wing.

21. : represents the aerodynamic control center of the top wing.

22. : represents the chord length of the bottom wing.

23. : represents the angle of the bottom wing.

24. : represents the aerodynamic control center of the bottom wing.

25. : represents the reference center point.

26. : represents the airflow inhale region of the cyclorotor.

27. : represents the in-cage flow.

28. : represents the downwash region of cyclorotor.

29. : represents the free-downwash flow of the cyclorotor.

30. : represents the flow portion entering the pair-wing cascade.

31. : represents the induced flow from DBD plasma actuators.

32. : represents the yaw angle of the left-side rear cyclorotor.

33. : represents the yaw angle of the right-side rear cyclorotor.

34. : represents the inclined angle of the downwash flow from left-side rear cyclorotor.

35. : represents the inclined angle of the downwash flow from right-side rear cyclorotor.

6.6 Detailed Description

The invention is a flight propulsion system for vertical take-off and landing aircraft which comprises pair-wings (2) and two cyclorotors for each side of the craft. The illustration given herein reveals a declaration of this flight propulsion system which is considered for one side of the vehicle and thus can be then configured for both sides for real aircraft applications. Figure 1 shows a schematic of this flight propulsion system and the settlement of the components where the front cyclorotor (1) operates as the main component to inhale airflow for this flight propulsion system. This cyclorotor is positioned about the mid vertical location of the top wing (3) and bottom wing (4) with the possibility to be adjusted relative to lateral, vertical and inclination degree using the 3-DOF control mechanism for pair-wings (5). The two wings are at the same time playing the role of cascade with nozzle-shape channel that with the assistance of the DBD plasma actuators (6) directs the airstream toward the rear cyclorotor (8). Both of the cyclorotors are equipped with

bar-mechanism for pitching oscillation controls of cyclorotors (7) which provide the desired rotational speed and pitching oscillations for each cyclorotor and each single blade, respectively. In spite of the pitching oscillation variations in both cyclorotors that gives a reasonable control and maneuverability, a yawing control mechanism of the rear cyclorotors (9) is also considered which results in instant shift to flight direction. Figure 2 illustrates the functional dynamics specifications of this flight propulsion system. Four principal center locations are defined where the center location of cyclorotors (16), the aerodynamic control center of top wing (21), aerodynamic control center of bottom wing (24) and the reference center point (25) to compute the coordinates of each of these mentioned components in accordance with that to ensure the relative horizontal and vertical distances. Like the profile and type of the wings, the chord length of the top wing (19) and the chord length of the bottom wing (22) as well as the angle of the top wing (20) and the angle of the bottom wing (23) are going to be chosen individually according to the desired outcome. The type of the blade profile of the cyclorotor (10), maximum pitching oscillation angle of cyclorotor (11), rotation speed of cyclorotor (12), the distance between pivot point and leading edge of the blade in cyclorotor (13), pivot point of the blade in cyclorotor (14), the radius of cyclorotor (15) are technically considered and analyzed for each of the front and rear cyclorotors, uniquely. Using the 3-DOF control mechanism for pair-wings (5), the inlet patch of the pair-wings cascade (17) and outlet patch of the pair-wings cascade (18) can be actively changed to control the passing flow portion, and the velocities at the entrance and the exit sections of the cascade. Figure 3 reveals the working principles of the fluid flow passing through this flight propulsion system where the initial airstream enters the front cyclorotor (1) from the airflow inhale region of the cyclorotor (26) and exits from the downwash region of cyclorotor (28). As is defined in this figure, and from what the fundamentals of cyclorotors declare, in a counter clock-wise rotating cyclorotor, the flow enters from the airflow inhale region of the cyclorotor (26) and receiving and upward inclination while exiting from the downwash region of cyclorotor (28). The reason of the larger distance of the top wing (3) from the front cyclorotor (1) is to let the airstream enter the cyclorotor in its ultimate flow rate and to avoid limitations in this regard. The nature of the flow inside the cyclorotor is vertically downward direction as is shown with in-cage flow (27). The bottom wing (4) is thus located in the mid-way to the flow downwash region of front cyclorotor (1) splitting the flow into two separate proportions. One portion convects inside pair-wings nozzle-shape cascade as flow portion entering the pair-wing cascade (30), and the other portion sheds as free-downwash flow of the cyclorotor (29). This downwash portion contributes as the front lift force production of this flight propulsion system. By adjusting the inlet patch of the pair-wings cascade (17) and also the outlet patch of the pair-wings cascade (18), the free-downwash flow of the cyclorotor (29) from the front rotor, and the shedding flow toward the rear cyclorotor (8) can be controlled. In addition, the flow portion entering the pair-wing cascade (30) can be subjected to different angles and speeds by the different arrangements of the top wing (3) and bottom wing (4). Two lateral movements and a rotation motion can be assigned to the aerodynamic control center of the top wing (21) and aerodynamic control center of the top wing

(24) using the 3-DOF control mechanism for pair-wings (5). These adjustments can play significant roles in controlling aircraft lift and thrust forces in different flight phases like forward cruise flight, take-off, landing and hover states. Inducing higher speed airstream and pressure difference toward rear cyclorotor is the key mission of the pair-wings nozzle-shape cascade and the the induced flow from DBD plasma actuators (31). The other major task of DBD plasma actuators are to minimize the flow perturbations and relaminarization of the airstream while convecting toward rear cyclorotor (8). This fact results in a considerably more stable operation, less fatigue and more efficient functional status for the rear cyclorotor (8). Plasma actuators used in the present invention are composed by at least two electrodes and one dielectric layer, which electrically insulates the covered electrode. Typically, the electrodes are made of copper or aluminum foil. For the dielectric layer is typically used Kapton, Teflon, Macor ceramic, silicon or rubber. Plasma actuators operate in such a way that the flow over the bottom wing is attached to the surface and its separation point is delayed. In one embodiment plasma actuators are supplied by an AC high voltage and high frequency signal generator circuit able to produce voltages in a range of 5-80 kVpp and frequencies in a range 1-80 kHz. In other embodiment plasma actuators are supplied by a nanosecond pulse generator circuit which produces a signal with a pulses width between 10-100ns. In another embodiment the plasma actuators may comprise a third electrode which operates as a sliding discharge electrode and it is supplied by a DC power source. In any of the referred embodiments the plasma actuators may present a dielectric layer with constant thickness or a dielectric layer mounted in a stair shaped configuration. During the plasma discharge, the surface temperature may achieve temperatures higher than 100°C [65]. Therefore, if necessary, plasma actuators are also used to perform deicing and/or ice formation prevention. The outlet patch of the pair-wings cascade (18) is configured in such a way that exerts flow induction in the airflow inhale region of the cyclorotor (26). The taken strategy leads to efficiency enhancement in the rear cyclorotor (8) where the rotation speed of cyclorotor (12) is considerably higher in rear cyclorotor than the one in the front cyclorotor (1). The outlet patch of the pair-wings cascade (18) is covering a significant portion of the airflow inhale region of the cyclorotor (26) at rear side. This fact technically changes the functional state of the cyclorotor since it is not working in null-velocity anymore. The flow volume rate entering and leaving the rear cyclorotor (8) is then needs to be analyzed in order to sustain the controllability of the whole propulsion mechanism. The nature of the flow exiting the pair-wings cascade (2) can highly affect the in-cage flow (27) in rear cyclorotor with both direction and velocity. The in-cage flow (27) direction is basically vertical downward, but in the case of rear cyclorotor herein, since there is an adjacent flow entrance from the subsequent settled passage, the in-cage flow direction might alter significantly. This fact can be positively attributed to a better thrust production procedure. Figure 4 describes an aircraft equipped with this flight propulsion system on both sides. The main concern in this figure is the effect of yawing control mechanism of the rear cyclorotors (9) on the free-downwash flow of the cyclorotor (29) of rear side. While considering the aircraft from the top view, as in Figure 4.a, for the downwash flow from the rear cyclorotor, positive yaw is attributed

to the right inclined and the negative is regarded for when the downwash flow is inclined leftward. These positive and negative signs has arbitrarily been assigned for further clarifications and discussions. So, as is demonstrated in bot Figure 4.a and b, when the yaw angle of the left side rear cyclorotor (32) goes positive, a reverse format occurs for the yaw angle of the right side rear cyclorotor (33). Any assigned yaw angle has an impact on the inclined angle of the downwash flow from left-side rear cyclorotor (34) and inclined angle of the downwash flow from right-side rear cyclorotor (35). The main reason to employ the yawing control mechanism of the rear cyclorotors (9) is to attain a considerably higher control for the the last flow exiting this flight propulsion system. By the use of the yawing control mechanism of the rear cyclorotors (9), we can achieve instant shifting of the aircraft flight direction. This characteristic is considered a lack of control efficiency in most of the aircraft to respond to instant altering the flight direction.

6.7 Application Examples

The invention presented here can be applied as a potential flight propulsion system for different scales of aircraft. The proposed invention can provide vertical take-off and landing (VTOL) or even short take-off and landing (STOL) flights for aircraft operating in variety of missions such as UAVs, MAVs, rescue aircraft, payload carriage crafts, commercial aircraft and etc. Considering the significant features that this flight propulsion system proposes, it can be an efficient substitution for the others in aircraft which might handle critical missions where they definitely face VTOL states and even take-off and landing circumstances on marrine and sea surfaces.

6.8 Claims

1. A flight propulsion system is proposed for aircraft providing capability of Vertical Take-Off and Landing (VTOL) using front cycloidal rotor, Pair-wings and rear Cycloidal rotor on each side of the vehicle.

2. In this flight propulsion system, the front cycloidal rotor according to claim 1, is larger in size and lower in rotation speed compared to the rear cycloidal rotor. The front Cycloidal rotor is considered as the main airflow thruster.

3. The pair-wings according to claim 1, are functioning as like high-load gas turbines in which the blades are imposing a value of less than unity for outlet to inlet proportion that decreases the airflow exit area compared to the entered. This fact yields to higher floe velocities while leaving the pair-wings cascade.

4. In this flight propulsion system, according to claims 1 and 2, DBD plasma actuators are employed on the lower wing to induce airstream velocity towards downstream

heading to rear cyclorotor in order to minimize the perturbations shedding from the front cycloidal rotor to avoid flow separation and subsequent losses.

5. In this flight propulsion system according to claims 1, 3 and 4, the pair-wings design are 3-DOF to have the possibility to adjust themselves in optimum operational status in all functional conditions and flight phases such as: take-off, landing, hover, ground and marine working states, VTOL an STOL.

6. In this flight propulsion system, according to claim 1, in addition to pitching oscillation and rotation which are the fundamental operating conditions of both front and rear cycloidal rotors, the rear rotor is capable of yawing from the mid-span position. This feature extremely enhances the controllability and maneuverability of the aircraft to instantly shift the flight direction in all working phases even in hover state.

7. This flight propulsion system can be applied to different craft sizes and for several missions.

8. With this flight propulsion system, the aircraft is capable of VTOL and STOL while carrying payloads or passengers.

9. This flight propulsion system is highly environmental friendly with negligible pollution.

10. This flight propulsion system provides the possibility for the aircraft to take-off and land from/on both ground and marine surfaces.

6.9 Numerical and Experimental Studies

Vertical take off and landing (VTOL) is termed to the aircraft that is capable of vertical take-off and landing and also forward cruise speeds [88]. According to the numerous operational advantageous of these aircraft types, they are increasingly utilized for various missions where we are in short terrains for the VTOL phases. Depending on the main purpose of the aircraft, there have been several operating types designed over years. Conventional helicopters using screw propellers are of the most well-known VTOL crafts. The principal difference of the different VTOL aircraft are mostly regarded to their propulsion systems in order to provide VTOL phases of flight. Cycloidal rotor is one of the multi-bladed systems which has been studied since a century [19]. Tug-boats and sub-marines in naval thrusters, wind turbines in power and energy industry, and airships and aerial crafts in aerospace branch are some of the applications of cycloidal rotors [2]. Since the initial report of cyclorotor usage from Kirsten-Boeing in 1926 [3], more designs of aircraft

with this system as propulsion device in projects like ACROSTAT [6], MAAT [16], CROP [31], BOSCH and IAT21 were further investigated.

Yun et al. [1] studied an unmanned aerial vehicle (UAV) operating with cycloidal rotor in both numerical and experimental approaches. In micro air vehicles (MAV), Benedict et al. [131] conducted extensive numerical and experimental tests in order to higher efficiency achievements in flights. They successfully launched cyclorotor on a 290 gram micro-scale aerial craft with appreciable flight and control capabilities [20]. Rami and Pascoa [41] studied the ground effect on the performance and efficiency of the cyclorotor on an UAV-scale aircraft in take-off or landing phase. In a complementary survey, Habibnia and Pascoa [47] proposed active control of pitching oscillations of the blades using artificial intelligence and neural network analysis. They stated that usign active control method, higher performances are achievable. Aerodynamic operation analysis for cyclorotor-thruster crafts at hovering state was the issue which was investigated both numerically and analytically by Leger et al. [28].

In further improving the cyclorotor efficiency, Xisto et al. [32, 54] performed plasma enhanced blades with the aim of enhanced aerodynamic characteristics. In fact, they implemented dielectric barrier discharge (DBD) plasma actuators on blade surfaces in order to gain higher control on the flow over the rotating-oscillating blades in cycloidal rotor. DBD plasma actuators have been widely proposed to be manipulated for flow controls, separation and flow loss prevention and many other applications in mechanical and aerospace engineering over decades [65, 67, 64]. Plasma actuators are highly featured for their precise and rapid responses, extra-low weight, quite simple implementation and their robustness [65, 127]. DBDs construct three layers with 2 electrodes and one separating dielectric layer in the middle. As the device functions, an electric field configures which ionize the air, then, a generated body force accelerates the ionic charged particles [73, 74].

In the present chapter, a new propulsion design for a VTOL aircraft (Cyclo-craft) is introduced. The system is comprised of two cycloidal rotors combined with pair-wing in between the rotors. Each of these combinations will be launched at both sides of the aircraft. The main concept of the mentioned device is to get the most advantage from the downwash jet flow from the cyclorotor rather than releasing it away. The pair-wing structure in the middle of the two rotors acts as a nozzle vane that guides the flow towards the rear cyclorotor. To be mentioned that the front cycloidal rotor is in a bigger scale than the rear one. This new concept is already passing the international patent considerations as a novel propulsion system for VTOL aircraft.

The plasma actuators are utilized on the surfaces of the wings for better flow control and avoidance of flow losses. One of the main reasons can be to prevent the boundary/shear layer separation while the flow is approaching to the trailing edge of the wings [59, 58]. In this work, the operating mechanism of the proposed propulsion system is studied both numerically and experimentally. Firstly, the system model is undergone through computational fluid dynamics (CFD) approach to further study the flow mechanism and performance evaluation. The other phase of the current study is to experimentally test a multi-DBD plasma fabricated system on the pair-wing assembly. Further illustrations

are accordingly explained and discussed in the subsequent sections.

6.10 Cyclo-craft Design

The proposed propulsion system for VTOL aircraft is a set of consecutive devices with which all are technically influential on each other. This design is basically one of the rare or first structures where it gain advantage from the cyclorotor flow for further thrust production in a system. As is schematically depicted in Fig. 6.6, the front cycloidal rotor is considered bigger in rotor and blade size compared with the rear rotor. In the frontal portion of the system, it is intended to get higher amount of flow stream involved through the system. As will be further explained in subsequent simulations, the downwash jet flow from a cyclorotor gets an inclination when passed out from the bottom-half of the rotor. Imposing counter-clock wise rotational direction for both cyclorotors, their downwash will shift rightward (Fig.6.7), which is the reason of designating the pair-wing right after the front cycloidal rotor. This in fact is to pull a portion of the downwash flow inside the pair-wing vane, and eventually passing it to the rear cyclorotor.
However, to avoid flow separations, and also to further damp the turbulent intensity of the passing flow through the nozzle-shape vane, DBD plasma actuators are proposed as efficient devices to be implemented on the wing surfaces. The experimental tests on applying plasma is discussed later in its specific section. The rear cyclorotor, as shown in Fig. 6.6, is positioned closely after the pair-wing exit patch. Smaller size of this rotor compared with the front one, and the forward flow streaming towards the rear rotor gives the opportunity of running it in comparatively higher rotational speeds.

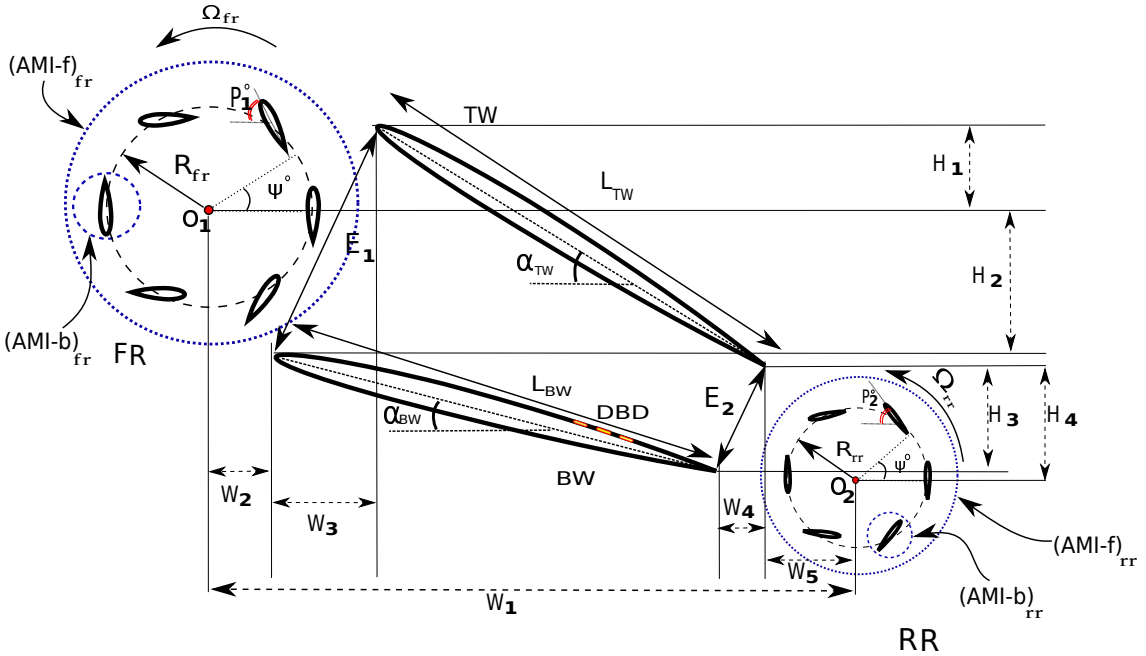

Figure 6.6: Schematic and the specifications of the cyclo-craft design.

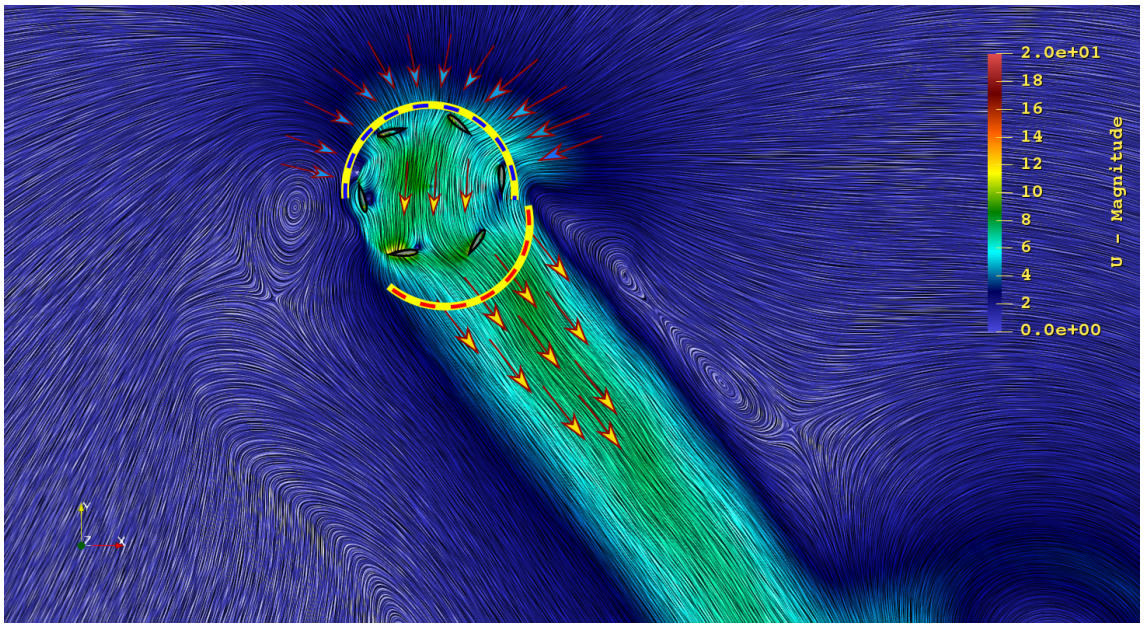

Figure 6.7: Typical LIC contour of a counter-clockwise rotating cycloidal rotor; P:30 degrees, and 400 rpm rotation speed.

Cycloidal rotor were also determined to reveal high maneuverability, low noise production and stable hovering phase as a thruster for VTOL aircraft. On the other side, the rear cyclorotor in the current design can be altered laterally with the origin of the attached point from the craft. This functionality provides high control and fast direction shift of the aircraft since it changes the thrust vector produced by rear cyclorotor. In addition, the proposed propulsion mechanism is also able to perform VTOL from both marine and ground surfaces.

6.11 Numerical Simulation

6.11.1 OpenFOAM Framework

The current CFD simulations are fully conducted using OpenFOAM toolbox. PimpleDyM-Foam solver is appropriately chosen for the numerical approach. The optimum turbulence model for the present cycloidal rotor simulations is k-ω-SST which was recommended for rotational and sensitive flows. The 2 dimensional computational consists of 200 K cells for the coarse and 300 K for fine mesh. For all displacing (rotating and oscillating) zones, *cyclicAMI* technique is used for the overlapping interfaces. The grids are full structured in the whole domain which are completely performed within OpenFOAM using *blockMesh* and *snappyHexMesh* utilities (Fig.6.8).

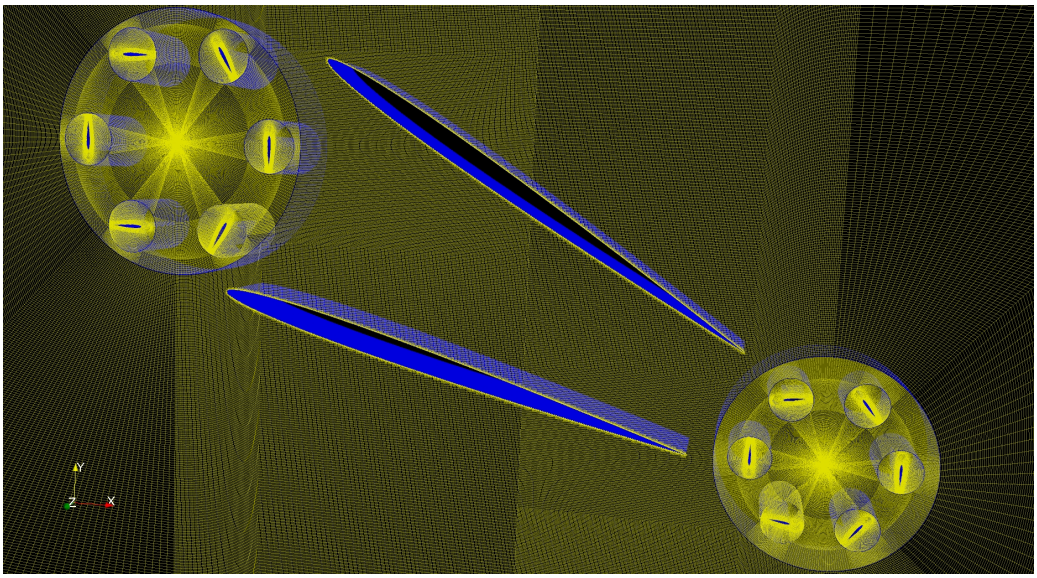

(a) Domain-Mesh View

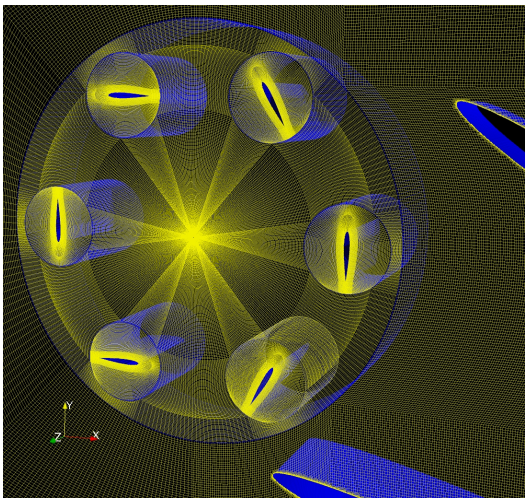

(b) Blade-Mesh View

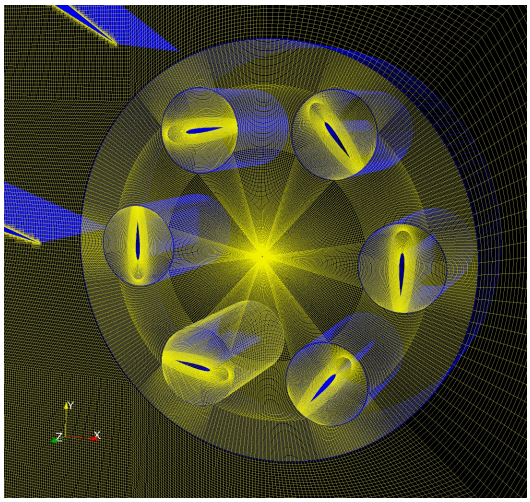

(c) Rotor-Mesh view

Figure 6.8: Mesh Configuration of the cyclo-craft configuration with both 6-bladed cycloidal rotors in front and rear sides.

6.11.2 Code Validation

For the validation of the CFD results with the experiment [1] for cycloidal rotor operation, power and thrust coefficients are used for the comparisons. The experimental results and CFD results for different operating conditions and grids are presented in Fig.6.9. Grid comparisons are shown for different pitch angles and different rotating speeds. All the blade profiles are with NACA0012 airfoils. The front and rear rotors are 0.8 and 0.6 m in diameter, respectively. In the current simulations, the front cyclorotor operates at 400, 500, 600 RPM with constant 35° pitching oscillation, whereas the same parameters for the rear rotor are 700, 800, 900 RPM with 25°, respectively. It should be noted that the rotations are happening in order, meaning that while the front runs at 400, the rear runs at 700 RPM.

Table 6.1: The specifications of the baseline cyclo-craft model design.

Parameter	Value
Number of blades	6
Airfoil profile	NACA0012
R_{fr}	0.3 m
R_{rr}	0.2 m
O_{fr}	(0,0)
O_{rr}	(1.95,-0.8)
C_{Bfr}	0.09 m
C_{Brr}	0.06 m
α_{TW}	31.75°
α_{BW}	14.92°
E_1	0.759 m
E_2	0.334 m
W_1	1.95 m
W_2	0.1696 m
W_3	0.3094 m
W_4	0.1408 m
W_5	0.2347 m
H_1	0.2596 m
H_2	0.4342 m
H_3	0.303 m
H_4	0.2943 m
$D_{AMI(B_1)}$	0.16 m
$D_{AMI(f_1)}$	0.8 m
$D_{AMI(B_2)}$	0.12 m
$D_{AMI(f_2)}$	0.6 m
L_{TW}, L_{BW}	1.454 m
Mesh type	Structured
CFD simulations	2D, 3D
Mesh motion	Dynamic oscillating-rotating, AMI
Turbulence model	k-ε, k-ω-SST
Inlet Turbulence Intensity	2%
Fluid	Air

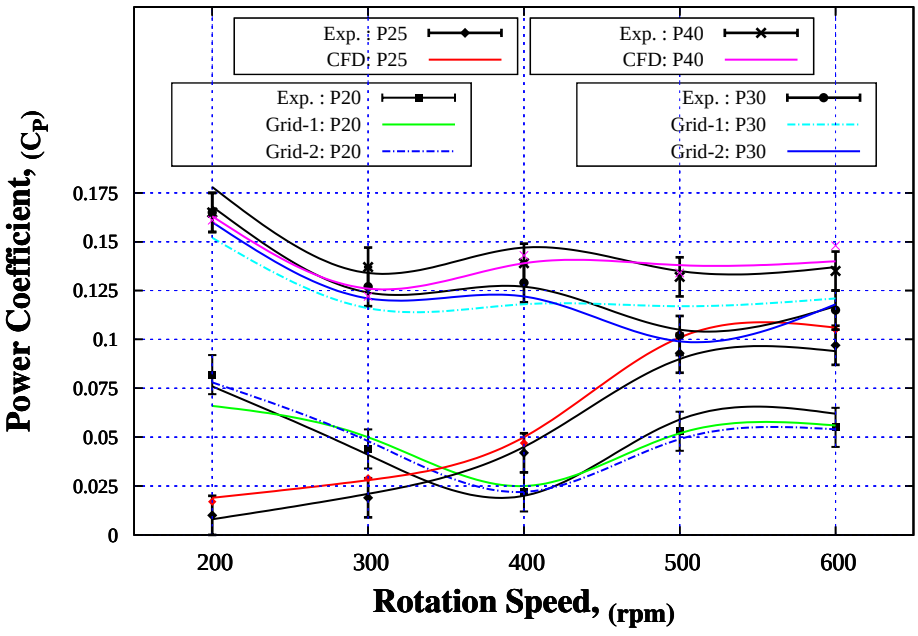

Figure 6.9: Power loading coefficient comparison for different operating conditions and grid structures between CFD and experiment results.

6.12 Experimental setup

To analyse the flow behavior in the pair-wing system of the aircraft flow visualization measurements and Pitot tube measurements were conducted. The experimental setup used is shown in fig. 6.10.

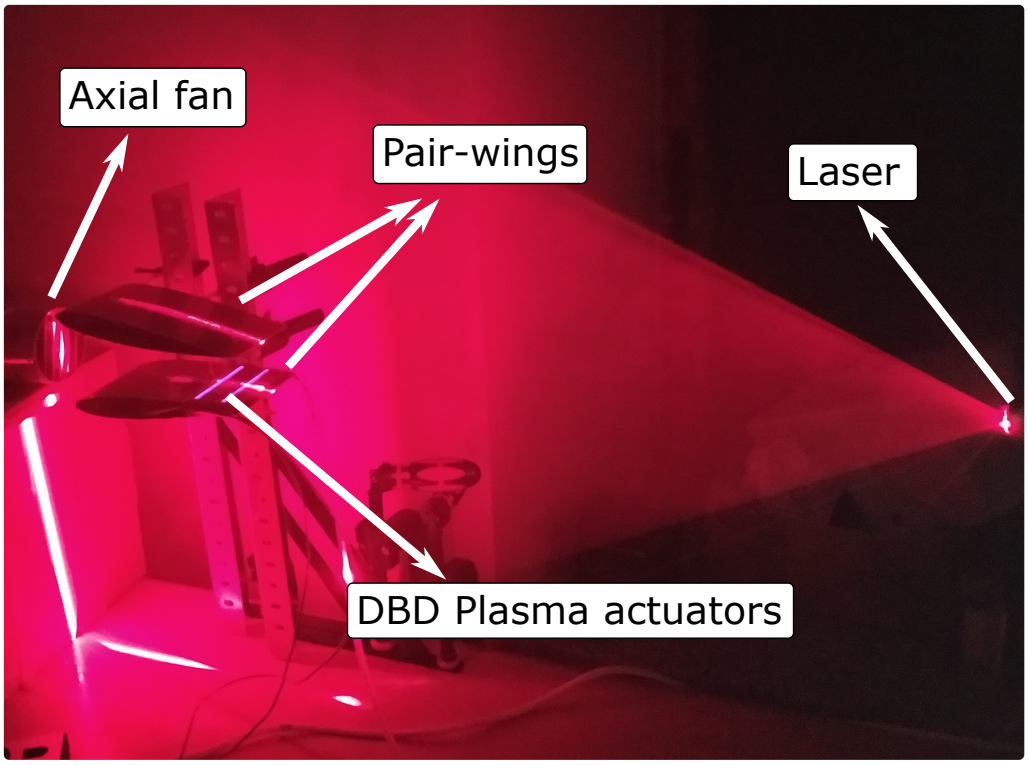

Figure 6.10: Experimental facilities.

The DBD plasma actuators were fabricated with Kapton as dielectric layer and copper tape as electrodes. The electrodes presented $80\ \mu m$ thickness and $80\ mm$ length. The exposed electrode presented a width of $5\ mm$ thickness while the embedded electrode presented a width of $15\ mm$. The dielectric layer presented a thickness of $1.02\ mm$, a width of $50\ mm$ and a length of $100\ mm$. The DBD plasma actuators were supplied by an high voltage power source, model PVM 500, which allows to produce voltages up to $20\ kV$ AC peak-to-peak with frequencies within the range of $20\ kHz$ to $50\ kHz$. The input signal was monitored by a digital oscilloscope model PicoScope $5443A$ connected with an high voltage probe. The DBD plasma actuators were implemented in the top surface of the bottom wing as shown in figure 6.10.

The pair-wing system was constituted by two $NACA\ 0012$ airfoils with a chord length of around $190\ mm$. Considering the complexity of cycloidal rotor thrusters, the inlet flow of the pair-wing system was provided by an axial fan model $HET\ EDF\ 6904$ powered by a brushless motor $Typhoon\ \ EDF$. The brushless motor rotation speed was controlled by means of an electronic speed controller, model $80A-Eco-6S\ ESC$, connected to a pulse-width modulation (PWM) pulse generator, model $PWM\ Hobbyking\ LED\ Servo\ Tester$. This axial fan allows to achieve velocities up to $30000\ rpm$. The axial fan was supplied by a power source model $Puls\ SL\ 30$, which is able to provide $24\ V$ or $28\ V$ DC with a

current up to $30\ A$. The flow visualization images were captured by a digital camera CCD $''C10600-10BOrca-R2''$ which presents a resolution of 1344×1024. A smoke generator, model $Crenova\ FM-02$, with a power of $400\ W$, was used to mark the flow which was illuminated by a laser system model $1\ L2S-SL-660-130-S-A-60$ ***SteamLine Laser System***. Velocity measurements were performed by using a stainless steel Pitot tube, model "167-6" coupled to a micro-manometer, model Extech HD 350. This micro-manometer presents a resolution of $0.01\ m/s$, an accuracy of $1\ \%FS$ and it provides a data live streaming to the computer.

6.13 Results and Discussion

6.13.1 CFD Simulations

The current numerical simulations for the proposed VTOL propulsion system are run for the hovering phase with null velocity. Technically, the desirable condition is to guide a portion of downwash jet from the front cyclorotor toward the pair-wing vane. The downwash jet velocity is relatively high according to the rotating speed of the rotor, hence, the attempts are to avoid full release of this flow to dissipate without extracting the maximum energy from it. This fact facilitates the operation of the rear cyclorotor to comparatively higher angular velocities rather than operating with no induced flow. The entering flow from the pair-wing nozzle vane to the rear rotor provides forward flight state for this rotor as well. The flow velocity contour is depicted in Fig.6.11 for 500 and 800 RPM rotational speeds for the front and rear cyclorotors, respectively. The mid-wings length are both equal and 1.45 m, but each of them are differently positioned and inclined.

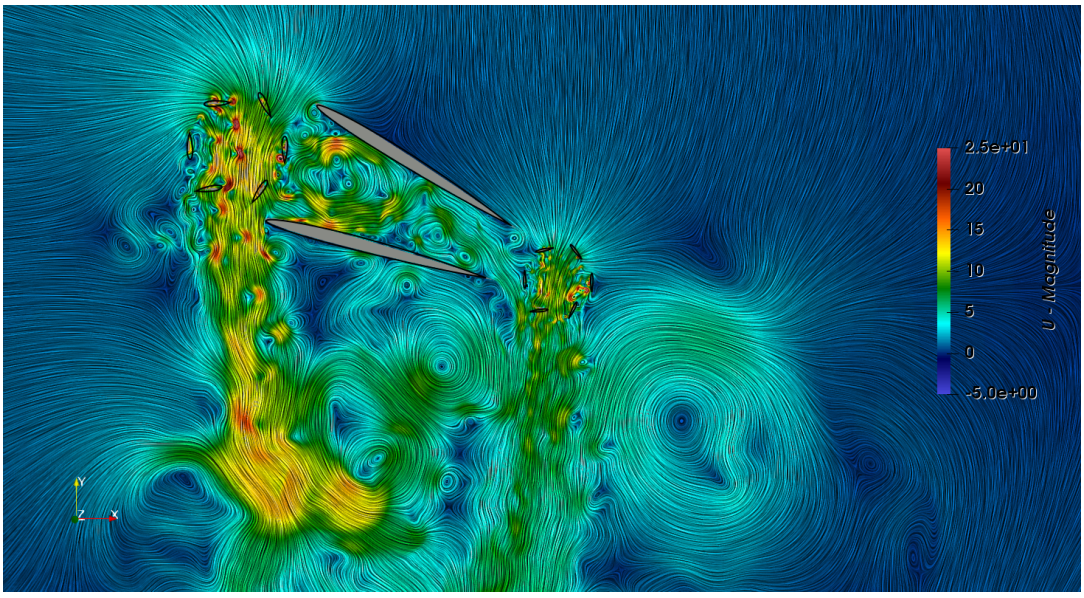

Figure 6.11: Flow velocity contour of the propulsion mechanism at hover-state operation of the cycloidal rotors.

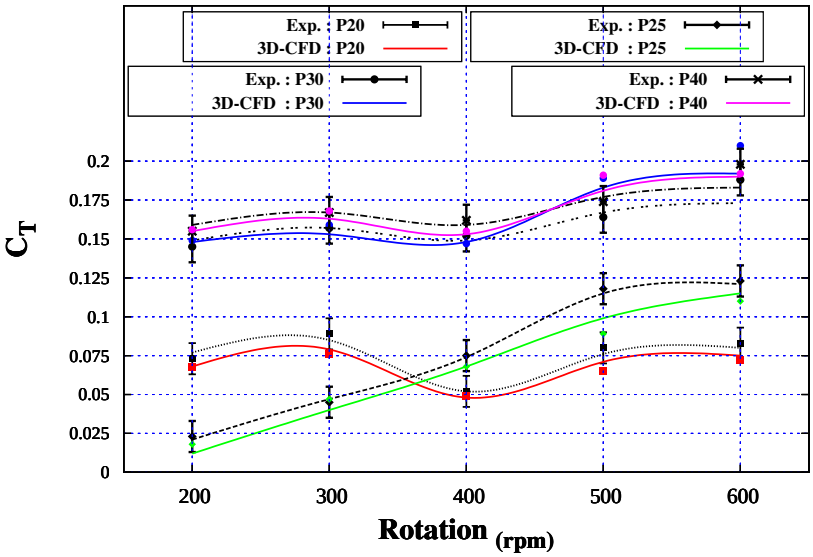

Figure 6.12: Thrust coefficient comparisons for both rotors in single and the coupled cyclo-craft system under different rotational speeds.

As is shown, the proposed design is capable of providing the flow functionality as was expected. The downwash jet flow from the front cyclorotor is shedding rightward as a result of CCW rotational direction. This jet flow splits in two portions as it reaches the pair-wing section. The combination of the cycloidal rotors and the wings in this propulsion mechanism resulted in a considerable higher thrust productions compared with a single-cycloidal rotor thrusters studied for UAV size VTOL aircraft. The plots of the thrust coefficients for each of the cyclorotors (front and rear) individually, and the proposed combined propulsion mechanism is shown in Fig.6.12. The comparisons reveal a higher thrusting performance of the cyclo-craft mechanism than those of single operating cycloidal rotors. This figure shows thrust coefficients for cycloidal rotors with front and rear ones size and operating conditions with red and blue, respectively. This means the a cycloidal rotor with diameter of 0.8 m and 35° pitch angle for the front and one with 0.6 m and 25° for the rear cyclorotor are separately calculated. The front rotor were analyzed at the 3 last rotational speeds and the first 3 values (400, 500 and 600) are set for the rear rotor. For the proposed cyclo-craft, a combination of 3 different sets of rotating speeds are considered. For instance, 400/700 regards to a combination of operating at 400 and 700 RPM for the front and rear cyclorotors, respectively. It is shown that the thrusting performance has increased considerably compared with the individually running cyclorotors.

6.13.2 Experimental Tests

The pair-wing system was experimentally tested for an inlet height section of $8\ cm$ and an outlet height section of $5\ cm$, which means a decrease ratio of 0.625 from the inlet to the outlet. The flow visualization images obtained with and without plasma actuation are presented in figure 6.13.

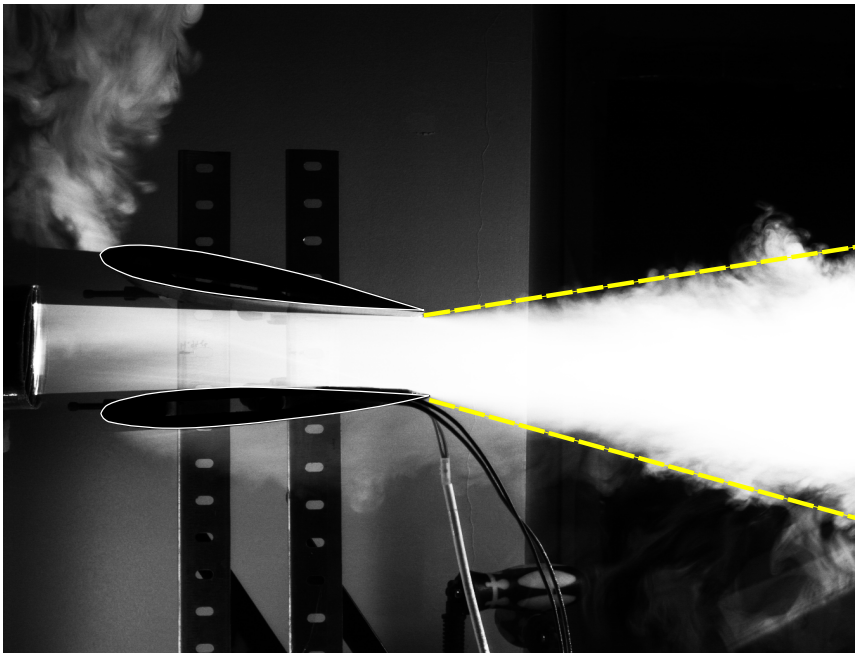

(a) Straight jet flow with plasma actuation off.

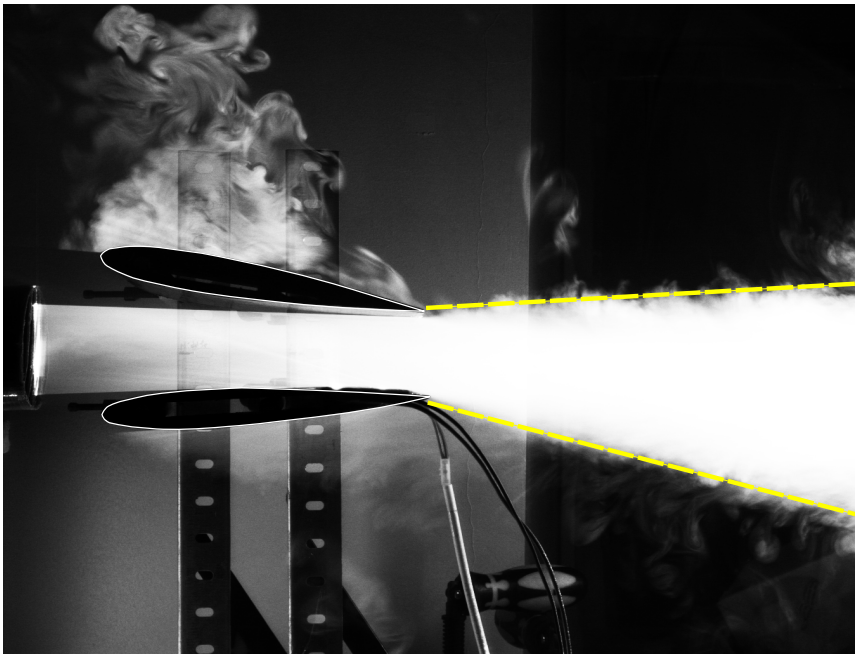

(b) Straight jet flow with plasma actuation on.

Figure 6.13: Flow jet behavior with and without plasma actuation.

In figures 6.13 we present the flow visualization images obtained with the wings positioned for a straight jet flow. The plasma actuators were supplied with a voltage of $10\ kVpp$ and a frequency of $24\ kHz$. In the flow visualization images, two tangent lines to the top and bottom limits of the flow were drawn. At a first look, the plasma actuation effect is not evident but with the help of these lines we see that the flow has a tendency to attach more to the bottom wing. This effect is not that evident because the pair-wing system works as nozzle whose section area is reduced from the outlet to the inlet. Therefore, there is no flow separation in the bottom wing and the plasma actuation effect is reduced. How-

ever, to confirm the plasma actuation effect on the flow velocity field, Pitot tube velocity measurements were performed at the outlet of the system. Notice that the Pitot tube has a diameter of $3\ mm$ thus, the point zero, it actually corresponds to a distance of $1.5\ mm$ from the wall. Figure 6.14 shows the velocity results obtained with an without plasma actuation.

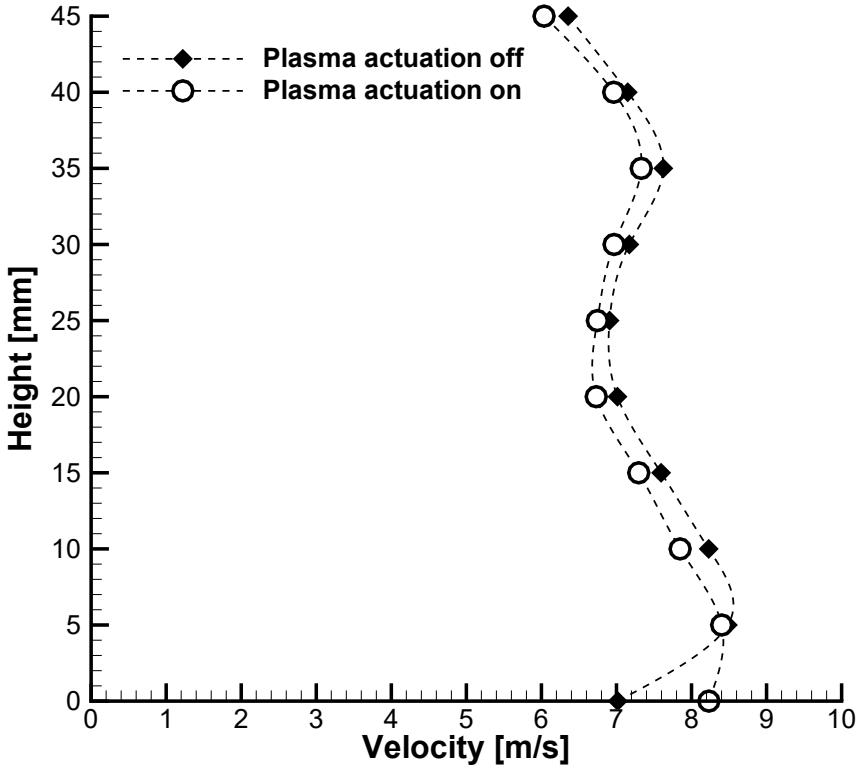

Figure 6.14: Velocity profiles at the pair-wing outlet.

Figure 6.14 shows that the velocity near to the top surface of the bottom wing increases significantly when the plasma actuators are on. We can see that the velocity in this region is approximately $1.25\ m/s$ higher when the plasma actuation is operating. Therefore, we may conclude that when the plasma actuators are turned on, the flow is attached to the surface where they are applied and the flow velocity in this region increases. Due to that, in the regions above the flow velocity slightly decreases since the main flow is slightly displaced to the bottom region. We may conclude that the use of plasma actuation in the pair-wing system may be useful to control the output jet direction and also to reduce the flow losses in the system.

6.14 Neural Network Methodology

Artificial neural network (ANN) has widely shown its practical usage in numerous fields of science and technology and hence it is getting more involved in recent fast-going global industry. This approach is proposed to be able to dynamically analyze the optimum efficiency of cyclorotor in different operating states (Habibnia and Pascoa 2019). Therefore, it has been declared in (Naphon et al. 2019) that ANN can play a significant role while

a combination of datasets in real tests and numerical predictions are going to decide the optimum state of operation.

In the current study 8 parameters are selected as the primary values to be fed into the input nodes, as is depicted in Fig.6.15. These parameters include vertical force (F_Y), horizontal force (F_X), total (net) thrust (T_N), power and thrust coefficients (C_P and C_T), power and disk loadings ($P.L$ and $D.L$) and figure of merit ($F.M$).

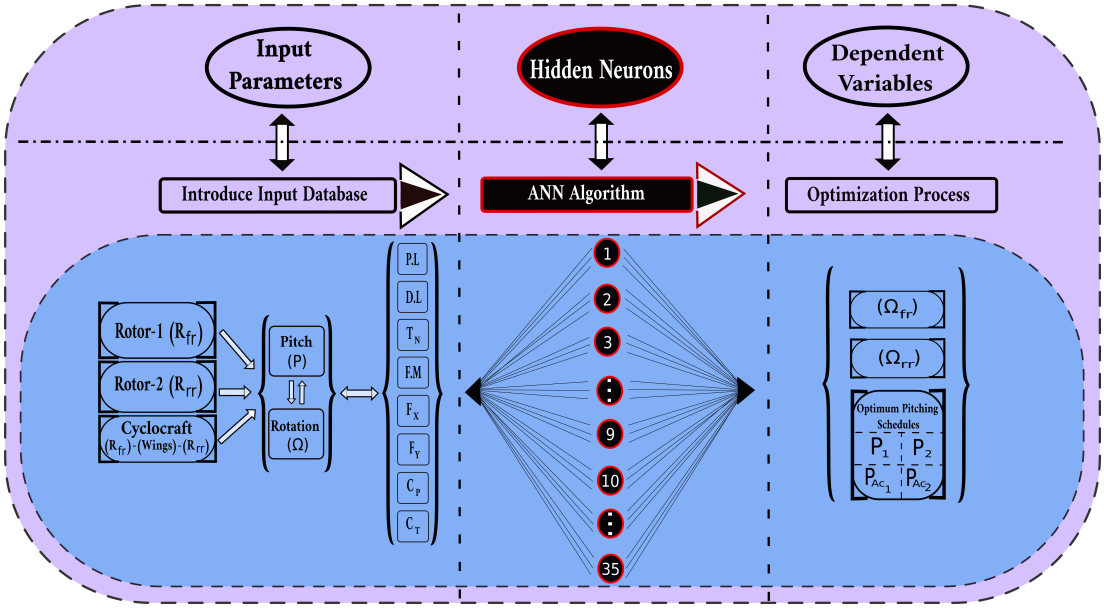

Figure 6.15: Diagram of the optimization procedure proposed, by using neural network analysis.

6.14.1 ANN Performance Analysis

For the current ANN analysis, the approach of forward-feed is chosen, and this demands for a series of layers in order to be able to pursue the entire data-input, training procedure, model validation and desired output. In doing so, the progress of data mapping among the values of input data and outputs has been accomplished by using hidden neurons for training the scheme (Fig.6.16).

Figure 6.17 reveals the evaluation of errors which has reduced sufficiently at a 35 hidden neuron layer. Noteworthy that reaching to higher levels of accuracy is highly dependent to testing and training the database through the ANN model.

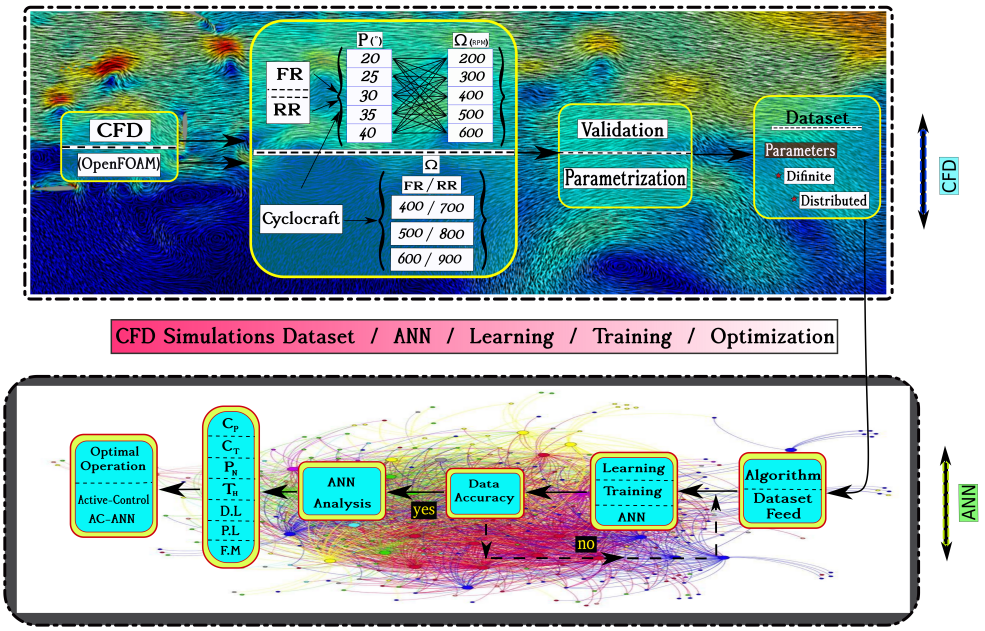

Figure 6.16: Active control flowchart for optimization analysis of ANN and numerical data.

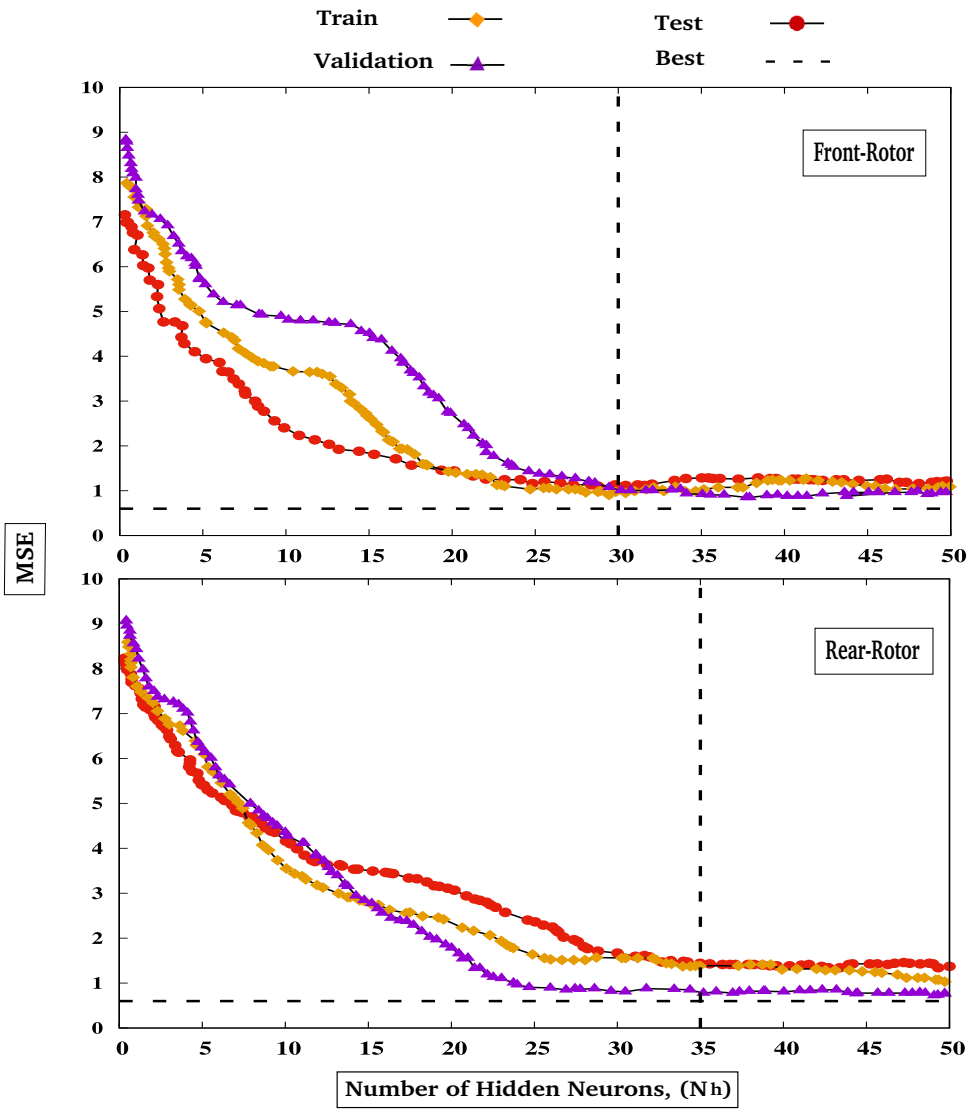

Figure 6.17: Mean square error variation and optimal state vs. number of hidden neurons.

Furthermore, it is shown in Figures 6.18,6.19 that R_C plot tends to rise-up to the maximum level nearly at 35 layers. Therefore, the optimal hidden layer for the current ANN analysis is chosen at 35 which resulted in convenient convergence.

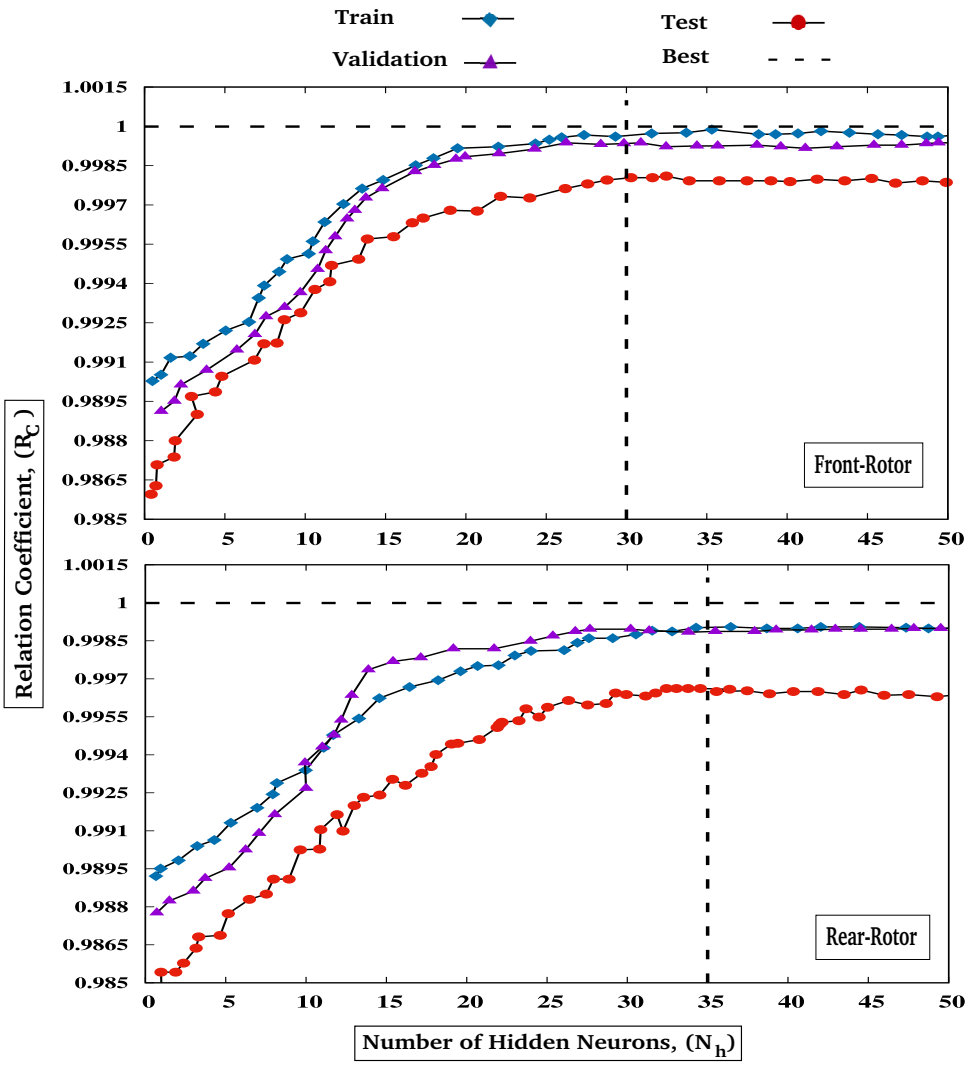

Figure 6.18: Relation coefficient and optimal state vs. number of hidden neurons.

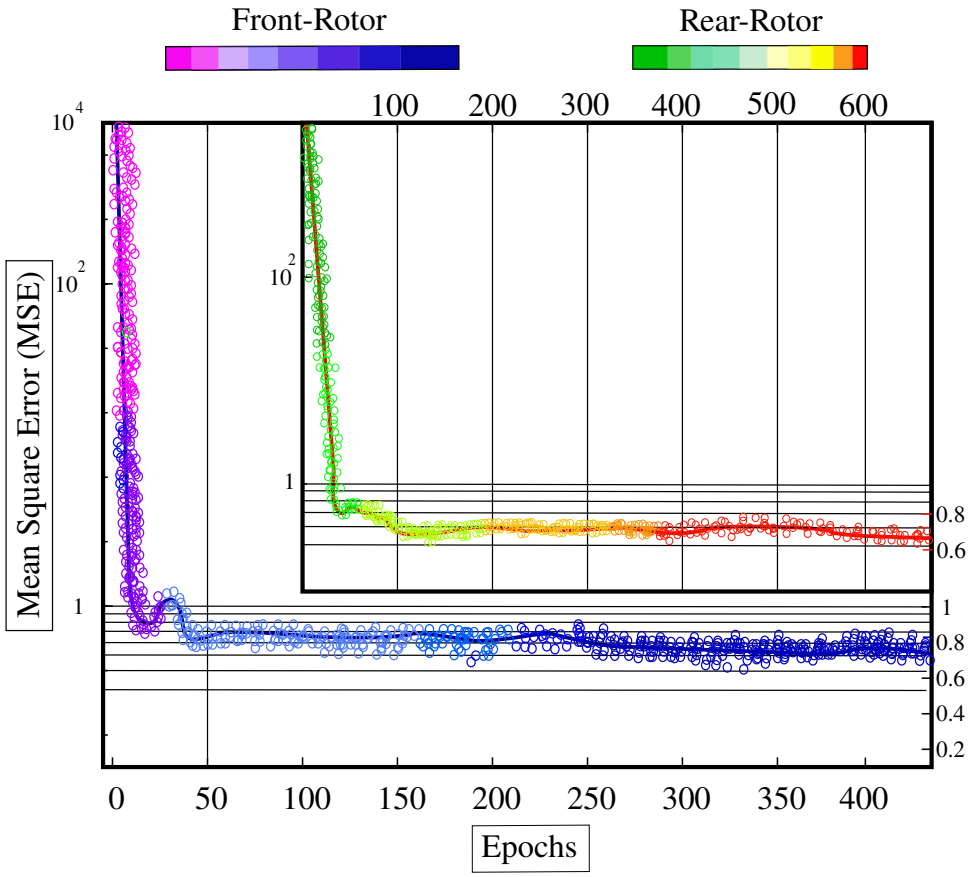

Figure 6.19: Mean square error variation and optimal state vs. number of hidden neurons.

A parametric study of the values of disk loading ($D.L$) (eq.4.12), power loading ($P.L$) (eq.4.13), C_T and C_P at 450 rpm and 30° is shown in table6.2. This is to obtain better vision of the deviations among real tests, numerical predictions and the ANN analysis. The exact value of each parameter, with the corresponding error percentage, as a sign of deviating from experimental tests are all compared in this table.

Table 6.2: Comparison of aerodynamic results of experiments, CFD and ANN optimizations at 30° pitching amplitude, and 450 rpm rotation, in hover state.

Variable	Exp.	2D (CFD)	Error, %	3D (CFD)	Error, %	ANN	Error, %
C_T	0.1582	0.1529	-3.21	0.1552	-1.87	0.1529	-3.32
C_P	0.1196	0.1155	-2.86	0.1203	0.59	11.53	-3.57
D.L	52.81	51.769	-1.97	52.461	-0.66	53.554	1.39
P.L	0.0761	-0.07409	-2.63	0.0749	-1.47	0.0733	-3.65

By using the database which is derived from numerical simulation in CFD, and the data analysis in ANN, the optimum performance of the current cyclo-craft model based on horizontal and vertical forces are proposed in Figures6.20 and 6.21. In doing so, each of the forces are continuously computed over complete cycloidal traces in different rotational speeds for the front and rear rotors independently. The blue and the red curves indicate the front and rear rotor force distributions, respectively.

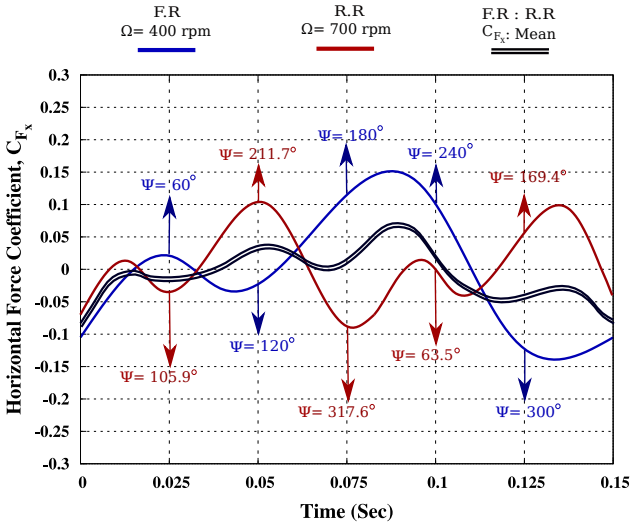

(a) Horizontal force distribution for a front (400rpm) and rear (700rpm) combination

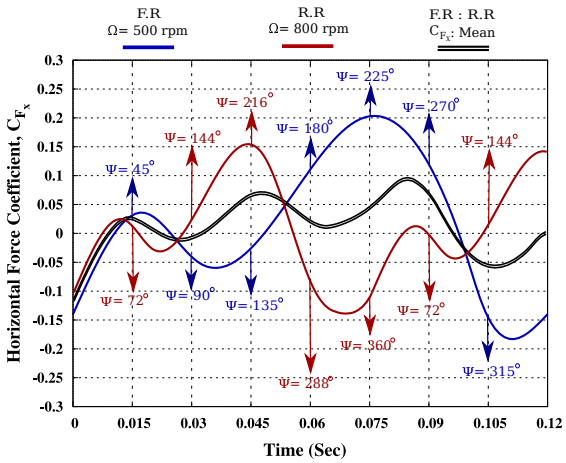

(b) Horizontal force distribution for a front (500rpm) and rear (800rpm) combination

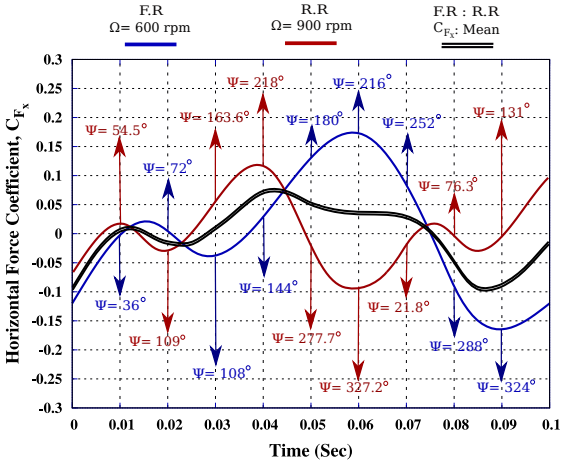

(c) Horizontal force distribution for a front (600rpm) and rear (900rpm) combination

Figure 6.20: The qualitative and quantitative horizontal force coefficient distribution in a complete cycloid trace of cyclo-craft system.

As is shown in these force distribution plots (Figures6.20 and 6.21) the lateral axes are extended according to the longest rotation period which regards to the lowest angular velocities correspondingly. Thus, the faster cycles which apparently belongs to the rear cyclorotor with smaller radius and higher rotation speeds are finishing their cycles in a shorter period compared with those of lower speeds from front rotor. Besides, an average of the force distribution is also calculated through each time scales at which the cyclo-craft is running.

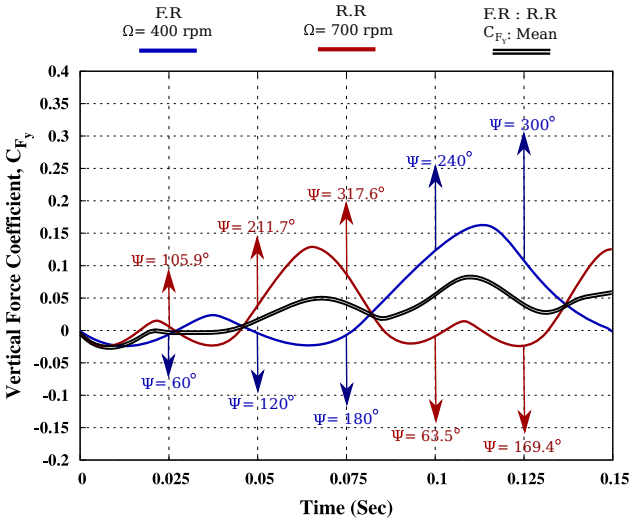

(a) Vertical force distribution for a front (400rpm) and rear (700rpm) combination

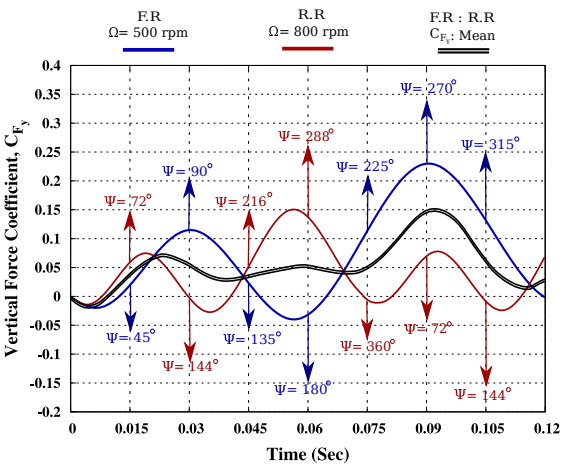

(b) Vertical force distribution for a front (500rpm) and rear (800rpm) combination

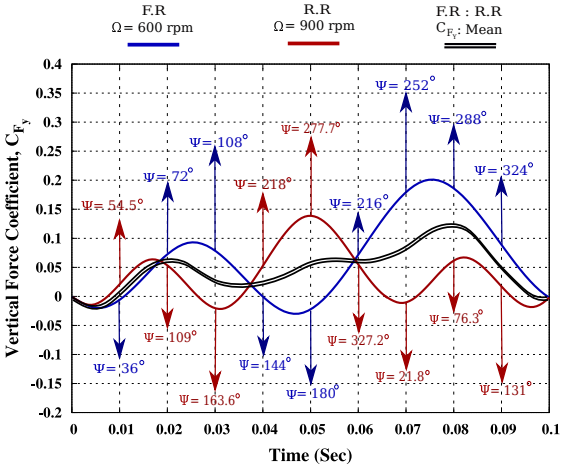

(c) Vertical force distribution for a front (600rpm) and rear (900rpm) combination

Figure 6.21: The qualitative and quantitative vertical force coefficient distribution in a complete cycloid trace of cyclo-craft system.

6.15 Conclusion

A novel propulsion system design that is patented internationally for VTOL capable aircraft is demonstrated in the present chapter. This mechanism (cyclo-craft), is based on two cycloidal rotors (front and rear), and a pair-wing settled between the two rotors. The current study includes CFD simulations, artificial neural network analysis, and experimental tests for the presented system. The numerical study is more specified to the operating flowfield through the system from the front downwash jet to the rear cyclorotor. The CFD results revealed higher thrusting performance of the proposed propulsion system. On the basis of the ANN, the achieved database from numerical work is further analyzed for performance optimizations. The other phase of the current study relates to the experimental evaluations of the presence of DBD plasma actuators on the wing surfaces.

Plasma implementation also showed flow enhancement while passing the pair-wing passage toward the rear cyclorotor. It should be noted that the current study on the patent model is specified to a significant design and operating conditions for initial analysis. All of the including parameters can be varied for other applications and designs.

Chapter 7

Summary Remarks, Conclusions and Future Work

7.1 Conclusions

7.1.1 Hovering Performance and Optimization

The hovering performance of a UAV-scale cyclorotor as a highly significant phase of a VTOL-capable aircraft is numerically studied in this initial chapter. A detailed analysis of the flowfield produced by the cyclorotor blades over the 360° operating cycle was initially performed. In doing so, the study comprises a combination of the blade attitude while traversing the circular cycle and the corresponding flow behavior accordingly. The concept achieves a comprehensive understanding of the flow dynamics in order to propose an active control approach for the cycloidal rotor. This means that instead of imposing constant pitch angles, the blades follow an optimized oscillation schedule. To this end, the current study was carried out in two phases, namely the CFD simulations and the neural network analysis. The CFD phase is accomplished for a sufficiently wide variety of operating conditions, maximum pitch angles (20°, 25°, 30°, 35° and 40°) and rotating speeds (200–600 rpm with +50 intervals). These CFD predictions led to an appropriate database to be used in the subsequent ANN analyses. The second phase of the present study implies to propose a feasible active oscillating schedule for the operating blades, according to performance analysis. Based on the CFD results, the attained values from various parameters in different conditions were fed to the ANN algorithm for the training procedure. Associated with comparatively high accuracy of ANN approach, the output results are further interpreted and solutions are proposed from the optimization analysis. A summary of the conclusions from both the CFD simulations and ANN analysis are illustrated as follow:

1. The highest efficiency achieved from CFD simulations for the base-reference cyclorotor in hover state was found for the operation at 30° of pitch angle and 500 rpm rotating speed.

2. Although from the theoretical point of view, the top-most and bottom-most locations of the cycloidal rotors are producing the highest lift-up force, there might be some deviations from the defined positions for both vertical and horizontal force productions. This was clearly observed from the plots of forces corresponding to azimuthal angle in diverse conditions.

3. CFD results describe the occurrence of an unfavorable induced flow entering the cage at the location range of approximately 340° to 360°, that can be the source of horizontal force negative sign.

4. At a constant rotating speed, the higher pitch angle is defined, the higher speed the induced flow experiences.

5. According to the ANN approach, which has been taken for the active control concept, the following highlighted comments came noticeable:

   a) Keeping the pitching ultimates at the top and bottom positions of the cyclorotor, the top location experiences comparatively higher pitch angle than the bottom.

   b) ANN has proposed to decrease the speed of the IDS phase in order to minimize the efficiency loss, which is originated from induced flow before reaching the end point of the circular cycle.

   c) ANN proposed a pitch varying schedule of the blades for each defined operation state, based on parametric analysis of variables such as thrust, lift, drag, and aerodynamic efficiency. This approach resulted in improved efficiencies by 12 percent for the cyclorotor operating in hover state.

   Overall, the mutual collaboration of the CFD and ANN, resulted in a detailed study of the concept of active control for cycloidal rotors. However, these calculations can be further investigated in real tests to evaluate the performance of the proposed control mechanism of the blades. The way to incorporate the pitch schedule in a real system will constitute a challenge. This includes the use of oscillating frequencies, the feasibility of control at different flight phases, like forward-cruise and vertical lift-up. All these can be studied for future work which might lead to more efficient and even increased performances for a future generation of cycloidal rotors operating at diverse scales.

7.1.2 3D Effects of The Cyclorotor Endwalls

A detailed analysis of the endwalls effect in cycloidal rotors is presented using a coupled methodology based on CFD and ANN optimization. Three different designs of hovering-mode cyclorotor with free sides (SF), single-endwall (SE) and double-endwalls (DE) have been simulated and analyzed at various operating conditions. This study features in calculating the blade aerodynamic parameters over the 360° circular trace continuously. According to the complexity of the flow interactions while the blades are subjected to a combination of rotational and pitching oscillations, the cyclorotor characteristics are all extracted through the four mentioned EUS, EDS, IUS and IDS quarters. A huge database is collected from numerous simulations by considering a representative number of parameters. The database is then used for the learning and training of the ANN algorithm for further optimization analysis. The novel concept in the current work is to propose the optimum pitching schedule for the blades at each corresponding rotational speed, instead of assigning a constant pitch angle to the operations. In this approach, all the three endwall designs are simulated, predicted and optimized for higher performances, and the main contribution of the work is the active control mechanism which is proposed

for the operation of the cyclorotor at different rotational speeds. According to the performed CFD and ANN analysis, the single side endwall design results in about 18.8%, and the doubled design at about 13.6% lower efficiencies than the free sided cyclorotor. However, it has computed that regardless of the overall efficiency, the SE model generates 8% and 11% higher horizontal force values compared with those of DE and SE, respectively. On the other side, the vertical force production has been estimated to be by average 7% and 16% higher in values for DE design compared with the SF and SE models. These features can strongly influence the selection of which design to employ for different applications and purposes in aircraft designs.

7.1.3 Forward-Flight and Lift-up Phases

A combined collaboration of numerical simulations joined with neural network analysis is illustrated. The study is conducted with the aim of optimizing the operating states in a UAV-size cyclorotor for lift-up and forward flight phases. The procedure herein undertaken is to sequentially track the blade and flow in a complete route of 360° trajectory. In doing so, CFD predictions have been accomplished for a range of operating conditions (pitching angles and rotation speeds) in both forward-flight and lift-up modes with different horizontal and vertical speeds, respectively. Subsequently, using the achieved database from CFD post-processing, to train the ANN algorithm, active control optimization analysis was proposed on the second phase. A list of findings from both CFD results and ANN analysis are summarized here:

(a) CFD;

i) Forward-Flight:

a) The arc between $\Psi \approx 90^\circ$ and $\Psi \approx 280^\circ$ is predicted for the inhale region, and the rest belongs to the exhaling part. These regions do not significantly change for different horizontal speeds.

b) Higher pitching angles induce higher flow velocities at constant rotational speed. Likewise, higher forward speed causes higher values of the induced flow velocity.

c) In both horizontal and vertical force distributions, forward-flight shows more deviation from those of hover-state force curves. However, they follow the same peaks and oscillations as the hover mode does.

ii) Lift-up:

a) This phase has shown very similar behavior as hover-state operation. It was presented that merely one third ($210^\circ \leq \Psi \leq 330^\circ$) of the circular trajectory belongs to the exhale arc and from the rest area the flow is inhaled by the cyclorotor.

b) Higher pitching angles induce higher flow velocities at constant rotational speed. Also, same as forward mode, higher lift-up speeds result in higher values of the induced flow velocity.

c) Force distributions in this phase is much closer to the hover-state force curves. Furthermore, they follow the same peaks but with a small variation in the values and a lag in azimuth angle.

(b) AC-ANN;

On the basis of the attained results, and collected database from CFD simulations, the neural network proposed the following items to active control the operating mechanism, in order to achieve higher efficiency levels:

i) Forward-Flight:

a) The strokes of EUS and IUS are assigned to happen with decreased rates, whereas the EDS and IDS are proposed to speed-up while passing the strokes in forward-flight. Top-side point is experiencing about +2° higher AOA compared with the bottom-side position.

b) At constant forward speed, the lower rotation speed is proposed to operate at higher pitching angles and vice versa. Furthermore, higher forward speeds are subjected to sharper incidents of strokes while traversing.

c) The optimum state for forward-flight is assumed to be with 20 $m/_S$ at 570 rpm and active pitching schedule using ANN which results in 0.77 F.M value.

ii) Lift-up:

a) The strokes rates is proposed to happen conversely of in lift-up phase. Meaning that the strokes of EDS and IDS are assigned to pass with decreased rates, while EUS and IUS are proposed to speed-up. Top-side point is experiencing about +3° higher AOA compared with the bottom-side position.

b) Likewise in forward-flight, the lower rotation speed is proposed to operate at higher pitching angles at constant lift-up speeds. Moreover, higher forward speeds are subjected to sharper incidents of strokes while traversing.

c) For lift-up phase, the optimum operating state among three vertical speeds is proposed with 4 $m/_S$ at 370 rpm which brings 0.67 of F.M value.

This study is suggesting the mutual collaboration of CFD simulations and neural network analysis in order to reach higher operating efficiencies in cyclorotors. The active control concept can be further investigated for future real tests to reveal a detailed understanding of the controlling needs, the feasibility of mechanical means to actively change the oscillation schedules and to obtain a practical insight while the cyclorotor is functioning as a thruster for VTOL aircraft in forward-flight and lift-up phases are yet to be fully developed.

7.1.4 Vertical Take-off and Landing Performance at Near-Ground Levels

A numerical study of the operating status of a typical cyclorotor which was previously proposed for unmanned aircraft is investigated through this chapter. The focus was laid to study the role of ground effects on ascending and descending of a

typical unmanned size cyclorotor in VTOL phases. The aim was to clearly predict and propose the optimum conditions using the most influential parameters such as operational altitude, rotation speed and pitching oscillation angle. Furthermore, a neural network field was included as the second phase of this study to obtain better estimative predictions from the already assessed CFD results.

Training the CFD results using neural network analysis truly provided further predictions of the cyclorotor performance in various conditions. CFD results revealed that the optimum operational performance for the close-ground levels is achieved by 30° and 200 rpm for pitching and rotating speed, respectively. Evaluations from ANN also admit that the optimum operational performances are highly dependent to ground distance of the working cyclorotor. This necessitate active control of pitching oscillation angles and rotation speeds to have the cyclorotor operate at its optimum condition at different situations. Active control of cyclorotors can be the subject of future investigations which has not been the point of concern yet.

7.1.5 Novel Flight Propulsion System for VTOL/STOL Aircraft

A novel propulsion system design that is patented internationally for VTOL capable aircraft is demonstrated in chapter-6. This mechanism (cyclo-craft), is based on two cycloidal rotors (front and rear), and a pair-wing settled between the two rotors. The current study includes CFD simulations, artificial neural network analysis, and experimental tests for the presented system. The numerical study is more specified to the operating flowfield through the system from the front downwash jet to the rear cyclorotor. The CFD results revealed higher thrusting performance of the proposed propulsion system. On the basis of the ANN, the achieved database from numerical work is further analyzed for performance optimizations. The other phase of the current study relates to the experimental evaluations of the presence of DBD plasma actuators on the wing surfaces. Plasma implementation also showed flow enhancement while passing the pair-wing passage toward the rear cyclorotor. It should be noted that the current study on the patent model is specified to a significant design and operating conditions for initial analysis. All of the including parameters can be varied for other applications and designs.

7.2 Current Concepts, and Recommendations for future work

Several areas of research in accordance with the efficiency augmentations of cycloidal rotors are yet needs to be performed in all different methods of CFD, experimental tests, and analytics. In the present research, the attempt is laid to follow different perspectives of the operational status of a UAV-scale cyclorotor to be applied on an aircraft. The including approaches in the current work are numerical

simulations and modelings using CFD, experiments, and ANN optimizations which were so far utilized for each of the design aspects individually. Overall, the main concept of the work was to reach to the most optimal operating conditions for each design in all chapters. Except chapter.6 which corresponds to our patent description as a novel propulsion system, the rest were all studied for a constant properties cyclorotor in terms of rotor scale, blade profile and size,and pitching and rotation centers. It is tried to propose an active-control methodology on the basis of pitching schedules at each rotational speed for each of the specific designs discussed in the chapters. This novel methodology are achieved from the CFD computations data and the artificial neural network analysis. One of the possibilities is to consider different scales, design parameters and functional targets to independently study the effectiveness of the proposed methodology in other cases. In addition, designing and running an experimental test based on a new control system that can provide us a feasible pitching oscillations according to the active-controlling schedules would be a significant challenge to pursue.

The other possible area of research is the patent design which is illustrated in the previous chapter. Regardless of the base design properties and specifications, only a single design is performed and all the scaling is just once considered through the simulations and analysis. There is a wide range of parameters in this novel design that can be analyzed to finally reach the optimum design in terms of scaling, operating conditions, the front and rear rotor positions and functions, the pair-wing structure and many other things that can be initiated to study in a comprehensive project framework. This was far beyond the possibility of the current work to provide a deep and detailed study of this design in all aspects and parameters. Various configurations can be subsequently investigated for all designs of all the previous chapters by utilizing optimization analysis.

Bibliography

[1] C. Y. Yun, I. K. Park, H. Y. Lee, J. S. Jung, I. S. Hwang, and S. J. Kim, "Design of a new unmanned aerial vehicle cyclocopter," *Journal of the American Helicopter Society*, vol. 52, no. 1, pp. 24–35, 2007. xvii, xviii, xix, xx, 2, 7, 14, 18, 19, 31, 41, 49, 51, 52, 76, 83, 84, 85, 106, 113, 116, 117, 118, 149, 152

[2] G. Ilieva, J. Páscoa, A. Dumas, and M. Trancossi, "A critical review of propulsion concepts for modern airships," *Open Engineering*, vol. 2, no. 2, pp. 189–200, 2012. 1, 3, 7, 41, 75, 76, 105, 107, 136, 148

[3] H. Sachse, "Kirsten-boeing propeller," *NACA Technical Memorandum*, no. 351, p. ., 1926. 1, 7, 41, 75, 105, 148

[4] R. Gibbens, J. Boschma, and C. Sullivan, "Construction and testing of a new aircraft cycloidal propeller," in *13th Lighter-Than-Air Systems Technology Conference*, 1999, p. 3906. 2, 105

[5] M. Onda, K. Matsuuchi, N. Ohtsuka, and Y. Kimura, "Cycloidal propeller and its application to advanced lta vehicles," in *AIAA's 3rd Annual Aviation Technology, Integration, and Operations (ATIO) Forum*, 2003, p. 6832. 2, 75, 106

[6] M. Onda and Y. Morikawa, "An acrobatic airship 'acrostat'," *SAE transactions*, pp. 2101–2105, 1991. 2, 106, 149

[7] M. Onda, K. Matsuuchi, Y. Kimura, and S. Hashimoto, "Aerobatic airship robot with advanced propulsors," in *Robotics and Automation, 2004. TExCRA'04. First IEEE Technical Exhibition Based Conference on*. IEEE, 2004, pp. 91–92. 2, 106

[8] M. Onda, M. Sano, K. Iwata, K. Tomita, M. Watanabe, N. Koyama, W. Akinaga, and M. Maruyama, "Airship-type crane robot with cycloidal propellers," in *6th AIAA Aviation Technology, Integration and Operations Conference (ATIO)*, 2006, p. 7718. 2, 106

[9] H. Nozaki, Y. Sekiguchi, K. Matsuuchi, M. Onda, Y. Murakami, M. Sano, W. Akinaga, and K. Fujita, "Research and development on cycloidal propellers for airships," in *18th AIAA Lighter-Than-Air Systems Technology Conference*, 2009, p. 2850. 2, 75, 106, 137

[10] I. S. Hwang, C. S. Hwang, and S. J. Kim, "Structural design of cyclocopter blade system," in *46th AIAA/ASME/ASCE/AHS/ASC Structures, Structural Dynamics and Materials Conference*, 2005, p. 2020. 2, 106

[11] I. S. Hwang, S. Y. Min, M. K. Kim, and S. J. Kim, "Multidisciplinary optimal design of cyclocopter blade system," in *46th AIAA/ASME/ASCE/AHS/ASC Structures, Structural Dynamics and Materials Conference*, 2005, p. 2287. 2, 75, 106

[12] I. S. Hwang, S. Y. Min, C. H. Lee, and S. J. Kim, "Development of a four-rotor cyclocopter," *Journal of Aircraft*, vol. 45, no. 6, pp. 2151–2157, 2008. 2, 8, 75, 106

[13] C. Y. Yun, I. K. Park, I. S. Hwang, and S. J. Kim, "Thrust control mechanism of vtol uav cyclocopter with cycloidal blades system," *Journal of intelligent material systems and structures*, vol. 16, no. 11-12, pp. 937–943, 2005. 2, 76, 106

[14] C. Y. Yun, I. Park, H. Y. Lee, J. S. Jung, I. S. Hwang, S. J. Kim, and S. N. Jung, "A new vtol uav cyclocopter with cycloidal blades system," *American Helicopter Society International*, vol. 6, no. 6, pp. 406–412, 2004. 2, 7, 76, 106, 137

[15] J. Strickland, "The darrieus turbine: A performance prediction model using multiple streamtubes. sandia national laboratories, albuquerque, nm," 1975. 2, 76, 106, 137

[16] G. Ilieva, J. Pascoa, A. Dumas, and M. Trancossi, "Maat–promising innovative design and green propulsive concept for future airship's transport," *Aerospace Science and Technology*, vol. 35, pp. 1–14, 2014. 3, 76, 107, 149

[17] X. Wang and L. Cai, "Mathematical modeling and control of a tilt-rotor aircraft," *Aerospace Science and Technology*, vol. 47, pp. 473–492, 2015. 4, 77, 107

[18] P. Zhao, Q. Quan, S. Chen, D. Tang, and Z. Deng, "Experimental investigation on hover performance of a single-rotor system for mars helicopter," *Aerospace Science and Technology*, 2019. 4, 107

[19] C. Boirum and S. Post, "Review of historic and modern cyclogyro design," in *45th AIAA/ASME/SAE/ASEE Joint Propulsion Conference & Exhibit*, 2009, p. 5023. 4, 76, 107, 148

[20] M. Benedict, M. Ramasamy, I. Chopra, and J. G. Leishman, "Performance of a cycloidal rotor concept for micro air vehicle applications," *Journal of the American Helicopter Society*, vol. 55, no. 2, pp. 22 002–22 002, 2010. 4, 107, 149

[21] M. Benedict, M. Mattaboni, I. Chopra, and P. Masarati, "Aeroelastic analysis of a micro-air-vehicle-scale cycloidal rotor in hover," *AIAA journal*, vol. 49, no. 11, pp. 2430–2443, 2011. 4, 76, 107

[22] L. Gagnon, G. Quaranta, M. Morandini, P. Masarati, M. Lanz, C. M. Xisto, and J. C. Páscoa, "Aerodynamic and aeroelastic analysis of a cycloidal rotor," in *44th AIAA Fluid Dynamics Conference*, 2014, p. 2450. 4, 107

[23] L. Gagnon, M. Morandini, G. Quaranta, V. Muscarello, P. Masarati, G. Bindolino, C. Xisto, J. C. Páscoa *et al.*, "Feasibility assessment: a cycloidal rotor to replace conventional helicopter technology," in *European Rotorcraft Forum*, 2014, pp. 2–5. 4, 107

[24] L. Gagnon, M. Morandini, G. Quaranta, V. Muscarello, and P. Masarati, "Aerodynamic models for cycloidal rotor analysis," *Aircraft Engineering and Aerospace Technology: An International Journal*, vol. 88, no. 2, pp. 215–231, 2016. 4, 107

[25] L. Gagnon, M. Morandini, G. Quaranta, P. Masarati, C. M. Xisto, and J. C. Páscoa, "Aeroelastic analysis of a cycloidal rotor under various operating conditions," *Journal of Aircraft*, vol. 55, no. 4, pp. 1675–1688, 2018. 4, 107

[26] H. Navazi and M. Hojjati, "Nonlinear vibrations and stability analysis of a rotor on high-static-low-dynamic-stiffness supports using method of multiple scales," *Aerospace Science and Technology*, vol. 63, pp. 259–265, 2017. 4, 107

[27] "Cycloidal rotor optimized for propulsion," https://cordis.europa.eu/project/rcn/106045/factsheet/en.pdf, European Eunion- FP7. 4, 77, 107

[28] J. A. Leger, J. C. Páscoa, and C. M. Xisto, "Analytical modeling of a cyclorotor in hovering state," *Proceedings of the Institution of Mechanical Engineers, Part G: Journal of Aerospace Engineering*, vol. 229, no. 12, pp. 2163–2177, 2015. 4, 8, 43, 77, 107, 149

[29] J. A. Leger Monteiro, J. C. Páscoa, and C. M. Xisto, "Aerodynamic optimization of cyclorotors," *Aircraft Engineering and Aerospace Technology: An International Journal*, vol. 88, no. 2, pp. 232–245, 2016. 4, 8, 43, 77, 107

[30] J. Leger, J. Páscoa, and C. Xisto, "3d effects in cyclorotor propulsion systems," in *ASME 2015 International Mechanical Engineering Congress and Exposition*. American Society of Mechanical Engineers, 2015, pp. V001T01A004–V001T01A004. 4, 8, 43, 107

[31] "Crop report- european commission fp7." https://cordis.europa.eu/project/rcn/106045_en.pdf, European Eunion-FP7. 4, 77, 107, 149

[32] C. M. Xisto, J. C. Páscoa, M. Abdollahzadeh, J. A. Leger, M. Schwaiger, D. Wills, P. Masarati, and L. Gagon, "Pecyt-plasma enhanced cycloidal thruster," in *50th AIAA/ASME/SAE/ASEE Joint Propulsion Conference*, 2014, p. 3854. 4, 8, 43, 77, 107, 149

[33] M. T. Dakhrabadi and M. Seif, "Influence of main and outer wings on aerodynamic characteristics of compound wing-in-ground effect," *Aerospace Science and Technology*, vol. 55, pp. 177–188, 2016. 4, 5, 8, 76, 108

[34] Y. Qin, P. Liu, Q. Qu, and T. Hu, "Wing/canard interference of a close-coupled canard configuration in static ground effect," *Aerospace Science and Technology*, vol. 69, pp. 60–75, 2017. 4, 8, 108

[35] J. Y. Hwang and O. J. Kwon, "Assessment of s-76 rotor hover performance in ground effect using an unstructured mixed mesh method," *Aerospace Science and Technology*, vol. 84, pp. 223–236, 2019. 4, 8, 108

[36] Q. Qu, X. Jia, W. Wang, P. Liu, and R. K. Agarwal, "Numerical study of the aerodynamics of a naca 4412 airfoil in dynamic ground effect," *aerospace Science and Technology*, vol. 38, pp. 56–63, 2014. 4, 8, 108

[37] J. Hu, J. Huang, Z. Gao, and H. Gu, "Position tracking control of a helicopter in ground effect using nonlinear disturbance observer-based incremental backstepping approach," *Aerospace Science and Technology*, vol. 81, pp. 167–178, 2018. 4, 8, 108

[38] B. B. Kocer, T. Tjahjowidodo, and G. G. L. Seet, "Centralized predictive ceiling interaction control of quadrotor vtol uav," *Aerospace Science and Technology*, vol. 76, pp. 455–465, 2018. 5, 76, 108

[39] Y. Hu, G. Wang, H. Zhang, J. Liu, X. Yang, and B. Zhu, "The effects of advance ratio and blade number on the forward flight efficiency of cycloidal rotor," in *55th AIAA Aerospace Sciences Meeting*, 2017, p. 0096. 5, 77, 108

[40] K. Singh and J. C. Páscoa, "Numerical modeling of stall and poststall events of a single pitching blade of a cycloidal rotor," *Journal of Fluids Engineering*, vol. 141, no. 1, p. 011103, 2019. 5, 27, 42, 49, 77, 82, 108

[41] M. H. Rami and J. Pascoa, "Numerical analysis of a cycloidal rotor under diverse operating conditions and altitudes," SAE Technical Paper, Tech. Rep., 2019. 5, 8, 42, 47, 76, 82, 108, 149

[42] A. J. Wadcock, L. A. Ewing, E. Solis, M. Potsdam, and G. Rajagopalan, "Rotorcraft downwash flow field study to understand the aerodynamics of helicopter brownout," NATIONAL AERONAUTICS AND SPACE ADMINISTRATION MOFFETT FIELD CA AMES RESEARCH ..., Tech. Rep., 2008. 5, 77, 109, 138

[43] G. Iosilevskii and Y. Levy, "Experimental and numerical study of cyclogiro aerodynamics," *AIAA journal*, vol. 44, no. 12, pp. 2866–2870, 2006. 7, 41

[44] J. Boschma, "Modern aviation applications for cycloidal propulsion," in *1st AIAA, Aircraft, Technology Integration, and Operations Forum*, 2001, p. 5267. 7, 41

[45] Y. Hu, H. Zhang, and G. Wang, "The effects of dynamic-stall and parallel bvi on cycloidal rotor," *Aircraft Engineering and Aerospace Technology*, vol. 90, no. 1, pp. 87–95, 2018. 7, 41

[46] D. Shukla, N. Hiremath, and N. Komerath, "A cycloidal rotor and airship system for on-demand hypercommuting," SAE Technical Paper, Tech. Rep., 2016. 7

[47] M. Habibnia and J. Pascoa, "Ann assisted flow modeling and analysis for a cyclorotor in ground effect," *Aerospace Science and Technology*, p. 105495, 2019. 7, 8, 42, 44, 47, 49, 58, 76, 81, 85, 90, 93, 149

[48] J. Morgado, M. Abdollahzadeh, M. Silvestre, and J. Páscoa, "High altitude propeller design and analysis," *Aerospace Science and Technology*, vol. 45, pp. 398–407, 2015. 7

[49] J. Tang, Y. Hu, B. Song, and H. Yang, "Unsteady aerodynamic optimization of airfoil for cycloidal propellers based on surrogate model," *Journal of Aircraft*, vol. 54, no. 4, pp. 1241–1256, 2017. 7, 31, 42, 65

[50] C. H. Lee, S. Yong Min, J. W. Lee, and S. J. Kim, "Design, analysis, and experimental investigation of a cyclocopter with two rotors," *Journal of Aircraft*, vol. 53, no. 5, pp. 1527–1537, 2016. 7, 42

[51] M. Benedict, T. Jarugumilli, V. Lakshminarayan, and I. Chopra, "Effect of flow curvature on forward flight performance of a micro-air-vehicle-scale cycloidal-rotor," *AIAA journal*, vol. 52, no. 6, pp. 1159–1169, 2014. 8, 42

[52] Z. Adams and J. Chen, "Flux-line theory: A novel analytical model for cycloturbines," *AIAA Journal*, pp. 3851–3867, 2017. 8, 42

[53] D. Sun, F. Qu, J. Bai, and C. Yan, "An effective low dissipation method for compressible flows," *Aerospace Science and Technology*, p. 105757, 2020. 8

[54] C. M. Xisto, J. C. Pascoa, J. A. Leger, P. Masarati, G. Quaranta, M. Morandini, L. Gagnon, D. Wills, M. Schwaiger *et al.*, "Numerical modelling of geometrical effects in the performance of a cycloidal rotor," in *6th European Conference on Computational fluid dynamics*, 2014. 8, 43, 77, 149

[55] D. Jürgens, M. Palm, S. Singer, and K. Urban, "Numerical optimization of the voith-schneider® propeller," *ZAMM-Journal of Applied Mathematics and Mechanics/Zeitschrift für Angewandte Mathematik und Mechanik: Applied Mathematics and Mechanics*, vol. 87, no. 10, pp. 698–710, 2007. 9, 43

[56] V. Turbo, "The voith schneider propeller current applications and new developments." 9, 43

[57] N. L. Ficken and M. C. Dickerson, "Experimental performance and steering characteristics of cycloidal propellers," DAVID W TAYLOR NAVAL SHIP RESEARCH AND DEVELOPMENT CENTER BETHESDA MD, Tech. Rep., 1969. 9, 43

[58] M. H. Rami, S. Vakilipour, M. H. Sabour, R. Riazi, and H. Hassannia, "Shear layer investigation through a high-load cascade in low-pressure gas turbine conditions," *International Journal of Mechanical and Mechatronics Engineering*, vol. 13, no. 3, pp. 216–226, 2019. 9, 43, 77, 149

[59] S. Vakilipour, M. Habibnia, M. Sabour, R. Riazi, and M. Mohammadi, "Surface pressure characteristics of a highly loaded turbine blade at design and off-design conditions; a cfd methodology," *Thermophysics and Aeromechanics*, vol. 24, no. 3, pp. 469–482, 2017. 9, 43, 77, 149

[60] K. Ma, J. Li, Q. Li, and Y. Liu, "Experimental study on evolution characteristics of plane subsonic-supersonic shear layer," *Aerospace Science and Technology*, p. 105791, 2020. 9

[61] K. Zhang and A. Wang, "Analysis of near stall condition of high bypass fan rotor based on airworthiness certification," *Aerospace Science and Technology*, p. 105733, 2020. 9

[62] M. Righi, V. Pachidis, and L. Könözsy, "On the prediction of the reverse flow and rotating stall characteristics of high-speed axial compressors using a three-dimensional through-flow code," *Aerospace Science and Technology*, p. 105578, 2019. 9

[63] M. Abdollahzadeh, F. Rodrigues, J. Pascoa, and P. Oliveira, "Numerical design and analysis of a multi-dbd actuator configuration for the experimental testing of acheon nozzle model," *Aerospace Science and Technology*, vol. 41, pp. 259–273, 2015. 9, 43

[64] M. Abdollahzadeh, J. Pascoa, and P. Oliveira, "Modified split-potential model for modeling the effect of dbd plasma actuators in high altitude flow control," *Current Applied Physics*, vol. 14, no. 8, pp. 1160–1170, 2014. 9, 43, 77, 149

[65] F. Rodrigues, J. Pascoa, and M. Trancossi, "Experimental analysis of dielectric barrier discharge plasma actuators thermal characteristics under external flow influence," *Journal of Heat Transfer*, vol. 140, no. 10, p. 102801, 2018. 9, 43, 77, 146, 149

[66] A. R. Sangtabi, A. Ramiar, A. A. Ranjbar, M. Abdollahzadeh, and A. Kianifar, "Influence of repetitive laser pulse energy depositions on supersonic flow over a sphere, cone and oblate spheroid," *Aerospace Science and Technology*, vol. 76, pp. 72–81, 2018. 9, 43, 77

[67] M. Abdollahzadeh, J. Pascoa, and P. Oliveira, "Comparison of dbd plasma actuators flow control authority in different modes of actuation," *Aerospace Science and Technology*, vol. 78, pp. 183–196, 2018. 9, 43, 149

[68] B. Cabral and L. C. Leedom, "Imaging vector fields using line integral convolution," Lawrence Livermore National Lab., CA (United States), Tech. Rep., 1993. 12, 122

[69] B. Loring, H. Karimabadi, and V. Rortershteyn, "A screen space gpgpu surface lic algorithm for distributed memory data parallel sort last rendering infrastructures," Lawrence Berkeley National Lab.(LBNL), Berkeley, CA (United States), Tech. Rep., 2014. 12, 122

[70] H. G. Weller, G. Tabor, H. Jasak, and C. Fureby, "A tensorial approach to computational continuum mechanics using object-oriented techniques," *Computers in physics*, vol. 12, no. 6, pp. 620–631, 1998. 13, 48, 113

[71] M. R. Pendar and E. Roohi, "Detailed investigation of cavitation and supercavitation around different geometries using various turbulence and mass transfer models," in *Journal of Physics: Conference Series*, vol. 656, no. 1. IOP Publishing, 2015, p. 012070. 14

[72] A. Kolahan, E. Roohi, and M.-R. Pendar, "Wavelet analysis and frequency spectrum of cloud cavitation around a sphere," *Ocean Engineering*, vol. 182, pp. 235–247, 2019. 14

[73] M.-R. Pendar and J. C. Páscoa, "Numerical modeling of electrostatic spray painting transfer processes in rotary bell cup for automotive painting," *In-*

ternational Journal of Heat and Fluid Flow, vol. 80, p. 108499, 2019. 15, 149

[74] M. R. Pendar and J. Pascoa, "Numerical investigation of electrostatic spray painting transfer processes for vehicle coating," SAE Technical Paper, Tech. Rep., 2019. 15, 149

[75] S. Wang, D. B. Ingham, L. Ma, M. Pourkashanian, and Z. Tao, "Numerical investigations on dynamic stall of low reynolds number flow around oscillating airfoils," *Computers & Fluids*, vol. 39, no. 9, pp. 1529–1541, 2010. 19

[76] J. J. Hopfield, "Neural networks and physical systems with emergent collective computational abilities," *Proceedings of the national academy of sciences*, vol. 79, no. 8, pp. 2554–2558, 1982. 20, 126

[77] K. Elsayed and C. Lacor, "Modeling, analysis and optimization of aircyclones using artificial neural network, response surface methodology and cfd simulation approaches," *Powder technology*, vol. 212, no. 1, pp. 115–133, 2011. 20, 52, 126

[78] D. Kolokotsa, D. Tsiavos, G. Stavrakakis, K. Kalaitzakis, and E. Antonidakis, "Advanced fuzzy logic controllers design and evaluation for buildings' occupants thermal–visual comfort and indoor air quality satisfaction," *Energy and buildings*, vol. 33, no. 6, pp. 531–543, 2001. 20, 53

[79] D. Westphalen, K. W. Roth, and J. Brodrick, "Fuzzy logic for controls," *ASHRAE Journal*, vol. 45, no. 6, p. K31, 2003. 20

[80] F. Calvino, M. La Gennusa, G. Rizzo, and G. Scaccianoce, "The control of indoor thermal comfort conditions: introducing a fuzzy adaptive controller," *Energy and buildings*, vol. 36, no. 2, pp. 97–102, 2004. 20

[81] K.-T. Yang, "Artificial neural networks (anns): a new paradigm for thermal science and engineering," *Journal of heat transfer*, vol. 130, no. 9, p. 093001, 2008. 20, 22

[82] A. Viano, G. Ottino, L. Ratto, and G. Spataro, "Coupled cfd-ann procedure for extending heat transfer correlations out of their range of validity," in *ASME Turbo Expo 2012: Turbine Technical Conference and Exposition*. American Society of Mechanical Engineers Digital Collection, 2012, pp. 645–655. 20

[83] P. Naphon, S. Wiriyasart, T. Arisariyawong, and L. Nakharintr, "Ann, numerical and experimental analysis on the jet impingement nanofluids flow and heat transfer characteristics in the micro-channel heat sink," *International Journal of Heat and Mass Transfer*, vol. 131, pp. 329–340, 2019. 21, 85, 126

[84] Q. Zhang, K. Ye, Z.-y. Ye, and W.-w. Zhang, "Aerodynamic optimization for hypersonic wing design based on local piston theory," *Journal of Aircraft*, vol. 53, no. 4, pp. 1065–1072, 2016. 21, 53

[85] A. P. Antunes and J. L. F. Azevedo, "Studies in aerodynamic optimization based on genetic algorithms," *Journal of Aircraft*, vol. 51, no. 3, pp. 1002–1012, 2014. 21

[86] S. Haykin, *Neural networks: a comprehensive foundation*. Prentice Hall PTR, 1994. 22, 55, 86

[87] B. Moble, "Fundamental understanding of the cycloidal-rotor concept for micro air vehicle applications," Ph.D. dissertation, University of Maryland, 2010. 28, 31, 36

[88] B. W. McCormick, *Aerodynamics of V/STOL flight*. Courier Corporation, 1999. 41, 148

[89] F. Balduzzi, A. Bianchini, R. Maleci, G. Ferrara, and L. Ferrari, "Blade design criteria to compensate the flow curvature effects in h-darrieus wind turbines," *Journal of Turbomachinery*, vol. 137, no. 1, 2015. 41

[90] M. Raciti Castelli and E. Benini, "Effect of blade inclination angle on a darrieus wind turbine," in *Turbo Expo: Power for Land, Sea, and Air*, vol. 44007, 2010, pp. 857–869. 42

[91] M. Tadjfar and E. Asgari, "Active flow control of dynamic stall by means of continuous jet flow at reynolds number of 1× 106," *Journal of Fluids Engineering*, vol. 140, no. 1, 2018. 42

[92] A. Poels, D. Rudmin, A. Benaissa, and D. Poirel, "Localization of flow separation and transition over a pitching naca0012 airfoil at transitional reynolds numbers using hot-films," *Journal of Fluids Engineering*, vol. 137, no. 12, 2015. 42

[93] D. Rudmin, A. Benaissa, and D. Poirel, "Detection of laminar flow separation and transition on a naca-0012 airfoil using surface hot-films," *Journal of fluids engineering*, vol. 135, no. 10, 2013. 42

[94] P. Ouro, T. Stoesser, and L. Ramírez, "Effect of blade cambering on dynamic stall in view of designing vertical axis turbines," *Journal of Fluids Engineering*, vol. 140, no. 6, 2018. 42

[95] S. Ravelli, G. Barigozzi, E. Casartelli, and L. Mangani, "Assessment of transition modeling and compressibility effects in a linear cascade of turbine nozzle guide vanes," *Journal of Fluids Engineering*, vol. 139, no. 5, 2017. 42

[96] J. P. Gostelow, M. Platzer, and W. E. Carscallen, "On vortex formation in the wake flows of transonic turbine blades and oscillating airfoils," 2006. 43

[97] R. Corral and A. Vega, "Quantification of the influence of unsteady aerodynamic loading on the damping characteristics of airfoils oscillating at low-reduced frequency—part i: Theoretical support," *Journal of Turbomachinery*, vol. 139, no. 3, 2017. 43

[98] A. Vega and R. Corral, "Quantification of the influence of unsteady aerodynamic loading on the damping characteristics of airfoils oscillating at low reduced frequency—part ii: Numerical verification," *Journal of Turbomachinery*, vol. 139, no. 3, 2017. 43

[99] O. Sharma and T. Butler, "Predictions of endwall losses and secondary flows in axial flow turbine cascades," in *Turbo Expo: Power for Land, Sea, and Air*, vol. 79283. American Society of Mechanical Engineers, 1986, p. V001T01A098. 64

[100] R. Gibbens, J. Boschma, and C. Sullivan, "Construction and testing of a new aircraft cycloidal propeller," in *13th Lighter-Than-Air Systems Technology Conference*, 1999, p. 3906. 75, 137

[101] S.-J. Cha, J.-S. Song, H.-H. Lee, S. Na, J.-H. Shim, and P. Marzocca, "Dynamic response control of rotating thin-walled composite blade exposed to external excitations," *Journal of Aerospace Engineering*, vol. 27, no. 5, p. 04014025, 2014. 76

[102] E. Cestino, G. Frulla, E. Perotto, and P. Marzocca, "Experimental slender wing model design by the application of aeroelastic scaling laws," *Journal of Aerospace Engineering*, vol. 27, no. 1, pp. 112–120, 2014. 76

[103] M. Mikilyan and P. Marzocca, "Vibration and stability of coaxial cylindrical shells with a gap partially filled with liquid," *Journal of Aerospace Engineering*, vol. 32, no. 6, p. 06019006, 2019. 76

[104] A. Ceruti and P. Marzocca, "Conceptual approach to unconventional airship design and synthesis," *Journal of Aerospace Engineering*, vol. 27, no. 6, p. 04014035, 2014. 76

[105] A. Rahdan, H. Bolandi, and M. Abedi, "Design of on-board calibration methods for a digital sun sensor based on levenberg–marquardt algorithm and kalman filters," *Chinese Journal of Aeronautics*, vol. 33, no. 1, pp. 339–351, 2020. 78

[106] P. Farrell and J. Maddison, "Conservative interpolation between volume meshes by local galerkin projection," *Computer Methods in Applied Mechanics and Engineering*, vol. 200, no. 1-4, pp. 89–100, 2011. 115

[107] E. L. de Angelis, F. Giulietti, and G. Pipeleers, "Two-time-scale control of a multirotor aircraft for suspended load transportation," *Aerospace Science and Technology*, vol. 84, pp. 193–203, 2019. 126

[108] H. A. Gerhardt, "Paddle wheel rotorcraft," Nov. 30 1993, uS Patent 5,265,827. 134

[109] T. H. Sharpe, "Lift augmenting device for aircraft," Mar. 25 1980, uS Patent 4,194,707. 134

[110] Y. Feldman, "Aircraft," Dec. 29 2016, uS Patent App. 14/751,180. 134

[111] A. G. Bergman, "Vertical-rising airplane," Apr. 15 1930, uS Patent 1,754,977. 135

[112] B. A.G. Crimmins, Jr., "Cyclorotor composite aircraft," Apr. 15 1984, uS4482110. 135

[113] W. G. A. Auguste, "Aircraft with mixed type propulsion and sustaining means," May 16 1950, uS Patent 2,507,657. 135

[114] P. Peebles, "Fluid dynamic lift generation," May 15 2001, uS Patent 6,231,004. 135

[115] ——, "Aerodynamic lift generating device," Mar. 4 2003, uS Patent 6,527,229. 135

[116] K. Kirsten, "Propeller," Mar. 4 1921, uS1432700. 136

[117] H. M. Heuver, "Cycloidal rotor for aircraft," Jan. 1 1952, uS Patent 2,580,428. 136

[118] P. Servanty, "Rotor for developing sustaining and propelling forces in a fluid, steering process, and aircraft equipped with such rotor," Mar. 31 1992, uS Patent 5,100,080. 136

[119] M. Benedict, C. C. Runco, and D. A. Coleman, "Cycloidal rotor micro-air vehicle," Nov. 7 2019, uS Patent App. 16/473,698. 136

[120] H. Sachse, "Kirsten-boeing propeller," 1926. 137

[121] M. Onda, K. Matsuuchi, N. Ohtsuka, and Y. Kimura, "Cycloidal propeller and its application to advanced lta vehicles," in *AIAA's 3rd Annual Aviation Technology, Integration, and Operations (ATIO) Forum*, 2003, p. 6832. 137

[122] M. Onda and Y. Morikawa, "An acrobatic airship'acrostat'," *SAE transactions*, pp. 2101–2105, 1991. 137

[123] M. Onda, K. Matsuuchi, Y. Kimura, and S. Hashimoto, "Aerobatic airship robot with advanced propulsors," in *IEEE Conference on Robotics and Automation, 2004. TExCRA Technical Exhibition Based.* IEEE, 2004, pp. 91–92. 137

[124] X. Xiao, D. McRae, H. Hassan, F. Ruggiero, and G. Jumper, "Modeling atmospheric optical turbulence," in *44th AIAA Aerospace Sciences Meeting and Exhibit*, 2006, p. 77. 137

[125] C. Yun, I. Park, H. Lee, and J. Jung, "H is (2007) design of a new unmanned aerial vehicle cyclocopter," *Journal of the American Helicopter Society*, vol. 52, no. 1. 137

[126] H. Yu, W. Geng Qi, Z. Hai Lang, F. Xu Yang, and F. Hussain, "The effects of advance ratio and blade number on the forward flight characteristics of cycloidal rotor," *Proceedings of the Institution of Mechanical Engineers, Part G: Journal of Aerospace Engineering*, vol. 233, no. 2, pp. 573–588, 2019. 137

[127] F. Rodrigues, J. Pascoa, and M. Trancossi, "Heat generation mechanisms of dbd plasma actuators," *Experimental thermal and fluid science*, vol. 90, pp. 55–65, 2018. 138, 149

[128] N. J. Vickers, "Animal communication: when i'm calling you, will you answer too?" *Current biology*, vol. 27, no. 14, pp. R713–R715, 2017. 138

[129] M. L. Post and T. C. Corke, "Separation control using plasma actuators: Dynamic stall vortex control on oscillating airfoil," *AIAA journal*, vol. 44, no. 12, pp. 3125–3135, 2006. 138

[130] F. R. M. Abdollahsadehsangroudi, J.C. Pascoa, "System for ice detection/prevention and flow control based on the impression of sliding plasma actuators with dielectric discharge barrier," Nov. 7 2018, wO2018/060830 A1. 139

[131] M. Benedict, E. Shrestha, V. Hrishikeshavan, and I. Chopra, "Development of a micro twin-rotor cyclocopter capable of autonomous hover," *Journal of Aircraft*, vol. 51, no. 2, pp. 672–676, 2014. 149

Appendix A

Publications and Achievements During Current Project

A.1 International Patent

M.HabibniaRami, F. Rodrigues, J. Pascoa: Flight Propulsion System Based on Rotary and Stationary Devices, Application Ref.: PPP 2020/9959.

A.2 Articles in international journals and conferences

M.HabibniaRami, J. Pascoa: ANN assisted flow modeling and analysis for a cyclorotor in ground effect, Journal of Aerospace Science and Technology, 2019 Dec 1;95:105495, P(1-13), DOI: 10.1016/j.ast.2019.105495.

M.HabibniaRami, J. Pascoa: Numerical Analysis of a Cycloidal Rotor under Diverse Operating Conditions and Altitudes, SAE, International Journal of Advances and Current Practices in Mobility, 2019, 2.2019-01-1872: 792-802, DOI: 10.4271/2019-01-1872.

F. Rodrigues, *M.HabibniaRami*, J. Pascoa: Novel Propulsion System For VTOL Aircraft Based on Cycloidal Rotors Coupled With Wings, Proceedings of Fluids Engineering Division Summer Meeting-FEDSM, Orlando, Florida, USA, 2020, P(1-13), DOI: 10.1115/FEDSM2020-20292.

M.HabibniaRami, F. Rodriues, J. Pascoa: A Novel Propulsion System Based on Cycloidal Rotors coupled with Pair-wing for VTOL Aircrafts; Cyclo-Craft, Progress in Canadian Mechanical Engineering, 2020, V.3, P(1-6), DOI: 10.32393/csme.2020.55.

M.HabibniaRami, J. Pascoa: Active Control Assessments towards Optimizing the Performance of a Cycloidal rotor at Hover; A Coupled CFD and ANN Methodology, Submitted to Journal of Aerospace Science and Technology, n° pages (50) , 2020.

M.HabibniaRami, J. Pascoa: A Coupled Active Control Technique for Oscillating Blades in a Cycloidal Rotor Using CFD and ANN Analysis by Including 3D Endwall

Effects, Submitted to Journal of Fluids Engineering, n° pages (21), 2020.

M.HabibniaRami, J. Pascoa: Performance Optimization of Forward-Flight and Lift-Up Phases in a Cycloidal rotor Using an Active Control Mechanism, Submitted to Journal of Aerospace Engineering, n° pages (57), 2020.